Application and Patterning of Atomic and Small-Molecule Resists for Area-Selective Deposition on Silicon

By

Patrick R. Raffaelle

Submitted in Partial Fulfillment of the

Requirements for the Degree

Doctor of Philosophy

Supervised by Alexander A. Shestopalov

Department of Chemical Engineering

Arts, Sciences and Engineering

University of Rochester

Rochester, New York

2024

Table of Contents

Biographical Sketch

The author graduated *cum laude* from the Rochester Institute of Technology (RIT) in 2018 earning a Bachelor of Science degree in chemical engineering. He was then awarded a Master of Science degree in advanced chemical engineering from Imperial College London (IC) in 2019 with a designation of merit. In the summer of 2019, he then enrolled into the chemical engineering doctoral program at the University of Rochester (UR) and began research under Dr. Alexander Shestopalov. During his time at UR he published two first author papers in *ACS Applied Materials & Interfaces* and *Langmuir* and gave two talks at ACS Fall 2023 and one talk at AIChE Annual Meeting 2023. He also helped organize social activities within the department as a student representative on the Graduate Student Activities Committee (GSAC) from March, 2023 to March, 2024.

Publications

1). **Raffaelle, P. R.**, Hoffman, B. N.; Demos, S. G., Wang, G. T., Shestopalov A. A. "Formation of Ultra-Thin Oxide on Hydrogenated Si(100) via Pulsed Laser Radiation". *ACS Applied Materials & Interfaces*. 2024, in submission.

2). **Raffaelle, P. R.**, Wang, G. T., Shestopalov, A. A. Light-Mediated Contact Printing of Phosphorus-Species Onto Silicon Using Carbene-Based Molecular Resists. *Langmuir*. 2024, 40 (23), 12027-12034.

3). **Raffaelle, P. R.**, Wang, G. T., Shestopalov, A. A. Vapor-Phase Halogenation of Hydrogen-Terminated Silicon(100) Using N-Halogen-succinimides. *ACS Applied Materials & Interfaces*. 2023, 15, 47, 55139–55149.

4). M. K. Wilsey, K. R. Watson, O. C. Fasusi, B. P. Yegela, C. P. Cox, **Raffaelle P. R.**, L. Cai, A. M. Müller, Selective Hydroxylation of Carbon Fiber Paper for Long-Lasting Hydrophilicity by a Green Chemistry Process. *Adv. Mater. Interfaces*. 2023, 10, 2201684.

Acknowledgments

Firstly, I would like to sincerely thank my thesis advisor Dr. Alexander Shestopalov for allowing me the opportunity to engage in meaningful work within his group. His endless support and patience proved crucial to my finishing this journey. Whenever I needed feedback for a presentation or just had a mundane laboratory question, he always responded in a well-thought out and timely manner. His expertise in the field of surface chemistry was indispensable to me and served as a guiding light while I was fumbling around in the darkness during the various stages of my research projects. His organized supervision of my thesis projects brought the proper amount of structure that I needed to complete this work. Lastly, although I'm sure I tested his patience on several occasions, he never let it show! And for that I am very much in his debt. I have no doubt that the experience I have gained will prove invaluable in the future.

I would also like to thank Dr. George Wang, Dr. Lewis Rothberg, and Dr. John Lambropoulos for agreeing to sit on my PhD thesis committee. I deeply appreciate all the time and consideration they afforded me as I consulted with them on these various projects. Specifically, I wish to thank Dr. Wang for all the feedback and edits he provided for each manuscript that I submitted to academic journals. I greatly enjoyed meeting with him during his visit to the University of Rochester and very much hope to discuss more with him in the future. I want to thank Dr. Rothberg for allowing me access to his lab resources and the considerable time he devoted in putting together the BASI setups for both the vapor phase reaction cell and the laser patterning system. Lastly, I want to acknowledge the thermal modeling developed by Dr. Lambropoulos which gave us pivotal insight into the oxidative mechanism of our laser patterning experiments.

Speaking of the laser patterning studies, I would also like to acknowledge the invaluable assistance from the Laboratory for Laser Energetics (LLE) Optical Materials Technology group led by Dr. Stavros Demos. Dr. Demos, Brittany Hoffman, and Alexi Kozlov each helped me carry out every laser experiment over a three year span. I wouldn't have been able to collect any results without their key participation. Dr. Demos made it all possible by allowing me the more than generous access to his group's lab resources and instrumentation. The bulk of the laser experiments were conducted with Brittany and for that I want her to know that I am deeply appreciative. Her expertise provided a significant guiding influence during experimentation and ensured that meaningful results were always gathered. I hope that I wasn't too much a nuisance to her, especially when there was troubleshooting, which she was always able to accomplish.

Throughout my PhD, I relied heavily on the considerable resources of the URNano shared facilities. In the course of using their tools and equipment, I relied on the continued support of the staff including Bill McIntyre, Jim Mitchell, Will Houlihan, Dr. Gregory Madejski, and Dr. Sean O'neal. Bill and Sean provided essential expertise and advice when it came to using their high-power microscopes. Sean was also immensely helpful when it came to the x-ray photoelectron spectrometer. Both Jim and Greg always lent a helping hand in the cleanroom. Additionally, each one of them trained me on various tools and for that I am deeply grateful.

I would like to acknowledge our collaborators in the Teplyakov group at the University of Delaware. Dr. Andrew Teplyakov, Dr. Dhamelyz Quinones, Tyler Parke, and John Mason were all very pleasant to work with and made the collaborative experience one of the highlights of my PhD. I would especially like to thank Dr. Teplyakov for his considered feedback on some of my results that always gave me a lot to think about. I learned a lot from my visits to their lab and their trips to our lab.

Lastly, I wouldn't have gotten very far without the continued support and assistance from the other members of the Shestopalov group that I had the privilege to work with during my five years at the U of R. I want to thank Dr. Jason Wallace, Dr. Soyoun Kim, Dr. Nan Liu, Dr. Fakhraddin Dourbash, and Dr. Ruobin Jia for helping me orient myself during my first years in the group. The lab atmosphere that I was greeted with was conducive to learning and allowed me to acclimate myself in a timely manner. Whether I needed to know how to set up a new reaction or find something in the lab, everyone in the group was more than willing to assist me in those early months. I want to especially thank Dr. Dourbash and Dr. Jia who became very close friends of mine. I would also like acknowledge all the members of the Shestopalov group that have arrived since I was member. Russell Dent, Zonglun Li, and Leonid Solodov have all helped to maintain the same dynamic research atmosphere that the former members fostered. I especially enjoyed working alongside Zonglun as he continues some of the same projects that I have worked on. I am excited to see the progress that he makes and am sure that it will exceed that of mine!

Abstract

The fabrication of 2D devices with micro/nano-scale features often rely on assembly from a top-down perspective, where the design emphasis is on the removal of material to generate surface features. Common “top-down” approaches to fabrication often include “pattern and subtract” techniques which require energy-intensive processing and result in a high volume of material waste of substances such as photoresists, etchant, and developers. In addition to high energy and material dissipation, traditional “top-down” approaches have also struggled to adapt to the continuous downsizing of critical dimensions of 3D device components. Thus, instead of generating devices from a “top-down” perspective, there has been a push over the last two decades to instead leverage the intrinsic differences in chemical behavior between surface species, such that feature deposition selectively begins at the surface and grows vertically in an additive fashion via reaction from the “bottom-up”. Here, I will evaluate the ability of different small molecule and atomic layers to enable selective deposition on a silicon substrate. Specifically, I will be investigating a carbenylated organic molecule, a perfluorinated amine, and atomic halogen species on their ability to inhibit deposition atomic layer deposition (ALD) of a metal oxide. When paired with a hydrolyzed surface (which promotes metal oxide growth), these inhibiting species may be used to form complementary resist systems which can enable area-selective ALD (AS-ALD) on a surface. Another primary consideration in “bottom-up” approaches to feature fabrication is the ability to pattern these small molecule and atomic surface layers such that they form a template for selective growth. To this end, I will explore using ultrafast laser patterning and contact transfer printing to selectively deposit or alter these surface layers to generate complementary surface domains that can serve as a foundation for a AS-ALD platform.

Contributors and Funding Sources

The members of the PhD thesis committee were Dr. Lewis J. Rothberg, Dr. Alexander A. Shestopalov, and Dr. George S. Wang. All data gathered in this document represents my independent work. The laser patterning project reported in **Chapter 4** was conducted in collaboration with member from the Optical Materials Technology group at the LLE. This work was supported by the National Science Foundation CMMI division under Grant No. 2225896. The project was also funded by the Laboratory Directed Research and Development program at Sandia National Laboratories, a multi-mission laboratory managed and operated by National Technology and Engineering Solutions of Sandia, LLC., a wholly owned subsidiary of Honeywell International, Inc., for the U.S. Department of Energy's National Nuclear Security Administration under contract DE-NA-0003525. Lastly, the material is in part based upon work supported by the "National Inertial Confinement Program" under Award Number(s) DE-NA0004144.

List of Tables

List of Figures

List of Acronyms

IC	Integrated Circuit
MOSFET	Metal–Oxide–Semiconductor Field-Effect Transistor
CD	Critical Dimension
DIBL	Drain-Induced Barrier Lowering
SIA	Semiconductor Industry Association
MtM	More-than-Moore
FinFET	Fin Field-Effect-Transistor
GAA	Gate-All-Around
EUV	Extreme Ultraviolet
DUV	Deep Ultraviolet
UHV	Ultra-High Vacuum
EBL	Electron Beam Lithography
SEM	Scanning Electron Microscopy
PMMA	Polymethylmethacrylate
FIB	Focused Ion Beam
RIE	Reactive Ion Etching
EPE	Edge Placement Errors
PVD	Physical Vapor Deposition
CVD	Chemical Vapor Deposition
ALD	Atomic Layer Deposition
TSMC	Taiwan Semiconductor Manufacturing Company
AS-ALD	Area-Selective Atomic Layer Deposition

GS	Growth Surface
NGS	Nongrowth Surface
SAM	Self-Assembled Monolayer
ODTS	Octadecyl-trichlorosilane
SMI	Small Molecule Inhibitor
ALE	Atomic Layer Etching
PUA	Polyurethane Acrylate
PDMS	Polydimethylsiloxane
CLL	Chemical Liftoff Lithography
SPL	Scanning-Probe Lithography
DPL	Dip-Pen Lithography
AFM	Atomic Force Microscopy
HDL	Hydrogen De-passivation Lithography
STM	Scanning Tunneling Microscopy
XPS	X-ray Photoelectron Spectroscopy
TMA	Trimethylaluminum
GPC	Growth Per Cycle
ASF	Atomic Sensitivity Factors
NCS	*N*-chlorosuccinimide
NBS	*N*-bromosuccinimide
NIS	*N*-Iodosuccinimide
ARXPS	Angle-Resolved X-ray Photoelectron Spectroscopy
ASD	Area-selective Deposition

Chapter 1 Introduction

1.1 Semiconductor Devices

Electronics have been integrated into nearly every facet of our daily lives and society. Appliances such as cellular phones, computing systems, and digital displays have become quintessential aspects of our lifestyles and have also been irrevocably integrated into every economic sector, from agriculture to healthcare. Different types of sensors such as temperature sensors, biosensors, and photosensors are widely utilized to monitor and regulate processes across manufacturing and research. We have seen recent advances in sustainable energy technology including electric vehicles, fuel cells, and photovoltaic devices. What do all these devices have in common? Their functionality is determined from internal silicon chips which possess some combination of diodes, transistors, resistors, capacitors, and logic gates. These chips and their components are fabricated from semiconductors which undergo a variety of processes that add logic components to the surface that are ultimately wired together to create an integrated circuit (IC). The shape, size, and orientation of the IC components are dependent on design parameters (i.e. material, deposition, patterning) and device specifications (i.e. power, voltage, processing speed). In general, the continued miniaturization of device designs and the further advancement of device performance, for applications such as computer processors, are facilitated by the progressive densification of chips with shrinking transistors. Notably, the number of transistors required for new chips is said to have doubled every two years since the 1960s as a result of this downsizing in component size[1, 2]. Specifically, the number of transistors on a standard Si chip has increased from about 65,000 in 1975 to 50 billion on a $1in^2$ chip in 2024[3]. This accelerated phenomenon has been dubbed “Moore’s Law” as it was initially predicted by Gordon E. Moore, the co-founder of Intel.

The single most important factor for the development of modern electronics was the invention of the metal–oxide–semiconductor field-effect transistor (MOSFET) by Mohamed M. Atalla and Dawon Kahn in 1959. The primary components of a MOSFET consist of a gate, a source, and a drain which are all connected with a Si channel. The gate controls the charge that runs through the channel from the source to the drain when the transistor is powered on. When multiple MOSFETs are laid on a chip, they can be turned on and off in different series enabling computation on a mechanical system. The densification of chips relies on the downsizing of lithographically printed surface features that make up a transistor. The size of the smallest feature in a transistor is often referred to as the critical dimension (CD) and for MOSFETs usually pertains to the gate. The volume manufacturing of MOSFETs reached a CD of 32 nm around 2009[4]. However, as development of sub-90 nm transistors progressed, the chips that were researched began to suffer from both confinement effects and thermal management breakdown[5, 6]. These errors are enhanced at sub-32 nm dimensions because the size of the charge depletion zone on the drain side of the transistor is similar to that of the conducting channel, which results in the drain bias influencing charge injection across the gate and subsequent drain-induced barrier lowering (DIBL). Thus, electron movement in an ultrashort channel deviates from established long channel behavior. These deviations are known as short-channel effects and can result in the uncontrolled enhancement of a local electric field which leads to current leakage and even junction damage[7]. These ICs are also known to overheat due to the proximity of one ultrathin and long interconnect to another. Consequently, it has become increasingly challenging for MOSFET technology to maintain Moore's law in a manufacturing setting[8].

In addition to these problems associated with 2D downscaling, according to the Semiconductor Industry Association (SIA), the total consumption of electricity by electronic

devices will surpass global energy production by 2040[9] unless radical changes are made in the efficiency, design, and manufacturing of electronic device components. These current trends can only be counteracted by inventing new device architectures that are more efficient and improve chip performance through hierarchical designs, or so-called "More-than-Moore" (MtM) designs, rather than relying on unsustainable planar scaling. For example, with regard to chip structures, MtM designs aim to replace traditional 2D planar gates with stacked architectures such as Fin Field-Effect Transistors (FinFETs) and 3D Gate-All-Around (GAA) transistors as shown in **Figure 1.1**.

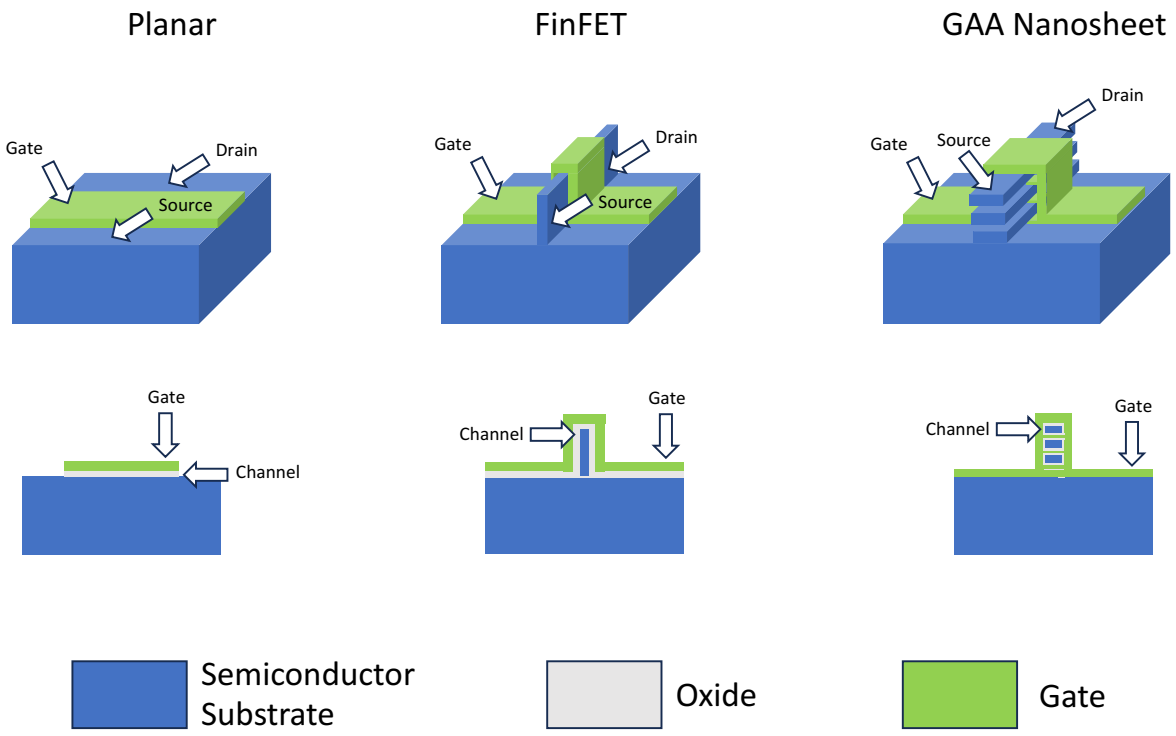

Figure 1.1 Evolution of FET design from planar structure to structures that can be stacked vertically such as FinFETs and GAA FETs.

These architectures consist of fins with multiple vertical conducting channels that facilitate the negation of short-channel effects and enables chip operation at lower voltage and leakage[10]. These fins now constitute the CD of a transistor and when paired with channels can be stacked upon each

other in multilayers enabling upscaling in the vertical dimension[11] and further densifying chips, pushing Moore's law even further. Since 2009, FinFET and GAA designs have enabled volume manufacturing of 13 nm node chips. Current chip development platforms are able to fabricate transistors at the 8 nm technology node. At these dimensions, chipmakers will be able achieve transistor densities nearly three times higher than 32 nm node MOSFETs can offer[12].

1.2 Capabilities and Limitations of Top-Down Processing

1.2.1 Top-Down Processing

To keep pace with this trend in shrinking ICs, semiconductor manufacturing has long relied on parallel thin film deposition, patterning, and etching methods (**Figure 1.2)** that are said to remove surface material from a "top-down" perspective to fabricate geometric features. These surface features are in-turn converted into (or facilitate) the addition of IC components. These "pattern and subtract" micromachining techniques can include the application of gas phase, solution phase, or plasma-based etching, and light-based exposure that extends down to extreme ultraviolet (EUV) wavelengths.

Figure 1.2 Schematic of conventional "top-down" method involving; sputtering of metal layer and deposition of a masking resist, lithographically removing portions of the resist layer to form a pattern, etching away the unmasked metal layer, and cleaning off the remaining resist to reveal the patterned metal features underneath.

An apt analogy for "top-down" processing would pertain to a sculptor carving out a statue from a featureless block of marble. The inherent nature of this "sculpting" requires that most of the

materials used to construct a semiconductor-based device such as; photoresists, developers, resist removers, and etched semiconducting material, are disposed of or need to be recycled using complex reclamation processes. Additionally, the energy required for the "top-down" manufacture of certain devices such as Si-based optoelectronics or sensors often exceeds their total electricity consumption during a typical 5-year lifespan[13]. Nevertheless, these same "top-down" techniques have demonstrated unparalleled success with respect to the mass production of ICs. Here, we will briefly survey the current capabilities and limitations of various lithographic and etching techniques often integrated into "top-down" manufacturing process flows.

1.2.2 Photolithography

The most common "top-down" approaches to semiconductor device fabrication involve optical lithographic techniques which consist of using short-wavelength optical sources, photomasks, and corresponding resist materials. In general, photolithography utilizes surface masking to partially block photosensitive resist films which are designed to either polymerize or depolymerize upon light exposure. For example, with positive resists, the irradiated regions become more soluble and are subsequently removed with the use of a caustic developer that translates the mask's pattern onto the substrate surface. Alternatively, with negative resists, the resist will polymerize under light exposure resulting in patterns which are the reverse of those from the photomask. After developing these photoresist films, the patterns can be further translated to the substrate interface by wet or dry etching.

In the micro- and nano- electronics industry, optical lithography has been scaled up both effectively and efficiently such that a large amount of chips can be manufactured at one time. However, it is estimated that at least a third of the manufacturing cost of a chip stems from lithography[14]. For example, the photosensitive polymers and photomasks that are often necessary

to the process are costly. Furthermore, these methods struggle to accommodate patterning of complex surfaces such as non-planar interfaces. Lastly, lithography is the primary technical limiter in both the further 2D and 3D densification of chips. Thus, these techniques represent a key area for optimization.

Conventional photolithography uses light (typically 350-480 nm) and a photomask to pattern photosensitive resist layers deposited onto inorganic substrates[15]. The resolution of the resulting features is predominantly limited by the light wavelength and diffraction effects. The CD resolution of any given photolithographic process can be determined using the Rayleigh equation:

$$CD\ Resolution = \kappa_1 \frac{\lambda}{NA} \qquad (Eq\ 1.1)$$

where, κ_1 is a process-related constant, λ is the projection wavelength, and NA is the numerical aperture of the imaging system lens. Thus, by either reducing λ or increasing NA can the lithographic feature resolution be enhanced (lower CD gives higher resolution). So-called deep UV (DUV) lithography techniques have been developed which utilize shorter wavelength light (193-250 nm), often from excimer lasers, to downsize feature CD past 40 nm[16, 17]. However, light diffraction around the photomask can be observed at these wavelengths, sometimes reducing the edge resolution of features[18]. The furthest extent that DUV has been realized is with EUV photolithography, which utilizes ultrashort wavelength light (13.5 nm) to pattern down to sub-10 nm CD resolution onto surfaces such as ICs[19-21]. However, the equipment required to generate EUV exposures such as a synchrotron light source are extremely large, expensive, and require ultra-high vacuum (UHV) environments[12]. Current industrial processes utilize DUV equipment to manufacturer processers with CD's down to 14 nm[4, 12]. However, to realize reliable ICs on the sub-10 nm node, EUV must be used and therefore should be made more cost practical for wider implementation in manufacturing environments.

In addition to parallel patterning, other serial writing lithographic methods can be used to assist or even augment photolithography. One such technique is electron beam lithography (EBL) which patterns a surface using a beam of electrons capable of writing intricate arrangements into a resist with sub-10 nm resolution[22]. The working principle of EBL is a combination of scanning electron microscopy (SEM) and photolithography. The exposure beam interacts with an electron sensitive surface to selectively modify the solubility of certain regions by adjusting the energy output of the beam. After writing a pattern into the resist, features can be translated down to the sample surface via etching or lift-off of the negative resist. Polymethylmethacrylate (PMMA) and other methacrylates are widely used resists in EBL that can act as either positive or negative resists depending on the beam dose[23]. Contrary to photolithography, EBL pattern resolution is not limited by exposure wavelength (since the wavelength of electrons is exceedingly small) but is instead constrained by the lateral size of the exposure beam and the resolution of the resist molecules, both of which allow for much room for optimization. This technique does not rely on masking and is in fact the primary means for which photomasks are fabricated. Focused ion beam (FIB) lithography is an iteration of EBL that emits heavier ions, typically Ga, to prevent backscattering that is sometimes observed in EBL where scattered electrons interact with unexposed areas. EBL and FIB are reliable tools for high resolution patterning in laboratory-scale “top-down” nanofabrication. However, due to the serial writing nature of these techniques, the overall throughput is exceedingly low. Whereas photolithography can pattern whole wafers within a few minutes, it can take up to a day to process a 1 cm^2 region with EBL[24]. Furthermore, in addition to backscattering, these methods also experience perturbations within the exposure beam due to common background noise, resulting in edge pattern defects. Due to these limitations, EBL and FIB are not used as parallel patterning techniques in semiconductor manufacturing. Instead, they are primarily

employed as a prototyping tool for research and development, but can also be used to assist larger photolithographic processes (i.e. fabricating photomasks).

1.2.3 Continuous Etching

Most “top-down” patterning techniques rely on continuous etching methods to facilitate the translation of patterned features to a substrate surface. This is accomplished either through the direct etching of resists or removal of bulk material from the substrate. This can be carried out using either dry or wet etching. Typically, wet etching involves substrate immersion into a reactive solution which dissociates and degrades unwanted regions of a surface's layer while leaving others intact. Common wet etchants include hydrofluoric acid (HF) (often mixed with a buffer), potassium hydroxide (KOH), mixtures of sulfuric acid and hydrogen peroxide (i.e. Nano-Strip or Piranha), and phosphoric acid. HF etching is an effective remover of both SiO_2 and some photoresists that doesn’t stain or contaminate Si. Although it requires robust safety protocols, it is used throughout the semiconductor industry for wafer cleaning and for surface roughness mitigation. KOH etching is used to directly remove Si atoms and form surface cavities on a wafer, However, it is not compatible with removing most photoresists and the etch rate is often controlled by adding corrosive alkaline compounds to the etchant solution which require extra safety measures while handling. Nano-Strip or Piranha etching will remove most organics from Si including photoresists. But because these mixtures are strong oxidizers they are again dangerous to handle. They will also sometimes produce toxic off-gases when interacting with organics. Phosphoric acid is an effective remover of photoresists when paired with a silicon nitride (SiN) mask. However, sometimes undercut etching beneath the SiN mask is observed if conditions aren’t closely monitored. Overall, these wet etching methods are often challenging to integrate into semiconductor device fabrication schemes as they require processing outside the primary

manufacturing environment (i.e. outside deposition and lithographic chambers). Thus, industry often turns to dryer methods for surface material removal.

Dry etching refers to methods which remove surface layers using surface reactive gases and/or various iterations of ion-beam or plasma-beam surface bombardment. For example, in reactive ion etching (RIE) a plasma source emits high-energy ions in vacuum that bombard and react with a substrate to dissociate surface atoms. A negative resist can first be selectively deposited to a surface to direct the etching chemistry. An advantage of RIE over other surface etching methods is that this technique facilitates highly preferential anisotropic etching in a controlled direction. Although traditional RIE techniques are limited to moderate etch depths (e.g., a few microns) and arbitrary patterns, there are newer methods such as inductively coupled plasma (ICP) RIE which facilitates much deeper etch depths with higher control and aspect ratios[25]. However, these processes require substantial amounts of energy, most of which must be absorbed as heat by advanced cooling systems. Additionally, since the removal mechanism is dependent on the delivery of species emitted from a plasma source that establishes an interfacial gradient of material etching, these processes are both transport-limited and may result in uneven layers if not properly tuned due to the mixture of different plasma species emitted at similar energies[26]. Tuning the process conditions to isolate desired plasma species for anisotropic etching is not trivial. Others have explored vapor phase etching of SiO_2 with HF/H_2O mixtures, where H_2O particles adsorb onto the Si surface and weaken Si-O bonds which then allows the HF to attack the SiO moiety[27]. This method can only be facilitated in a tightly controlled environment and requires robust safety controls.

1.3 Capabilities and Limitations of Bottom-Up Processing

1.3.1 Bottom-Up Processing

Although many of the aforementioned lithographic and etching techniques demonstrate high resolution at the nanoscale, they all have inherent limitations and exhibit some combination of material-intensive, energy-intensive, or low-throughput characteristics. Additionally, the multi-stack architectures of FinFETs and GAA FETs are very difficult for most "top-down" techniques to realize at sub-32 nm dimensions without edge placement errors (EPEs), described in **Figure 1.3**.

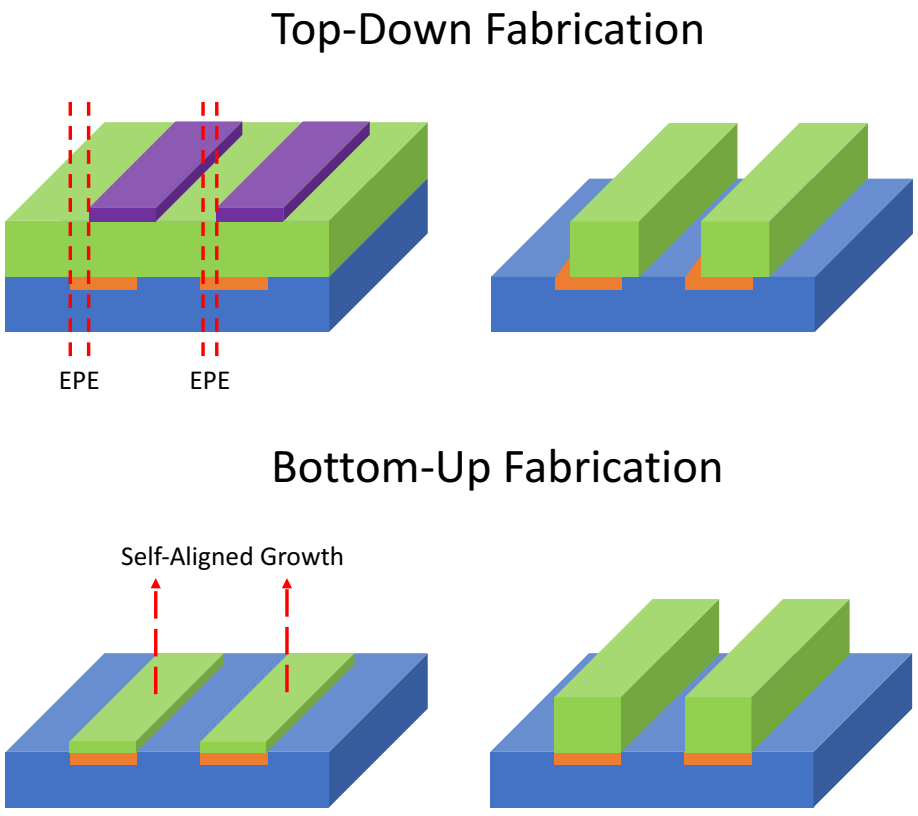

Figure 1.3 Illustration of how EPEs form using conventional "top-down" patterning techniques and how selective "bottom-up" feature growth avoids these same errors. These errors occur when there is imprecise alignment of a photoresist or mask which leads to overlap of the deposited feature onto undesired surface domains. EPEs may also occur due to imperfect subtractive steps such as chemical etching necessary to translate patterns to a surface[28]. Whereas "bottom-up" fabrication enables self-aligned feature growth by leveraging the inherent chemistry of materials.

Photolithography is not very suitable for the fabrication of 3D architectures because it is inherently a 2D pattern translation method from a mask to a planar surface, and it also suffers from wavelength and/or cost (in the case of EUV lithography) limitations. A fundamental flaw of most "top-down" schemes is that it emphasizes mechanical/optical processing instead of leveraging differences in chemical behavior between surface species. When tailored properly, these systems of self-limiting surface reactions can result in both self-aligned feature growth that avoids EPEs and a favorable shift in thermodynamic profile that will alleviate high energy requirements. Instead of patterning and then removing material, this contrasting form of deposition begins at the surface and grows vertically in a layer-by-layer fashion via reaction from the "bottom-up". An example of such a process is shown in **Figure 1.4**.

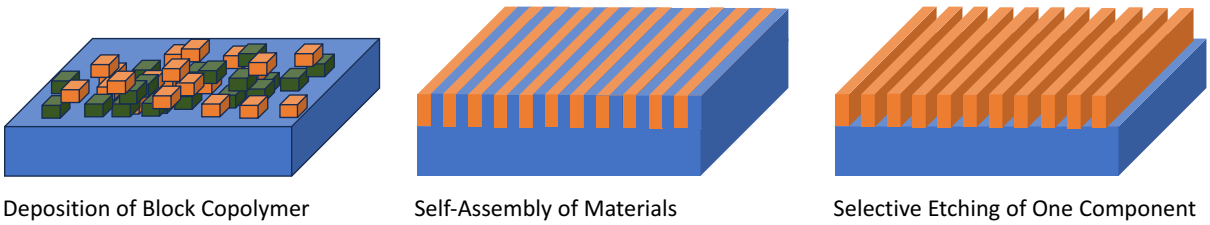

Figure 1.4 Schematic of an inherently "bottom-up" fabrication method that relies on a block copolymer system that self-assembles on a chemically tuned surface and enables subsequent feature formation upon a chemically selective etch. Although promising, "bottom-up" Block Copolymer deposition has encountered many difficulties due to structure disordering at surface defects[29, 30].

Stacking stone blocks in a patterned fashion to create a castle would be an example of a "bottom-up" process. Whereas, "top-down" processing largely centers on removing bulk material or resist fragments from a surface, "bottom-up" processing starts at a substrate surface and relies on stacking clusters of atoms and molecules. Theoretically, the resolution of these techniques will only be limited by the size of the molecules or atoms used in the chemical system. This shift in design philosophy was epitomized by Gordon E. Moore in a 2005 interview where he said "…the

fact that materials are made of atoms is the fundamental limitation [for transistor downscaling] and it's not that far away."[31] It is expected that by 2028 researchers will have established reliable transistors with CD's on the scale of 3–4 atoms of Si[12]. Thus, the nanofabrication industry is now focused on the shift from 2D planar chips to 3D multistack chips that are predominantly accessible via "bottom-up" device processes that rely on mono-atomic and mono-molecular deposition, etching and patterning steps to build and assemble device components in an additive manner though precise and self-aligned surface chemical reactions.

1.3.2 Deposition

The proliferation of these 3D hierarchical designs has relied on selective and high conformality thin film deposition methods that proceed at lower processing temperatures (≤450 ◦C) overtop prepatterned templates. The three most widely used thin film growth processes are physical vapor deposition (PVD), chemical vapor deposition (CVD), and plasma-assisted CVD. Whereas both PVD and CVD can generate uniform films with decent control on thickness[28, 32], the process temperatures required can be higher than what the thermal budget will allow for a given semiconductor application. PVD especially requires a significant amount of energy in the form of heat for conformal growth. Alternatively, plasma-assisted CVD operates at lower temperature regimes that are more typical for semiconductor manufacturing[33]. However, during this process reactive radicals and ions are sometimes generated from the plasma which promote non-conformal film growth at the surface[34], an example of which is shown in **Figure 1.6**. This phenomenon is hard to control and complicates the integration of plasma-assisted CVD processes into nanoscale processing. Additionally, CVD cannot be used to deposit metal films. In light of these limitations, for the last two decades device manufacturers have begun to transition away from PVD and CVD

to atomic layer deposition (ALD), which has widely demonstrated the ability to grow uniform films with superb thickness control at relatively lower process temperatures.

Atomic layer deposition (ALD) was originally known as an advanced coating technique that deposited homogenous films with great uniformity and thickness control. However, it has now been extended to non-coating applications such as semiconductor multi-patterning and is increasingly becoming incorporated into the micro- and nano-electronics industry. It shares many similarities with CVD but is unique in its deposition mechanism which is driven by substrate exposure to alternating pulses of precursor molecules delineated with purges of inert gas, as shown in **Figure 1.5**.

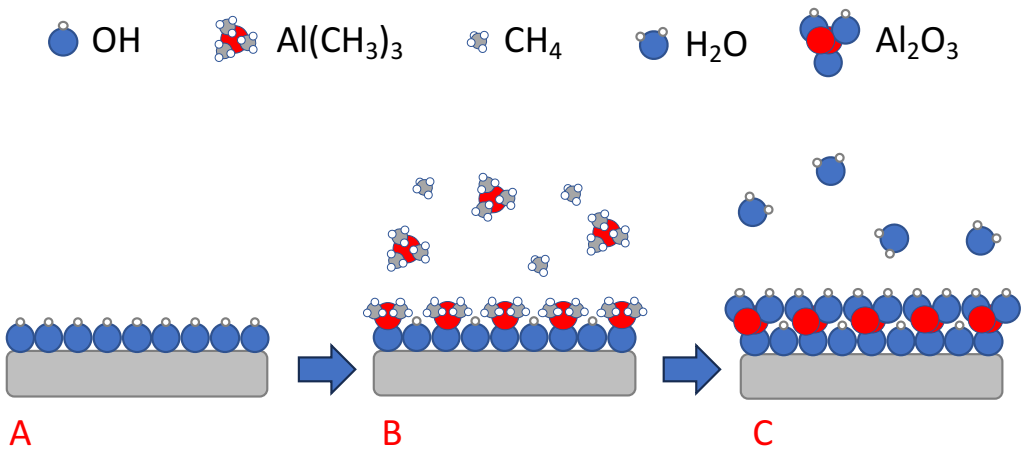

Figure 1.5 Schematic of standard cycle for Al_2O_3 ALD: (A) The first stage involves the initial physisorption and subsequent chemisorption of the film precursor molecule onto a reactive substrate. (B) While this precursor diffuses and organizes onto the substrate surface, there is dissociation and transfer of ligands between the precursor and surface material, followed by a purge of these dissociated fragments, byproducts, and of excess precursor molecules. (C) The second reaction stage entails the dosing of the sample surface with a coreactant molecule. For example, in the deposition of many metal oxide films, water is used as the coreactant to facilitate hydrolysis of the surface grafted precursor moieties bearing the metallic atoms (i.e. Al, Ti, Hf).

Under ideal processing conditions, each stage of precursor exposure should be surface reaction limited even in the presence of excess precursor, owing to the finite number of surface reaction

sites. This results in self-limiting growth that in turn enables the generation of highly conformal films. However, under non-ideal conditions, what instead will occur are near-simultaneous ALD and non-ALD surface reactions that may result in surface decomposition and impurity incorporation. Thus, identifying a window of favorable thermodynamics and kinetics for each precursor step is vital for preventing non-ALD surface reactions and enhancing the deposition rates of the desired ALD film. Because the mechanism of ALD is dependent on single layers of molecules, this technique is capable of growing ultra-thin films with excellent control. Owing to this excellent thickness control, the high-quality films that are generated, and the potential for high volume processing, ALD is fast becoming one of the more effective and efficient thin film deposition methods in semiconductor device manufacturing.

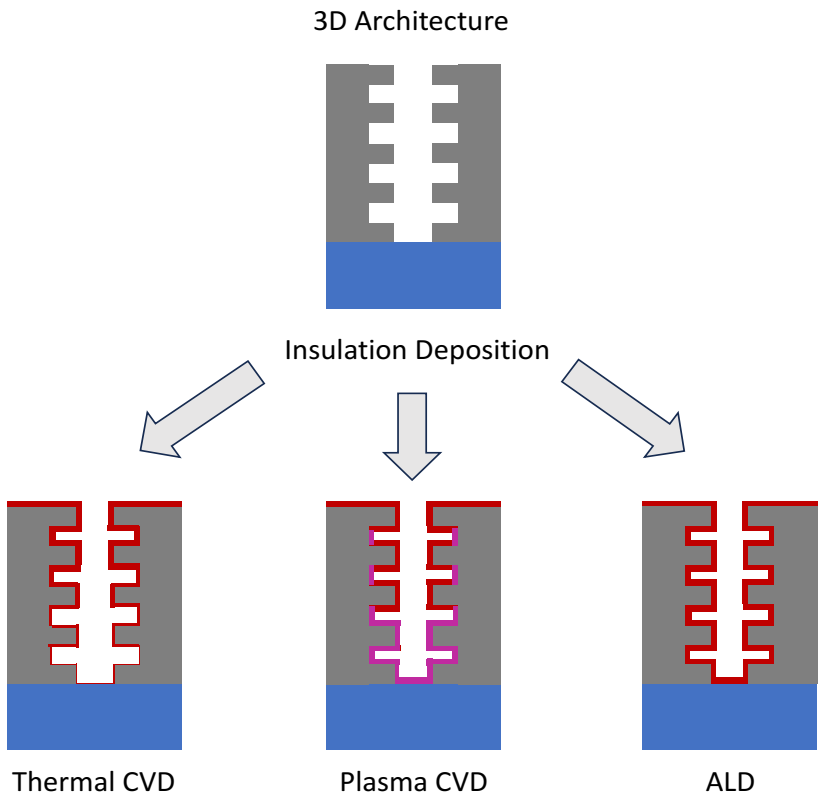

Figure 1.6 Comparison of CVD and ALD methods for coating of 3D chip structures. Thermal CVD (at semiconductor processing temperatures) results in nonuniform feature coverage, plasma CVD enables uniform coverage but variable film composition and properties, and ALD results in uniform film coverage, composition, and properties.

In the mid 2000s, ALD played an important role in volume manufacturing process flows as a cost-efficient and effective method to deposit high-κ gate dielectric layers for 45 nm node MOSFETs[35]. From there researchers increasingly looked to implement ALD to construct/form gates, insulators and interconnections for ICs. However, it was with the advent of 3D FinFET design that the true potential of ALD in semiconductor processing was fully realized, due to the highly controlled and vertical nature of its deposition mechanism. In a 2021 presentation, when discussing the future direction of transistor design, the CTO of ASM International Ivo J. Raaijmakers said, "…almost everything is going to 3D to enable scaling. We see a lot more thin films, complex stacks and more complex materials, and that requires more ALD."[36]. Intel utilizes ALD to form the Al_2O_3 gates for their 22 nm CD FinFETs and both Taiwan Semiconductor Manufacturing Company (TSMC) and Samsung are currently using ALD in the development of their 3 nm node GAA FETs[37]. Specifically, ALD is being used to interconnect GAA FETs and also deposit SiO_2 films between layers of the chip as an insulator to prevent current leakage. ALD will be essential to the further stacking of FinFETs and GAA FETs and the future development of GAA technologies.

1.3.3 Area-Selective Deposition

The rate of layer-by-layer deposition for ALD is primarily dependent on the chemical terminations of the receiver substrate, and thus reactivity, of specific surface domains. Consequently, there is an impetus to develop complementary molecule resists that, when applied to a homogeneous growth-promoting surface, both shield desired non-deposition areas from ALD chemistry while simultaneously permitting area-selective ALD (AS-ALD) growth on the surrounding intended deposition interfaces, as shown in **Figure 1.7**. Thus, the difference in film

growth on the growth and nongrowth surfaces (GS and NGS) will determine the resolution of the deposited patterned film.

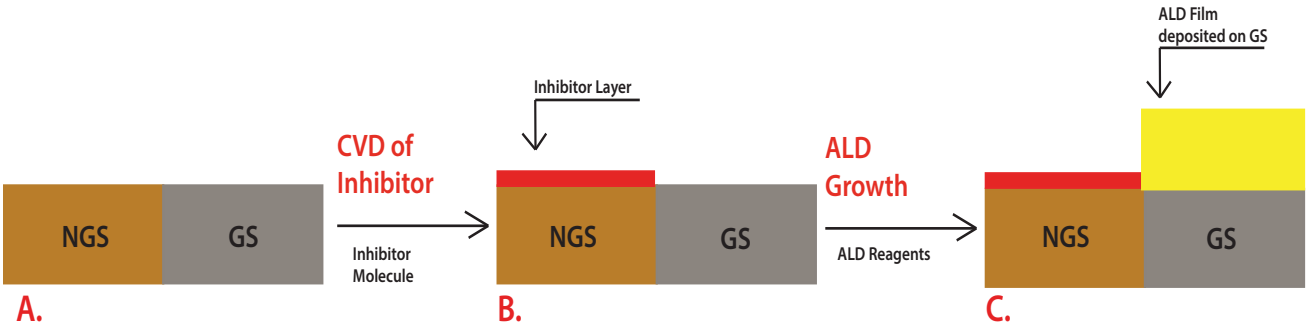

Figure 1.7 Schematic of theoretical AS-ALD process[38] showing; (A) a pre-patterned GS and NGS substrate that is (B) selectively modified with an inhibitor molecule reactive with the NGS, thus (C) promoting adsorption and reaction of the ALD film precursors on the GS region, resulting in selective film growth.

This process of localized ALD circumvents many of the more potentially harmful subtractive steps employed in photolithography[39-44]. The selective growth mechanism of AS-ALD is primarily dependent on the application of these ALD resist (or inhibitor) molecules. Although the initial reactivity of the ALD resist with the film precursor chemistry should be low, **Figure 1.8** demonstrates that continued accumulation and nucleation of the precursor molecules atop and within defects of the resist layer, after every ALD cycle, will eventually result in film growth on the NGS. This effect can be mitigated by carrying out plasma-assisted atomic layer etching (ALE) on the NGS, where alternating pulses of an etchant gas (reactive with the NGS) and low energy inert ions work together to remove the reacted etchant/NGS interface in a layer-by-layer fashion until the original NGS is renewed.

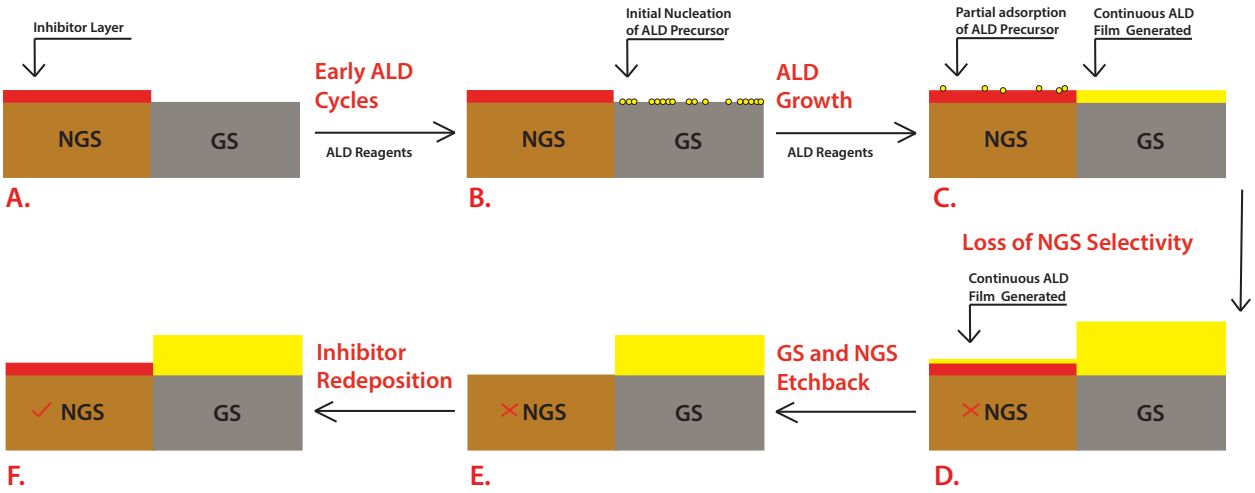

Figure 1.8 Schematic of AS-ALD "Super-Cycle": (A) Prepatterned AS-ALD template post-selective CVD of inhibitor onto NGS. (B) GS interface undergoes nonuniform film growth during first 1-3 cycles. (C) With more cycles a continuous ALD film is generated on GS and there is partial adsorption and nucleation of ALD chemistry atop NGS and within defects in the inhibitor layers. (D) This results in the eventual loss of NGS selectivity and continuous ALD film generation across entire substrate. (E) The ALD process is then paused to allow for etchback of the ALD film on both GS and NGS until original NGS is reestablished. (F) Lastly, the ALD inhibitor molecule is reapplied to the NGS and ALD can start again.

In the last five years there has been significant movement in the integration of ALD with ALE to construct a single AS-ALD "super cycle" process that is able to regenerate a NGS after it loses its inhibiting ability, overall improving the AS-ALD growth selectivity. AS-ALD exhibits many advantages over other thin film deposition methods. For instance, by relying on a predefined substrate template, film growth is naturally self-aligning and precludes additional lithographic processing during deposition. Additionally, it can achieve nanoscale resolution while also alleviating the higher energy processing conditions of CVD and PVD. Consequently, AS-ALD has become a viable platform for enabling selective deposition, etching, and patterning in parallel processing flows.

Early AS-ALD resists included polymeric[45] and inorganic[46] thin films that were predominantly deposited though various iterations of photolithography or stenciling. As discussed, these techniques can significantly increase both the energy and material cost of a process.

Alternative approaches to resist deposition rely on so-called self-assembled monolayers (SAMs)[47] that chemically adsorb and assemble onto a surface. These molecules consist of a head group that is reactive to the surface and a tail group that renders the underlying substrate inert towards the ALD chemistry. SAMs have been widely validated as effective inhibitor molecules for AS-ALD[42, 48, 49]. For example, alkylsilanes and alkylphosphonic acids have been shown to react with metal oxide substrates to form dense monolayers of alkyl groups that in turn inhibit metal oxide ALD[42, 50, 51]. Studies also show that longer chain SAMs inhibit ALD precursor molecules more effectively than shorter ones due to their denser packing and bulkier sterics. However, these longer molecules (~2-3 nm) also adsorb more freely around and onto GSs and are therefore detrimental to nanometer-scale patterning due to EPEs. This is observed with octadecyl-trichlorosilane (ODTS) whose long aliphatic structure has been shown to cause edge defects in AS-ALD patterns below 50 nm[51]. Although SAMs don't require costly lithographic steps for application, issues still arise when considering that they are mainly distributed in the solution phase which is incompatible with vacuum-based processes such as ALD. Furthermore, the assembly of many SAMs is altered near or on surface defects, resulting in surface domains that may remain reactive with what is intended to be inhibited[52, 53]. Alternatively, the use of lighter, small-molecule inhibitors (SMIs) yields better results as ALD blockers. As evidenced by their name, SMIs are smaller than SAMs and they do not self-assemble. However, they are structured similarly, consisting of a headgroup reactive to some surfaces and a tail bearing inert/blocking functional groups. Unlike SAMs, SMIs are able to fully adsorb onto complex surfaces, enable much smaller feature deposition dimensions, and can be deposited using vapor chemistry compatible with vacuum deposition systems[54]. A large pool of SMIs have been studied to assess their potential for nanopatterning, for example, acetylacetone (Hacac), propargylamine, and aniline have all demonstrated good blocking ability in AS-ALD

schemes [38, 42, 48, 55-58]. Researchers will continue to investigate SAMs and SMIs candidates for their inhibiting properties as they have displayed great potential for integration into AS-ALD schemes.

Like ALD, the technique of ALE has been around for decades, but only in the last 10 years has there been a renewed interest in the process as a potential alternative to continuous etching techniques for AS-ALD schemes. As has already been mentioned, an effective AS-ALD process must rely on ALE reactions capable of regenerating the inhibiting characteristic of a NGS after it has been rendered noneffective due to interfacial adsorption, accumulation, and nucleation of the ALD chemistry. To accomplish this the technique utilizes sequential self-limiting reactions, like in ALD, where the first step involves forming a reactive overlayer with a surface that is easier to remove than the underling species, and then the removal of the entire overlayer by a second species, thus reestablishing the surface to its original state. A typical ALE process is presented in **Figure 1.9**.

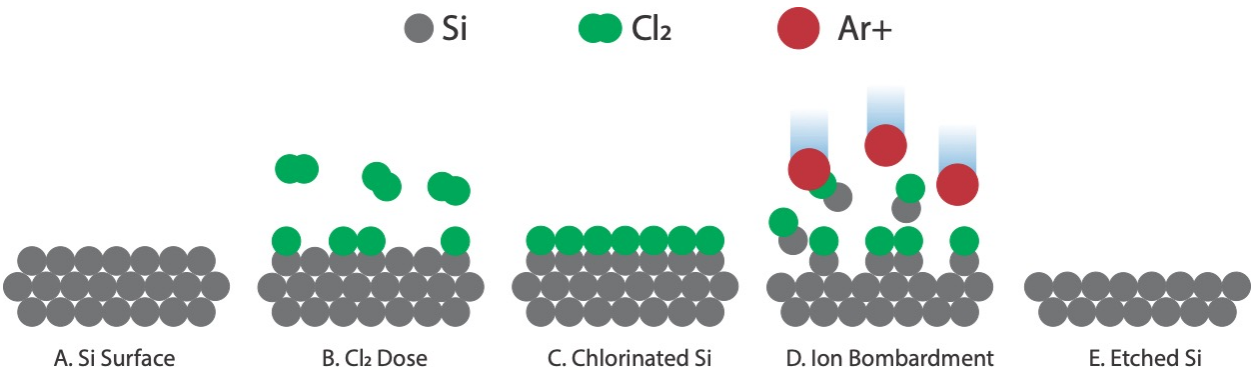

Figure 1.9 Schematic of ALE of Si layer: (A) A Si substrate is (B) exposed to Cl_2 gas which reacts with the substrate surface to form a (C) more easily dissociated chlorinated surface that is then (D) bombarded with high-energy Ar^+ ions to remove the Cl overlayer and the (E) top surface layer of Si.

ALE precursors are usually delivered via vapor phase or plasma-based chemistry. Unlike in continuous etching processes like RIE, ALE relies on intervals of clearly defined self-limiting reactions which don't suffer from transport issues associated with the unlimited flux of different

species from a plasma source. Thus, all interactions between the etching species and the layer to be etched are able to complete until more species are introduced, whereas in RIE there is no self-limitation and removal is based local species fluxes that can form thick and uneven etching interfaces. Examples of ALE include the removal of metal oxides from Si using alternating doses of anhydrous HF and metal oxide precursors to remove Al_2O_3 and SiO_2[59, 60].

1.3.4 Bottom-Up Lithography

In addition to resist engineering and regeneration, another integral aspect of AS-ALD which still requires further optimization are the methods that are used to fabricate the pre-defined substrate templates that serve as the platform for selective film growth. These pre-defined templates are usually prepared using photolithography or RIE, although no universal method has yet to be established. The integration of these "top-down" lithographic techniques with vacuum-based ALD systems is not easy and resolution issues at a sub-14 nm level will be encountered. Thus, it may prove more practical and efficient to employ various "bottom-up" approaches to micropatterning AS-ALD templates instead.

Soft lithography, specifically microcontact printing (μCP), can be referred to as an early mode of "bottom-up" patterning[61-64]. This relatively fast and inexpensive method to patterning is carried out using shape-memory, elastomeric stamps (e.g., polydimethylsiloxane (PDMS) or polyurethane acrylate (PUA)) and primarily involves adding material to a surface instead of removing. A standard route for surface feature generation via a transfer printing process is shown in **Figure 1.10**.

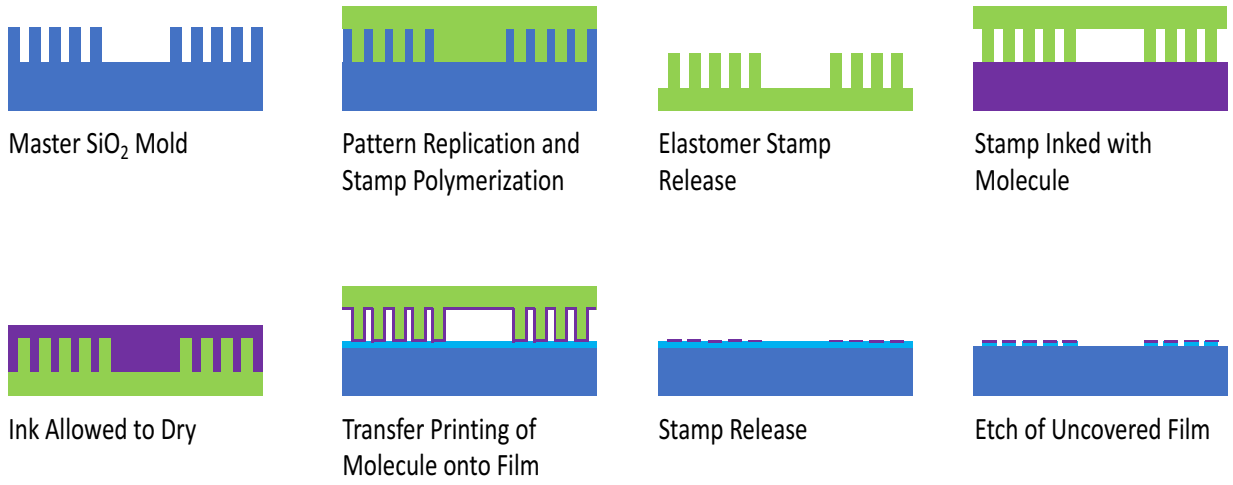

Figure 1.10 Transfer printing process where a stamp is cast onto a master mold and cured into a negative replica. This stamp is then inked with a molecule and put into conformal contact with a chemically receptive receiver substrate, resulting in the transfer of the master pattern onto the receiver substrate. The transferred molecular ink can be used as an etching mask (as in this example) or can be an active component thus chemically attached to the receiver substrate.

Although conventional μCP yields feature resolution on the order of microns, it can be further reduced by using heavy molecular inks such as alkanethiols[65] or dendrimeric polymers[66] which reduce the degree of ink diffusion within the stamp's pattern. This method has been utilized to pattern components for LED devices with sub-50 nm edge resolution[67]. This diffusionless mode of contact printing[68] has also been shown to pattern monomolecular layers of organic molecules that can possibly be used as ALD resists or ultra-shallow dopant layer precursors. Lastly, transfer printing can also be employed to selectively remove molecules from a surface using chemical "lift-off" lithography (CLL) that has generated features with down to 50 nm resolution[69, 70]. These scalable and versatile additive (or in some cases subtractive) printing techniques broadly benefit the nanomanufacturing capability of high-resolution displays, sensors, and optoelectronic devices.

Like contact printing, different iterations of scanning-probe lithography (SPL) have also demonstrated potential as effective patterning techniques for "bottom-up" processing. SPL relies on acute probe tips, with radii <10 nm, to write nanoscale patterns onto hard surfaces. The most

common SPL approach is dip-pen nanolithography (DPN) where a molecular ink is coated onto the end of an atomic force microscope (AFM) probe, or "pen", and deposited onto a substrate surface through the meniscus that is generated between the probe and the substrate upon close contact. Since it is carried out under ambient conditions, DPN is widely used to template various materials such as polymers[71], nanoparticles[72], and biomolecules[29]. It is also compatible with many substrate materials including semiconductors, metals, and insulators. Potential limitations of this technique include ink diffusion at the tip/substrate interface[73, 74], and low-throughput. DPN patterning output has been increased by using large arrays of tips (>50 tips)[75], however, even these systems struggle to facilitate large area patterning of complex surfaces[76] and are more expensive[77]. Additionally, there is no example in literature of DPN being utilized to pattern substrates intended for AS-ALD.

Another patterning method which demonstrates high precision in both the vertical and lateral directions is hydrogen de-passivation lithography (HDL). This technique is based on scanning tunneling microscope (STM) where the tunneling current between the STM tip and a conductive substrate is used to selectively and homolytically cleave resist atoms (usually H) and results in lithographically defined surface features. This process has been used to place dopant atoms on a Si surface with atomic precision[78, 79] and create p-n junctions[80]. However, the chemical bond breaking process by which patterns are written has only been shown to work on Si, Ge, and diamond surfaces[81]. Moreover, the atomically flat interfaces required for HDL are vastly different from those used in traditional semiconductor processing, where wet chemical preparation methods lead to relatively rough starting surfaces. This is also a serial write process, which necessarily results in far lower throughput than other parallel lithography processes. Furthermore, this process requires energy-intensive processing to control the cryogenic and UHV conditions required to

maintain the highly reactive nature of the dangling bonds that are uncovered on a surface during the patterning process.

Due to its capability of atomic-scale patterning, the ideal lithographic method for AS-ALD templating would be HDL. When combined with AS-ALD, this process has the potential to achieve truly atomically precise devices in both lateral and vertical dimensions. HDL defined surfaces have already been shown to be compatible with AS-ALD techniques to grow patterned TiO_2 thin films[82]. In this instance, HDL was used to generate a line pattern of reactive dangling bonds from a continuous H-terminated Si surface. This line pattern of unsatisfied bonds was then instantaneously saturated with a direct flux of O_2, as shown in **Figure 1.11**, and subsequently reactive for ALD of an oxide material. Meanwhile, the surrounding undissociated H resist remained intact for a limited period of time while the ALD film was deposited onto the line pattern[83]. Although these preliminary results demonstrate the great potential for HDL integration into AS-ALD schemes, the challenge becomes how to improve the throughput of the patterning technique and make it applicable to a wider range of substrates to be patterned and materials to be deposited. For example, due to the extremely precise nature of HDL, it is not practical to use this method with many of the large hydrocarbon molecules that make up conventional resists. Instead, HDL should be paired with SMIs or even single atomic species such as -H or -Cl surface terminations. Because this high precision patterning process is only feasible with the correct combinations of resist, deposited material and substrate, alternative methods to patterning ALD resists must still be explored.

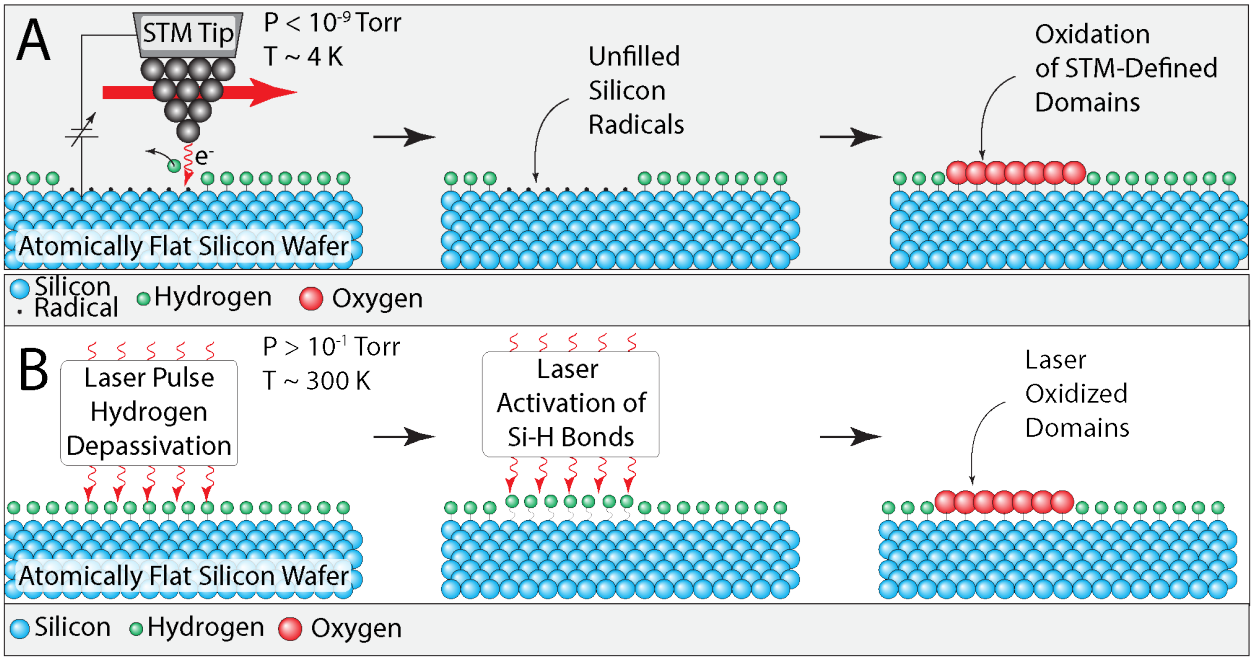

Figure 1.11 Illustration comparing HDL and pulsed laser patterning of H-terminated Si. (A) In HDL a STM tip removes small clusters of hydrogen atoms, thus exposing reactive Si radical sites, and allowing subsequent oxidation in a selective manner. (B) Pulsed laser-assisted oxidation method where Si-H surface bonds are excited under low vacuum and room temperature conditions.

Figure 1.11 shows that one such alternative to HDL may be ultrashort pulsed laser patterning. Whereas HDL initiates patterning using a flux of electrons from a STM tip to cleave surface bonds, it might also be possible to achieve a similar transition-state-induced effect by delivering a high photon flux just within a shallow adsorption depth beneath a surface, without dissipating a significant amount of heat into the bulk substrate. Such laser-initiated chemical activation of atomic or small molecule films can promote a variety of surface reactions if the gas-phase environment around the substrate has specific chemical reactivity. There are several advantages of using photons to initiate chemical modifications of the semiconductor interfaces. Like HDL, this technique would not be limited to specific atoms or molecules and activation can be achieved via controlling the laser parameters (wavelength, pulse duration, pulse energy). In addition, pulsed laser surface processing can be performed in parallel (unlike STM) on the entire

substrate. This increase in throughput would result in a significant decrease in processing time and energy consumption relative to STM-based patterning. Moreover, laser activation can be used on non-ideal interfaces, which are incompatible with the STM probes used in HDL. Pulsed laser-assisted ionization of organic molecules is a well-known phenomenon that is used in various analytical techniques, and when combined with photomask patterning, can achieve the same resolution as current state-of-the-art photolithographic processing[84-86], if the thermal diffusion is limited. Additionally, scanning laser systems are also scalable for conventional wafer-size substrates[87, 88] and can potentially be implemented into vacuum-based processes like ALD, enabling *in-situ* patterning of various substrate/resist combinations. The development of such a technique as shown in **Figure 1.12** should focus on universal, nanosecond and picosecond pulsed laser-promoted patterning of SMI and atomic ALD resists and the integration of the technique into diverse manufacturing development environments.

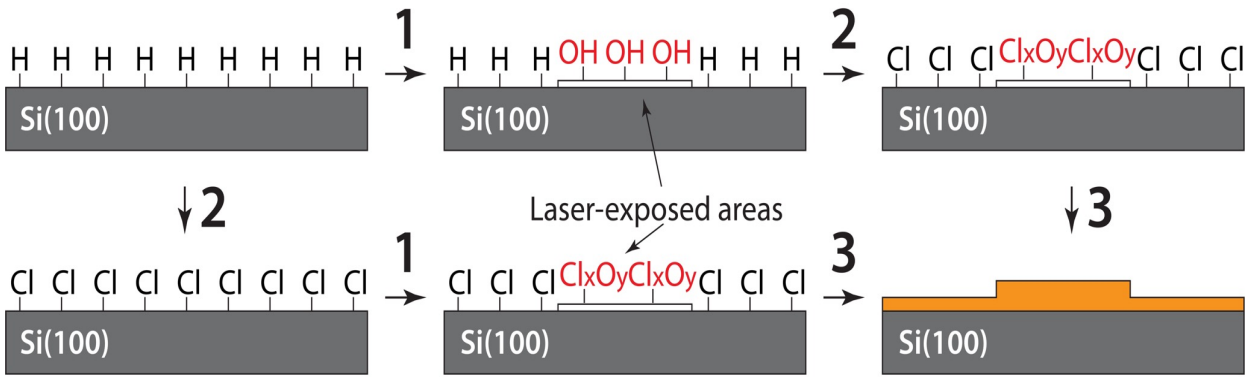

Figure 1.12 Two potential routes to a unified "bottom-up" approach to surface feature fabrication. Starting with H-terminated Si, this material can either be (2) chlorinated or (1) put directly under laser exposure. (1) Pulsed Laser radiation of either surface in mild vacuum will lead to oxidation of the laser exposed surfaces, leading to a complementary resist system for (3) AS-ALD, where film deposition should occur selectively on the laser-oxidized surface domains. Until this point, this process represents an exclusively "bottom-up" method to surface feature generation.

By fabricating templates using laser patterning that subsequently enables AS-ALD, this would represent an exclusively "bottom-up" platform for 3D feature fabrication. Only when the ALD template loses its selectivity would there have to be an etchback step that removes material (i.e. undesired ALD film atop NGS).

1.4 Thesis Outline

Advanced "bottom-up" fabrication processes are fast becoming the most efficient means to realizing the development of next-generation semiconductor devices which rely on 3D architectures to increase processing speed with lower power consumption. To enable such manufacturing, recently there has been an emphasis on finding universal and reliable techniques for controlling and modifying chemical reactivity of atomic and small molecule films on semiconductor materials. Through chemical modifications, these nanometer-scale systems can be tailored to incorporate various active device components such as patterned ultra-shallow doping layers[89-92], chemo-selective resists for AS-ALD[38, 93], and biological templates for sensors and molecular arrays[18, 94, 95]. However, one of the major challenges of nanofabrication that precludes widespread implementation of mono-atomic and mono-molecular platforms is the lack of unifying conditions for controlling and activating chemical reactivity of these systems in a spatially resolved manner, on a variety of different films and substrates. Thus, the guiding principle in this thesis work was to investigate the compatibility of several surface patterning and thin film deposition processes with various SMI and atomic layers that can be integrated into a primarily "bottom-up" fabrication scheme.

In chapter 2, I will examine the wide difference in chemical properties between hydroxyl-terminated silicon (OH-Si(100)), hydrogen-terminated silicon (H-Si(100)), and a SMI perfluorinated Si surface and evaluate each of these resists as potential inhibitors to block the

adsorption a common ALD precursors. This evaluation process will continue in chapter 3 where I will investigate the ALD inhibiting ability of atomic halogen resists on Si(100). Chapter 4 will explore the use of localized pulsed laser radiation as a “bottom-up” method to selectively oxidize and pattern H-Si(100). Chapter 5 will explore the compatibility of μCP with a carbenylated SMI for delivering patterned active components to a Si surface. Lastly, chapter 6 will look at the future direction of this new laser patterning method and also examine the future prospects of integrating the various ALD resists into a unified AS-ALD fabrication scheme. Overall, this work has the potential to open-up new approaches for integration of laser-patterning, surface functionalization, and AS-ALD, into current advanced semiconductor device manufacturing schemes.

Chapter 2 Carbene-Derived Small Molecule Resists for AS-ALD

2.1 Chapter Structure

In this chapter various considerations for metal oxide ALD will be discussed. A baseline for alumina (Al_2O_3) ALD on a standard OH-Si(100) GS and H-Si(100) NGS is also established. These baselines, namely the inhibiting behavior of H-Si(100), will be evaluated against a bilayer SMI resist system. This bilayer system consists of a succinimidyl-diazirine (NHS-diazirine) sublayer covalently attached to a perfluorinated amine (PFA). XPS is used to verify the surface functionalization of H-Si(100) with this resist system and its subsequent blocking ability against the reagents used in Al_2O_3 ALD.

2.2 Introduction

AS-ALD is a key technology for enabling atomically precise, self-aligned bottom-up manufacturing of thin-film electronic[96, 97], photonic[98] and quantum devices[99]. This method is often suggested as a higher-resolution replacement for current "top-down" micromachining techniques that can further advance the development of 3D ICs[100]. AS-ALD relies on patterned interfaces of GS and NGS which sequentially promote and block ALD reactions on the corresponding domains.[28, 39, 101, 102] Growth selectivity is typically achieved by patterning ALD resists that block deposition on the homogeneous growth-promoting interfaces.

Past studies have examined the effectiveness of ALD resists which focus on functionalizing Si(100) interfaces.[103, 104] In the (100) orientation, the Si/SiO_2 interface state density is generally lower than in the (110) and (111) planes, resulting in a lower density of dangling bonds, higher carrier mobility, and better drive current for Si-based electronics. Currently, hydrogen-terminated silicon (H-Si(100)) is employed as an effective NGS when paired with hydroxylated silicon (OH-Si(100)) which acts as the GS. This basic complementary

resist system is valued for its uniform composition and good growth/etch selectivity.[39, 105] However, H-Si(100) is reactive and unstable in air, limiting its use to UHV environments and hindering its application in commercial systems for "bottom-up" processing. Therefore, alternatives to H-Si(100) that maintain its attractive physical and chemical properties, inhibit partial oxidation, and improve ALD growth selectivity with OH-Si(100) are needed.

The objective of this study was to form a SMI resist system on Si(100) and evaluate its ALD inhibiting ability as potential NGS candidate. The resist system consists of a primary succinimidyl-diazirine (NHS-diazirine) layer subsequently bonded with a perfluorinated amine (PFA). The attachment of NHS-diazirine to Si(100) relies on a unique carbene-based (i.e. divalent carbons) mechanism, that when activated by UV-light, allows the molecule to insert itself into X-H bonds. Previously, our group demonstrated the UV-activated insertion of carbene groups into Si-H surface bonds[42, 47]. Carbenes can be generated from diazirines in either the solution or vapor phase and require a lower activation energy compared to most other organic radical-generating reactions[44-46]. The NHS-diazirine sublayer is necessary for enabling the attachment of PFA to Si(100). The bulky fluorinated terminal chain of the PFA molecule is expected to be inert towards the ALD chemistry and provide robust shielding of any underlying surface active sites for ALD.

2.3 Materials and Methods

All reagents and solvents were used as received without further purification. Solvents were purchased from Sigma-Aldrich and filtered through a 0.2 μm filter before use. The light sensitive carbene precursor molecule 2,5-dioxopyrrolidin-1-yl 4-(3-(trifluoromethyl)-3H-diazirin-3-yl) benzoate (NHS-Diazirine) was purchased from American Elements and stored in dark environments. Its application was carried out under yellow light only. The perfluorinated

amine used was 1H,1H-Perfluoropentylamine (PFA) and purchased from Sigma-Aldrich. P-doped <100> silicon wafers were purchased from University Wafer, Boston, Massachusetts. XPS spectra were recorded on a Kratos Axis Ultra XPS spectrometer equipped with a mono-Al x-ray source at 200 W power and a pressure of 3.0×10^{-8} mbar. Survey scans were obtained between 0 and 1200 eV with a step size of 1 eV, a dwell time of 200 ms, and a pass energy of 140 eV averaged over 2 scans. Core-level region scans were obtained at the corresponding binding energy ranges with a step size of 0.1 eV, an average dwell time of 260 ms, and a passing energy of 20 eV averaged over 10 scans. Data were processed using CasaXPS software and instrument-specific atomic sensitivity factors (ASF). All C 1s peaks were calibrated to 284.7 eV and this same binding energy shift was applied to all other spectra besides Si 2p to account for adventitious carbon contamination. The quantitative accuracy of the atomic percentages determined from XPS region spectra is approximately 90-95% of each peak area (0.05-0.10 At%)[106]. Prior to analysis, samples were transported in petri dishes under Ar from the preparation lab to the XPS. Ellipsometry was recorded using a J.A. Woollam M-2000 Ellipsometer whose error is roughly $\pm$ 0.5 nm under optimal testing.

2.3.1 Preparation of H-Terminated Silicon Surface

All glassware was washed with 1X Nano-Strip solution (a stabilized formulation of sulfuric acid and hydrogen peroxide) followed by rinsing with water and isopropanol (IPA) before being dried in an oven overnight at 130°C. A 4 cm^2 Si(100) substrates were soaked in Nano-Strip at 75 °C for 15 min to produce OH-Si(100) surfaces. Following the oxidation, the substrates were immersed in a 5% aqueous hydrofluoric acid (HF) solution for 6 min to chemically etch away the native oxide layer and form hydrogen terminated silicon. The

substrates were then quickly rinsed with water and isopropanol and dried under a filtered nitrogen gas.

2.3.2 Insertion of Carbene into Si-H Surface Bonds and Self-Assembly of Perfluorinated Amine

All glassware was washed with Nano-Strip solution (Cyantek) followed by rinsing with water and IPA 99.5% before being dried in an oven overnight at 130 °C. A 4 cm^2 Si substrate was soaked in Nano-Strip for 5 min and then submerged in 5% aqueous HF solution (9:1 vol%) for 6 minutes to chemically etch away the native oxide layer and form H-Si(100). The substrate was then rinsed briefly with water and isopropanol and dried under nitrogen gas. The vapor-phase deposition of the NHS-diazirine was carried out in a custom-built UV reactor. The H-Si(100) substrate was placed 10 cm away from 7.5 mg of NHS-diazirine. Reactor was pumped down (>200 mtorr) and heated to 89 °C. UV light was turned on and entered from the sides of the vacuum chamber. After 90 min, the reactor was vented and allowed to cool. The newly NHS-terminated surface (NHS-Si(100)) was removed and rinsed with isopropanol/ dichloromethane/ isopropanol, then dried under nitrogen gas. The NHS-Si(100) surfaces were then submerged in a 10mM solution of perfluorinated amine in isopropanol and 15 ul of triethylamine for 2 hours at room temperature to form fluorinated Si (PFA-Si(100)). The surfaces were removed and rinsed with isopropanol/water/isopropanol and dry under a stream of filtered nitrogen.

2.3.3 Atomic Layer Deposition of Al_2O_3 thin film.

Deposition of Al_2O_3 thin films were carried out using a Cambridge Savannah 200 ALD reactor. NHS-Si(100), PFA-Si(100), H-Si(100), and OH-Si(100) samples were taken from Ar storage and placed in the reactor and heated to 130 °C. $Al(CH_3)_3$ (Hi-k grade, Air Products) and H_2O were flowed into the reactor for 0.03 and 0.05 s, respectively, using a 20 sccm nitrogen

carrier gas. The reagent exposures were 6×10^{-4} torr-sec and 1×10^{-3} torr-sec during the $Al(CH_3)$ and H_2O pulses, respectively. The base pressure in the reactor between pulses was 0.3 mbar. A 20 s nitrogen purge followed each precursor pulse. On less otherwise stated, this process was repeated for 20 cycles of deposition.

2.4 Results and Discussion

2.4.1 Defining ALD Process Parameters

Before conducting selectivity studies with ALD one must ensure that their base ALD process conditions are adequate for uniform film growth. Each ALD cycle should more-or-less produce the same equilibrium growth behavior within the deposition chamber for a given set of process conditions. The primary kinetic parameters of ALD consist of; (1) process temperature (i.e. heating of reactant lines, reactor vessel, sample), (2) partial pressure of ALD film precursor (i.e. vapor pressure and carrier flow rate), (3) deposition time that allows for complete self-limiting reactions, and (4) reactor purge time that delineates flux of ALD reagents.

Metal oxide ALD is primarily a thermally activated growth process. Thus, temperature is the key parameter in controlling film growth. There must be adequate heating of the various ALD components, namely the reactant source and carrier lines, reactor chamber, and deposition substrate. The temperature of each of these parts will influence the growth per cycle (GPC) rate of the ALD film. If the temperature conditions are too low at any of these parts, then slow reaction kinetics may result in an incomplete and disordered monolayer. For example, if the temperature of the carrier lines is too low, then the ALD reactants, which are introduced as a vapor from a pressurized cylinder, may condense within the carrier lines and not reach the reactor. If the reactor vessel or growth substrate aren't adequately heated, then the reagents may condense and result in non-ALD type deposition on the substrate. Alternatively, if the process temperature of any

component is too high, then the reactant molecules may decompose during transport or subsequently desorb from the substrate. Both potentially resulting in low GPC or non-ALD substrate growth. Consequently, there exists a "temperature window" which promotes even saturation of the ALD chemistry upon the desired growth substrate. This window is of course specific to the ALD chemistry.

This work utilizes ALD chemistries which deposit alumina (Al_2O_3) thin films generated from reactions between trimethylaluminum (TMA, $Al(CH_3)_3$) and H_2O. Standard temperatures for Al_2O_3 thin film ALD range from 100-300°C[41, 43, 101, 107, 108] (although newer studies are looking at growth at <100 °C[109-113]). To find an operating temperature that fell within the "temperature window" for ALD using our reactor, separate Al_2O_3 films were grown at 100°C, 130°C, 150°C, and 200°C for 20 cycles. The resulting GPC rates as a function of ALD chamber temperature are shown in **Figure 2.1**.

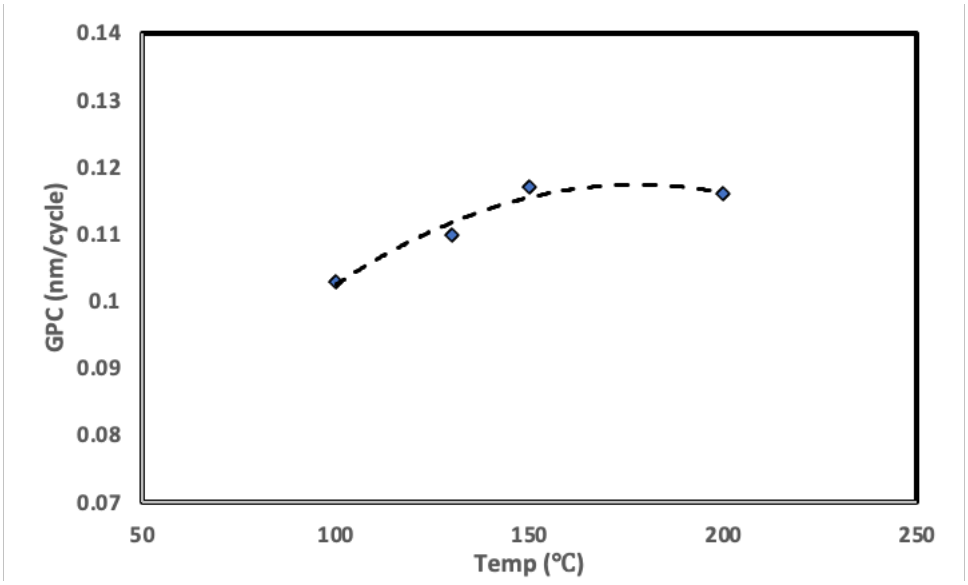

Figure 2.1 ALD film growth per cycle change (film thickness calculated using Eq 2.2) with reactor temperature.

The decrease in GPC under 130°C is probably the result of the slower reaction rate. Full thermal activation of the ALD reaction appears to be achieved when the reactor temperature is at least 150°C. At this point, ALD growth becomes independent of reactor temperature as approximately the same GPC is exhibited at both 150°C and 200°C. If the reactor temperature continues to increase above 200°C, it is expected that the GPC will hover around 0.115 nm/cycle and then eventually decrease due to decomposition. Overall, all the testing temperatures do appear sufficient for overcoming the thermal activation barrier required for precursor transport and grafting onto the growth substrate. In general, the lower the deposition temperature, the more favorable the process is for electronic device manufacturing.

The partial pressure of the ALD film precursors must be high enough to ensure saturation of the substrate growth surface. This is a function of both the vapor pressure of the precursor molecule and its pulse duration in the reactor. Since the same precursor molecule is used, TMA, the vapor pressure should be fixed at a given process temperature. Additionally, a constant N_2 carrier gas flowrate of 20 sccm was used. Thus, the precursor pulse duration is the one parameter that was more easily optimized. The pulse duration of the H_2O co-reactant is also controlled. The combination of both parameters and their effect on Al_2O_3 growth at 130°C is shown in **Table 2.1**.

Table 2.1 Combination of TMA and H_2O pulse durations and their effect on GPC.

TMA Precursor Pulse Duration (ms)	H_2O Coreactant Pulse Duration (ms)	
	30	50
15	--	0.04 nm/cycle
30	0.13 nm/cycle	0.09 nm/cycle
50	0.07 nm/cycle	0.10 nm/cycle

A GPC comparable to those observed in **Figure 2.1** is not achieved when the TMA pulse duration is below 30 ms and the water pulse duration is below 50 ms. This is most likely the result of incomplete saturation of the growth substrate with the adsorbed TMA intermediates ($Al(CH_3)_2$

and $AlCH_3$). When both molecules are pulsed in for 30 ms, the 0.13 nm/cycle is suggestive of some degree of non-ALD growth. Perhaps the H_2O pulse length requires a longer timescale to fully saturate the adsorbed intermediate film on the substrate, and consequently the unhydrolyzed intermediates promote a different form of deposition. The self-limiting nature of this reaction should result in little change in GPC as a function of the H_2O coreactant pulse time, as long as an initial threshold of pulse duration is surpassed. Both TMA pulse durations at either 30 or 50 ms produce standard GPCs (at 130°C) that are also observed in literature[43, 108, 112, 114] when paired with a 50 ms H_2O coreactant pulse time. Because there is little change in GPC when increasing the TMA pulse duration from 30 ms to 50 ms (relative to the change between 15 ms and 30 ms), it is likely that full precursor saturation of the substrate active sites occurs within this range. Therefore, any increase in TMA pulse length should theoretically only be in excess. However, it should be noted that there are examples in literature when much longer TMA and water pulse durations (up to 1 s) are used in Al_2O_3 ALD[109-111, 115]. Evidently this may be caused by a wide variety of factors including; component temperature, base reactor pressure, and/or carrier gas flowrate. In general, longer precursor dosing is required for lower process temperatures (<115 °C) and carrier gas flowrates (<20 sccm). The faster pulse lengths used in this work has the potential of reducing TMA waste, however, there is a chance that a higher number of initial cycles is required to form a complete monolayer. Overall, it is important that the surface reactions should be fast and irreversible.

Lastly, reactor purge times between each pulse of reagent must be long enough to ensure that any excess molecule that is not participating in the substrate surface reaction is removed. At temperatures below 150°C both TMA and water molecules may remain physiosorbed on the substrate surface or on the reactor interior[101]. Thus, longer purge times, typically four times the

precursor pulse duration, are required so that desorption and purge take place. All ALD experiments in this work were conducted with a 20 s N_2 purge between each reagent pulse.

Given the self-limiting nature of ALD, in theory film growth should be close to constant at a given set of conditions. However, in practice, results in literature do vary even under near equivalent conditions. For example, for Al_2O_3 ALD with TMA and water on OH-Si around 115°C, reported GPCs have ranged from 0.1 nm/cycle to 0.3 nm/cycle[116-119]. A potential source for these deviations may stem from hardware specific factors. For instance, some ALD systems experience a "conditioning effect" where GPC and film uniformity improve with preceding depositions in the same vessel. This effect has been observed in the ALD of Co films where consistent GPCs were not attained until multiple Co runs were carried on in the same reactor before adding the substrate[120, 121]. The authors of this study do not arrive at a definitive reason for why reactor conditioning was necessary but do state that "…the effect is crucial to facilitate reproducibility between labs.". Reactor design characteristics such as; line leaks, zones of stagnant flow, interior thermal variation, and valve blockage may all contribute to ALD run variability. Coincidently, a conditioning effect was observed with the Cambridge Savannah 200 ALD reactor used in this study.

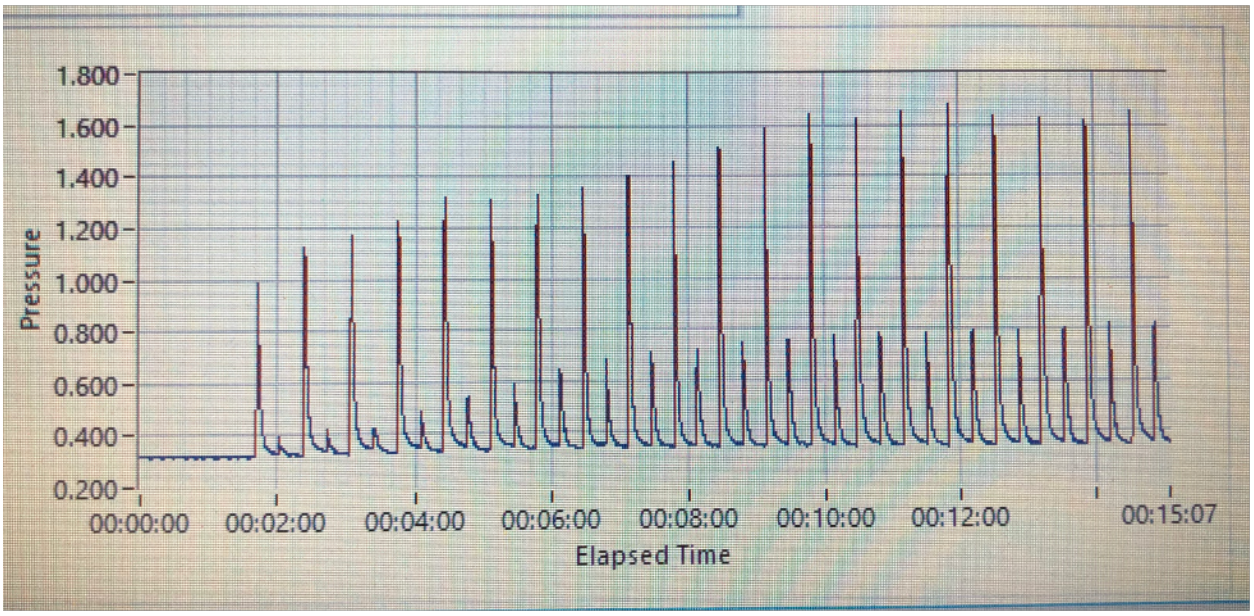

Figure 2.2 Realtime pressure readings from within ALD reactor during 20 cycles of Al_2O_3 deposition with TMA (first pulse) and water (second pulse).

The real time pressure measurements in **Figure 2.2** show that a consistent rise in pressure after either TMA or water pulse is only attained after 13 cycles. After this point the increase in pressure following each respective pulse is approximately the same. Thus, complete saturation of the substrate surface may not occur during the initial cycles. Again, the cause of this conditioning effect is not known and may vary from system to system. For this specific reactor, reagents are fed through a series of both stainless steel and plastic lines, thus, there may be a lag time required for the entire system to thermally equilibrate and reach saturation vapor pressure. Nevertheless, in this work each ALD run was preceded by 20 cycles of Al_2O_3 conditioning. The effect of this conditioning is shown in **Figure 2.3**.

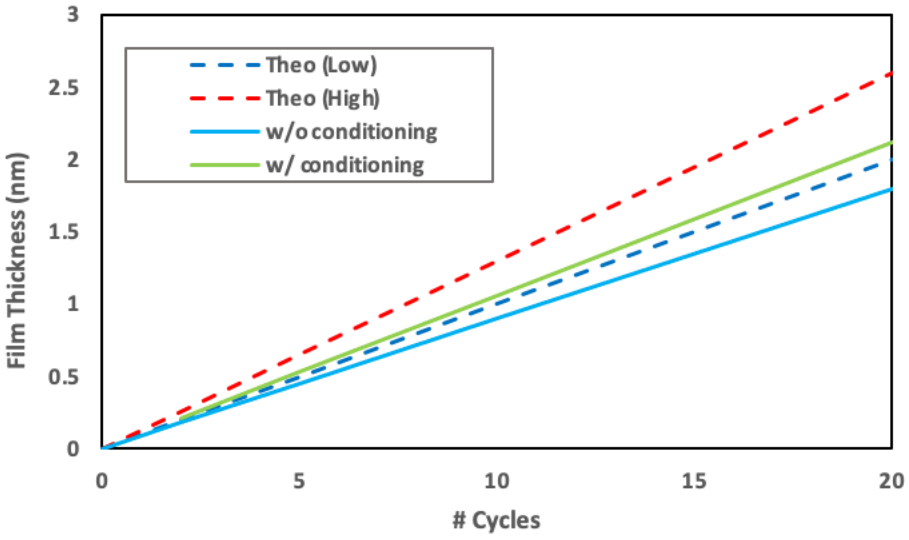

Figure 2.3 ALD thickness profiles measured using ellipsometry for Al_2O_3 film growth across 20 cycles. Dashed lines represent the upper and lower bounds of growth at similar processing conditions found in literature[117, 118, 120]. Solids lines represent ALD process in this study with and without prior reactor conditioning (profiles were generated by single film thickness measurements after 20 cycles and extrapolating GPC).

The ALD thickness profiles in **Figure 2.3** demonstrate that at identical ALD processing conditions, prior reactor conditioning resulted in increased GPC. Specifically, reactor conditioning appeared to be the difference between achieving or not achieving Al_2O_3 growth within the standard range of GPCs found in literature.

In summary, it was determined that Al_2O_3 ALD reactions will be carried out at 130°C (system and substrate temperature) with cycles consisting of 30 ms TMA pulse/20 ms N_2 purge/50 ms H_2O pulse, all preceded by 20 cycles of conditioning. A OH-Si(100) substrate will serve as a representative GS and H-Si(100) a NGS. These two standard samples were included in each subsequent ALD experiment as controls in case of any growth variability. The deposition rates on each of these surfaces also serve to gauge growth selectivity when evaluating potential ALD resists.

2.4.2 Evaluating OH-Si(100) and H-Si(100) as Complementary AS-ALD System

ALD of Al_2O_3 on OH-Si(100) is one of the most studied surface reactions in "bottom-up" deposition. Due to the ease in which H-Si(100) is generated from OH-Si(100), these two materials are often posed as complementary systems for AS-ALD. Other potential ALD resist candidates are often evaluated against H-Si(100) to determine their viability. Thus, it is important to first establish the performance of both OH-Si(100) and H-Si(100) towards Al_2O_3 ALD as a baseline.

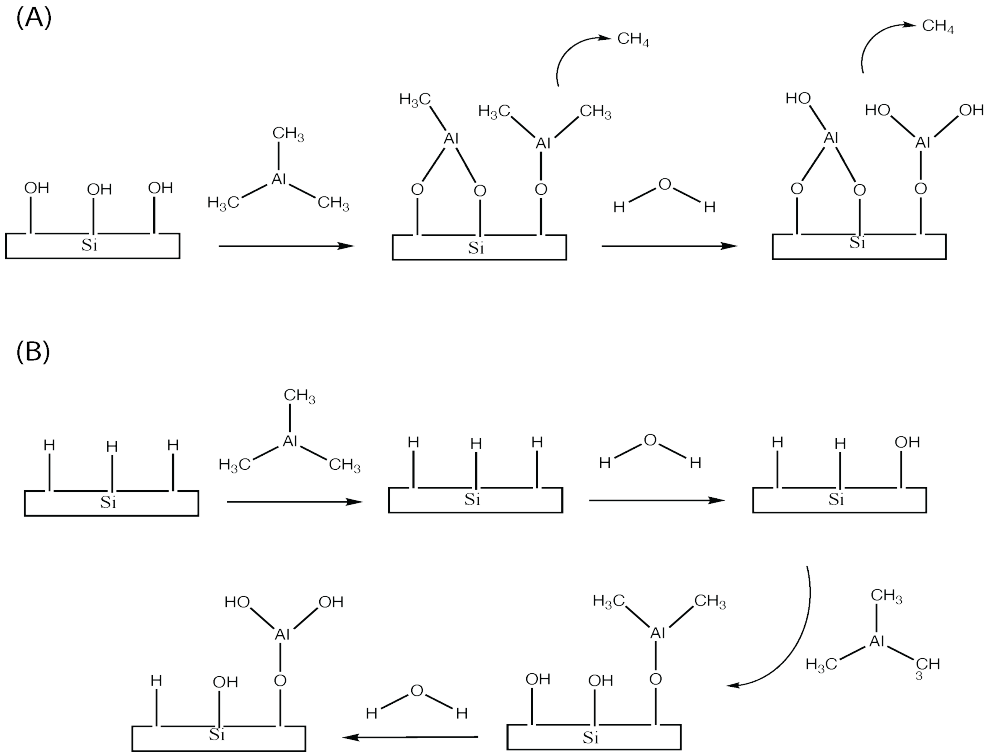

Figure 2.4 Established Al_2O_3 ALD mechanism on (A) OH-Si(100)[49, 105, 118] GS and (B) H-Si(100) NGS.

The schematic shown in **Figure 2.4** shows how both TMA and water should react to form Al_2O_3 on OH-Si(100). First, TMA dissociatively chemisorbs onto the hydroxylated surface. Next, the $AlCH_3$ surface intermediates are reacted with water vapor to form Al_2O_3 with CH_4 as a byproduct. Also shown in **Figure 2.4** is how the ALD reagents may interact with a H-Si(100) surface across multiple ALD cycles. The surface begins inert towards the TMA molecule, but during the next halfcycle of water exposure, partial hydrolysis of the surface allows local

chemisorption of the $AlCH_3$ intermediate on the surface. These intermediates form Al_2O_3 surface domains with water and will nucleate, eventually resulting in a continuous film given enough cycles.

The effectiveness of a complementary resist system for selective ALD is evaluated using the following equation;

$$Selectivity = \frac{X_{GS} - X_{NGS}}{X_{GS} + X_{NGS}} \quad \text{(Eq 2.1)}$$

where, X_{GS} is the amount of material on the defined GS and X_{NGS} the material measured on the NGS. The amount of material can be measured using ellipsometry or XPS. Measuring the early stages of film thickness on H-Si(100) is problematic due to partial oxidation on the surface and defects that may have formed during the HF etch, possibly rendering the top surface different than the bulk material. In order to accurately model refractive index on H-Si(100), additional calibration with other surface analysis techniques is most likely necessary. Therefore, unless otherwise specified, in this study ALD film thickness was determined using Si 2p XPS intensity measurements corrected for appropriate sensitivity factors (ASF). These estimates are compared with thicknesses determined using the increase in Al 2p XPS peak intensities to check for consistency. Thickness estimates are determined using the a well-established equation[122];

$$d_{Al_2O_3} = -\lambda_{Al_2O_3} \ln\left(\frac{I_{Si}}{I_{Si,o}}\right) \quad \text{(Eq 2.2)}$$

where, $d_{Al_2O_3}$ is the Al_2O_3 film thickness, $\lambda_{Al_2O_3}$ the photoelectron mean free path in Al_2O_3, I_{Si} the Si 2p signal intensity after ALD, and $I_{Si,o}$ the intensity before ALD. For Si 2p electrons passing through the Al_2O_3 film, a mean free path of 2 nm was used. Using **Equation 2.2** and Si 2p peak intensities from the spectra in **Figure A2.1**, Al_2O_3 film thicknesses were determined following 5, 10, 15, 20, 40, 60, and 80 cycles of ALD on OH-Si(100) and H-Si(100) are shown in **Figure 2.5**.

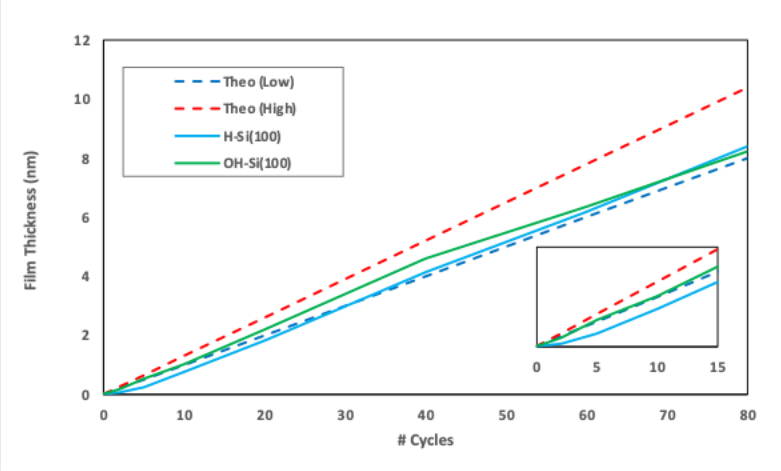

Figure 2.5 ALD thickness profiles for Al_2O_3 film growth across 80 cycles. Dashed lines represent the upper and lower bounds of growth at similar processing conditions found in literature[117, 118, 120]. Solids lines represent experimental ALD growth on OH-Si(100) and H-Si(100) surfaces.

Here, an initial growth selectivity is observed on OH-Si(100) relative to H-Si(100) during the first 60 cycles of deposition. This coheres well with the idea that OH-Si(100) is a suitable GS and H-Si(100) a NGS for ALD. However, unlike a true NGS, there appears to be Al atom deposition onto H-Si(100) from the very first cycle. The inset in **Figure 2.5** shows that the selectivity window for H-Si(100) was about a 6 cycles. Additionally, the growth selectivity between OH-Si(100) and H-Si(100) is only 20% between cycles 1-3, whereas others have reported selectivities of up to 60% between the same to surfaces for metal oxide ALD[123-125]. Both these observations are most likely the result of partial oxidation of the H-Si(100) surface during transport to the ALD reactor post-etching. Consequently, continued effort was made to reduce oxidation of H-Si(100) between steps throughout this study. As expected, selectivity wanes (dropping from 20% to 5.5% after 40 cycles) as H-Si(100) is continually hydrolyzed via exposure to the H_2O co-reactant. Adsorption of TMA then occurs at a higher rate on this increasingly oxidized surface and nucleates out to eventually form complete film growth on the previously inhibiting surface. This is a major issue that H-Si(100) encounters as a NGS for metal oxide ALD, as the co-reactant needs to be an oxidant (i.e. H_2O, O_2, O_3). Thus, the ability to passivate H-Si(100) with a molecule that is

also inert towards the ALD chemistry would be highly desirable. Interestingly, despite the initial deposition delay, film growth on H-Si(100) not only catches up with OH-Si(100) but even surpasses it after 60 cycles. It is not clear why the H-Si(100) surface would become even more reactive than OH-Si(100) after complete selectivity loss.

2.4.3 Evaluating Small Molecule Organics as ALD Resists

The Shestopalov group has previous demonstrated the attachment of NHS-Diazirine on H-Si(100). This molecule on its own was not expected to be an effective ALD inhibitor due to the presence of several carboxylic groups in the head group (when bonded to H-Si(100)) that should promote metal oxide growth. Therefore, in this work a PFA overlayer was covalently attached onto the diazirine functionalized surfaces as shown in **Figure 2.6** and this bilayer system was evaluated as an ALD resist.

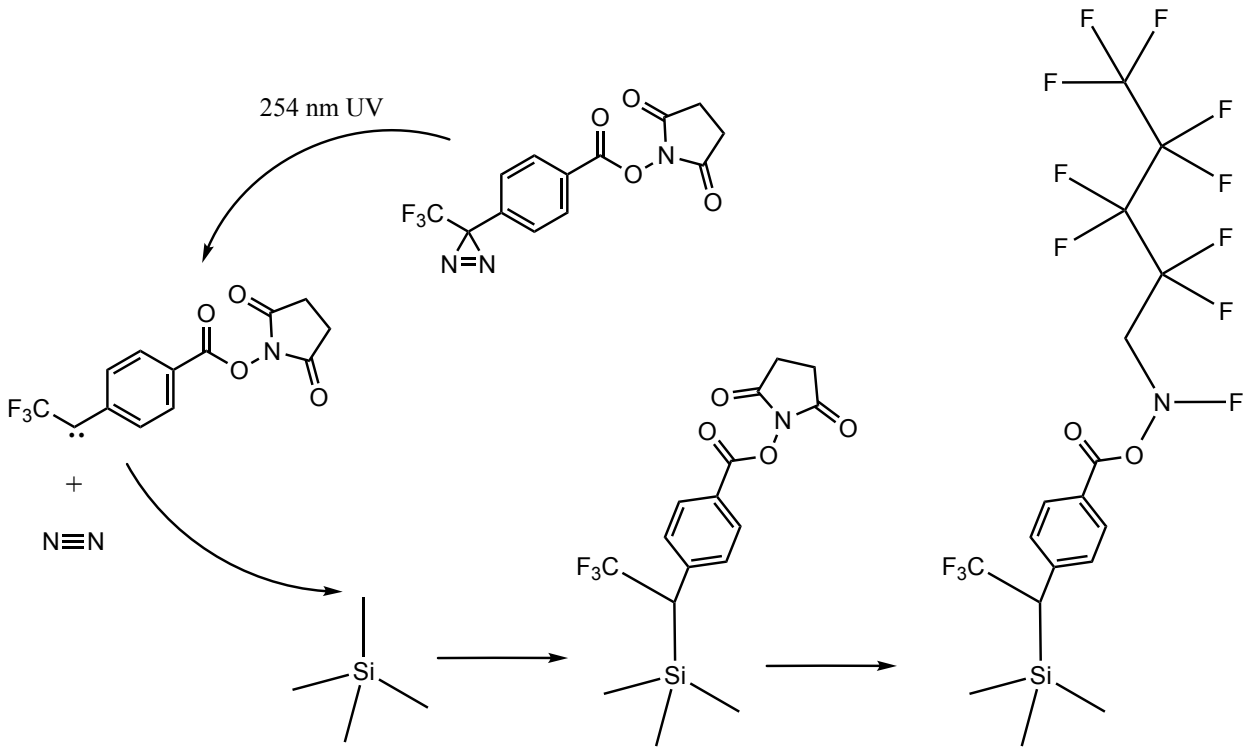

Figure 2.6 Reaction mechanism showing functionalization of H-Si(100) with NHS-Diazirine sublayer and subsequent attachment of PFA overlayer.

The NHS-diazirine functionalization strategy relies on the removal of the diazo group via UV exposure, thus forming a carbene (divalent C). This reactive dual-radical group will then directly attach itself into Si-H surface bonds. Subsequently, PFA is anchored to the surface via nucleophilic substitution between the amine and the carboxylic species present in the N-Hydroxysuccinimide (NHS) end group. The modification of NHS-terminated substrates with amines has been demonstrated elsewhere in literature[126, 127]. XPS was used to determine the efficacy of each surface reaction step and is shown in **Figure 2.7**.

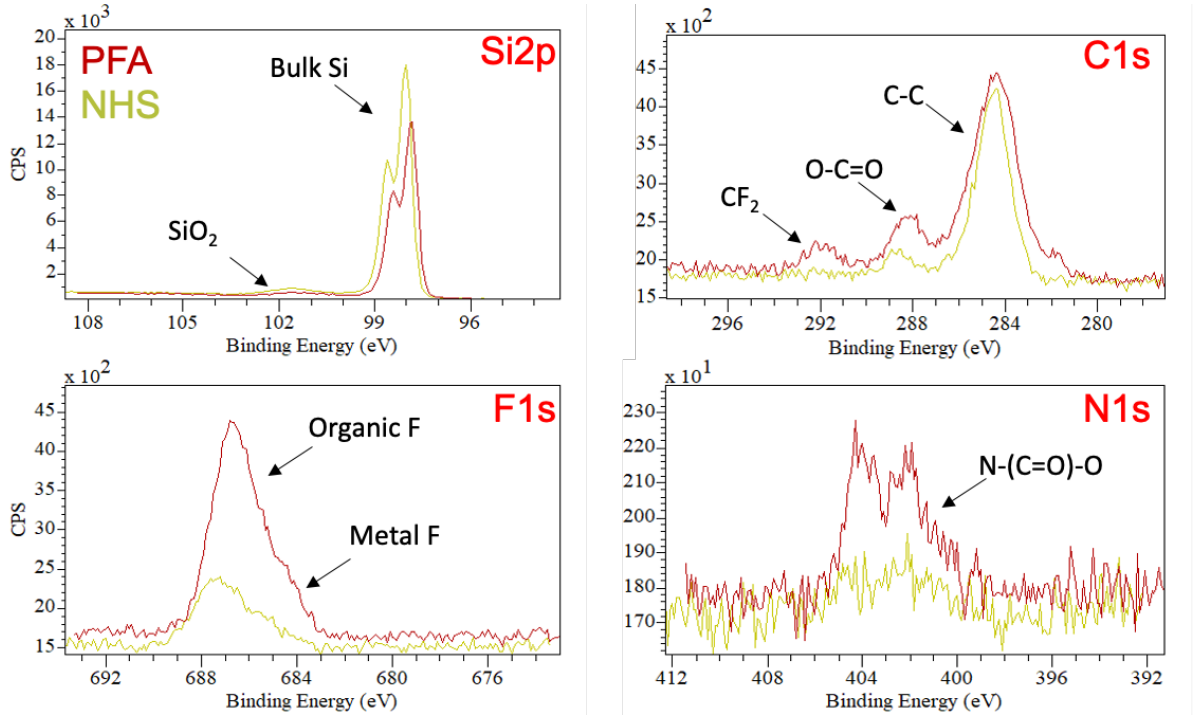

Figure 2.7 Si 2p, C 1s, F 1s, and N 1s XPS spectra measured from NHS-Si(100) and PFA-Si(100).

The Si 2p spectra in **Figure 2.7** demonstrates that the underlying H-Si(100) surface experienced minimal oxidation during each reaction step. This is evidenced by the weak signal detected at 101.5 eV in both spectra. This is important as NHS-diazirine is non-reactive with surface hydroxyls and any surface oxide will enhance the ALD growth behavior of the interface. The drop in bulk Si signal at 98 eV between the NHS-Si(100) and PFA-Si(100) surfaces is most

likely due to attenuation of the Si 2p signal from the denser attached PFA moiety. Both the slight peak shift detected at 286 eV in the C 1s spectra and N 1s signal detected for both surfaces is suggestive of NHS-diazirine attachment. Furthermore, the C 1s signal measured at 292 eV on PFA-Si(100) is highly suggestive of CF_2 species surface incorporation. It should be noted that signal at 288 eV in the C 1s spectra from both surfaces is likely the result of adventitious carbon contamination from the surrounding environment. It may also be partially derived from the carbonyl group present in NHS-Diazirine. Lastly, the growth of the F 1s signal between NHS-Si(100) and PFA-Si(100) surfaces is good evidence for the attachment of the fluorinated chain in PFA. The small shift to 684.5 eV is most likely from residue of the HF etch. Having established the functionalization of H-Si(100) with NHS-Diazirine and the subsequent attachment of PFA, both PFA-Si(100) and NHS-Si(100) surfaces underwent 20 cycles of ALD, along with OH-Si(100) and H-Si(100) controls.

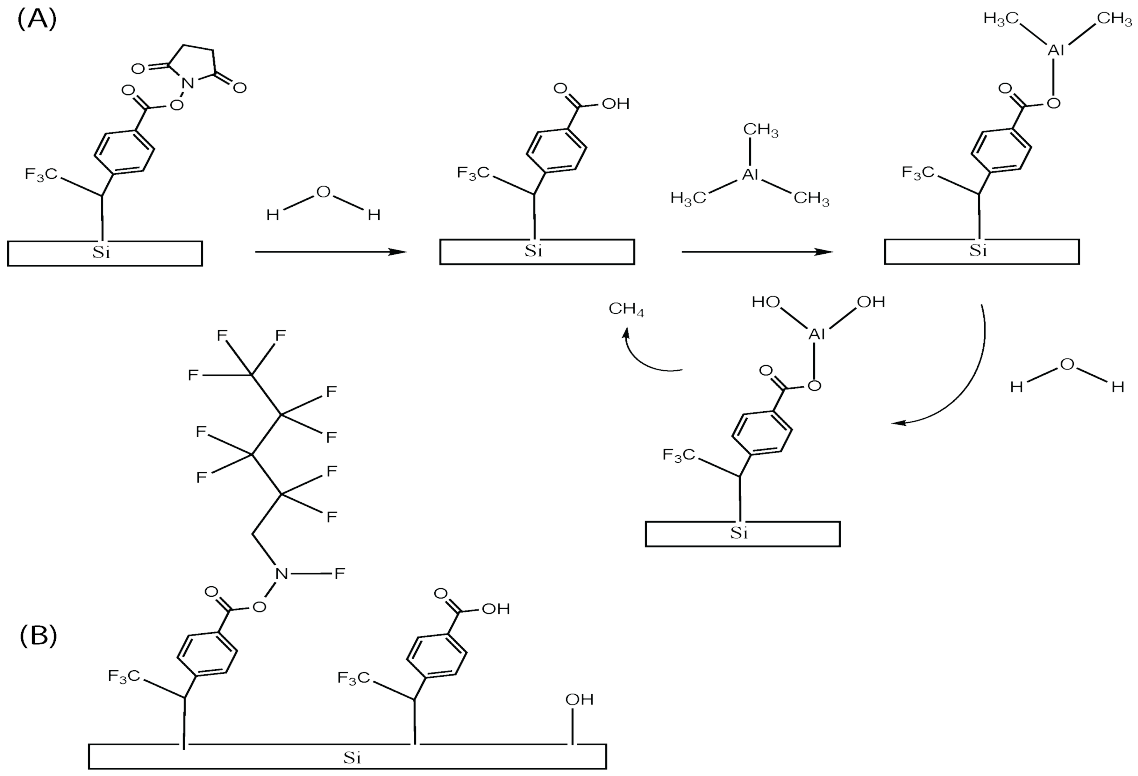

Figure 2.8 Possible Al_2O_3 ALD mechanisms on (A) NHS-Si(100) and (B) PFA-Si(100) NGS.

Figure 2.8 shows the possible mechanisms in which Al_2O_3 ALD may commence on NHS-Si(100) and PDA-Si(100) surfaces. Although used to passivate H-Si(100), as stated previously, the NHS-Diazirine molecule should be relatively reactive with ALD chemistry. Perhaps initially inert towards TMA, the water halfcycle pulse will likely hydrolyze the N-O bond and dissociate the NHS moiety from the surface. The remaining hydroxyl would then serve as an active site for TMA reaction. Hence, attachment of PFA is used to shield both the N-O bond and any underlying un-passivated surface domains. However, with repeated cycles the PFA-Si(100) surface too will lose its selectivity. As shown in **Figure 2.8** this could be due to uncovered diazirine and hydroxyl terminations scattered throughout the PFA layer. As has been shown, these species are reactive with the ALD chemistry and will form "islands" of $AlCH_3$ and Al_2O_3 deposition which will nucleate throughout the inhibiting layer. Thus, it is important to optimize the PFA reaction so that high monolayer coverage is achieved. However, this may be complicated by the sterics of the bulky perfluorinated chain.

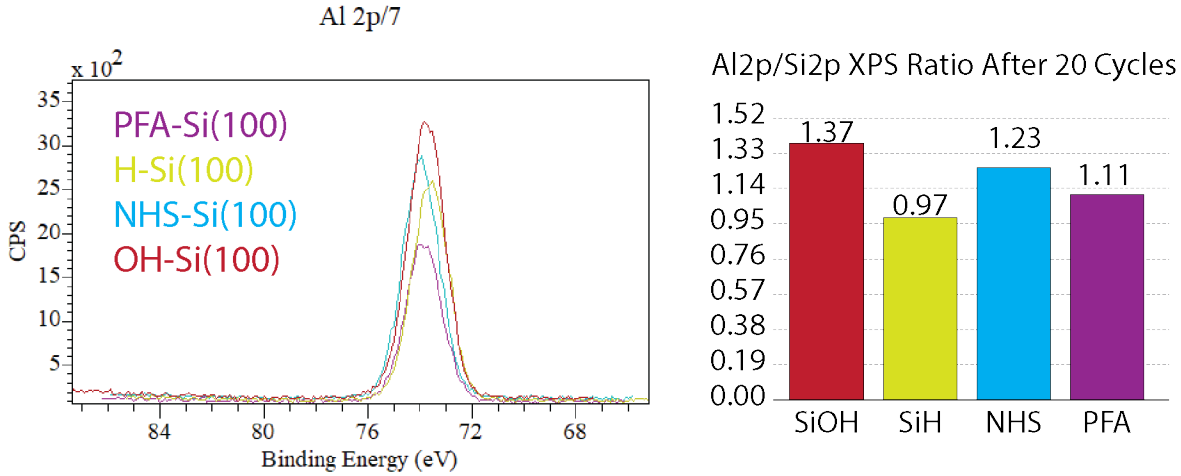

Figure 2.9 (*Left)* Al 2p XPS spectra and (*Right)* histogram of Al2p/Si2p XPS signal ratios (normalized to the Si 2p signal such that relative compositions (Al atoms to Si atoms) are being compared) for OH-Si(100), H-Si(100), NHS-Si(100), and PFA-Si(100) surfaces post 20 cycles of Al_2O_3 ALD.

The XPS data in **Figure 2.9** demonstrates that partial ALD film inhibition was observed on H-Si(100), NHS-Si(100), and PFA-Si(100) relative to OH-Si(100). In the Al 2p spectra, the

lowest signal was observed from the PFA-Si(100) surface. However, when normalizing this signal by the Si 2p peak intensity shown in **Figure A2.2** (Al atoms to Si atoms, each surface having approximately the same number of Si atoms), the lowest Al2p/Si2p signal ratio was actually measured from H-Si(100). Therefore, although PFA-Si(100) can act as a NGS for AS-ALD, its effectiveness at blocking deposition was inferior to that of H-Si(100). However, given the extreme volatility and low air stability of H-Si(100), PFA-Si(100) may possess some other advantages that make it a more ideal NGS. As was expected, NHS-Si(100) exhibited the second most deposition of Al atoms onto its surface. Lastly, Al2p/Si2p signal ratios were used to evaluate ALD inhibition and not Al_2O_3 thickness estimations, because it is difficult to make these estimates given the unknown monolayer density of the diazirine and PFA layers beneath the ALD film.

2.5 Conclusion

In this study, a baseline was established for Al_2O_3 thin film growth on OH-Si(100) and H-Si(100) surfaces using our ALD reactor. Next, the functionalization of H-Si(100) with NHS-diazirine and subsequent PFA attachment was validated using XPS. Both NHS-Si(100) and PFA-Si(100) were then evaluated against H-Si(100) as possible NGS for Al_2O_3 ALD. XPS results demonstrated that H-Si(100) exhibited greater ALD blocking than both SMI-functionalized surfaces. In addition to inferior blocking, the PFA molecule was also deposited in the solution phase rendering its use and reapplication in vacuum-based deposition processes such as AS-ALD highly problematic. Thus, it is important to find ALD resists which (1) demonstrate superior or comparable blocking to H-Si(100), (2) can be deposited onto a substrate in the vapor phase, and (3) are small-enough in length to prevent EPE on the sub-10nm level.

Chapter 3 Halogen Atomic Resists for AS-ALD

This chapter is a slightly modified version of "*Vapor-Phase Halogenation of Hydrogen-Terminated Silicon(100) Using N-Halogen-Succinimides*" published in *ACS Applied Materials & Interfaces* and has been reproduced here with the permission of the copyright holder.

3.1 Chapter Structure

The focus of this chapter is to demonstrate the vapor phase halogenation of Si(100) and subsequently evaluate the inhibiting ability of the halogenated surface towards ALD of Al_2O_3. Hydrogen-terminated silicon <100> (H-Si(100)) was halogenated using *N*-chlorosuccinimide (NCS), *N*-bromosuccinimide (NBS), and *N*-iodosuccinimide (NIS) in a vacuum-based chemical process. This vacuum-based halogenation leads to the formation of stable Si-halogen bonds while preventing subsequent generation of organic complexes observed in solution-based halogenation schemes with succinimides. The vapor reactions most likely proceed through a radical initiator mechanism where a steady-state and sustained flux of molecular halogen species is produced from the corresponding N-halogenated succinimides. The composition and physical properties of the prepared monolayers were analyzed using XPS spectroscopic ellipsometry (SE), and contact angle goniometry. XPS and contact angle measurements confirmed that all three reagents were more effective in halogenating H-Si(100) over OH-Si(100) in the vapor phase. The stability of the modified surfaces in air was also tested, with the chlorinated surface showing the greatest resistance to monolayer degradation and silicon oxide (SiO_2) generation within the first 24 hours of exposure to air. Lastly, angle-resolved XPS (ARXPS), SE, and AFM measurements all showed that the succinimide-derived Hal-Si(100) surfaces exhibited superior blocking ability to that of H-Si(100), a commonly used ALD resist. This halogenation method provides a dry chemistry alternative for creating halogen-based ALD resists on Si(100) in near-ambient environments.

3.2 Introduction

Considering the limitations of SAM and some SMI resists, recent efforts in AS-ALD have been directed toward the development of atomic resists that can promote or block ALD reactions by changing the surface termination of the deposition substrate. These studies are focused on developing chemo-selective atomic resists that can withstand multiple ALD cycles without losing their growth selectivity (i.e. the number of cycles before a resist loses its blocking ability)[44, 128-130]. Halogenated Si(100) (Hal-Si(100)) is a promising candidate for fabricating semiconductor interfaces used in electronics,[131] nanotechnology,[132, 133] and biosensing[134, 135]. It is a more stable alternative to H-Si(100) in air, and can better maintain the required difference in chemical reactivity on a surface for AS-ALD due to the bulkier structure of the attached halogen species, which effectively shield the underlying NGS from ALD chemistry[136]. Different halogen precursors can be used to passivate Si(100), potentially enabling versatility in inhibiting different types of ALD chemistries. For example, a Cl-terminated Si(100) surface (Cl-Si(100)) is more reactive with thiols such as 1-octadecanethiol than a Br-terminated surface (Br-Si(100))[137]. Cl-Si(100) also lowers the activation energy for attaching NH_2 species onto silicon surfaces using vapor-phase ammonia. Furthermore, halogen atoms have demonstrated great potential as possible passivation species for pattern preservation on H-passivated materials under UHV[138].

Most research on halogenation of crystalline silicon has focused on the Si(111) interface[131, 133-135], but the structural differences between Si(111) and Si(100) result in different reactivities[139, 140]. Thus, there is a need to investigate halogen formation on Si(100) more extensively, as it is a more relevant material in semiconductor manufacturing[141]. The current standard for producing Hal-Si(100) involves generating a halogen flux from a solid-state, electrochemical cell in UHV[142-145], which is slow and not directly compatible with common commercial deposition systems.

Others have employed chlorine gas (Cl_2) under low pressure conditions to chlorinate Si(111)[146, 147], however, due to the toxicity of Cl_2 gas and its problematic incorporation into most vacuum deposition systems, there is a need to find other halogenation molecules that are safer to handle. Some have developed Si(100) halogenation methods using wet chemistry in near-ambient conditions[133, 146, 148-150], but these often require to be refluxed and generate byproducts that accumulate on the Si(100) surface. Vapor phase halogenation in mild vacuum is more compatible with other low vacuum processes such as AS-ALD, but few studies outside of UHV have focused on vapor phase halogenation of H-Si(100). Nonetheless, H-terminated silicon quantum dots (H-SiQDs) were chlorinated using chlorine gas (Cl_2)[137, 151-155] but both methods have resulted in SiQD oxidation and only partial halogenation. Thus, a more efficient and milder vapor phase halogenation method for crystalline Si(100) is needed.

This study reports the use of *N*-halogen-succinimide molecules as vapor-phase halogenation reagents for crystalline H-Si(100) in near-ambient conditions. *N*-halogen-succinimide molecules are often used as a precursor of molecular halogens in radical type reactions.[133, 151, 156, 157] The reaction scheme in this study may follow a radical initiator mechanism[158], where the terminal H atoms on a H-Si(100) surface are replaced by Cl, Br, or I atoms. However, unlike in solution-based halogenation processes where there will be higher concentrations of radical intermediates, it is less likely that these same intermediates will subsist in the gas phase unless an adequate low pressure environment is maintained.[159-161] Although, it is also possible that the radical reaction occurs on the Si interface in a condensed form. Alternatively, the halogenation process may occur via a more straightforward dissociative thermolysis reaction pathway.

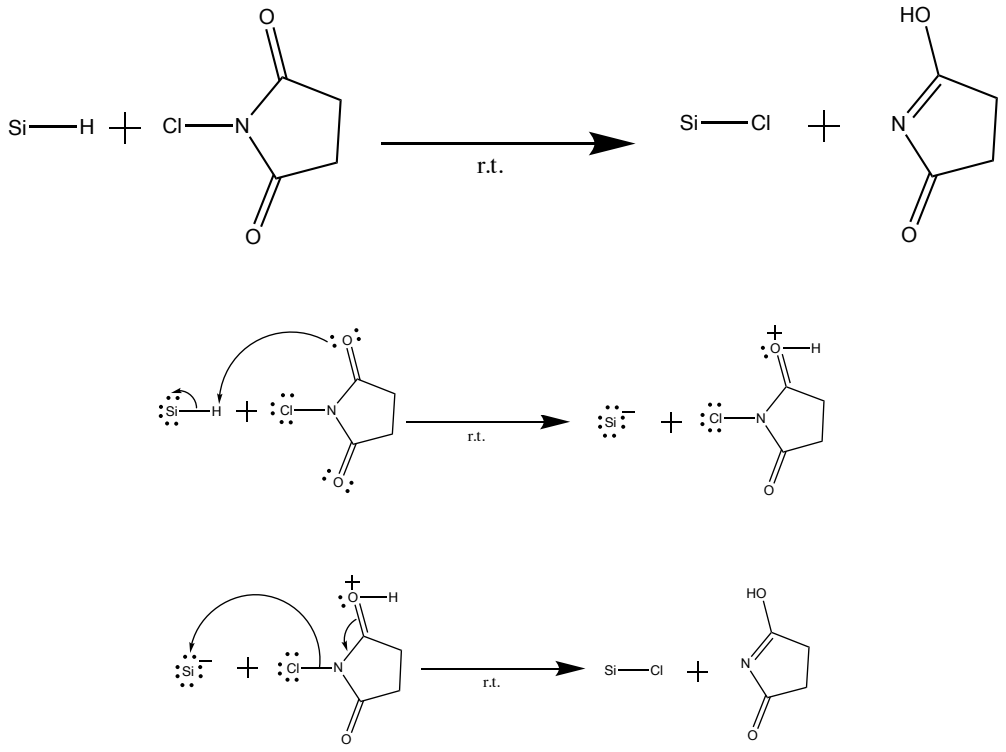

Here, the halogen molecule is dissociated from the succinimide via thermolysis to react with the high surface energy H-Si(100) interface, leaving a iminol, succinimide, or in the case some water molecules are present, hydroxy succinimide, vapor byproducts.

The halogen precursors used in this study were *N*-chlorosuccinimide (NCS), *N*-bromosuccinimide (NBS), and *N*-iodosuccinimide (NIS), which are all commonly used as halogenating and oxidizing agents in organic synthesis and can be handled in air.[134, 151, 162, 163] The resulting monolayers were characterized using XPS, SE, and contact angle goniometry. Calculations of surface coverage suggest that the Hal-succinimide halogenation process achieves a high level of coverage, albeit not complete. The reported halogenation reaction has been shown to have high chemo-selectivity and can be used to selectively halogenate H-Si(100) in the presence of hydroxyl-terminated surface sites. The stability of the Hal-Si(100) interfaces in air was investigated using XPS to monitor the concentration of oxide and halogen species on Si(100) over a 72-hour period. The results showed that the halogenated substrates degraded at a slower rate

compared than that of H-Si(100). When compared to other vapor phase halogenation techniques (i.e. halogen flux from an electrochemical cell in UHV, surface exposure to Cl_2 gas) N-Hal-succinimides require less of a low pressure demand and are safer to handle. Given these softer requirements, the described vapor-phase halogenation reactions are compatible with existing thin layer deposition systems. They could be used as an alternative to H resists on Si(100) in self-aligned AS-ALD. For example, any halogen resist regeneration in between ALD cycles can potentially be undertaken *in-situ* using certain line of sight evaporation techniques or the use of a rotary ALD chamber where a sample can be transferred from one vacuum chamber (for halogenation) to another (for ALD growth). Here, we studied the selectivity of the ALD of Al_2O_3 on Hal-Si(100) and on H-Si(100). Angle-resolved XPS (ARXPS) and ellipsometry data showed that the halogenated monolayers were better at inhibiting the ALD chemistry than H-Si(100). We believe that the development of highly selective and stable ALD resists, that can be deposited under mild vapor-phase conditions, would have numerous applications in bottom-up semiconductor manufacturing. However, more research is needed to understand the mechanism of defect formation during and after the reaction to further improve the coverage and stability of the halogen resists.

3.3 Materials and Methods

All reagents and solvents were used as received without further purification. Solvents were purchased from Sigma-Aldrich and filtered through a 0.2 μm filter before use. Light sensitive molecules NCS, NBS, NIS all with 99% purity were purchased from Sigma-Aldrich and stored in dark environments. Their application was carried out under yellow light. P-doped <100> silicon wafers were purchased from University Wafer, Boston, Massachusetts. XPS spectra were recorded on a Kratos Axis Ultra XPS spectrometer equipped with a mono-Al x-ray source at 200 W power

and a pressure of 3.0×10^{-8} mbar. Survey scans were obtained between 0 and 1200 eV with a step size of 1 eV, a dwell time of 200 ms, and a pass energy of 140 eV averaged over 2 scans. Core-level region scans were obtained at the corresponding binding energy ranges with a step size of 0.1 eV, an average dwell time of 260 ms, and a passing energy of 20 eV averaged over 10 scans. Data were processed using CasaXPS software and instrument-specific atomic sensitivity factors. All C 1s peaks were calibrated to 284 eV and this same binding energy shift was applied to all other spectra besides Si 2p to account for adventitious carbon contamination. Separately, the bulk Si signal in the Si 2p spectra were calibrated to 99 eV for better quantitative assignment of shifts in the spectra. Prior to analysis, samples were transported in petri dishes under Ar from the preparation lab to the XPS. AFM images were recorded on a NT-MDT AFM Microscope using a silicon nitride probe (Manufacturer: NanoWorld) with a tip radius of <15 nm, a resonance frequency of 67 kHz, and a force constant of 0.32 N/m. The same probe was used for each sample in tapping mode. The RMS roughness measurements should have an uncertainty of $\pm 0.01\ nm$ under optimal testing parameters. Goniometry measurements were conducted using ultra-pure water. SE scans were recorded using a J.A. Woollam M-2000 Ellipsometer.

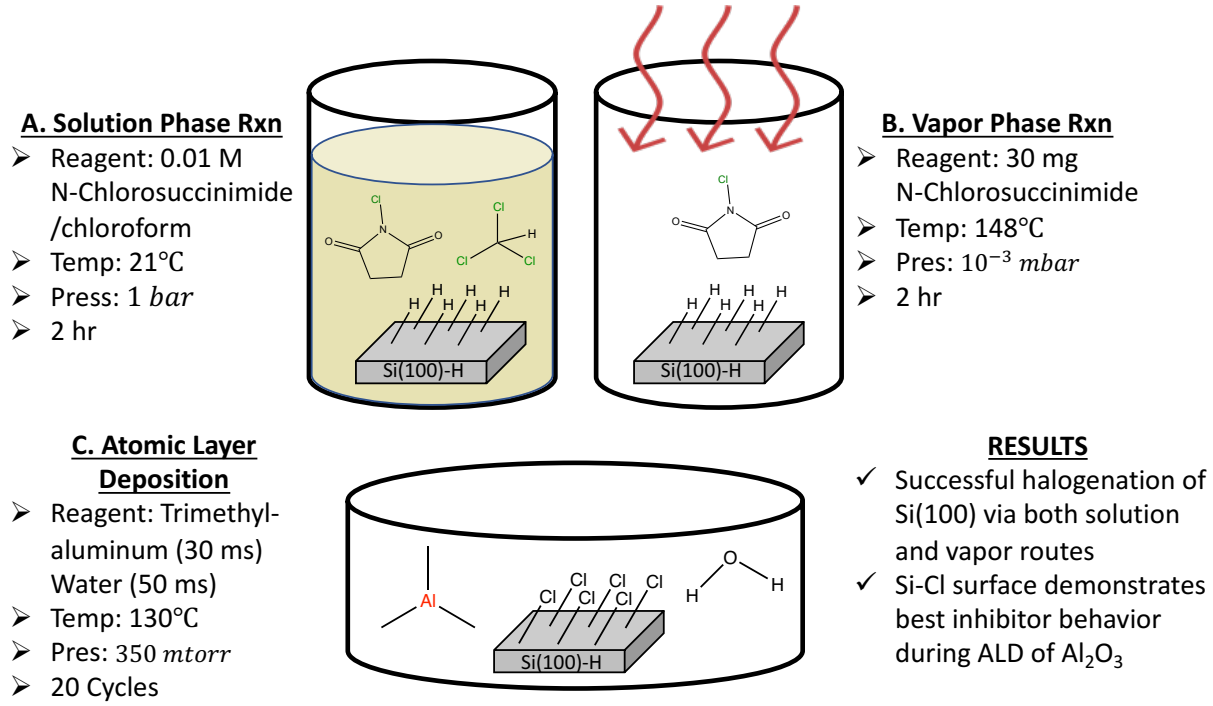

Figure 3.1 Illustration of experimental methods used in this chapter. (A) Solution phase reactions were carried out at ambient conditions with mixtures of each N-Hal-Succinimide molecules in chloroform. (B) Vapor phase reactions were carried out via the sublimation of N-Hal-Succinimide molecules under low vacuum and elevated temperature. (C) Lastly, the halogenated surfaces underwent 20 cycles of Al_2O_3 ALD to evaluate their effectiveness as inhibitors. H-Si(100) was halogenated via both solution phase and vapor phase reactions, however, undesired byproducts were also observed on the solution prepared samples, rendering them problematic for controlled ALD inhibition. Overall, chlorinated silicon demonstrated the highest degree of ALD film blocking.

3.3.1 Preparation of H-Terminated Silicon Surface

All glassware was washed with 1X Nano-Strip solution (a stabilized formulation of sulfuric acid and hydrogen peroxide) followed by rinsing with water and IPA before being dried in an oven overnight at 130°C. A 4 cm^2 Si(100) substrates were soaked in Nano-Strip at 75 °C for 15 min to produce OH-Si(100). Following the oxidation, the substrates were immersed in a 5% aqueous HF solution for 6 min to chemically etch away the native oxide layer and form H-Si(100). The substrates were then quickly rinsed with water and isopropanol and dried under a filtered nitrogen gas.

3.3.2 Solution-Phase Halogenation of H- and OH- Terminated Silicon with N-Halogen-Succinimides

A 10 mM solution of N-Hal-Succinimide in chloroform was prepared. Cleaned OH-terminated Si(100) substrates were formed in Nano-Strip at 75 °C for 15 min, thus undergoing robust hydroxylation and rendering the surface OH-terminated. OH-Si(100) and freshly prepared H-terminated Si(100) substrates were placed in a vial containing the solution. The solution-phase reaction was carried out under yellow light (due to the white-light sensitivity of the N-Hal-Succinimide molecules) for 2 hours at room temperature. Following the reaction, the substrates were rinsed with chloroform and isopropanol, dried with a filtered N_2 stream.

3.3.3 Vapor-Phase Halogenation of H- and OH- Terminated Silicon with N-Halogen-Succinimides

Cleaned OH-terminated Si(100) substrates were formed in Nano-Strip at 75 °C for 15 min, thus undergoing robust hydroxylation and rendering the surface OH-terminated. OH-Si(100) and freshly prepared H-Si(100) substrates were placed in a vacuum jar along with 0.5 g of *N*-Hal-succinimide. The jar was evacuated to $\sim 10^{-3}$ mbar and heated to a temperature that was 25 °C below the melting point of each *N*-Hal-succinimide molecule (ex. N-bromosuccinimide M.P. = 174 °C, hence the reaction temperature employed was 149°C). These temperatures were selected through experimentation in order to ensure adequate volatility of the N-Hal-succinimide molecules at the vacuum jar pressure. The sample was left in the jar for 2 hours as that was observed to be necessary/sufficient to fully vaporize 0.5 g of N-Hal-succinimide molecule. This time was selected primarily on transport considerations rather than on kinetics. 2 hours was observed to be necessary/sufficient to both fully vaporize 500 mg of N-hal-succinimide molecule and result in discernable halogen surface coverage (verified by XPS measurements). Lastly, Samples were then rinsed with IPA and dried under nitrogen.

3.3.4 Atomic Layer Deposition of Al_2O_3 thin film.

Deposition of Al_2O_3 thin films were carried out using a Cambridge Savannah 200 ALD reactor. Hal-Si(100), H-Si(100), and OH-Si(100) samples were taken from Ar storage and placed in the reactor and heated to 130 °C. Trimethylaluminum ($Al(CH_3)_3$) (Hi-k grade, Air Products) and H_2O were flowed into the reactor for 0.03 and 0.05 s, respectively, using a 20 sccm nitrogen carrier gas. The reagent exposures were 6×10^{-4} torr-sec and 1×10^{-3} torr-sec during the $Al(CH_3)$ and H_2O pulses, respectively. The base pressure in the reactor between pulses was 0.3 mbar. A 20 s nitrogen purge followed each precursor pulse. This process was repeated for 20 cycles of deposition.

3.4 Results and Discussion

3.4.1 Halogenation of H-Si(100) and OH-Si(100) Using N-Halogen-Succinimides

Here we present the solution-phase and vapor-phase reaction of NCS, NBS, and NIS with H-Si(100) via a radical initiator reaction between a H-terminated silicon surface and the succinimide molecule, replacing the surface H atom with either a Cl, Br, or I atom.

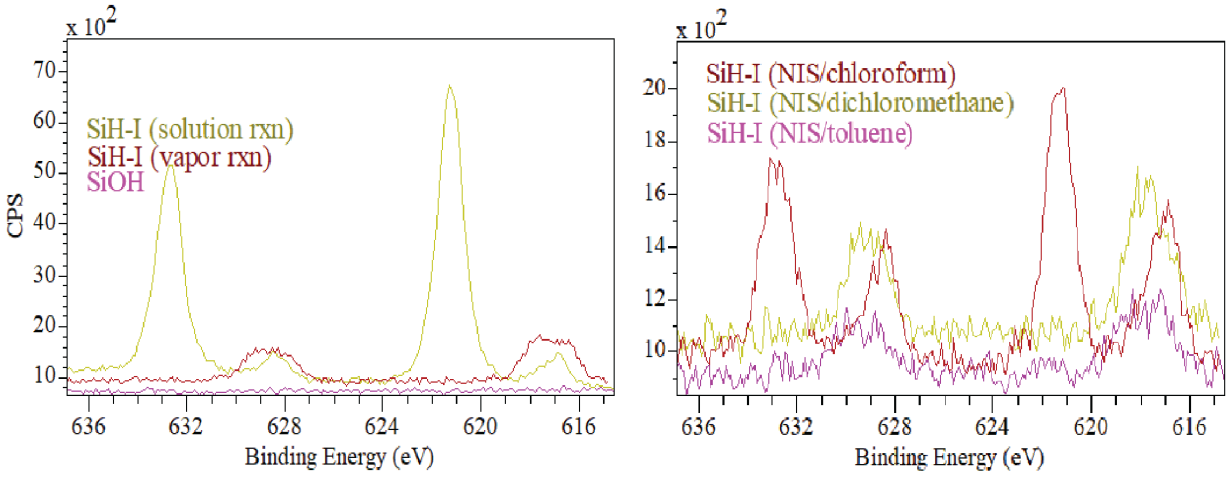

Figure 3.2 I 3d XPS spectra of (*Left*) a H-Si(100) surface iodinated using either solution-phase or vapor-phase reactions and (*Right*) a H-Si(100) surface iodinated using solution-phase reaction with different solvents.

The I 3d XPS signal for a theoretically Si-I surface should exhibit two distinct peaks centered at 617 Ev and 629 Ev due to spin orbit splitting, an effect where due to electromagnetic interaction between each electron spin (i.e. magnetic dipole effect), a doublet in the spectra is formed. The distance between doublets for I 3d orbitals is known to be 12 eV, which approximates the distance in the above scans.[41] **Figure 3.2** shows that the vapor-phase iodination of H-Si(100) results in this expected XPS signal. However, on the surface prepared using solution-phase iodination, there is a significant second signal centered at 621.5 eV and 633.5 eV. This is the result of a I-containing byproduct that also forms on the surface. In this reaction, the NIS molecule was dissolved in chloroform and probably followed the Wohl–Ziegler Halogenation scheme[133, 148].

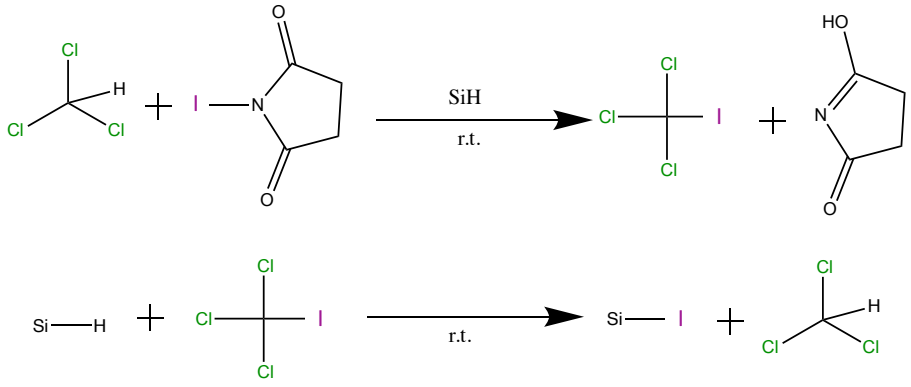

Here, a trichloro(iodo)methane (CCl_3I) intermediate acts as an effective iodinating agent of the H-passivated substrate. However, an iminol byproduct and the iodinated intermediate also forms that may also graft onto the surface (the full reaction pathway is shown in **Figure A3.1**). **Figure 3.2** also shows that this effect can be mitigated by employing other solvents. In toluene, there is only a slight byproduct signal at 621.5 eV and 633.5 eV. With dichloromethane (DCM) no byproduct is observed at these signals, however, there is a 1 eV shift in the primary Si-I signal which may possibly be the result of oxidation of the halogen film due to the longer reaction time required for the NIS/DCM solution.

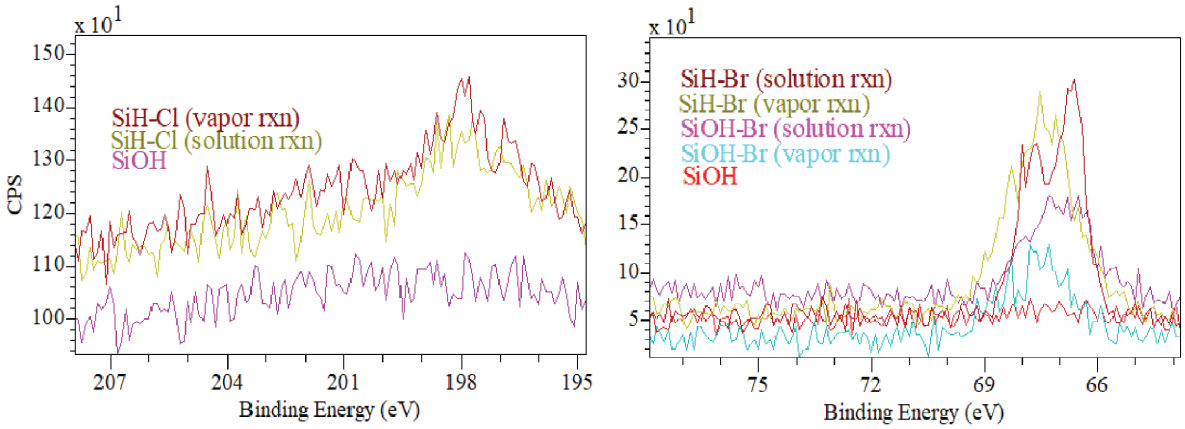

Figure 3.3 Comparison of solution-phase and vapor-phase halogenation showing (*Left*) Cl 2p XPS spectra of a H-Si(100) surface post-chlorination and (*Right*) Br 3d XPS spectra for both OH-Si(100) and H-Si(100) surfaces post bromination.

Although solution-based halogenation does lead to some degree of stable Si-halogen bond formation, **Figure 3.3** demonstrates that both vapor-phase chlorination and bromination can achieve comparable, if not greater, halogen coverage than the respective solution phase reactions using DCM. Considering this and the fact that dry halogenation is also much more compatible with prolonged vacuum-based processes such as AS-ALD for *in-situ* NGS regeneration, vapor-phase application of these halogen ALD resist is much more practical.

The Br 3d spectra in **Figure 3.3** also demonstrates preferential reactivity of the N-hal-succinimide molecules with H-Si(100) over OH-Si(100), in both the solution and vapor phases. A mild, vapor-based functionalization method that selectively halogenates H-Si(100) over OH-Si(100) can be applied in AS-ALD processes to (1) create initial NGS for area-selective thin-film deposition and (2) regenerate NGS during thin-film deposition to extend the selectivity window. Such selective H-Si(100) halogenation can be achieved by exploring the higher reactivity of H-Si(100) interfaces. In this study, *N*-Cl/Br/I-succinimides were used to halogenate H-Si(100) under mild vapor-phase conditions. The reactivity of the *N*-Cl/Br/I-succinimides with OH-Si(100)

interfaces was also examined to determine halogenation selectivity between H-Si(100) and OH-Si(100).

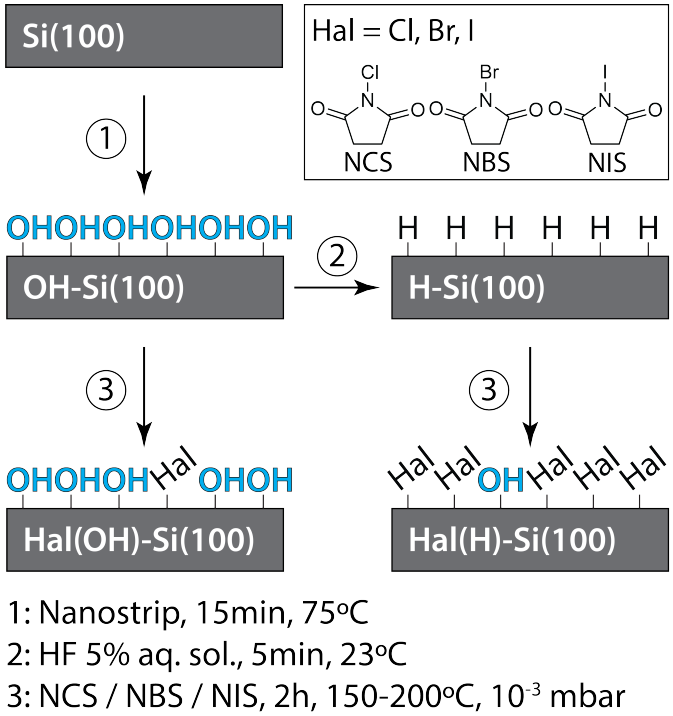

Figure 3.4. Schematic procedure of reaction steps and process conditions for the vapor-phase halogenation of H-Si(100) and OH-Si(100) with *N*-Hal-succinimides. (1) Si(100) is cleaned and oxidized in Nano-Strip solution before (1⇒3) direct exposure to a *N*-Cl/Br/I-succinimide molecule in the vapor phase, alternatively (1⇒2) the new oxide is re-etched in HF and then (2⇒3) exposed to the *N*-Cl/Br/I-succinimide molecules.

The steps and experimental conditions of these reactions are shown in **Figure 3.4**. Si(100) substrates with native oxide were immersed in Nano-Strip solution for 15 minutes at 65°C and then rinsed in ultra-pure water and isopropanol to remove organic impurities. The native oxide layer was then etched away during a 5-min dip in a 5% HF solution to form a H-Si(100) surface. The freshly prepared H-Si(100) surfaces were exposed to a *N*-Cl/Br/I-succinimide molecule for 2 hours in a flask evacuated to 10^{-3} mbar and heated to the melting point of the succinimide molecules which range from 148°C to 206°C. Similarly, freshly oxidized OH-Si(100) substrates were also reacted with the *N*-Cl/Br/I-succinimide molecules to assess halogenation selectivity towards H-

Si(100) and OH-Si(100). Following the reaction, the substrates were rinsed with isopropanol, dried with a filtered nitrogen gas, and analyzed using XPS and contact angle measurements to assess the atomic composition and the halogen coverage before and after the reactions.

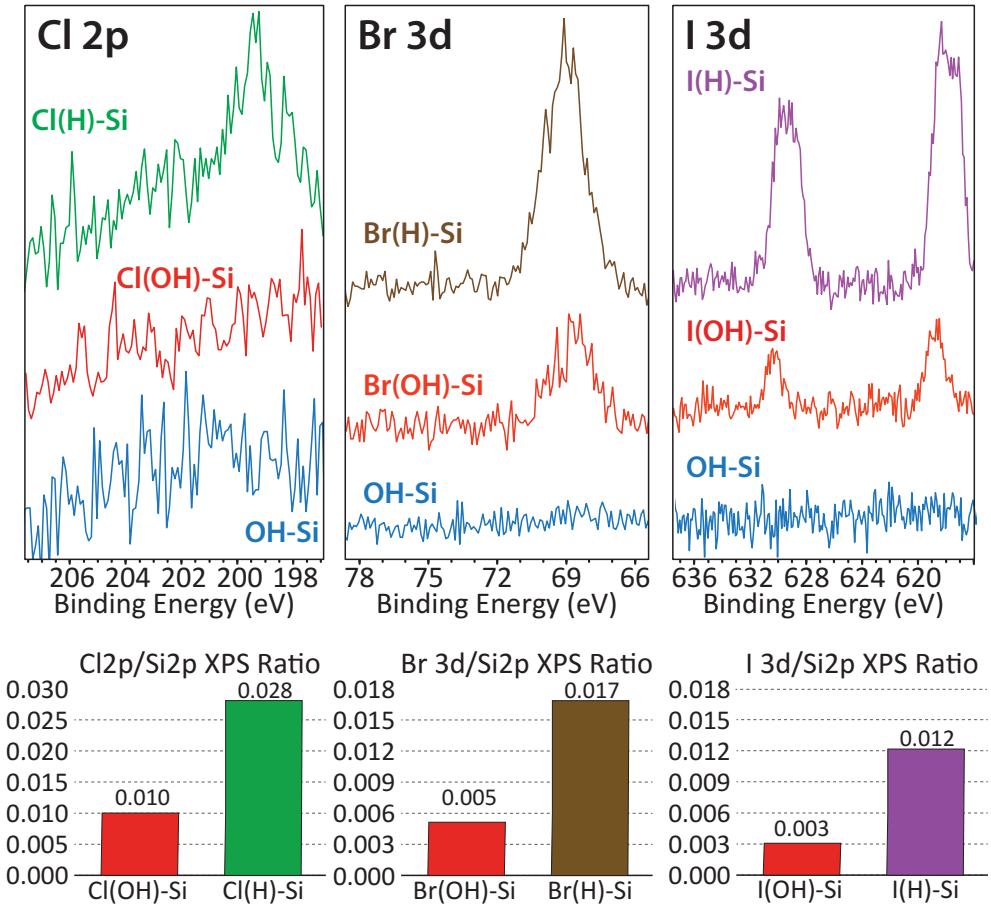

Figure 3.5 (Top) Comparison of XPS spectra from Hal(H)-Si(100) and Hal(OH)-Si(100) surfaces post reaction and a OH-Si(100) standard. Region scans for each respective halogen (Cl 2p, Br 3d, I 3d) are depicted from left to right. (*Bottom*) Corresponding histograms showing quantitative representation of XPS spectra, normalized to Si 2p signal from each respective surface.

The XPS Cl 2p, Br 3d, and I 3d spectra in **Figure 3.5** all confirm the formation of Si-Hal bonding on the halogenated H-Si(100) (Hal(H)-Si(100)) substrates. In contrast, the XPS signal intensity on halogenated OH-Si(100) (Hal(OH)-Si(100)) was significantly lower. **Table 3.1** shows relative XPS peak intensities of Cl 2p, Br 3d, and I 3d electrons adjusted by atomic sensitivity factors (ASF) and normalized by the total Si 2p peak intensity in each sample (Hal atoms to Si

atoms, each surface having approximately the same number of Si atoms). Overall, **Table 3.1** shows that halogenation with *N*-Hal-succinimides resulted in XPS signal intensities 2.8 – 4 times higher on H-Si(100) than on OH-Si (100). This result was expected due to the more reactive nature of Si-H bonds in interfacial radical-type reactions.[164]

Table 3.1 XPS ratios of the Hal 2p (or 3d) over Si 2p electron signals corrected by the atomic sensitivity factors on Hal(H)-Si(100) and Hal(OH)-Si(100) substrates after the halogenation reaction with *N*-Hal-succinimides. Halogenation selectivity of *N*-Hal-succinimides.

Halogenating agents	**NCS (Cl)**	**NBS (Br)**	**NIS (I)**
	XPS signal ratios of Hal 2p (or 3d) / Si 2p electrons		
H-Si(100)	0.028	0.017	0.012
OH-Si(100)	0.010	0.005	0.003
	OH-Si/H-Si halogenation selectivity		
	1:2.8	1:3.5	1:4

The binding energies of the halogen electrons are consistent with literature data that reports halogenation of H-Si(100). Their values suggest the formation of silicon-halogen species. Specifically, signals at 199.5 eV, 69.5 eV, and 619/631 eV are indicative of Si-Cl, Si-Br, and Si-I formation, respectively.[136, 165, 166]

Previous studies have relied on XPS to identify the type of halogenated species bonded directly to Si(100). For instance, Silva-Quinones et. al. paired XPS measurements with STM imaging to demonstrate that their method for the chlorination of H-Si(100) resulted in the formation of silicon dichloride ($SiCl_2$) surface species, while bromination yielded complete monobromide (SiBr) monolayer formation.[165] The position of their Cl 2p and Br 3d peaks are consistent with those in this study and suggest that our method primarily results in the formation of $SiCl_2$ and SiBr bonds.

In order to assess the degree of halogen coverage on each surface the established Haber and Lewis's substrate-overlayer model (Φ)[167] was used. This model is based on the assumption

that the newly formed halogen species comprise a single monolayer that interfaces directly with the silicon substrate. All other organics are assumed to sit on top of this halogen layer.

$$\Phi_{Hal} = \left[\frac{\lambda \sin\theta}{a_{Hal}}\right]\left(\frac{ASF_{Si}}{ASF_{Hal}}\right)\left(\frac{\rho_{Si}}{\rho_{Hal}}\right)\left(\frac{I_{Hal}}{I_{Si}}\right) \qquad (Eq\ 3.1)$$

Where λ is the penetration depth (calculated for each element using escape depth); θ is the angle in which electrons take off from sample surface (90.0°); a_{Hal} is the atomic diameter of the halogen species; ASF is the atomic sensitivity factor which scales XPS peak signals such that the area corresponds to surface concentration; ρ is the vapor density of each element; and I is the integrated area under the XPS peaks, processed by CasaXPS software.

Table 3.2 Halogen surface coverage on Hal(H)-Si(100) substrates treated with *N*-Hal-succinimides. Water contact angle measurements of Hal(H)-Si(100) and Hal(OH)-Si(100) substrates and a bare OH-Si(100) substrate before the reaction.

Halogenating agents	**NCS (Cl)**	**NBS (Br)**	**NIS (I)**
	Mono-halogen surface coverage (%)		
H-Si(100)	145	88	62
	Contact angle (°) and contact angle hysteresis (°)		
Hal(H)-Si(100)	72.5 ± 1.6 27.1 ± 0.1	46.9 ± 0.6 24.0 ± 0.1	26.2 ± 0.9 20.4 ± 0.1
Hal(OH)-Si(100)	21.9 ± 0.4 17.9 ± 0.1	24.4 ± 0.5 19.2 ± 0.1	25.2 ± 0.7 17.1 ± 0.1
Bare OH-Si(100) before halogenation Bare H-Si(100) before halogenation	20.7 ± 0.4 67.0 ± 0.4		

In order to assess the degree of halogen coverage on each surface, we compared theoretical values, derived from **Equation 3.1**, with the values Silva-Quinones et. al.[165] calculated in their study on H-Si(100) halogenation. Their STM results demonstrated that an overlayer model coverage of 0.4

corresponds to a complete mono-brominated Br-Si(100) interface. The overlayer model coverage of the Br(H)-Si(100) substrate in our study was calculated to be 0.35, indicating that the bromination of H-Si(100) with N-Br-succinimide resulted in approximately 88% mono-bromide termination of the surface-exposed silicon atoms. The surface coverages of the chlorinated and iodinated H-Si(100) substrates were subsequently calculated by comparing the ASF corrected ratio of Br 3d/Si 2p XPS signals with the ASF corrected ratios of the Cl 2p/Si 2p and I 3d/Si 2p XPS electron signals **(Tables 3.1** and **3.2**). Our findings suggest that NCS chlorination achieved either an incomplete di-chloride termination or a complete mixed mono-/di-chloride termination of the surface-exposed silicon atoms, while NBS bromination achieved 88% coverage of the mono-bromide silicon species. However, NIS iodination resulted in only 62% mono-iodine coverage of the surface silicon atoms. This decrease in halogenation efficiency from chlorine to bromine to iodine could potentially be attributed to the increase in the atomic size of the halogen species or to the decrease in the Si-Hal bond energy.

Table 3.2 shows that the Hal-terminated surfaces display higher hydrophobicity than unreacted OH-Si(100) and similar or lower hydrophobicity than untreated H-Si(100), based on the static water contact angle measurements of halogenated and non-halogenated substrates shown in **Figure 3.6**.

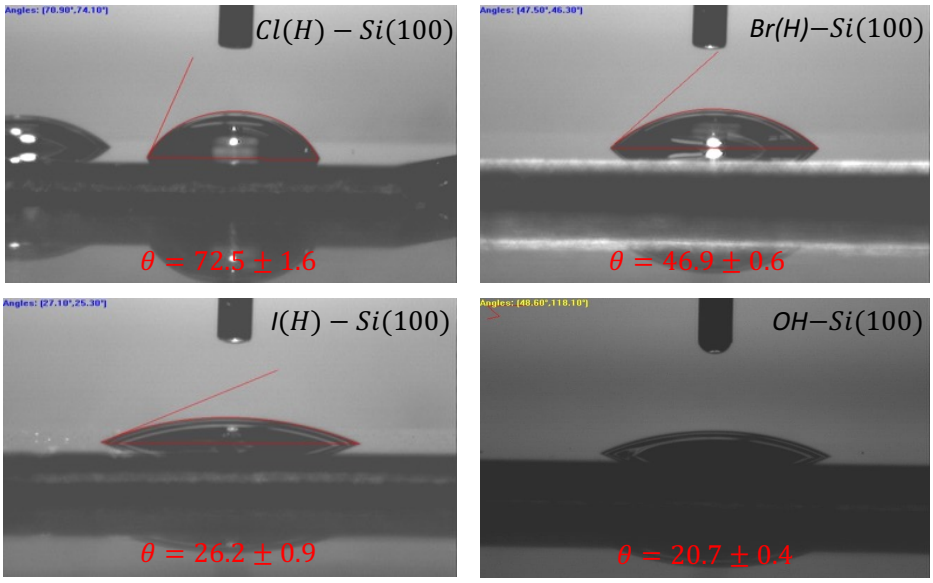

Figure 3.6 Water contact angle pictures of the three halogenated surfaces and a reference OH-Si(100) surface. Surface hydrophobicity rises with increasing halogen coverage.

This decrease in hydrophobicity from Cl to I can partially be attributed to the increasing polarizability of the halogen atoms in that same order. Consequently, the high surface energy of I-Si(100) rendered it the most reactive to its environment. Notably, the water contact angle of I-Si(100) was within 6° of that of OH-Si(100), this is suggestive that the Si-I bonds experienced a high rate of hydrolysis upon contact with water, whether from the air or during the contact angle measurement itself, relative to the Si-Cl and Si-Br bonds of the other surfaces. This may complicate the use of I-Si(100) as an inhibitor in ALD processes which rely on water as a reagent. The observed high water contact angle hysteresis of the halogenated surfaces, calculated from the advancing and receding contact angle measurements shown in **Figure A3.2**, is likely due to the reactivity of Hal-Si(100) with water, as well as the incomplete coverage of the halogen species on the surface. As expected, the water contact angles of the halogenated OH-Si(100) substrates are comparable with the native OH-Si(100) surface due to the low yield of the halogenation reaction on the oxidized surface.

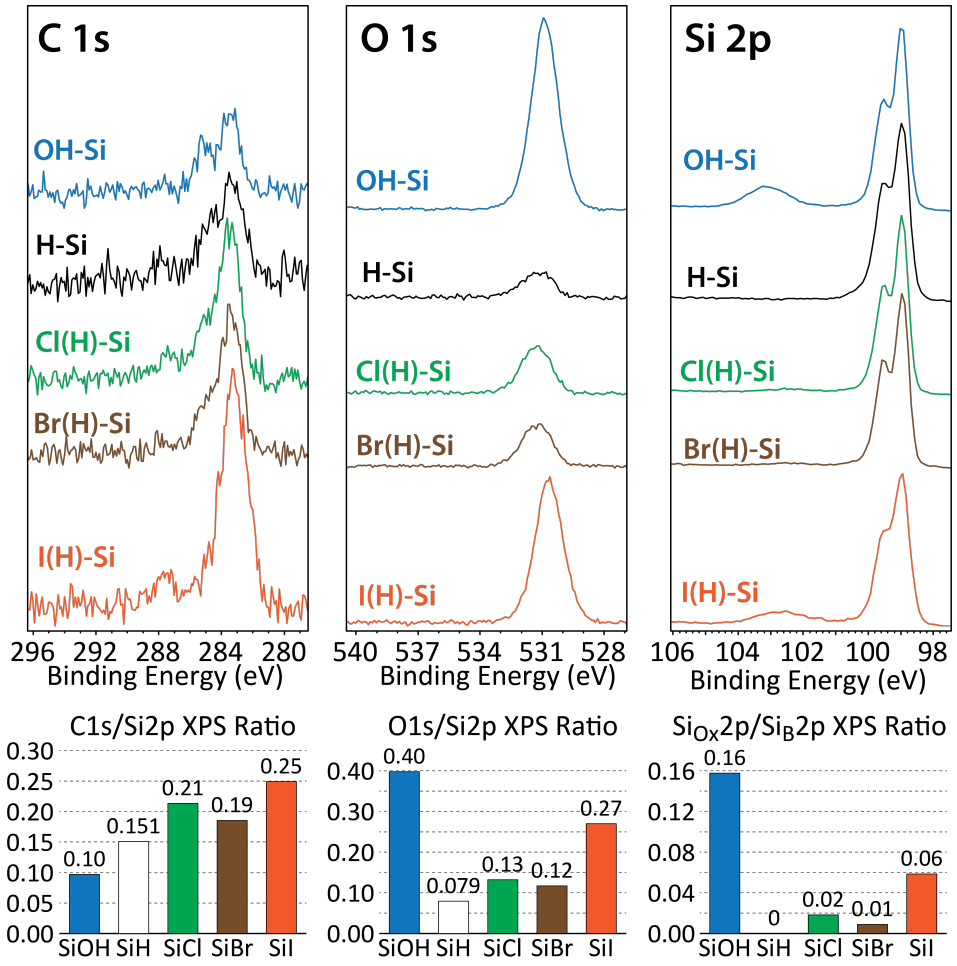

Figure 3.7 Comparison of XPS region scans of C 1s, O 1s, and SiO_2 (from Si 2p) spectra depicted from left to right for OH-Si(100), H-Si(100), Cl(H)-Si(100), Br(H)-Si(100), and I(H)-Si(100) surfaces. In the bottom row are histograms showing the quantitative XPS characterization of region scans (C 1s, O 1s, SiO_2 from Si 2p) for each Hal(H)-Si(100) surface and reference unreacted OH-Si(100) and H-Si(100) surfaces, all normalized by the Si 2p peak intensity which includes contributions from both the bulk Si (Si_B) and surface oxide (Si_{Ox}) interfaces (the values in the Si_{Ox} histogram was normalized by only Si_B).

XPS region scans of C 1s, O 1s, and SiO_2 signal (from the Si 2p spectra) shown in **Figure 3.7** were collected to discern compositional differences in the prepared halogenated monolayers. With a negligible SiO_2 peak observed, and only a slight O 1s and C 1s signal detected, the spectra for the H-Si(100) sample demonstrates that the initial oxidative cleaning and HF etching steps effectively removed a majority of organics from the sample surface prior to halogenation. The region scans for each of the surfaces post-halogenation show little variability in composition. The primary contribution to each of the C 1s spectra are from C-C/C=C bonds at 284 eV. The highest

degree of carbon contamination was seen on I(H)-Si(100), a likely result of the higher polarizability of the I atom and therefore the higher surface energy of the entire surface. There is good agreement in the size and shape of the O and SiO_2 peaks between both the Cl(H)-Si(100) and Br(H)-Si(100) surfaces and H-Si(100). However, in relation to the OH-Si(100) surface, the SiO_2 signal for each of the halogenated surfaces is slightly shifted to a lower binding energy. This is most evident when comparing the SiO_2 peaks for OH-Si(100) and I(H)-Si(100) where there is about a 0.3 eV difference in peak center. This shift is most likely indicative of the newly formed Si-Hal species found on the halogenated samples and absent on the OH-Si(100) and H-Si(100) references. Overall, the dry halogenation process effectively prevents silicon oxidation in the case of chlorination and bromination. The low O content that is observed on these two surfaces can be attributed to the physisorption of water. The O and SiO_2 peak areas measured on the I(H)-Si(100) sample were larger likely due to the lower halogen coverage observed on that surface which allowed surrounding O species to more effectively access the underlying Si-H bonds. This likely explains the higher degree of hydrophilicity that was also observed on I(H)-Si(100), in addition to any hydrolysis of the Si-I bonds. Nevertheless, the degree of Si oxidation that I(H)-Si(100) experiences is still only about a third of what was observed on the reference OH-Si(100) sample.

3.4.2 Stability of Hal(H)-Si(100) Surfaces in Air

The stability of Cl(H)-Si(100), Br(H)-Si(100), and I(H)-Si(100) in an ambient environment was examined by monitoring the surface composition of each surface via ex-situ XPS characterization over a 72 hour timespan. **Figure A3.3** demonstrates how H-Si(100) naturally oxidizes during 72 hours of air exposure. For each halogenated surface, after the reaction, the samples were directly transferred into the XPS for measurements. After collecting the data, the samples were unloaded and kept at ambient laboratory conditions for 4 hours. Following this, each

sample was reloaded into the XPS for additional testing. This same process was repeated at both 24 and 72 hours post reaction.

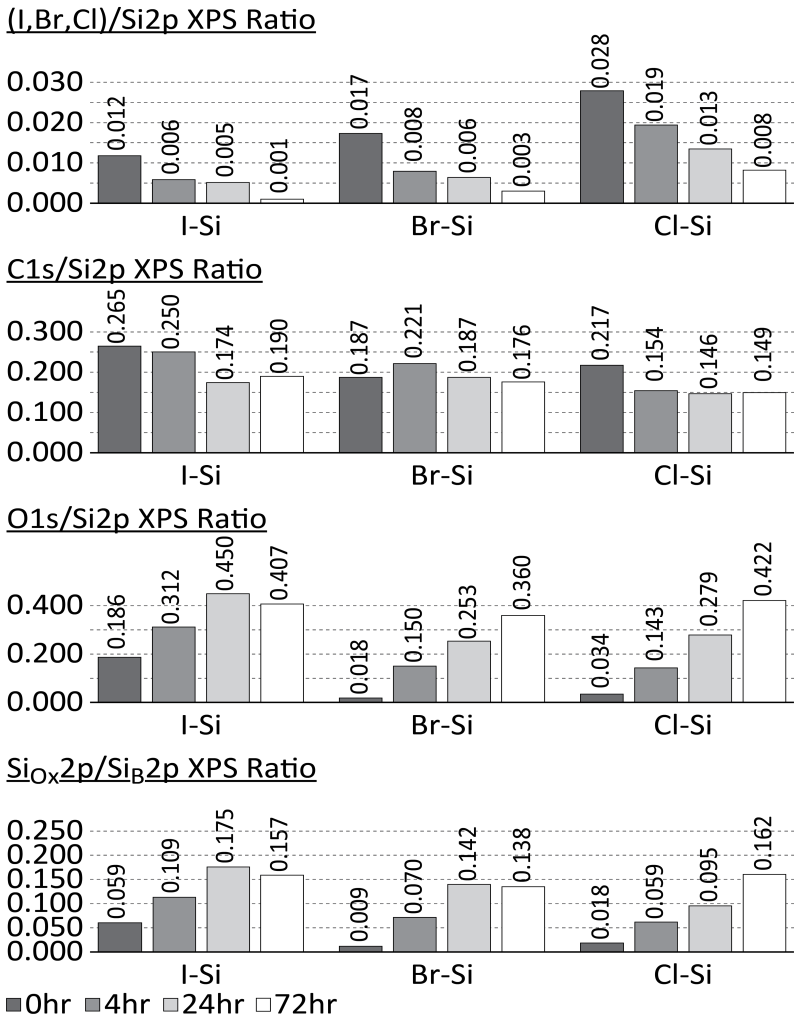

Figure 3.8 Stability study consisting of histograms showing the quantitative XPS characterization of halogen, C 1s, O 1s, and SiO_2 (from Si 2p) region scans shown from top to bottom, respectively, for I-Si(100), Br-Si(100), and Cl-Si(100) surfaces shown from left to right, respectively, over a 72 hour period of air exposure.

XPS characterization in **Figure 3.8** (and the corresponding spectra in **Figure A3.4**) demonstrated that although each halogenated sample attained roughly the same degree of surface oxidation after 72 hours of air exposure, the rate of halogen degradation on Cl(H)-Si(100) was slower than on the other two surfaces. Br(H)-Si(100) and I(H)-Si(100) both experienced more than a 50% drop in halogen signal during the first 4 hours, while Cl(H)-Si(100) only exhibited a 32%

drop. Deterioration then proceeded slowly during the next 20 hours with each surface experiencing less than a 20% additional drop in halogen signal, and by 72 hours there was near-complete desorption of halogen atoms, except on Cl(H)-Si(100) which was retained 29% of its original halogen content. It should be noted that all Cl 2p signals are partially obscured by a Si plasmon, as seen in **Figure A3.4**, which renders peak identification and characterization slightly more difficult than the other halogen signals. The plasmon was subtracted from all Cl 2p spectra using a reference Cl 2p spectrum from a bare OH-Si(100) sample.

All three surfaces experienced similar rates of O accumulation in the 24 hours post-reaction, with I(H)-Si(100) having a head start due to its lower initial halogen coverage and higher likelihood of Si-I hydrolysis relative to Si-Br and Si-Cl, as previously discussed. A reference for a theoretical maximum in Si oxidation is the native oxide layer on the freshly oxidized OH-Si(100) surface in **Figure 3.7**, where the $Si_{Ox}2p/Si_B2p$ XPS ratio is 0.16. The SiO_2 plot in **Figure 3.8** illustrates that I(H)-Si(100) reached the threshold for full oxide growth after 24 hours and then leveled off, while Cl(H)-Si(100) reached full growth after 72 hours. Only Br(H)-Si(100) exhibited a SiO_2 signal below the max threshold at the end of 72 hours. This surface also demonstrated the lowest O 1s signal after 72 hours. Frederick et. al. also determined that Br(H)-Si(100) demonstrated the highest resistivity to oxidation in their study where they evaluated the stability of UHV-prepared Cl(H)-Si(100), Br(H)-Si(100), and I(H)-Si(100) in a nitrogen gas environment.[136] Consequently, after 72 hours the three halogenated surfaces more or less resembled each other with respect to organic and oxide concentration. Within the first 24 hours, the results clearly demonstrate that Cl(H)-Si(100) resisted both surface oxidation and halogen deterioration most effectively.

3.4.3 Hal(H)-Si(100) Surfaces Ability to Inhibit ALD Precursors

Many researchers are now focused on developing chemo-selective molecule resists that can withstand multiple ALD cycles without losing their growth selectivity.[44, 128-130] Several publications have shown that typical organosilane or phosphonic acid SAMs of organic molecules on Si(100) will act as viable ALD resists, but they too lose their selectivity due to the hydrolytic desorption promoted by the ALD conditions.[115, 168] Nevertheless, due to the long linker chains and larger terminal groups associated with SAMs, these molecules should provide more shielding of the underlying surface from the ALD chemistry and are viable as resists down to sub-10 nm features.[47] However, atomic-scale halogen resists should enable even higher resolution fabrication with sharper vertical wall profiles due to their near-monoatomic nature. Additionally, SAM resists are primarily deposited from solutions[169, 170] (conditions incompatible with *in-situ* resist regeneration), whereas halogen monoatomic resists can be applied in the vapor phase. SAMs have also been shown to fail to block ALD film growth near surface defects where self-assembly deteriorates.[50, 52, 168, 171] They also suffer from structural instability under ALD processing conditions.[50, 52] Such dependence of stability on surface morphology complicates the use of many potential SAM resists. As halogen monoatomic resists can be applied in the vapor phase on a variety of surface geometries due to their higher adsorption mobility, in the future they may represent a more effective alternative to SAMs as ALD inhibitors. Hence, the halogenated monolayers investigated in this study were next examined on whether they (1) formed stable enough bonds with Si(100) to adequately block ALD chemistry and (2) if they could withstand multiple deposition cycles.

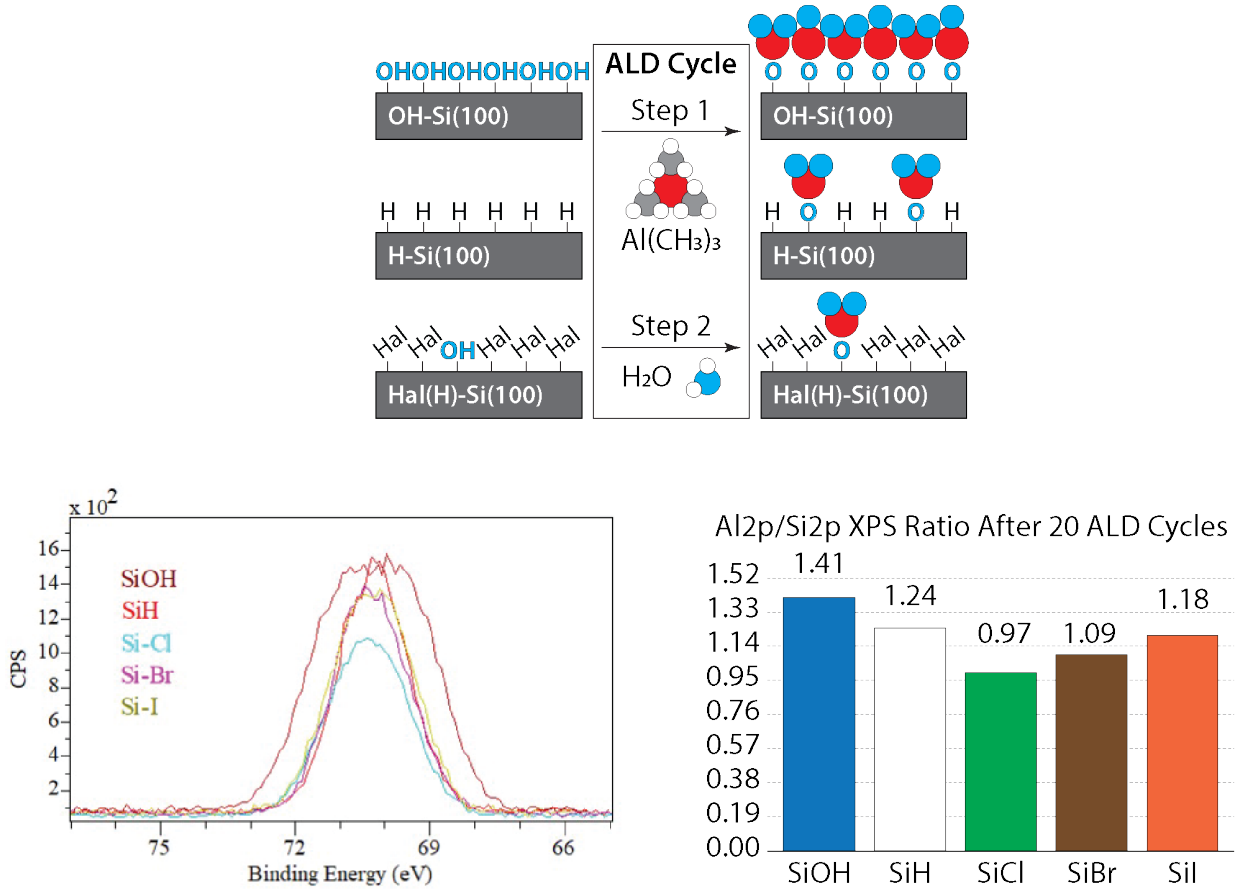

Figure 3.9 *(Top)* Schematic illustration of traditional ALD cycle of Al_2O_3 onto OH-Si(100), H-Si(100), and Hal(H)-Si(100) surfaces. In step 1, the dosed $Al(CH_3)_3$ precursor readily adsorbs onto the OH-Si(100) surface while H-Si(100) and Hal(H)-Si(100) surfaces exhibit total and partial blocking of the same molecule, respectively. In step 2 the H_2O coreactant binds with the adsorbed metal precursor to form a complete metal oxide film on OH-Si(100) and a metal oxide island on Hal(H)-Si(100). Only H-Si(100) retains its original surface but it must be maintained under high vacuum and temperature. (*Bottom Left*) Al 2p XPS spectra for all three halogenated surfaces and reference H-Si(100) and OH-Si(100) surfaces with *(Bottom Right)* corresponding histograms showing the quantitative XPS characterization of the Al 2p region scans.

This study is specifically interested in the deposition of aluminum oxide (Al_2O_3), the most common metal oxide film deposited via ALD, and is often used in the production of electroluminescent displays and memory capacitors.[105] The ALD process was carried out at 130°C and a base pressure of 10^{-1} mbar. When considering that the halogen reaction temperatures ranged from 123°C to 170°C at 10^{-3} mbar, all three halogenated surfaces were likely thermally stable under the ALD conditions.

The XPS analysis in **Figure 3.9** demonstrates that after 20 cycles of Al_2O_3 ALD, the Al-to-Si ratios on H-Si(100) and OH-Si(100) were 1.24 and 1.41, respectively. This illustrates that the ALD chemistry was more selective towards OH-Si(100) which agrees with many studies in literature.[39, 44, 83, 105, 168, 172] For example, Longo et al. used density functional theory (DFT) calculations to denote that the adsorption of the metal oxide precursor ($Al(CH_3)_3$) experiences a higher kinetic barrier on H-terminated surfaces (~1.5 eV) than on OH-terminated surface (~ 0.8 eV).[83] Thus, as OH-Si(100) serves as an ideal GS, it is important to evaluate the ability of each Hal(H)-Si(100) surface to block ALD precursor chemisorption so to determine their efficacy as potential complimentary NGS materials. To test this, Cl(H)-Si(100), Br(H)-Si(100), and I(H)-Si(100) surfaces underwent 20 cycles of Al_2O_3 deposition. **Figure 3.9** shows that all three halogenated surfaces exhibited lower Al 2p signals and Al-to-Si composition ratios than found on a corresponding H-Si(100) surface, thus demonstrating the superior blocking ability of the halogenated surfaces. Cl(H)-Si(100) was the most effective inhibitor followed by Br(H)-Si(100) and then I(H)-Si(100). This trend is likely due to the higher halogen coverage on Cl(H)-Si(100) than on Br(H)-Si(100) and I(H)-Si(100). Interestingly, despite there being a more than 2.5 times difference in water contact angle between the Cl-Si(100) and I-Si(100) surfaces, there was only a 12% difference in their respective Al-to-Si ratios, indicating that atom polarizability and/or bond hydrolysis don't play a significant role after 20 cycles of ALD with a water co-reactant. The ALD growth selectivities reported in **Table 3.4** represent the proportion between the surface concentration of Al atoms on the "inhibiting" NGS relative to that of the OH-Si(100) GS. The selectivity's of Cl(H)-Si(100), Br(H)-Si(100), and I(H)-Si(100) were 30.0%, 27.6%, and 24.2%, respectively. H-Si(100) demonstrated a slightly lower selectivity of 18.5%. Thus, in addition to their capability of being intermittently re-dosed directly into the ALD reactor when selectivity

wains (after etching away accumulated NGS Al_2O_3/TMA and reforming the halogen-reactive Si-H surface using either a vapor phase, plasma-based, or ALE method of Si-OH[27, 59, 60, 173, 174]), the halogenated substrates also exhibit a higher degree of ALD inhibition than that of H-Si(100).

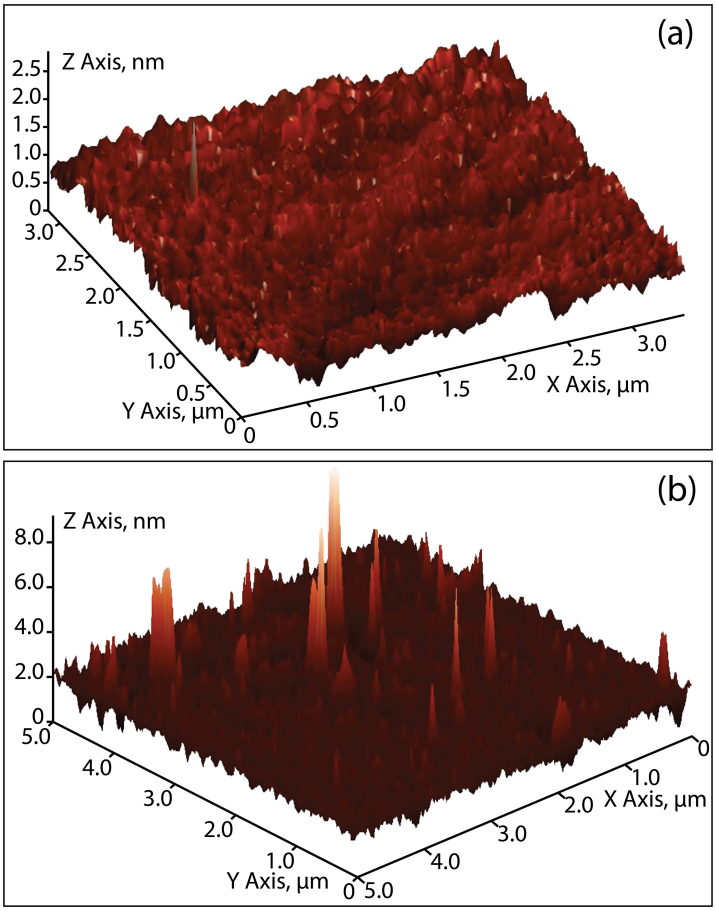

Figure 3.10 Three-dimensional AFM roughness topographies taken for the (a) OH-Si(100) and (b) Br(H)-Si(100) surfaces post ALD.

The inhibiting character of the halogenated surfaces can also be defined by the degree of conformality of the deposited thin films. For example, in **Figure 3.10** three-dimensional AFM roughness topographies are displayed for the OH-Si(100) and Br(H)-Si(100) surfaces post ALD. The OH-Si(100) surface exhibits both a lower RMS roughness measurement and a smoother topography compared to that of the Br(H)-Si(100) surface. This is as expected since the brominated monolayer does not promote homogenous nucleation of the precursor molecules and thus the

gradual Al_2O_3 film growth should remain uneven. And this phenomenon is observed in the surface topography for the Br(H)-Si(100) surface where there is a greater number of defects scattered across the entire area of measurement whereas OH-Si(100) exhibits a more homogenous surface.

A well-known ARXPS method was used to calculate the thickness of the deposited Al_2O_3 film on a OH-Si(100) GS.[175-179] This method utilizes ARXPS to collect background Si 2p signals at varying take-off angles and fit them into **Equation 3.2** to determine the total thickness of the film layers on top of the bulk silicon interface based on the intensity of Si 2p electrons detected through the layer system (namely SiO_2 and Al_2O_3 layers). **Equation 3.2** describes the relationship between the XPS area intensity of the substrate electrons, the electron collection angle, and the thickness of the film that covers the substrate.

$$I_{Si(s)corr} = A(\theta)_{corr} \times I_{Si(s)} = I_{Si(s)}^{inf} \times exp\left[-\frac{d}{\lambda_{Si(m)} \times \cos(\theta)}\right] \quad (Eq\ 3.2)$$

Where $I_{Si(s)corr}$ is the corrected area intensity of silicon in the substrate; $A(\theta)_{corr}$ is the correction factor measured on a bare Si substrate; $I_{Si(s)}$ is the measured area intensity of Si in the substrate; $I_{Si(s)}^{inf}$ is the bulk area intensity of Si in the unfunctionalized substrate; $\lambda_{Si(m)}$ is the inelastic mean free path (the attenuated length) of Si 2p electrons in the monolayer; d the monolayer thickness; and θ the collection angle between the sample normal and the analyzer. The Si 2p ARXPS spectra were taken from an extended analytical area (~600 × 900 μm) to maintain an adequate signal-to-noise ratio and to limit the molecule system's exposure to the X-ray radiation. Because of this wide analytical area, a drop in the Si 2p signal intensity was observed at the higher takeoff angles associated with the shallow depth of field of the XPS analyzer. The correction factors for this drop in intensity were measured using a bare Si substrate, in which both SiO_2 and Al_2O_3 layers were

absent, thus the change in the substrate intensity at different collection angles is not related to the attenuation of the substrate Si 2p electrons by the ALD film material and is only associated with the change in the sample focal area. This correction factor was then used to adjust the signal intensities of the Si 2p scans from the corresponding OH-Si(100) substrate with 20 cycles of Al_2O_3 deposited on them. The corresponding signal intensities, correction factors, and collection angles used in **Equation 3.2** are reported in **Table 3.3**.

Table 3.3 Halogen Si 2p ARXPS substrate peak areas, collection angles and correction factors used in the Equation 2.2 thickness calculations of the Al2O3 film deposited onto OH-Si(100) after 20 ALD cycles.

Collection Angle (θ)	1/Cos(θ)	I_{Si2p}	Correction Factor $A(\theta)_{corr}$	$I_{Si(s)corr} = A(\theta)_{corr} \times I_{Si(s)}$	ln ($I_{Si(s)corr}$)
0	1	7936.44	1	7936.44	8.98
15	1.0353	6466.11	1.034	6682.72	8.81
30	1.1547	5489.22	1.150	6310.96	8.75
45	1.4142	3290.14	1.452	4777.28	8.47
60	2	824.76	2.600	2144.71	7.67

Using these parameters, **Figure 3.11** was generated and demonstrated a strong linear fit. According to **Equation 3.2**, we can derive total surface layers thickness from the slope of the profile.

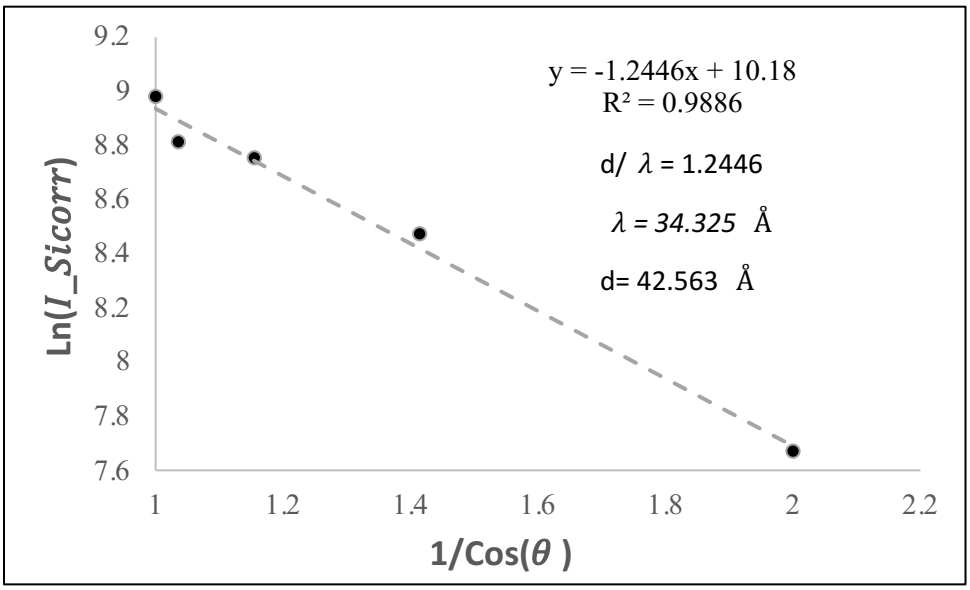

Figure 3.11 ARXPS Experiments of the SiO_2 and Al_2O_3 layers on OH-Si(100) following 20 ALD cycles: Linear Fit of the Corrected Si 2p Signal Areas from the Si Substrate as a Function of 1/cos(θ).

The measured thicknesses from **Figure 3.11** of the layer system comprising both a native SiO_2 base layer and the top Al_2O_3 ALD film was 42.563Å or 4.2563 nm. And after accounting for the thickness of just SiO_2 on a OH-Si(100) reference, nominally set at 2.10 nm based on a previous ellipsometry measurement shown in **Figure A3.5**, the thickness of the Al_2O_3 film deposited on OH-Si(100) after 20 ALD cycles was calculated to be 2.16 nm, as reported in **Table 3.4**. This thickness value was divided by the ellipsometry thickness measured on the same material to determine a correction factor that could be applied to each of the NGS surfaces (H-, Cl-, Br-, and I-) to determine the Al_2O_3 film thickness on them since the same ARXPS method could not be applied due to the uncertainty of how the ALD chemistry alters the thickness of the underlying halogen sublayers.

Table 3.4 Characterization of Al_2O_3 thin films deposited onto sample surfaces after 20 ALD cycles, including thickness calculations from ARXPS and ellipsometry measurements and AFM roughness measurements. Selectivity is defined as a proportion between the surface concentration of Al atoms on the OH-Si(100) reference and the surface concentration of Al atoms on the Hal-Si(100) surfaces, all values found using XPS and normalized to the Si 2p signal such that we were comparing relative compositions (Al atoms to Si atoms). $Selectivity(Al\ 2p : Si\ 2p\ ratio) = (SiOH - SiCl, Br, I)/(SiOH + SiCl, Br, I)$

Surface	Calculated Thickness (nm)	ALD Growth Rate (nm/cycle)	Selectivity (%) (Based on XPS)	AFM RMS Roughness (nm)
OH-Si(100)	2.16	0.11	--	0.49 ± 0.01
H-Si(100)	1.63	0.08	18.5	0.53 ± 0.01
Cl(H)-Si(100)	1.38	0.07	30.0	0.21 ± 0.01
Br(H)-Si(100)	1.43	0.07	27.6	0.76 ± 0.01
I(H)-Si(100)	1.45	0.07	24.2	0.78 ± 0.01

The resulting film thicknesses on the NGS are reported in **Table 3.4** and shows that the thinnest Al_2O_3 film was observed on Cl(H)-Si(100) followed by Br(H)-Si(100) and then I(H)-Si(100). This trend in film thickness mirrors that of the XPS halogen-to-silicon signal ratios, halogen coverage values, water contact angle, and blocking ability determined from XPS for all three surfaces. All three halogenated surfaces exhibited lower ALD film thicknesses than H-Si(100). Despite the three halogenated surfaces exhibiting similar Al-to-Si XPS ratios and Al_2O_3 film thicknesses, when factoring in the higher 24 hr air stability observed on Cl-Si(100), this material appears to be the most effective candidate for Al_2O_3 ALD surface blocking. Overall, the reduced reactivity that each halogenated surface showed towards the ALD chemistry demonstrates that they are each suitable candidates for effective ALD resists and when paired with a ALD growth material such as OH-Si(100) can participate in chemo-selective processing schemes such as AS-ALD.

3.5 Conclusion

In this study, XPS, ellipsometry, and contact angle goniometry measurements were used to demonstrate the covalent bonding of halogenated monolayers to a H-Si(100) surface prepared via a dry reaction process. NCS, NBS, and NIS were all found to be effective halogenating agents of H-Si(100). However, chlorination resulted in the highest halogen surface coverage by a significant margin followed by bromination and then iodination. This approach exhibited an exclusive bonding of halogen atoms to silicon while maintaining a low rate of oxidation of the

underlying silicon interface, especially in the case of chlorination and bromination. Stability tests in air were then undertaken to determine how long each surface could resist degradation and oxidation. Over the course of 24 hours, Cl(H)-Si(100) demonstrated the strongest resistance to both halogen deterioration and SiO_2 growth followed by Br(H)-Si(100) and then I(H)-Si(100). At the end of 72 hours each surface more or less resembled each other with respect to organic and oxide concentration, however, Cl(H)-Si(100) was able to retain about a quarter of its original halogen coverage, something the other two surfaces did not achieve. Surfaces halogenated via a vapor phase reaction can more feasibly be implemented into vacuum-based processes such as ALD. In such a process, the halogenating molecule can be dosed into reactor chamber in the same manner as the ALD chemistry. Applying inhibiting molecules to NGS on a sample surface will allow for patterned deposition of the desired thin film, using atoms as building blocks for synthesizing materials from the bottom-up. As a proof of principle, surfaces halogenated following our enumerated protocol underwent traditional ALD in order to examine the newly formed surface's blocking ability against a metal oxide precursor. Consequently, SE and AFM data demonstrated the improved shielding ability of the halogenated monolayers relative to H-Si(100) and OH-Si(100). Once again Cl(H)-Si(100) demonstrated the most effective blocking ability against the ALD chemistry followed by bromination and then iodination. However, the reduced reactivity that each halogenated surface showed with the ALD chemistry demonstrates that they are each suitable candidates for effective ALD resists and when paired with an ALD growth material such as OH-Si(100) can participate in chemo-selective processing schemes such as AS-ALD.

Chapter 4 "Bottom-Up" Laser Patterning of Ultra-Thin Oxides on Hydrogenated Silicon

4.1 Chapter Structure

A technique for forming thin oxide layers on hydrogen-terminated silicon (H-Si(100)) using Nd:YAG pulsed laser radiation (355 nm, 6 ns) under low vacuum and room temperature conditions is presented. The exposure wavelength was selected to limit photon absorption to a ~10nm depth below the Si-H interface, while nanosecond pulses were used to limit nonlinear excitation effects. Using XPS and SEM, a range of average laser beam fluences from 0.10 – 0.24 J/cm^2 was identified where the oxidation of H-Si(100) was promoted without causing observable physical damage or crystallographic modification of the substrate under SEM. Contrastingly, the same exposure to laser pulses produced limited physical and chemical changes on an already oxidized OH-Si(100) surface. Modeling of the transient temperature profile during and following the laser pulse is suggestive of a thermal mechanism associated with the surface oxidation process. The results suggest that exposure of a hydrogen layer on Si(100) to 355 nm nanosecond laser pulses can promote chemical oxidation of silicon without causing morphological damage to the underlying surface.

4.2 Introduction

To enable "bottom-up" manufacturing, recently there has been an emphasis on finding universal and reliable techniques for controlling and modifying chemical reactivity of atomic and/or ultra-thin layers on semiconductor materials.[21, 180] Through surface chemical modification, these nanometer-scale systems can be tailored to incorporate various active device components such as patterned ultra-shallow doping layers,[89-92] chemo-selective resists for AS-ALD and ALE[38, 93], or chemical and biological templates for sensors and molecular arrays.[18, 94, 95] However, one of

the major current challenges of nanofabrication of atomic and ultra-thin films is the lack of unifying conditions for controlling and activating chemical reactivity of these systems in a spatially resolved manner on a variety of different films and substrates. To date, atomic level patterning has been enabled mostly with HDL[181, 182]. Although this technique demonstrates atomic-scale precision, it is limited by extremely low throughput and requires energy-intensive processing to control the cryogenic and UHV conditions necessary for the patterning environment. Whereas HDL initiates patterning using a flux of electrons to homolytically cleave surface bonds, we hypothesize that it is possible to increase the surface reactivity to achieve a similar transition-state-induced effect by delivering a high photon flux just within a shallow adsorption depth beneath an interface, but without dissipating energy into the bulk substrate. Such laser-initiated chemical activation of atomic or small molecule films within a suitable gas-phase environment can promote a variety of surface reactions with specific chemical reactivity.

Oxidation of silicon is an important topic in microelectronics,[183] surface passivation,[184-186] and bio-engineering[187]. Current methods primarily aim at producing a continuous SiO_2 thin film, often requiring high processing temperatures[188-190]. Consequently, there has been a longstanding pursuit to find an approach that can achieve (1) localized silicon oxidation with good spatial resolution, (2) operate at lower processing temperatures, and (3) avoid introducing crystallographic damage to the surface. To gain better control of the oxidation process, researchers have turned to various growth techniques such as ion-beam, plasma, visible and UV radiation[191-193]. Of these techniques, oxide generation by UV light via pulsed laser exposures seems particularly promising in achieving these objectives[194]. Specifically, pulsed UV laser-assisted oxidation of silicon has garnered attention due to its ability to precisely control the growth of extremely thin silicon oxide layers on the scale of 1–2 nm[189-191]. These studies however, primarily focused on growing

continuous homogeneous oxide films without demonstrating spatial patterning. Additionally, the mechanism of this laser-assisted oxidation remains largely unexplored. SEM has been utilized to depassivate hydrogen-terminated silicon with spatial resolution of 200 nm but requires UHV[195]. Most promising, a 3.5 ns pulsed N_2 laser at 337 nm has been shown to locally initiate the photothermal dissociation of hydrogen from silicon under UHV[194]. This laser-defined area was then successfully phosphorus-doped to create a van der Pauw junction on previously H-terminated silicon. This work gestures towards a universal technique for the pulsed laser patterning for a whole host of substrates, resists, and small molecule precursors.

In this work, we demonstrate the formation of an ultra-thin oxide on H-Si(100) using exposure to 355 nm, 5 ns laser pulses, without causing undesirable physical damage to the underlying lattice. Thermal modeling of this process showed that the rise in surface temperature, brought upon by laser exposure, exceeded the thermal threshold for H desorption from Si. These laser-defined, H-desorbed sites then experienced oxidation with the surrounding low vacuum environment. A range of laser fluences where this effect occurs while remaining below the melting point of Si were determined both theoretically and experimentally. This laser-patterning has the potential to be integrated into a variety of deposition strategies which involve chemo-selective patterns with differences in reactivity between the chemically active OH-Si(100) regions and the chemically inert surrounding H-Si(100) surface.

4.3 Materials and Methods

All reagents and solvents were used as received without further purification. Solvents were purchased from Sigma-Aldrich and filtered through a 0.2 μm filter before use. P-doped, monocrystalline (100) silicon substrates were purchased from University Wafer, Boston, Massachusetts. XPS spectra were recorded on a Kratos Axis Ultra XPS spectrometer equipped

with a Al Kα (1486.6 eV) X-ray source at 200 W power and a pressure of 3.0×10-8 mbar. Survey scans were obtained between 0 and 1200 eV with a step size of 1 eV, a dwell time of 200 ms, and a pass energy of 140 eV averaged over 2 scans. Core-level region scans were obtained at the corresponding binding energy ranges with a step size of 0.1 eV, an average dwell time of 260 ms, and a passing energy of 20 eV averaged over 10 scans. XPS data were processed using CasaXPS software and instrument-specific atomic sensitivity factors. All C 1s peaks were calibrated to 284.7 eV and this same binding energy shift was applied to all other spectra to account for adventitious carbon contamination. Prior to analysis, samples were transported under low vacuum from the laser system to the XPS. SEM images were recorded on a Zeiss Auriga FIB-SEM microscope detecting secondary electrons at 2-4 mm working distance. An electron beam with low accelerating voltage (1-2 kV) was used in order to resolve secondary electron emissions indicative of different chemical terminations (i.e. OH-Si and H-Si). Under SEM, any change in contrast between a laser exposed and unexposed surface should be attributed to the higher emission of secondary electrons from the heavier O atoms present in the grown oxide[196]. The low voltage SEM beam may have also helped to prevent any adsorption of carbon on the sample surface or additional hydrogen desorption by the secondary electrons. AFM images were recorded on a NT-MDT AFM Microscope using a silicon nitride probe (Manufacturer: NanoWorld) with a tip radius of <15 nm, a resonance frequency of 67 kHz, and a force constant of 0.32 N/m. The same probe was used for each sample in tapping mode. All goniometry analysis was gathered using ultra-pure water.

4.3.1. Laser Parameters and Operation

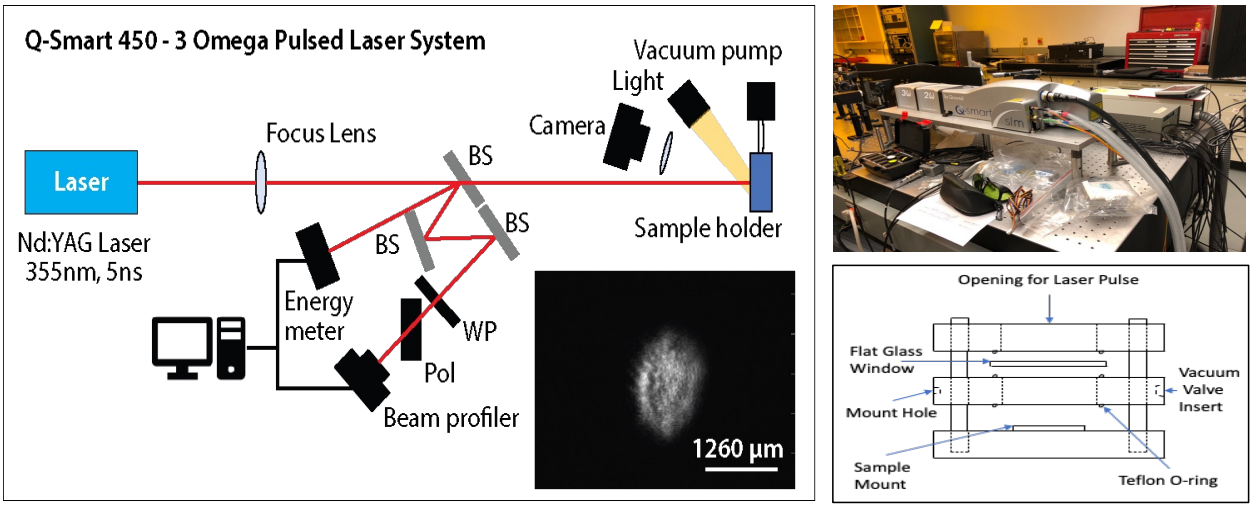

Figure 4.1 (*Left*) Schematic of laser system setup (BS: Beam Splitter, WP: Waveplate, Pol: Polarizer). (*Right*) (top) Q-smart 450 3 Omega Laser system, (bottom) schematic of sample vacuum holder.

Laser exposures were carried out using a Q-switched Nd:YAG laser (Q-Smart 450) equipped with second- and third-harmonic crystals, which produces 5 ns nearly Gaussian pulses with up to 80-mJ output pulse energy at 355 nm. A schematic illustration of the experimental apparatus is shown in **Figure 4.1.** The output beam power was controlled using a combination of a waveplate and polarizer. Single pulse excitation of the sample was enabled using a programmable shutter. The beam was subsequently directed onto the sample after passing a 1-m focusing lens that created a ~2 mm diameter laser spot at the sample plane. A wedged beam splitter was placed after the focusing lens to produce two auxiliary beams with ~4% of the energy per beam. One beam was directed into an energy meter, allowing the energy of each pulse to be measured, and the second beam was directed into a beam profiler to record the spatial intensity profile of the beam at an equivalent sample plane. The beam profile characteristics were recorded for each exposure pulse, necessitated by small variation from shot to shot and over the duration of the experiments. The relatively large beam size on the sample was required to enable modification of

a sufficiently large area on the sample to be characterized with XPS. An example of the beam profile is shown in **Figure 4.1**. The combination of the data from the power meter and beam profiler allowed for characterization of the spatial distribution of the pulse energy on the sample (fluence) and its peak fluence. The laser fluences reported in this work were originally measured as the peak energy density deposited by the beam. A calibration experiment was then conducted with the beam profiler, and the resulting energy distribution maps of the exposure beam were used to correlate peak fluence with average fluence. Average fluence from the beam profile was determined by converting pixel intensity values to an excel file and then averaging all cells with non-zero values.

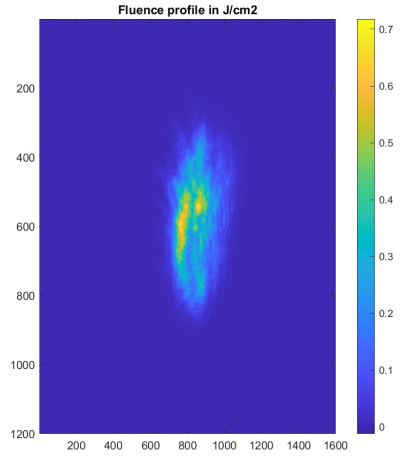

Peak Fluence: 0.720 J/cm^2

Avg Fluence: 0.066 J/cm^2

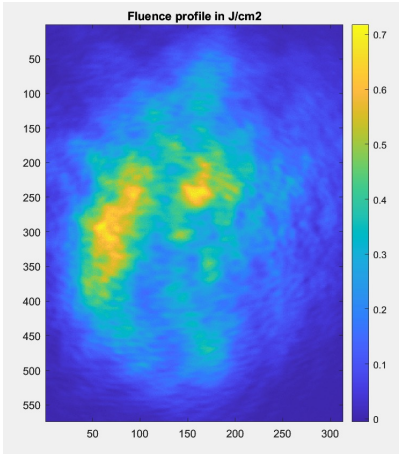

Peak Fluence: 0.720 J/cm^2

Avg Fluence: 0.240 J/cm^2

Peak Fluence (J/cm^2)	Avg Fluence (J/cm^2)
0.159	0.056
0.245	0.096
0.246	0.094
0.260	0.076
0.478	0.122
0.488	0.166
0.520	0.178
0.720	0.240
0.740	0.210
0.978	0.280
1.000	0.330

Figure 4.2 (*Left*) Fluence beam map for a 0.72 J/cm^2 exposure site, (Middle) same beam map magnified, and (*Right*) table showing reported peak fluence values and their corresponding average beam fluence before and after reflectivity loss from two separate laser experiments on H-Si(100).

As can be seen in **Figure 4.2**, the energy distribution across the exposure beam was nonuniform and therefore consisted of average fluences up to an order of magnitude lower than the reported peak fluence.

The location of each exposed site was determined using an initial fiducial generated at a higher laser fluence that could be visualized and subsequently generating a matrix of exposure sites a preset separation distances along the sample plane. The laser exposure parameters are summarized in **Table 4.1**.

Table 4.1 Laser Testing Parameters.

Wavelength	Pulse Duration	Peak Energy Density	Average Energy Density	Polarization	Incident Angle	Pulse Profile	Beam Height	Beam Width
355 nm	6 ns	0.10-1.25 J/cm^2	0.04-0.40 J/cm^2	P	7°	Vertical Oval	1.5 mm	1.0 mm

The laser beam has a varying intensity profile with the maximum intensity occurring on the left edge and dropping one order of magnitude across the entire width of the beam as seen in **Figure 4.1**. The main experimental peak laser fluence varies in the range between 0.10 and 1.25 J/cm^2 per pulse, with a significant increase in oxidation observed starting at 0.25 J/cm^2. The corresponding average laser fluence were 0.04 and 0.40 J/cm^2, with a significant increase in oxidation observed starting at 0.10 J/cm^2. Laser fluence was controlled using a polarizer and a rotating waveplate and a shutter was used to isolate single shots.

4.3.2. Sample Preparation

All glassware was washed with 1X Nano-Strip solution (a stabilized formulation of sulfuric acid and hydrogen peroxide) followed by rinsing with water and isopropanol before being dried in an oven overnight at 130°C. A 4 cm^2 Si(100) substrate was soaked in Nano-Strip at 75°C for 15 min to produce a OH-Si(100). Following this oxidation, the substrate was then immersed in a 5% aqueous HF solution for 6 min to chemically etch away the native oxide layer and form hydrogen terminated silicon H-Si(100). The substrate was then quickly rinsed with water and isopropanol and dried under a filtered nitrogen gas, before being mounted in a vacuum holder (10^{-2} torr)

underneath a silica viewport. This holder was then placed on the target stage of the laser system, where the laser exposure beam passes through the viewport and impinges on the H-Si(100) surface.

4.3.3. Estimating Si_xO_y Film Thickness

From the XPS data SiO_2 film thickness was calculated using **Equation 4.1**[122];

$$d_{\mathrm{SixOy}} = -\lambda_{SiO_2} ln\left(\frac{I_{Si}}{I_{Si,0}}\right) \quad \text{(Eq 4.11)}$$

where d_{SixOy} is the thickness of the Si_xO_y film, λ_{SiO_2} is the photoelectron mean free path through SiO_2, and lastly $I_{Si,0}$ and I_{Si} are the Si2p XPS signal intensities prior to and after laser exposure, respectively. A λ_{SiO_2} of 10 nm was used for Si2p electrons passing through SiO_2.

4.4 Results and Discussion

4.4.1 Defining Range of Energy Density for Enabling Oxidation

Initial considerations were focused on the selection of the laser parameters, based on the experimental aim of inducing material modification exclusively on the near-surface layer, with minimal heating of the bulk, in a manner that is reproducible and controlled. The selection of 355 nm laser excitation was based on limiting the absorption depth of laser radiation to the top 5-10 nm of the substrate material, as shown by the absorbance data in **Figure A4.2**. Initially, it was conceived that by increasing the carrier density we may induce a pseudo phase-transition state that allow for higher oxidative reactivity. However, the evidence presented here is instead suggestive of a thermal oxidation mechanism, future experiments with longer wavelength light should be carried out to determine if the same degree of oxidation is enabled with lower carrier density. Pulse lengths on a nanosecond scale were selected over shorter exposures to exert more precise control over the total amount of energy delivered to the substrate and to minimize contributions by

nonlinear absorption, which may introduce a competing photoelectronic mechanism for H-Si(100) oxidation. All exposures consisted of a single pulse as this allowed for only the study of the effect of varying laser fluence. Lastly, the effect of laser pulse intensity on Si(100) oxidation was examined by varying fluence exposure up to introducing laser induced damage (from 0.04 J/cm^2 to 0.40 J/cm^2). Example results are shown in **Figure 4.3**.

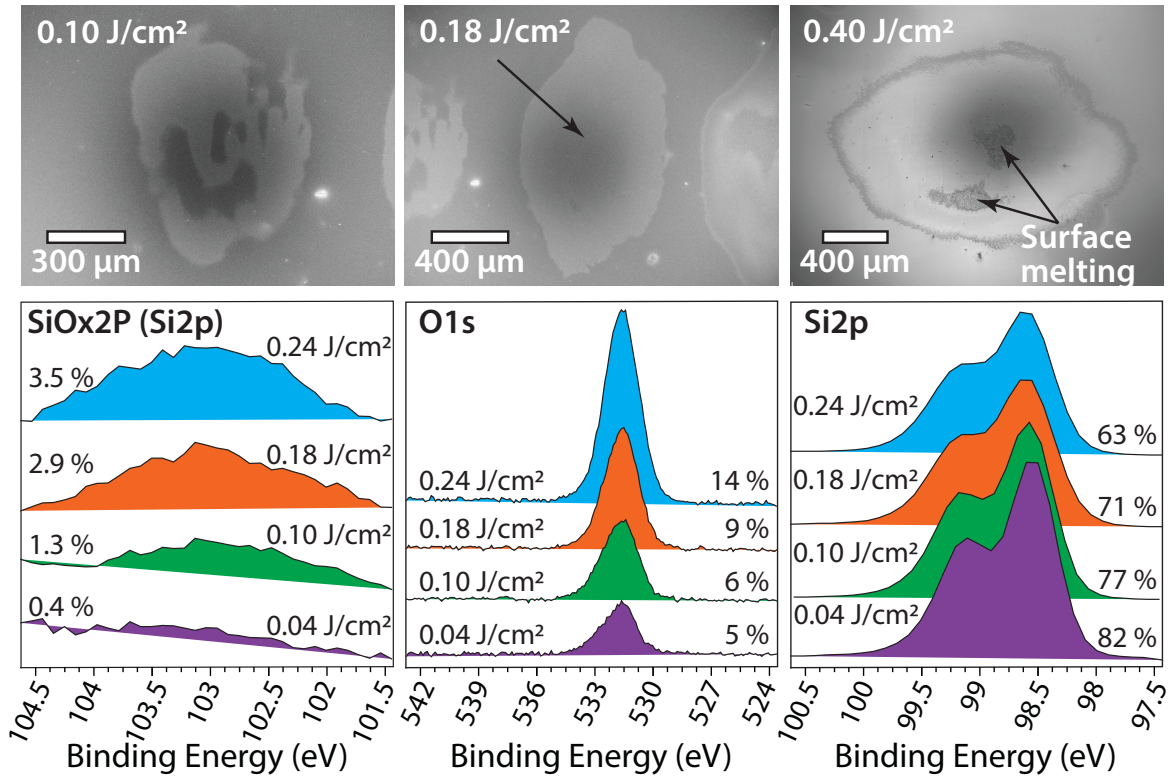

Figure 4.3 (Top) SEM imaging of H-Si(100) surfaces post-laser exposure with fluences of; 0.10 J/cm^2, 0.18 J/cm^2, and 0.40 J/cm^2. (Bottom) Si_xO_y2p, O 1s, and Si_{Bulk}2p XPS region spectra from H-Si(100) surfaces post-laser exposure with fluences of; 0.04 J/cm^2, 0.10 J/cm^2, 0.18 J/cm^2, and 0.24 J/cm^2. The same experiment was repeated using similar testing conditions on five separate H-Si(100) samples and the XPS and SEM results are shown in Figures A4.3 – A4.7.

The XPS and SEM results shown in **Figure 4.3** demonstrate that pulsed laser exposures of H-Si(100) can promote chemical oxidation within the irradiation site without causing physical surface damage. This is evidenced by the clear enhancement of the Si_xO_y2p XPS signal centered at 103.2 eV when the surface is exposed to a fluence of about 0.10 J/cm^2 compared to exposure at

a lower fluence (0.04 J/cm^2). Quantitatively, this signal enhancement translates to an increase in Si_xO_y surface concentration of 1.3 At% relative to a fully etched H-Si(100) surface. This effect is amplified when increasing the laser fluence exposure to 0.18 J/cm^2 and 0.24 J/cm^2, with Si_xO_y surface concentration increases of 2.9 At% and 3.5 At%, respectively. The relative rise in O1s XPS signal also scales very closely with Si_xO_y generation. For example, between 0.18 J/cm^2 and 0.24 J/cm^2 exposures there is a 1.2x increase in Si_xO_y surface concentration which shows good agreement with the 1.5x increase observed in overall O content found on the surface. Hence, the primary mode of O atom introduction onto the surface appears to be through Si_xO_y generation. Furthermore, there are two notable characteristics in how the $Si_{Bulk}2p$ spectra evolve with increasing fluence exposure which are indicative of interfacial chemical transformation. First, the overall $Si_{Bulk}2p$ signal decreases, and secondly, there is a blurring of the closely spaced spin-orbit components, both of which would occur as an oxide (and other oxygenated species) accumulates on the surface, due to increasing attenuation of the underlying $Si_{Bulk}2p$ signal. Additional experiments were conducted using similar testing conditions on five separate H-Si(100) samples and the XPS and SEM results are shown in **Figures A4.3 – A4.7**. Each shows a general enhancement of Si_xO_y2p XPS signal above 0.1 J/cm^2 laser exposure, albeit with differing degrees of oxidation observed. The differences in oxide generation may be the result of the contrasting amounts of initial F and C atom containing species found on each surface. Overall, the compilation of these results more-or-less resembles the results shown in **Figure 4.3**. All this is strong evidence of a precise laser-driven oxidative effect on H-Si(100). All this is a strong evidence of a laser-driven oxidation of the top H-Si(100) surface at fluences above approximately 0.10 J/cm^2.

We also determined a maximum fluence where physical surface damage begins to occur. The results showed that the surface morphology begins to physically alter starting at a fluence

above 0.25 J/cm^2, where subtle scattering from the surface morphology is first observed on camera. Although this damage is minimal at first, when the exposure fluence reaches 0.40 J/cm^2, significant surface melting is observed, as shown in **Figure 4.3**. The Si2p and O1s XPS spectra for a surface exposed with 0.38 J/cm^2 shown in **Figure A4.8** demonstrates that the rate of this laser driven surface oxidation effect continues to increase up until this threshold of melting. Overall, the apparent range of tunable energy density available for controlling the oxidation of H-Si(100) without surface rearrangement is in the range from 0.10 J/cm^2 to 0.24 J/cm^2, with further oxidation continuing until clear surface damage occurs as the fluence approaches 0.40 J/cm^2. This range is in good agreement with the lower bound of the range of energies that Katzenmeyer et. al. found for hydrogen depassivation from Si without surface damage (0.2-0.3 J/cm^2). Using STM, they found that acute lattice damage occurs at 0.3 J/cm^2, which is slightly below the melting threshold we defined with SEM.

SEM images in **Figure 4.3** show the gradual formation of the beam imprint onto the sample surface with increasing laser fluence, the generation of which scales closely with the increase in both Si_xO_y2p and O1s XPS signals with fluence. This is suggestive that the propagation of the beam imprint in SEM is due to a change in surface chemistry, rather than a change in the physical morphology of the surface. This same effect is observed in most of the data sets in **Figures A4.3 – A4.7**.

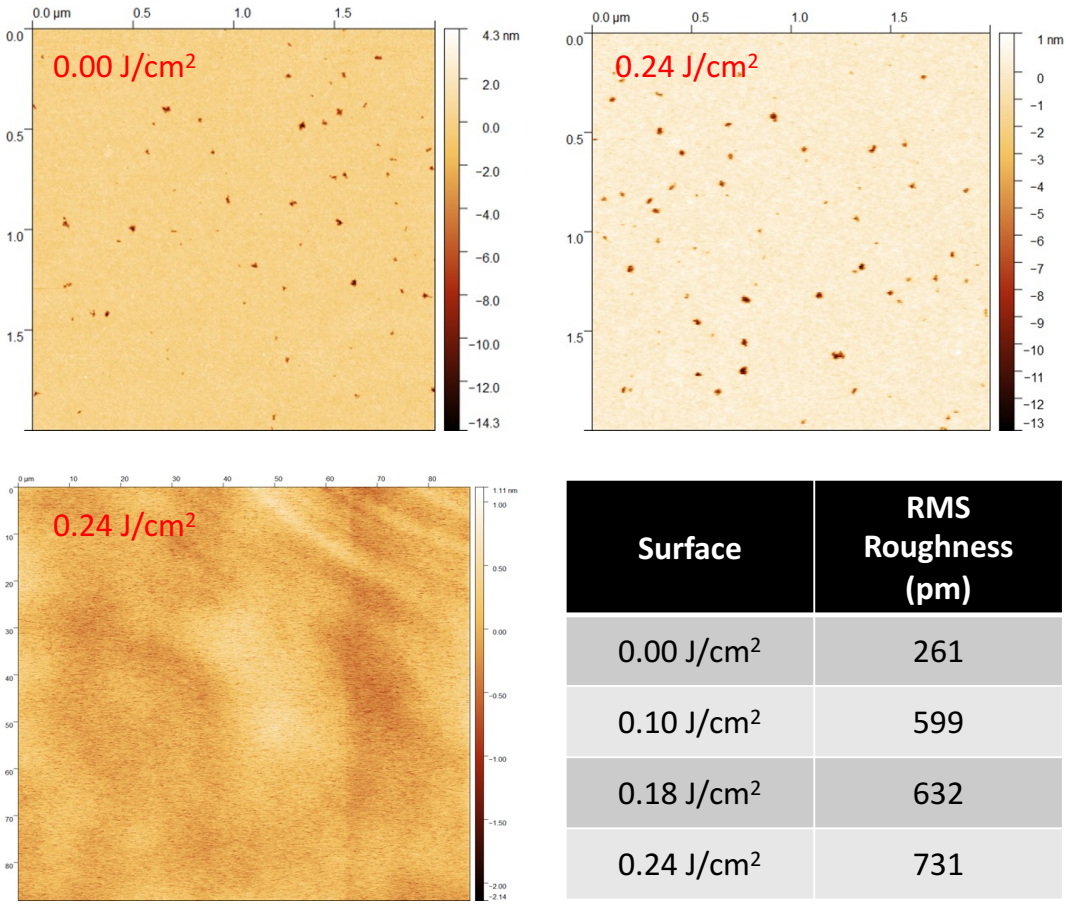

Surface	RMS Roughness (pm)
0.00 J/cm²	261
0.10 J/cm²	599
0.18 J/cm²	632
0.24 J/cm²	731

Figure 4.4 AFM micrographs of; (Top-Left) non-irradiated H-Si(100) surface, (Top-Right) H-Si(100) irradiated with 0.24 J/cm², (Bottom-Left) larger area H-Si(100) irradiated with 0.24 J/cm². (Bottom-Right) Table of RMS roughness values.

AFM imaging shown in **Figure 4.4** also validates this interpretation, as no significant increase in roughness was observed within the laser exposure sites as compared to the surrounding unirradiated surface.

4.4.2 Nature of Laser-Grown Thin Film Oxide

The role played by potential oxidizing agents in laser driven oxide growth is still not well established. Nayar et. al. theorized that SiO_2 growth via UV-light exposure is predominantly enabled by O^- ions, produced through photodissociation of oxygenated species in the surrounding environment that then experience self-limiting diffusion through the growing surface oxide interface[197]. It has been suggested that the fast rate of O^- recombination also limits the

concentration of oxidizing species that are able to access the silicon surface[190, 198]. To prevent this loss of surface oxidizing species, Kailath et. al. found that by heavily diluting a saturated O_2 environment with N_2 when oxidizing H-Si(100) with a 355 nm laser, that they were able to hinder both oxide diffusion and recombination that stimies surface oxidation, which enabled great control over SiO_2 film growth[189]. A similar phenomenon may also be occurring in this technique by virtue of the low-vacuum conditions (10^{-2} torr) which similarly limits the concentration of available oxidizing species. The oxidizing O anions in this work are most likely derived from water molecules in the surrounding environment.

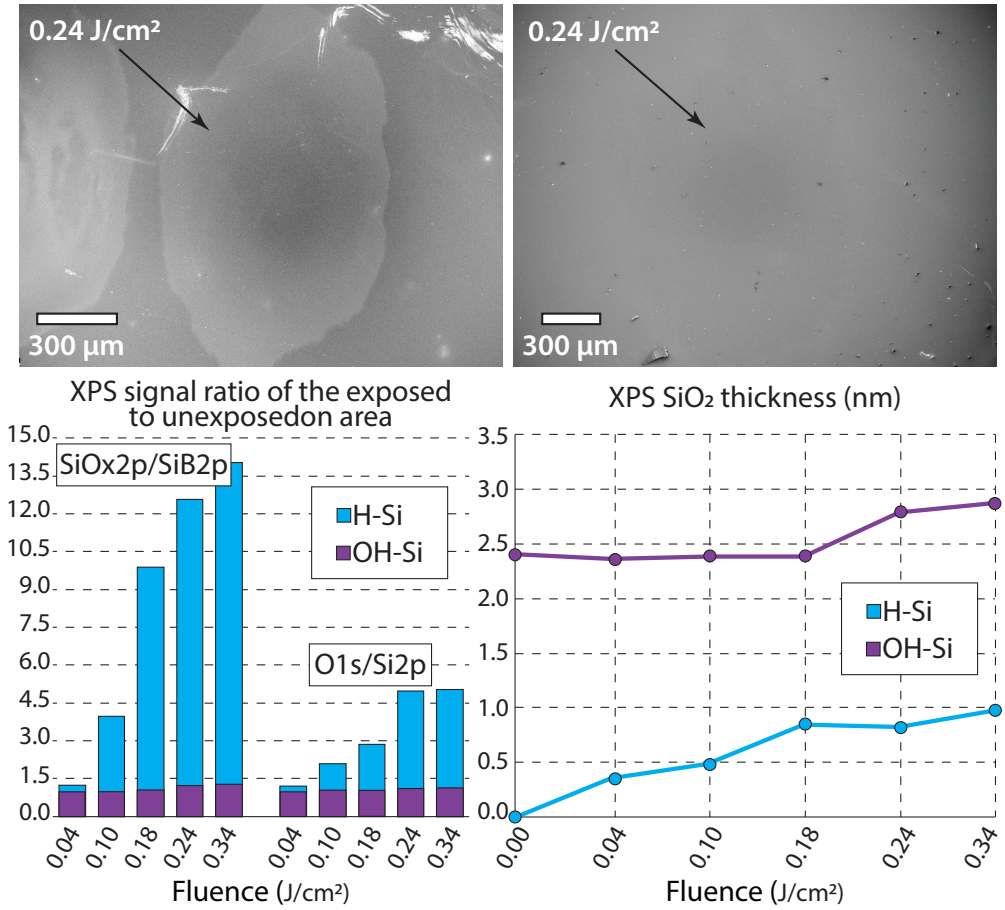

Figure 4.5 (*Top*) SEM imaging of (*Left*) H-Si(100) and (*Right*) OH-Si(100) surfaces post-exposure with 0.24 J/cm^2. (*Bottom*) Plots showing (*Left*) how many times greater the Si_xO_y2p and O1s XPS signals (SiO_x normalized by Si_{Bulk}2p and O 1s normalized by Si2p) are on both OH-Si(100) and H-Si(100) surfaces post laser exposure, relative to an unexposed area on the same surfaces, and (*Right*) the estimated SiO_2 film thickness calculated using Equation 4.1.

As a control experiment, the same laser exposure experiment was carried out with an already solvent-oxidized OH-Si(100) surface and a comparison between it and the laser-processed H-Si(100) sample is shown in **Figure 4.5**. SEM imaging shows that after exposure to 0.24 J/cm^2 there is clear imprinting of the laser beam onto the H-Si(100) surface, whereas, the beam imprint is much harder to discern on the OH-Si(100) surface, despite similar SEM detection settings, due to a smaller difference in contrast between the irradiated and non-irradiated areas. Furthermore, a histogram of showing the increase in Si_xO_y2p and O1s signals on both OH-Si(100) and H-Si(100) with increasing laser fluences relative to an unexposed area, demonstrates that there is significantly more oxidative change occurring on the H-Si(100) surface as laser energy is applied. For example, after exposure with 0.34 J/cm^2 there is a 14 times increase in the Si_xO_y2p/Si_B2p signal ratio on H-Si(100), while the OH-Si(100) surface exhibits only a 1.4 times increase in signal between the irradiated and non-irradiated areas. Below 0.24 J/cm^2 exposure, on OH-Si(100) both the Si_xO_y2p and O1s signals found on the irradiated sites are approximately the same to that found on the non-irradiated area. These observations show good correlation with the estimated SiO_2 thickness values displayed in **Figure 4.5**, where on OH-Si(100) an increase in thickness is only observed after exposure with 0.24 J/cm^2. Meanwhile, gradual growth in SiO_2 thickness is observed on H-Si(100) as higher laser fluence is applied. These observations suggest that the laser exposure is initiating a predominantly chemical modification rather than a morphological one. Furthermore, the estimated SiO_2 thickness values also show that after 0.24 J/cm^2 exposure on H-Si(100), the oxide thickness is still only 34% of the thickness found on the native OH-Si(100) surface. This, in addition to the Si_xO_y2p XPS spectra in **Figure A4.9** which shows that laser oxide growth is only a fraction of a fully formed native oxide, demonstrates there is still much room for further tuning of exposure fluence when it comes to the laser driven oxidation of H-Si(100). Lastly, although it would be

expected that the relative increase in O1s signal would scale evenly with that of the Si_xO_y2p signal, if only surface oxidation is occurring, which is not the case on H-Si(100). However, as can be observed in the O1s spectra in **Figure 4.3**, the H-Si(100) surface begins with a discernable amount of O surface concentration as opposed to SiO_x, specifically, at a 0.04 J/cm^2 exposure site there is already 5 At% of O content, whereas there is only 0.4 At% of SiO_x surface concentration. Therefore, with increasing laser fluence, the overall increase in O1s signal is less than that of Si_xO_y2p due to higher initial amount of non-Si_xO_y, O-containing species found on the surface.

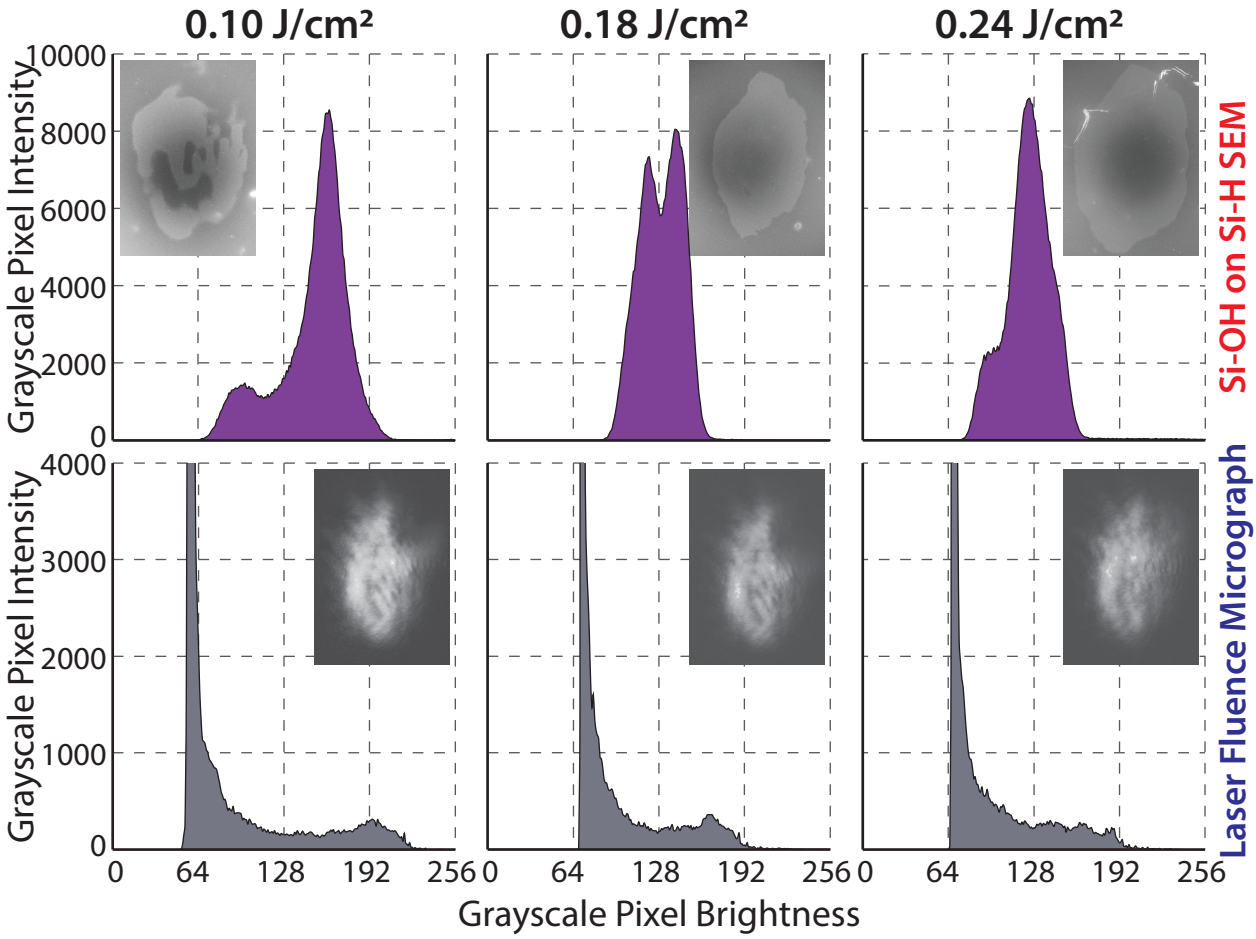

Figure 4.6 Array of greyscale pixel intensity profiles for (Top) SEM imaging of sites (image subsets) matched with (Bottom) fluence maps (image subsets) generated with the corresponding laser fluence.

Fluence maps across the exposure area were collected using a beam profiler and converted to topographies in MATLAB™. An array of fluence maps and SEM of the corresponding exposure

sites are shown in **Figure 4.6** and demonstrate the general uniformity of the laser beam shape and dimensions. Moreover, visual alteration of the sample surface is limited to within the beam imprint and no dissipation (whether chemical or physical) is observed outside the confines of the beam profile, as is shown more closely in **Figure A4.10**. Both the fluence maps and SEM images were converted into greyscale images and the pixel intensities across each image were plotted in the accompanying intensity profiles in **Figure 4.6**. These profiles show that although the SEM images of the exposure sites are characterized by a narrow bi-modal distribution of the pixel intensities attributed to the H-Si(100) background (dark) and the OH-Si(100) exposed spots (bright), the beam fluence maps have a wide distribution of the pixel intensities due to the non-uniform range of laser intensities within the beam. Furthermore, the SEM images of the laser-exposed samples demonstrate increasing homogeneity of the exposed spots with increasing fluence, whereas the images of the fluence maps remain non-uniform. This suggests that the OH-Si(100) areas in the laser exposed samples have relatively consistent and constant contrast with the H-Si(100) background and, therefore, should have a uniform and constant distribution of the oxide. However, with the increasing laser fluence the ratio of the oxidized to non-oxidized areas within the exposure spot decreases. Yet, the XPS data demonstrates that the degree of oxidation increases with the average fluence of the exposure beam. This is because the XPS analysis averages the overall oxide amount within the exposed area and cannot discriminate between uniform spots with thinner oxide layers vs. non-uniformed spots with both oxidized and non-oxidized areas. This is also supported by the reduction of the apparent oxide growth after a thin oxide layer (~1 nm) develops at ~0.24 J/cm^2 fluence and even with increasing laser fluence (up to the physical damage at 0.4 J/cm^2) the formation of thicker oxide films does not occur. Thus, the laser-assisted oxidation effect observed

in this study appears to be a threshold event where a certain minimum value of the laser fluence is required to initiate oxidation.

4.4.3 Elucidating Mechanism of Laser-Assisted Oxidation Effect

In order to effectively modulate surface chemical reactions, it is important to understand the mechanism by which light absorption induces them. The primary potential processes are photoelectrochemical processes induced by carrier generation in the substrate, thermal processes due to substrate heating, and direct electronic absorption by the molecular species at the interface. Although there have been some general studies into the mechanism of laser-assisted oxidation of H-Si(100)[188, 190, 197, 199, 200], the photoinduced oxidation kinetics is not well understood. Gibbons was the first to employ CW lasers to grow SiO_2 on Si(100)[201] and in an attempt to enumerate a possible oxidative mechanism, Boyd et. al. hypothesized that the continuous laser radiation enhanced carrier population by progressively weakening surface Si dimers[202] via promotion of valence electrons (Si bandgap: 1.12 eV) and subsequent electron-induced lattice heating. Using continuous laser radiation to weaken and gradually break surface bonds through a predominantly thermal effect is an example of a linear process since the probability of bond activation/dissociation increases with exposure duration. If the mechanism behind this laser driven oxidation effect is due to a linear process than the energy of the photons at 355 nm (3.5 eV) must deliver enough energy to overcome the threshold for Si-H dissociation within the 6 ns laser pulse. The reported values for hydrogen desorption from silicon range from 2.82-3.9 eV for monohydride species[203-205] and 1.86-3.19 eV for dihydride species[205]. Additionally, the Gibbs free energy of oxide formation for Si is -35.4 J/mole at ambient temperature and pressure and thus is significantly prone to oxidation in most states. The activation energy for hydrogen desorption from Si(100) is reported to be 49±3 kcal/mol (1.99 eV±0.3 eV)[206]. To determine the role of thermal oxidation in this laser driven

technique, the time-resolved thermal analysis of silicon was performed as a function of both silicon properties (absorption coefficient, reflectivity, thermal conductivity, and diffusivity) and laser exposure parameters (wavelength, pulse time, and fluence). For this thermal modeling, the average fluence values were reduced by 58% to account for reflectivity loss (roughly 50% loss for Si and 8% loss due to the sample holder glass viewport) at 355 nm. Additionally, although material reflectivity is a temperature dependent property, this effect is negligible at our experimental conditions[207].

Assuming 1-D transient heat transfer, the heat flux (q_s) to the topmost surface can be defined as **Equation 4.2**;

$$q_s = \Delta T \sqrt{\frac{\pi}{4} k \rho c_p t} \qquad \text{(Eq 4.2)}$$

where k is the thermal conductivity, ρ and c_p are the density and heat capacity of the substrate material, respectively, and t is the laser exposure pulse time (described using step function). After expanding ΔT and rearranging, **Equation 4.3** is as follows;

$$T(z = 0,\ t) - T_i = \dot{q}_s \sqrt{\frac{4t}{\pi\left(k \rho c_p\right)}} \qquad \text{(Eq 4.3)}$$

where the final surface temp (T) is only a function of laser exposure time. To consider the volume of thermal absorption from laser exposure, **Equation 4.3** should first account for the loss of laser energy that the photons experience as they travel through the substrate bulk. Thus, after incorporating absorption depth (δ) **Equation 4.4** is;

$$T(z = 0,\ t) - T_i = \delta \frac{\dot{e}_{gen}}{k} \left(-\delta + \sqrt{\frac{4t}{\pi\left(k \rho c_p\right)}}\right) \qquad \text{(Eq 4.4)}$$

where $\dot{e}_{gen}$ is the volumetric power absorbed. When the thermal absorption depth (z) is also varied **Equation 4.5** is;

$$T(z,\ t) - T_i = \delta\frac{\dot{e}_{gen}}{k}\left[-\delta exp\left(-\frac{z}{\delta}\right) + \sqrt{\frac{4\alpha t}{\pi}}exp\left(-\frac{z^2}{4\alpha t}\right) - zerfc\left(\frac{z}{2\sqrt{\alpha t}}\right)\right] \qquad \text{(Eq 4.5)}$$

where α is the thermal diffusivity of the substrate material, and the complementary error function (erfc) term is added to account for heat diffusion length. However, k and α have strong nonlinear dependence on surface temperature[208], as is demonstrated by **Figure 4.7**.

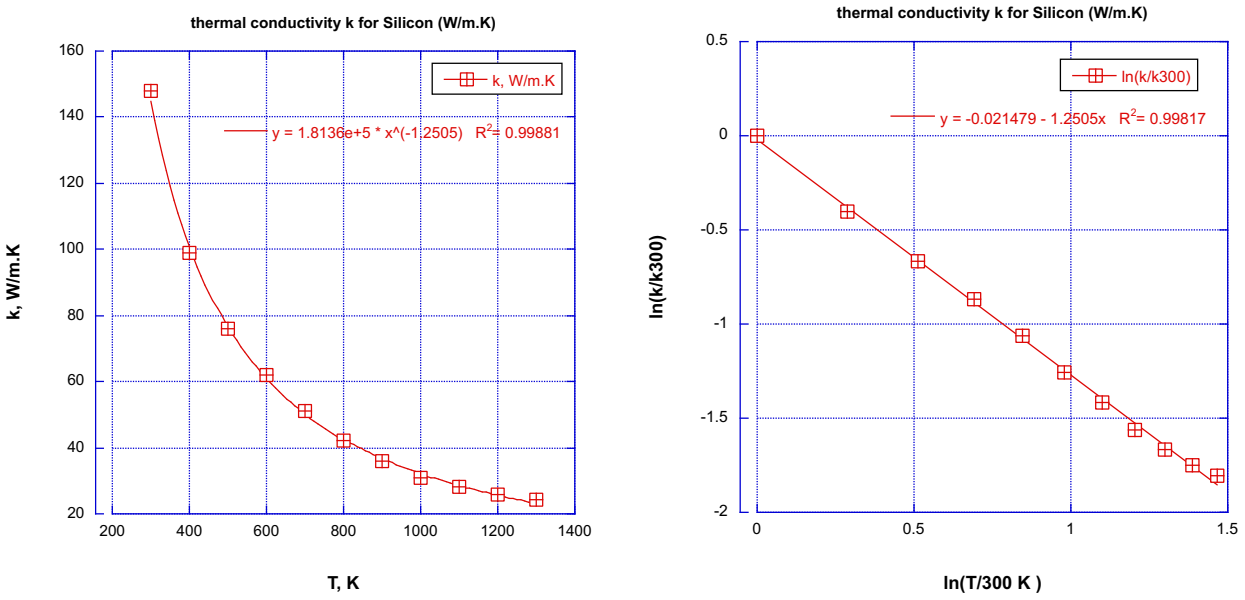

Figure 4.7 (*Left*) Thermal conductivity of silicon as a function of temperature[208], (*Right*) conversion of profile from a logarithmic scale to a linear scale.

Here, the k vs. T profile exhibits a R^2 value of 0.9988 with a logarithmic line of best fit. However, this profile was converted to a linear scale using;

$$\frac{k(T)}{k(T_o)} = (\frac{T_o}{T})^n \; where \; T_o = 300\ K \; and \; n = 1.25$$

So that a linearized version of the model could be solved. Furthermore, α can be derived from k using **Equation 4.6**.

$$\alpha = \frac{k}{\rho c_p} \qquad \text{(Eq 6)}$$

Thus, for each iteration of $T(z,\ t)$ calculated, new k and α values should be determined. Here, we solve a linearized version of **Equation 4.5** based on a range of fixed values for k between 130 W m^{-1} K^{-1} at 21°C and 30 W m^{-1} K^{-1} at 1500°C to generate temperature profiles as a function of z, t, and average exposure fluence shown in **Figure 4.8**. **Equation 4.5** was coded into Matlab™ and the script is shown in **Equation A4.11**.

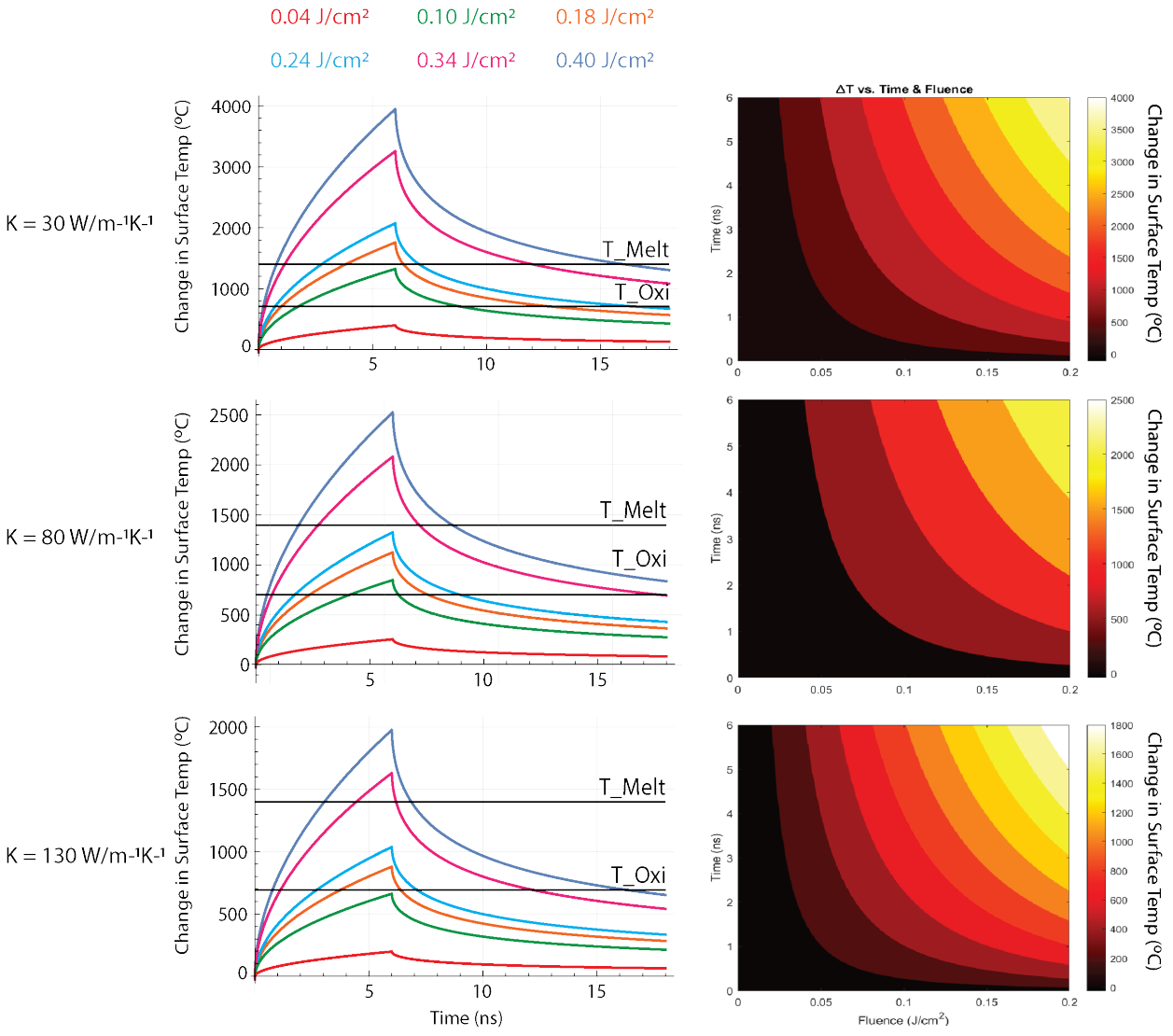

Figure 4.8 (Left Column) Change in temperature profiles at substrate surface for varying peak fluence exposures (average fluence used in calculation) for a low, mean, and high thermal conductivity, and (Right Column) change in temperature profile at substrate surface as a function of laser intensity (i.e. pulse time and average laser fluence) for a low, mean, and high thermal conductivity.

The temperature profiles at the substrate surface ($z = 0.01\ nm$) for each specific exposure fluence and k value, shows that fluences at or above 0.10 J/cm^2 results in a surface temperature change above the threshold for dry thermal oxidation of Si (700 °C[209]), although some papers report monohydride desorption of Si at temperatures as low as 430 °C[205]. This correlates well with the XPS data shown in **Figure 4.5** which demonstrate a 2.25 times increase in Si_xO_y surface content between 0.10 J/cm^2 and 0.18 J/cm^2 exposures. Additionally, **Figure 4.8** also shows that peak fluence exposures at or above 0.34 J/cm^2 results surface temperature change above the melting threshold for Si at each k value too. This coheres well with SEM of a 0.40 J/cm^2 exposure site in **Figure 4.3** which exhibits observable melting of the surface. Both these observations are suggestive of a thermal mechanism driving surface oxidation. It should also be noted that even though the temperature change after a 0.10 J/cm^2 exposure with a low k value is 20 °C under the thermal oxidation temperature threshold, **Figure 4.5** shows that there is still about a 4% increase in Si_xO_y concentration on the surface at this same exposure fluence. But because the model outputs surface temperature change, it is reasonable to assume that the surface is initially at or around room temperature (21 °C) prior to laser exposure, and thus the temperature change after a 0.10 J/cm^2 exposure should be approximately 701 °C. It appears that the mean k value of 80 W cm^{-1} K^{-1} best approximates the reality of the material during laser exposure as the temperature profiles generated between 0.10-0.24 J/cm^2 indicate surface temperature changed above the threshold for thermal oxidation but below the threshold for surface melting.

It has been reported that the fastest oxidation rate of Si between 800-1200 °C is 0.042 nm/sec[210], but the results in this study demonstrate 0.9 nm of Si_xO_y growth during the 6 ns laser exposure pulse after 0.18 J/cm^2. This previously reported rate pertained to oxide growth of thick layers (from 0 to 1 micron in increments of 40 nm), thus, it's probable that at the lowest thickness

regime (~ 0-2 nm) at which this study is interested in, the initial rate of oxide growth is much faster for the initial monolayer or two, and then slows significantly due to the transport limitations. This discussion on oxide growth rate is only speculative as it is not clear whether oxidation is predominantly occurring during or after the exposure pulse. However, if the laser is desorbing hydrogen from the surface, the unsatisfied silicon sites will be extremely reactive with its immediate environment. And given the relatively low vacuum conditions of the sample holder (10^{-2} torr), the surface is most likely interacting with 2-4 ppm of oxidizing species, and so the kinetics of the subsequent oxidation reaction should be ultrafast. **Figure 4.8** shows 3D profiles that relates laser intensity (laser fluence/pulse time) to surface temperature change that will help to define a window in laser intensity where thermal oxidation of Si can be enabled without surface melting. These profiles were generated using the code shown in **Figure A4.13**. To attain a 700 °C surface temperature change at k = 80 W cm^{-1} K^{-1}, the minimum intensity needed is 0.009 nW/cm^2 (0.0525 J/cm^2 for 6 ns). For the same 6 ns pulse, the minimum intensity that induces a surface temperature change above the melting point of Si (1412 °C) is 0.0233 nW/cm^2 (0.140 J/cm^2 for 6 ns).

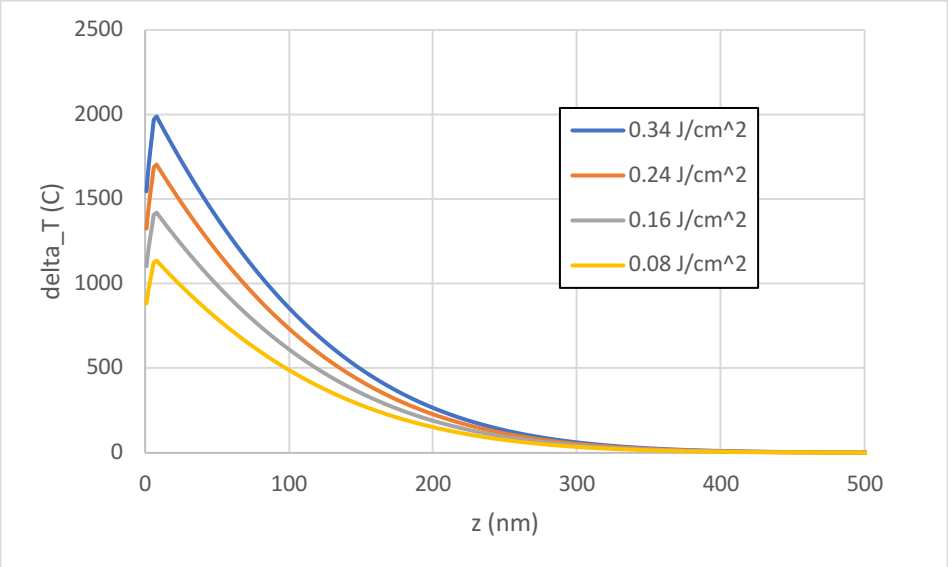

Figure 4.9 Heat dissipation of substrate as a function of heat diffusion length at selected average exposure fluences (i.e. 0.34 J/cm^2, 0.24 J/cm^2, 0.16 J/cm^2, 0.08 J/cm^2) after a 6 ns exposure pulse.

Thermal dissipation length profiles in **Figure 4.9** show that the heat diffusion length is roughly 375 nm after a 6 ns exposure pulse at average fluences ranging from 0.08 J/cm^2 to 0.34 J/cm^2.

4.4.4 Air Stability Study of Exposed and Nonexposed Laser Sites

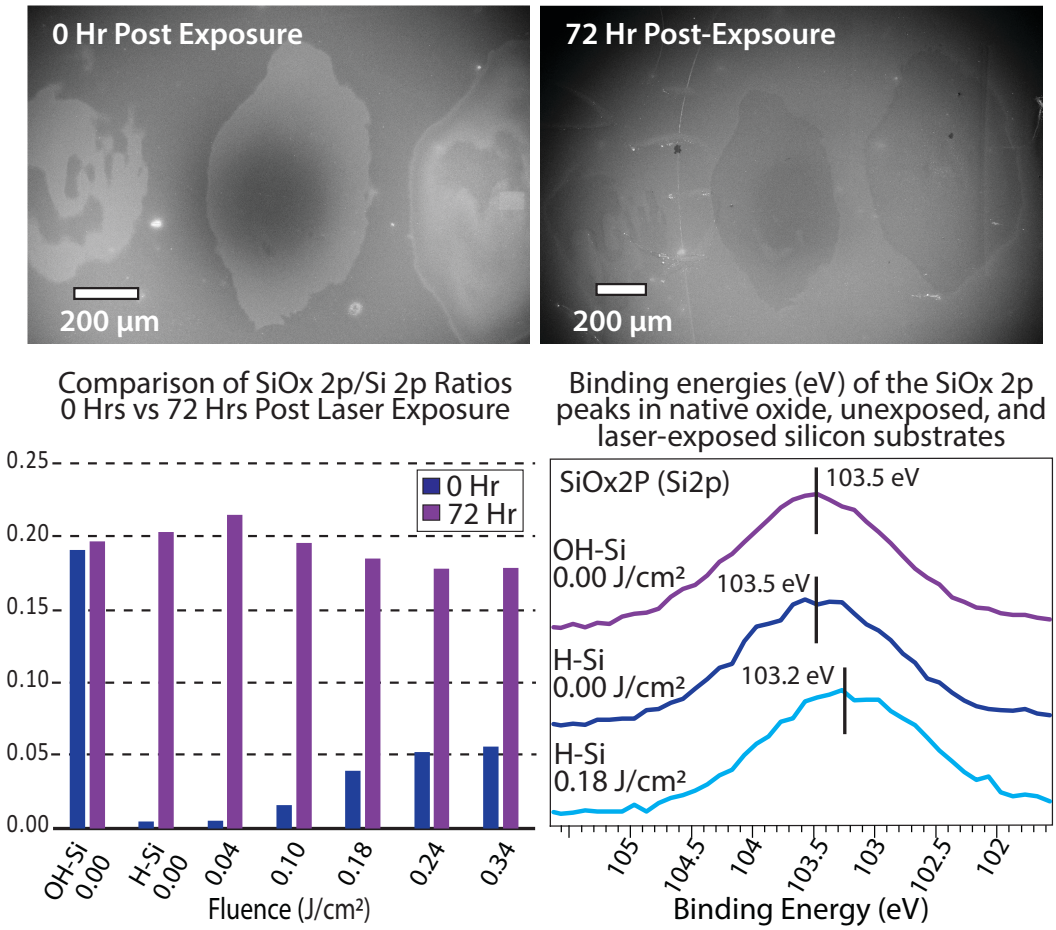

Figure 4.10 (*Top*) SEM imaging of H-Si(100) surface (*Left*) immediately following laser exposure, and (*Right*) after 72 hr in an ambient environment post-exposure. (*Bottom*) (*Left*) Histogram showing $Si_xO_y2p/Si_{Bulk}2p$ signal ratios for a native oxide, unexposed H-Si, and laser exposed H-Si sites before and after 72 hours of air exposure, and (*Right*) a comparison of Si_xO_y2p spectra from a 0.09 J/cm^2 laser exposed H-Si(100) surface and unexposed H-Si(100) and OH-Si(100) surfaces.

To further evaluate whether the beam imprint observed with SEM was primarily a product of chemical or physical surface transformation, the irradiated H-Si(100) surface was allowed to passively re-oxidize in an ambient laboratory setting for 72 hours. The subsequent XPS and SEM results are shown in **Figure 4.10** and reveal a nebulous picture of how additional oxidation of the

laser exposed sites progresses. SEM shows that a change in contrast occurs within the H-Si(100) exposure sites after prolonged exposure to the ambient environment compared to the same surface immediately following laser exposure. This change occurs despite almost identical SEM detection settings, yet still the laser site appears to be charging electrons differently. The darker shade on the 72 hr post exposure sample more closely resembles that of the exposure site observed on the OH-Si(100) surface in **Figure 4.5**. And although the beam resolutions are still high compared to that of the OH-Si(100) site, one can begin to see fading around the edges of the beam imprints on H-Si(100) 72 hours post exposure. However, the majority of each beam imprint did remain across the 72 hours. Interestingly, after 72 hours of air exposure, the histogram in **Figure 4.10** shows that the Si_xO_y2p XPS signal on H-Si(100) is lower in the irradiated sites (above 0.04 J/cm^2) compared to an non-irradiated site. For example, the Si_xO_y2p signal measured from the site irradiated with 0.24 J/cm^2 is about 12.5% less than the signal measured on the non-irradiated site. **Figure A4.**13 also shows that the O1s signal is also lower on H-Si(100) sites irradiated with at least 0.24 J/cm^2. This same reduction in Si_xO_y2p and O1s signals is not found on laser exposed OH-Si(100) sites, all of which more or less resemble the chemical composition of the corresponding non-irradiated site. Therefore, just as the rate of oxidation on H-Si(100) increased with laser fluence exposure in **Figure 4.3** and **Figure 4.5**, the rate of subsequent passive oxide formation decreases with increasing laser fluence following 72 hours of air exposure. This, in conjunction with the beam imprints still visible but with a change in contrast, may suggest that the original oxide formed on H-Si(100) post exposure may differ chemically from that of oxides generated in air or in a solution phase oxidizer (i.e. Nano-Strip). This reasoning is further validated by the Si_xO_y2p XPS spectra in **Figure 4.10** which shows that the signal measured from a H-Si(100) site irradiated with 0.18 J/cm^2 is shifted to a lower binding energy by 0.3 eV compared to signals found on both non-irradiated

OH-Si(100) and H-Si(100) sites. Thus, it is possible that rather than stoichiometric SiO_2, a slightly different form of oxide is generated using this technique, possibly some derivation of Si_2O_3 which is reported to be 0.9 eV down energy from the SiO_2 signal[211]. It is not clear whether this difference in oxide structure is the result of a predominantly thermal oxidation mechanism and future studies should focus on examining the difference in chemical structure of native grown oxide and thermal oxide.

4.5 Conclusion

Presented here is a methodology for universal patterning of atomic and small molecule resists using nanosecond pulsed laser radiation. Specifically, Nd:YAG pulsed laser radiation was employed to increase the rate of oxidation on hydrogen-terminated Si(100) under low vacuum and room temperature conditions. An interval of average laser beam energy density (0.10 – 0.24 J/cm^2) was established in which the rate of surface oxidation on H-Si(100) is enhanced, whereas a corresponding OH-Si(100) surface saw minimal oxide growth. Furthermore, XPS demonstrated that the degree of surface oxide content on H-Si(100) increased with energy density and correlated with the formation of small spots (matching the profile of the laser beam) observed with SEM. This imaging was paired with laser fluence mapping to demonstrate the local nature of the oxidizing effect. AFM analysis was used to verify that the oxide areas were morphologically similar to the unexposed H-Si(100) areas suggesting that the laser radiation below the damage threshold fluence does not lead to physical changes of the exposed interface. Thermal modeling demonstrated that the rise in surface temperature, brought upon by laser exposure between 0.10-0.30 J/cm^2, exceeded the thermal threshold for H desorption from Si, while remaining below the melting point of Si. These laser-defined H-desorbed sites then experienced oxidation with the surrounding low vacuum environment. Lastly, ambient stability studies over 72 hours

demonstrated that subsequent passive oxidation within the irradiated spots progressed differently than on the surrounding non-irradiated area, indicating that laser radiation grows a different form of oxide (most likely Si_2O_3) than that of stoichiometric SiO_2. From these results it was concluded that pulsed laser exposures of a monoatomic hydrogen-resist layer on Si(100) can promote chemical oxidation of the resist without causing morphology damage to the underlying surface. Such an oxidative patterning technique has the potential to enable universal, *in-situ* patterning of various substrate/resist combinations for ASD manufacturing platforms.

Chapter 5 Soft Lithography of Carbene-Based Small Molecule Layer

This chapter is a slightly modified version of "*Light-Mediated Contact Printing of Phosphorus-Species onto Silicon Using Carbene-Based Molecular Layers*" published in *Langmuir* and has been reproduced here with the permission of the copyright holder.

5.1 Chapter Structure

The ability to deposit pattern-specific molecule layers onto silicon with either regional p-/n- doping properties or that act as chemo-selective resists for area-selective deposition, is highly sought after in the bottom-up manufacturing of microelectronics. In this chapter, we demonstrate a simple protocol for the covalent attachment and patterning of a phosphorus-based dopant precursor onto silicon(100) functionalized with reactive carbene species. This method relies on selective surface reactions which provide terminal functionalities that can be photochemically modified via UV-assisted contact printing between the carbene-functionalized substrate and an elastomeric stamp inked with the inorganic dopant precursor. XPS analysis combined with SEM imaging was used to characterize the molecule attachment and patterning ability of this technique. The XPS spectra are indicative of the covalent bonding between phosphorus-containing molecules and the functionalized surface after both bulk solution-phase reaction and photochemical printing. SEM analysis of the corresponding printed features demonstrates the effective transfer of the phosphorus species in a patterned orientation matching that of the stamp pattern. This simple approach to patterning dopant precursors has the potential to inform the continued refinement of thin-film electronic, photonic and quantum device manufacturing.

5.2 Introduction

Strategies for the bottom-up manufacturing of semiconductor devices are increasingly relying on the selective functionalization of surfaces with small molecules or monoatomic films that can act as deposition resists[38, 93], dopants[91], or active device components[94]. When combined with parallel patterning techniques, these small molecule and atomic-scale interfaces can play an integral role in self-aligned fabrication schemes for bio-templates[94, 212], doping of ultra-shallow junctions[92, 213], or act as effective resists in ASD techniques[28, 92, 171, 214, 215]. However, traditional patterning methods such as photolithography and shadow mask deposition are not directly compatible with monomolecular or atomic layers, which are projected to play a bigger role in electronic device manufacturing due to the continuous downsizing of device components[216]. Alternatively, contact transfer printing has been shown to be a viable bottom-up fabrication method for the patterning of molecules with up to 50 nm lateral resolution[217, 218]. This technique utilizes an elastomeric stamp inked with a molecule to transfer the species onto a chemically receptive receiver surface in a patterned orientation. Unlike traditional photolithographic techniques, photochemical transfer printing reactions are not always limited by light diffraction because the resolution is primarily determined by the diffusivity of the transferring molecules and the quality of the mechanical stamp-substrate contact[219]. This technique is also naturally compatible with a wide range of materials such as organics[220], inorganics[63, 221], polymerics[222], and biologics[223]. Furthermore, contact printing is inherently more efficient and less expensive than UV-based photolithographic techniques. Another advantage of transfer printing with elastic stamps is the ability to pattern nonplanar surfaces while still maintaining high feature uniformity and resolution[64] – an impossible task for techniques such as photolithography[30, 216] and shadow mask deposition[224, 225].

When paired with a reactive interface, transfer printing can enable the delivery of monomolecular layers with regional p-/n- doping properties onto a semiconductor interface necessary for the development of ultra-shallow doping strategies. Specifically, the immobilization of inorganic atoms such as phosphorus and boron to silicon is an essential component in the fabrication of ultra-shallow doping interfaces for next generation complementary metal–oxide–semiconductor (CMOS) transistors[226, 227]. In order to maintain low series resistance in sub-10 nm CMOS transistors, surface junctions should exhibit abrupt depth profiles and high phosphorus/boron concentrations that help to negate short-channel effects[89, 228, 229]. Such properties cannot be achieved with current ion beam implantation techniques, which either produce broad, low concentration dopant zones or inflict crystallographic damage upon a substrate's surface over a micrometer range[229-231]. Alternatively, plasma doping studies have demonstrated the ability to generate more conformal doping profiles[232], however, surface quality concerns arising from the entrapment of dopant molecules at the oxide interface during implantation have also been reported[233]. STM has been shown to produce atomically precise phosphorus-doped regions on silicon using an STM probe to cleave Si-H bonds and generate strong and chemically inert Si-P bonds in a site-by-site manner[92, 234]. However, this deposition and patterning technique has very low throughput and requires ultra-high vacuum conditions. Consequently, techniques such as transfer printing which facilitate selective surface doping similar to that of STM, but in parallel fashion and at milder conditions[235] are essential to circumvent the inherent throughput, material, and energy intensive constraints of STM-based patterning.

To accomplish selective surface doping via contact printing, the receiver substrate needs to be reactive to the species being delivered via the transfer process. In this study, receiver substrates functionalized with a carbene-based molecule layer were examined on their ability to

immobilize a printed phosphorus-based dopant precursor via stable C-P surface bonding. A carbene is a divalent carbon which can be photogenerated from diazirine or diazo-based compounds. They can be generated from diazirines in either the solution or vapor phase and require a lower activation energy compared to most other organic radical-generating reactions[236-238]. In our previous work we have demonstrated the UV-activated insertion of carbene groups into Si-H surface bonds[179, 235]. However, carbene species can also provide a viable platform for chemically trapping organic and inorganic species at the solid interfaces from the gas or liquid phase via a similar UV-facilitated X-H insertion mechanism. Unlike other phosphorus-containing dopant precursors, which are typically immobilized using Si-O or C-O bonds, carbenes can directly insert into the P-H bond creating strong and direct C-P attachment of phosphorus atoms[239, 240]. For example, diphenylphosphine (DPP) is a disubstituted phosphine derivative that can potentially be trapped by surface immobilized carbene species via the insertion into the P-H bond and formation of the P-C bond. When coupled with the contact transfer printing, this would enable the selective immobilization of phosphorus-containing molecules via a direct C-P surface bonding.

In this study, a simple approach to selectively modify and pattern phosphorus-containing monolayers onto silicon(100) is demonstrated. Contact printing coupled with a carbene-based molecule system was utilized to introduce new surface functionality via conformal contact between functionalized silicon and a DPP inked elastomeric stamp. XPS coupled with SEM and SE were used to characterize the phosphine attachment and patterning ability of this printing technique. This work has demonstrated (1) the direct trapping of phosphorus species by UV-generated surface carbenes immobilized to silicon and (2) the patterning of these species onto silicon with micrometer resolution and high feature uniformity, using contact printing under close-to-ambient conditions.

5.3 Materials and Methods

All reagents and solvents were used as received without further purification. Solvents were purchased from Sigma-Aldrich and filtered through a 0.2 μm filter before use. The light sensitive carbene precursor molecule 2,5-dioxopyrrolidin-1-yl 4-(3-(trifluoromethyl)-3H-diazirin-3-yl) benzoate (NHS-Diazirine) was purchased from American Elements and stored in dark environments. Its application was carried out under yellow light only. P-doped, monocrystalline (100) silicon substrates were purchased from University Wafer, Boston, Massachusetts. XPS spectra were recorded on a Kratos Axis Ultra XPS spectrometer equipped with a Al Kα (1486.6 eV) X-ray source at 200 W power and a pressure of 3.0×10^{-8} mbar. Survey scans were obtained between 0 and 1200 eV with a step size of 1 eV, a dwell time of 200 ms, and a pass energy of 140 eV averaged over 2 scans. Core-level region scans were obtained at the corresponding binding energy ranges with a step size of 0.1 eV, an average dwell time of 260 ms, and a passing energy of 20 eV averaged over 10 scans. ARXPS was used to collect P 2p spectra at varying emission angles in order to detect electrons from different surface depths (i.e. increasing grazing angle limits detection to upper portion of surface). XPS data were processed using CasaXPS software and instrument-specific atomic sensitivity factors. All C 1s peaks were calibrated to 284.7 eV and this same binding energy shift was applied to all other spectra to account for adventitious carbon contamination. SEM images were recorded on a Zeiss Auriga FIB-SEM microscope detecting secondary electrons at ~3.5 mm working distance. All goniometry analysis was gathered using ultra-pure water. Ellipsometry data were collected using a J.A. Woollam M-2000 Ellipsometer and fitted using the Cauchy refractive index model.

5.3.1 Functionalization of Si(100) Substrate with Carbene Precursor

All glassware was washed with Nano-Strip solution (Cyantek) followed by rinsing with water and isopropanol 99.5% before being dried in an oven overnight at 130 °C. A 4 cm^2 Si substrate was soaked in Nano-Strip for 5 min and then immersed in a 7:1 buffered oxide etch solution (hydrofluoric Acid – 12.5%, ammonium fluoride - 87.5%) for 30 s to chemically etch away a contaminated native oxide layer and then re-immersed in Nano-Strip for an additional 15 min at 70 °C to reform a clean oxide layer and to generate surface hydroxyl-groups. The substrate was then rinsed with water and isopropanol and dried under nitrogen gas. The sample was then placed into a glass bottle containing 30 μL of 3-aminopropyltrimetoxy silane 97% (APTMS) purchased from Alfa Aesar and 5 μL of triethylamine 99.5% purchased from Sigma-Aldrich. The bottle was capped and heated to 65 °C and left for 2 h. After silanization, the sample was removed and rinsed thoroughly with dichloromethane and isopropanol, and then dried under nitrogen gas. The amino-terminated surface (NH_2-Si) was subsequently immersed in a 10 mM solution of NHS-diazirine in carbon tetrachloride 99.9% for 2 h under yellow light. Postreaction, the diazirine-terminated surface (Diaz-Si) was rinsed with dichloromethane and isopropanol, and then dried under nitrogen gas. The sample was stored in the dark under nitrogen until subsequent photochemical dopant species attachment.

5.3.2 Light-Induced Generation of Reactive Carbene Species and Subsequent Covalent Attachment of Phosphine Derivative

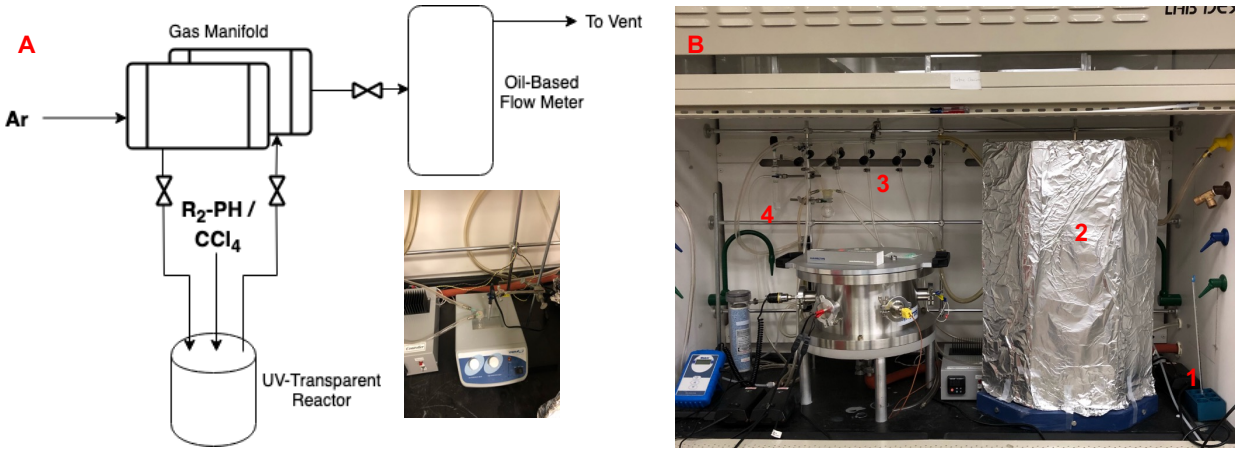

Figure 5.1 (A) Schematic of photochemical reactor setup for attaching DPP to Diaz-Si surface with inset of reactor vial and UV lamp setup. (B) Picture of full setup showing; (1) UV Lamp power supply, (2) UV shield blocking UV lamp and reactor vial, (3) reactor manifold, (4) oil-based flowmeter.

A Diaz-Si sample was placed into a UV-transparent vial and capped with a silicone septum. This vial is the UV transparent reactor shown in **Figure 5.1** along with the rest of the reactor setup. The vial was then purged for 5 min with argon before neat DPP was added dropwise to the surface of the sample via needle syringe. The substrate was then put under a UV-lamp (UVP UVGL-15, 365 nm, 4 watt) for 1 h forming the DPP reacted sample (PPh_2-Si). Following the reaction, the sample was removed from the vial and rinsed with carbon tetrachloride and dried under nitrogen gas.

5.3.3 Fabrication of Micropatterned SiO_2 Mold

NR9-1500PY (Futurrex) was spun on a clean silicon wafer at 3000 rpm for 40 sec. The resulting substrate was baked on a digital hot plate at 155°C for 2 min to produce 180nm of the resist on Si. Photolithography (Karl Suss MA6/BA6) was performed using a photomask (Photo Sciences, Inc.) bearing 8 μm squares with an exposure time of 11.5 sec. After UV exposure, the substrate was baked on a digital hot plate at 105°C for 70 sec, developed in RD6 (Futurrex) for 11

sec and immediately rinsed with water. The dried substrate was baked in an oven at 110 °C for 5 min and descumed in oxygen plasma for 1 min at 100 watts and 6×10^{-1} mbar O_2 pressure (Emitech K-1050X plasma asher). The oxide layer was etched away through the opening in photoresist using reactive ion etching (Trion Technology Phantom II) for 22 min using CF_4 and O_2. Any remaining oxide was removed using buffered oxide etch (BOE). The negative resist was removed with nanostrip (55 °C, 2 min) producing a patterned silicon/SiO_2 master.

5.3.4 Preparation of Reactive Polyurethane Acrylate Stamps

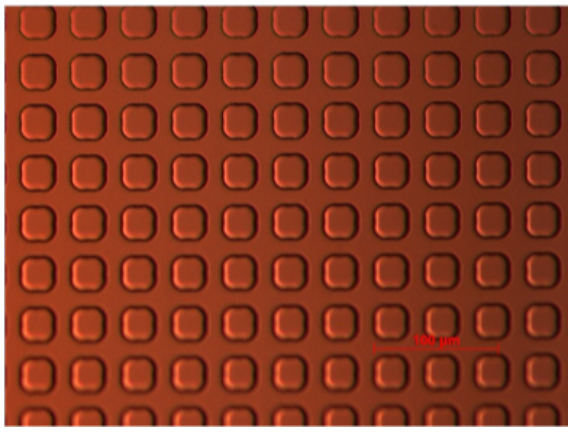

Figure 5.2 Micrograph of patterned PUA stamp surface.

Synthesis of the polyurethane acrylate (PUA) monomers were prepared according to a previously published protocol[45]. Under yellow light, 1 mL of PUA was transferred into a vial and de-gassed at 30 inHg for 2 h. The resin was dispersed onto the patterned portion of the SiO_2 mold and allowed to settle. A UV-transparent cover slide and 2.2 mm glass spacers were applied to control stamp thickness. The mold was exposed to 365 nm UV-light for 2 h. After removing the cover slide, the replication system was again exposed to UV-light overnight. The mold and resin were placed into a UV crosslinker system (SpectrolinkerTM XL-1500, 351 nm 6 x 15 W) for 600 s. After heating the system on a hotplate to 65°C for 10 min, the fully cured stamp was removed

with a sharp-ended tweezer and rinsed with isopropanol and dried under nitrogen. The resulting stamp surface is shown in **Figure 5.2**.

5.3.5 Generation of Micropatterned Phosphine Monolayers on Functionalized Si Substrate via Contact Printing

A PUA stamp patterned with 8 μm squares was inked with a 50 μL droplet of neat DPP and allowed to dry in ambient air for 10 min and then thoroughly dried under nitrogen gas. The stamp was placed on the top of a diazirine-terminated Si substrate at room temperature for 5 min with no external load. The stamp/substrate system was exposed to 351 nm UV-light for 2 min in the UV-crosslinker system. Postreaction, the substrate was carefully removed from the stamp and rinsed with isopropanol and dried under nitrogen gas.

5.4 Results and Discussion

5.4.1 Immobilization and Activation of Carbene for Subsequent Capture of Phosphorus Species

Transfer printing requires a receiver substrate chemically receptive to the species being delivered during the transfer step. In this study we evaluated the use of surface-immobilized carbenes as reactive species that can trap substituted mono-phosphines via direct insertion into P-H bonds. To immobilize unreacted carbene precursors onto Si, hetero-bifunctional molecules that consist of a carbene-precursor species and surface-reactive functional groups are required.

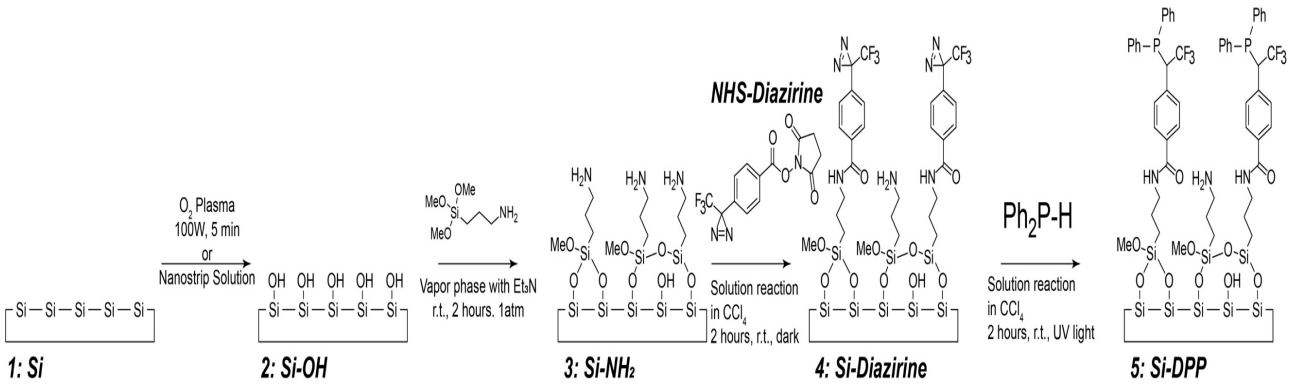

Figure 5.3 Functionalization strategy where; (1-2) generation of hydroxyl groups on the surface of a Si(100) substrate, which is then (2-3) functionalized with an amino-terminated monolayer via silanization, that is subsequently used for (3-4) covalent attachment of carbene precursor (diazirine) molecules via amide bond, allowing for (4-5) UV-initiated generation of immobilized carbene species and subsequent P-dopant capture.

As shown in the reaction scheme in **Figure 5.3**, we theorized that an NHS-diazirine molecule could react with a primary amine species via the *N*-hydroxy-succinimide constituent at one end of the molecule, while the diazirine headgroup can be independently activated under UV-light to generate carbenes. The functionalization strategy employed in this study relied on a bilayered system, consisting of a primary aminosilane layer attached to a secondary diazirine layer via stable amide bonding. Organosilanes have been shown to form homogeneously oriented monolayers on oxidized group IV semiconductors[241] and have good chemical and physical stability. From the diazirine precursor, metastable[242] surface carbenes were generated following exposure to UV-light at 365 nm. The dense primary silane layer increased chemical and physical stability of the substrate interface, while the secondary reactive overlayer provided a functional surface moiety that could directly trap P atoms via stable covalent C-P bonding without any additional linkers. The phenyl rings present in the immobilized DPP species can potentially be dissociated either photochemically or through low temperature annealing[243, 244]. XPS, SE thickness, and contact angle measurements were collected to characterize the incorporation of each functionalization step and are presented in **Figure 5.4** and **Table 5.1**.

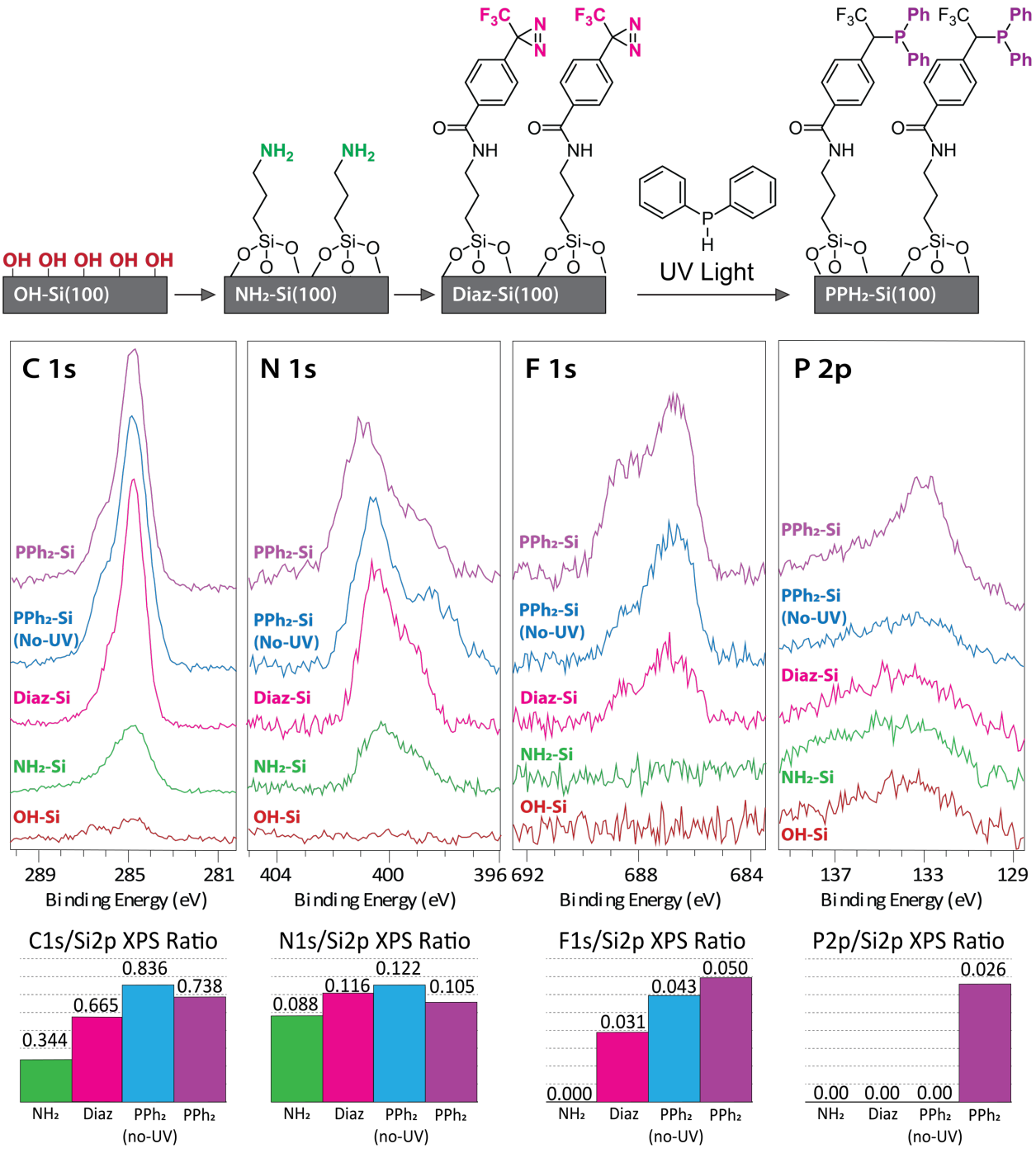

Figure 5.4 (*Top*) Illustration of carbene-based functionalization; (*Middle*) C 1s, N 1s, F 1s and P 2p XPS region spectra measured from the following surfaces: NH_2-Si, Diaz-Si, PPh_2-Si (No-UV), and PPh_2-Si represented by the green, pink, blue, and purple profiles, respectively; (*Bottom*) histograms showing the quantitative XPS characterization of region scans (C 1s, N 1s, F 1s, and Si 2p) for each surface, all normalized by the Si 2p peak intensity.

Table 5.2 Water contact angle and ellipsometry measurements performed on NH_2-Si, Diaz-Si, PPh_2-Si, PPh_2-Si (No-UV) substrates.

Surface	Ellipsometry		Goniometry	
	Layer Thickness (nm)	Theoretical Thickness (nm)	Contact angle (°)	Hysteresis (°)
NH_2-Si	0.98 ± 0.06	0.83	60.0 ± 0.1	17.0 ± 0.1
Diaz-Si	1.34 ± 0.06	1.31	68.0 ± 0.1	25.0 ± 0.1
PPh_2-Si	1.62 ± 0.06	1.37	55.0 ± 0.1	34.0 ± 0.1
PPh_2-Si (No-UV)	1.43 ± 0.06	1.31	64.0 ± 0.1	31.0 ± 0.1

Figure 5.4 shows the C 1s, N 1s, F 1s and P 2p core-level XPS spectra of hydroxyl-terminated silicon (OH-Si) following silanization, carbene activation and dopant attachment steps. A fourth control sample was also included to examine the necessity of UV-exposure for carbene generation and dopant capture. The primary contribution to each of the C 1s spectra was from C-C/C=C bonds centered around 284.7 eV. Following silanization there was a shift towards 286 eV which is indicative of the chemical contributions from C–N bonding arising from the attachment of the amino-terminated silane. Furthermore, in the N 1s spectra there was a broad signal detected at ~400 eV that was not also observed on the reference OH-Si surface, indicative of C-NH_2 bonding. In **Table 5.1**, the relatively small contact angle hysteresis found on the NH_2-Si surface suggests a homogeneous, dense, and well-ordered monolayer. The monolayer thickness measured on this surface also showed good agreement with the calculated theoretical value.

Figure 5.4 indicates that there was a significant increase in both the C 1s and F 1s peak intensities between the NH_2-Si and Diaz-Si surfaces. This was expected due to the addition of C and F atoms to the surface via attachment of NHS-diazirine. Furthermore, the N 1s spectra for the Diaz-Si, PPh_2-Si and PPh_2-Si (No-UV) surfaces all exhibited a shift towards 399.4 eV which is suggestive of amide bonding (N-(C=O)-C)[245]. In the F 1s spectra for the Diaz-Si, PPh_2-Si and PPh_2-Si (No-UV) surfaces, the peak centered around 687 eV indicates the incorporation of -CF_3 species[245] present in the attached diazirine moiety. Notably, the F 1s/N 1s XPS signal ratios indicate

that there were approximately 4 times more N atoms than F atoms on each surface. This is an indication that the surface concentration of the diazirine groups was ~ 10-12 times lower than that of the primary silane layer. This lower degree of coverage is likely attributed to the molecule size and symmetry difference between NHS-Diazirine and silane molecules. Nevertheless, goniometry and ellipsometry analysis in **Table 5.1** both indicate an increase in the hydrophobicity and thickness of the Diaz-Si surface relative to NH_2-Si, which was most likely due to the bulkier headgroups of the attached diazirine moiety. Overall, this evidence suggests covalent amide bond attachment of the carbene precursor into the amino-terminated surface.

The Diaz-Si surface was next reacted with DPP under UV-light to evaluate the degree of DPP attachment onto the bilayer system. The P 2p core-level spectra shown in **Figure 5.4** demonstrates an increase in signal peak intensity on PPh_2-Si that was not observed on the other surfaces. Specifically, there was a component at 133 eV which is indicative of the presence of C–P groups[245]. Furthermore, the only appreciable P 2p/Si 2p ratio was measured from PPh_2-Si following the photochemical deposition of DPP with UV exposure. This suggests the conversion of the diazirine headgroup to a carbene and subsequent reaction with DPP. **Table 5.1** shows that the contact angle of the PPh_2-Si surface also decreased relative to Diaz-Si, possibly due to the more polarizable nature of the immobilized P atoms and phenyl rings. The SE thickness measurement also increased post DPP and UV exposure. These observations are evidence of bonding between the phosphine group and the carbene-activated surface.

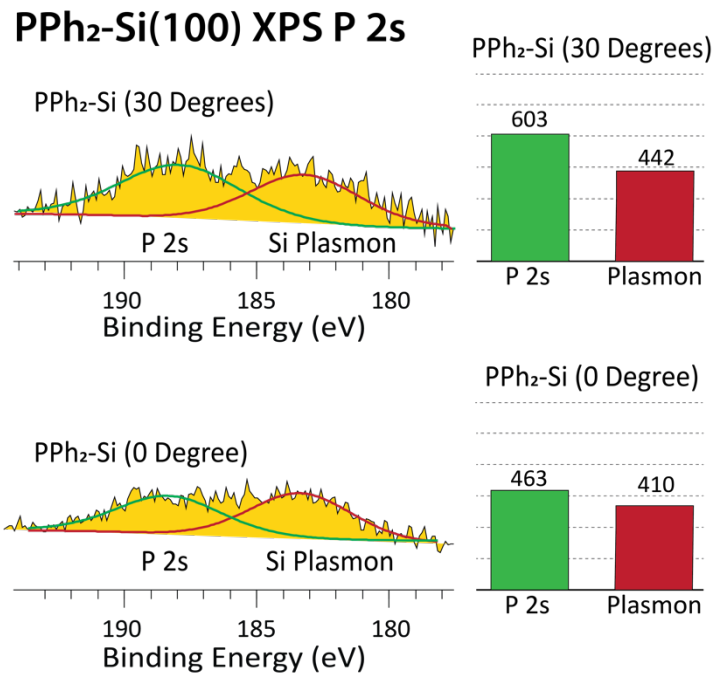

Figure 5.5 (*Left*) XPS P 2s core-level XPS spectra for; (*top*) a PPh_2-Si surface with electron detection carried out at an angle of 30˚, and (*bottom*) a PPh_2-Si surface with electron detection carried out perpendicular from surface. (*Right*) Histograms showing the integrated area (in arbitrary units) of each respective P 2s and Si plasmon peak.

It should also be noted that when analyzing the emission of electrons from only the topmost portion of the PPh_2-Si film (by varying the XPS detection angle), there was an increase in the peak area of the P 2s signal shown in **Figure 5.5**, which indicated that the P atoms were primarily bonded atop the Si interface and not distributed throughout the entire XPS analytical depth. Additionally, the ratio of P 2s to Si plasmon signals increased, showing that as the detection angle became shallower, there were less photo-emitted electrons from the Si bulk and more from the top layer of P atoms.

Finally, a control sample bearing the immobilized carbene precursor was also exposed to DPP in a similar manner but without UV-light exposure during deposition. This was to test the necessity of UV exposure for carbene generation and phosphine surface bonding. **Figure 5.4** demonstrates the negligible P 2p signal detected on this control surface and in **Table 5.1** there was

strong agreement in goniometry and ellipsometry measurements between the control and Diaz-Si samples. This all suggests that UV-radiation was a requirement for P atom surface capture. Overall, the strong agreement between the measured and theoretical thicknesses for each layer shown in **Table 5.1** validates the attachment of each chemical component and is highly suggestive of single monolayers.

Table 5.2 Ratio of XPS signals measured from NH_2-Si, Diaz-Si, PPh_2-Si (No-UV), and PPh_2-Si surfaces used to assess the relative completion of each reaction step.

Surface	N 1s/C 1s	F 1s/N 1s	O 1s/Si 2p	P 2p/N 1s
NH_2-Si	0.257	0.036	0.427	0.000
Diaz-Si	0.175	0.271	0.460	0.000
PPh_2-Si	0.143	0.475	0.503	0.235
PPh_2-Si (No-UV)	0.146	0.348	0.479	0.000

Table 5.2 shows that the N 1s/C 1s XPS ratio decreases after attachment of NHS-diazirine to the previously amine-terminated surface, as the surface concentration of C atoms. The N 1s/C 1s ratio drops post reaction with DPP (with UV-exposure) most likely because of the addition of C species onto the surface (in the form of phenyl ring attachment with respect to PPh_2-Si, in addition to the loss of the N=N groups). This same ratio also drops for the PPh_2-Si (No-UV) control relative to Diaz-Si, but that is probably the result of the additional handling required for DPP immersion. The F 1s/N 1s ratio increases after attachment of NHS-diazirine relative to NH_2-Si due to the addition of the $-CF_3$ headgroup. The largest increase in this ratio is seen on PPh_2-Si due to the addition of $-CF_3$ and subsequent removal of N=N. The rise in O 1s/Si 2p ratio following each step indicates an increasing addition of oxygenated species on each surface. This in turn most likely had a dampening effect on each rate of reaction and resulted in lower molecule coverage. Lastly, the P 2p/N 1s ratios show that P 2p signal was only detected from the PPh_2-Si surface.

It should be noted that the functionalization strategy presented here will most likely require further refinement before implementation in ultra-shallow doping applications due to limitations of the carbene sub-layers. As such, our approach employs a dense sub-layer of organic molecules attached to an oxidized silicon. Although similar systems were used in the past for ultra-shallow doping[246], (1) the underlying oxide interface may limit diffusion of P atoms to Si; and (2) C-P and Si-P defects may form (e.g. large diffusion coefficient of C in Si), and induce electrical deactivation of Si[247]. For example, O'Connell et. al. demonstrated that when annealing a P modified self-assembled monolayer into Si (~100:1 C:P atomic ratio) up to 20% of the P-dopant species were deactivated due to C contamination[248]. Although the molecule system that was used in this study was much smaller (~24:1 C:P), further reduction in concentration of C atoms (or F atoms) at the Si interface may be achieved by exploring alternative diazirine or diazo-based compounds with shorter organic linkers.

5.4.2. Photoreactive Microcontact Printing of P-dopant onto Functionalized Si(100)

Microcontact printing is a parallel and scalable technique[249] for the patterning of small molecules onto inorganic substrates that avoids light diffraction limitations of i-line and UV photolithographic techniques. Its resolution is primarily limited by the lateral diffusivity of the printed molecules and the mechanical deformations of the elastomeric stamps. Here, the previously validated carbene-based functionalization scheme was integrated into a microcontact printing method in order to orthogonally pattern DPP molecules onto the reactive Si(100) interface. To facilitate this, the reactive layer on the substrate must be sufficiently stable to enable efficient coupling of DPP to the activated carbene species. As such, the functionalization approach in this study exploited the stability and order imposed by both the organosilane and carbene precursor compounds to form homogeneously oriented monolayers which could withstand both stamp

contact and removal during attachment of DPP. For a stamping material, PUA was selected due to its good moldability, low roughness, and surface energy compatibility with the polarity of the DPP molecle[250]. This was important as the DPP ink needed to be completely wet and be uniformly distributed over the polymer surface to facilitate defect-free complete transfer. Additionally, PUA as a UV-transparent material would enable the activation of the DPP-trapping mechanism of the underlying carbene-terminated substrate. Gas-phase carbene generation and subsequent X-H bond insertion have fast kinetics[251-253], which can help facilitate a high rate of pattern transfer in actual applications.

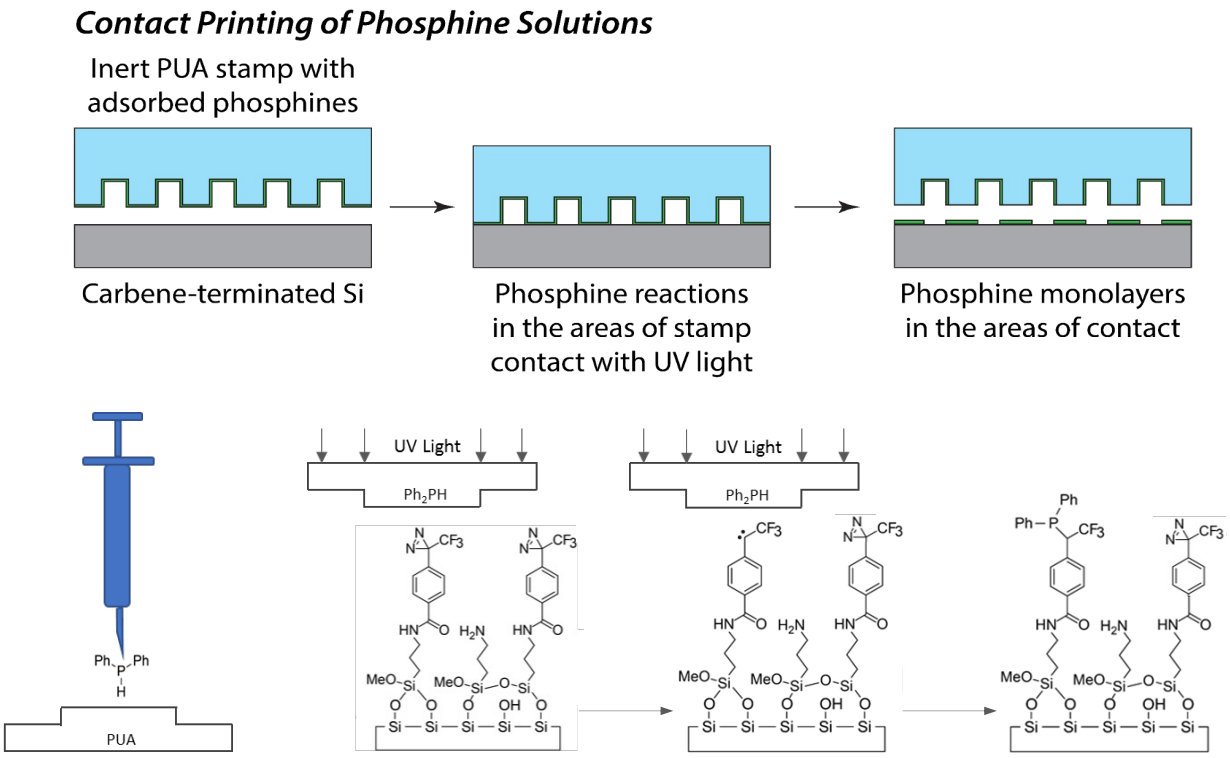

Figure 5.6 (*Top*) Schematic of contact printing method for delivering DPP onto Diaz-Si in a localized manner. (*Bottom*) Surface chemistry strategy for facilitating the printing of DPP.

The PUA stamp was prepared bearing 8 μm squares to enable site-specific immobilization of the phosphines on the receiver surface. As shown in **Figure 5.6**, the stamp was inked with DPP and then placed in conformal contact with a Diaz-Si surface prior to UV-light exposure. After placing

the stamp atop the Diaz-Si substrate no further force was applied to the stamp/substrate system to avoid the potential for force-induced diffusion and smearing of the DPP molecules. SEM and XPS characterization of the resulting surface post photoreactive contact printing is shown in **Figure 5.7**.

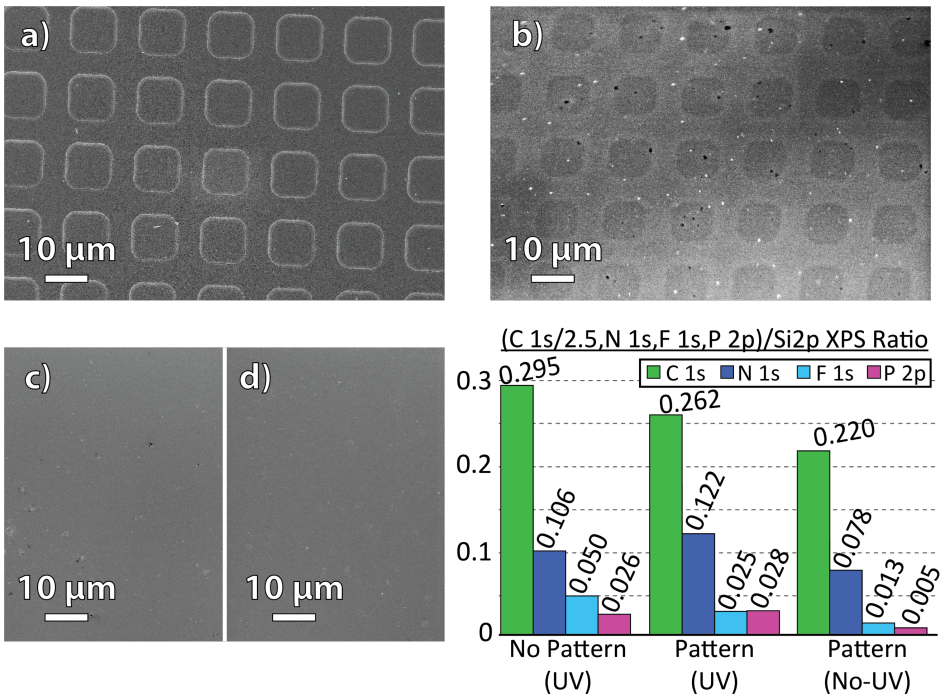

Figure 5.7 SEM images of; (a) PUA stamp mold bearing 8 µm squares and (b) the corresponding P-doped Si(100) surface post-printing. SEM image (c) of Diaz-Si surface post-printing with DPP-inked stamp and no UV-exposure, SEM image (d) of Diaz-Si surface post-printing with an inkless stamp and UV-exposure. (Bottom right) histogram showing XPS ratios of the C 1s, N 1s, F 1s, and P 2p over Si 2p electron signals (corrected by the atomic sensitivity factors) on PPh_2-Si, stamped PPh_2-Si, and stamped PPh_2-Si (No-UV) substrates.

The dimensions and orientation of the resulting surface features shown in **Figure 5.7** displayed good agreement with the stamp pattern, indicating effective transfer. To examine whether the change in contrast observed between the 8 µm squares and the background substrate was the result of P coupling or due to the transfer of PUA material to the Diaz-Si surface, a control sample (following the same functionalization and stamping protocol) was made using an inkless stamp under UV-exposure. The resulting SEM in **Figure 5.7** showed minimal surface change. The

source of this small change was most likely the result of transfer of debris from a dirty portion of the stamp to the substrate, as shown in **Figure A5.1**. Overall, the change in contrast observed between the 8 μm squares and the background substrate is attributed to the higher emission of secondary electrons from the heavier P atoms[196]. Another image of the successfully patterned PPh_2-Si surface at lower magnification is also shown **Figure A5.1**. Lastly, another control sample with the same functionalization and stamping protocol was performed but without the presence of UV-light. SEM imaging shown in **Figure 5.7** revealed no apparent pattern transfer, further evidence of stamping selectivity in this photoreactive contact printing process.

This approach to patterning small molecule films was demonstrated at the micrometer resolution. We believe that by adjusting the ink system and the mechanism of the contact printing activation it will be possible to further increase the resolution to sub-100 nm dimensions. For example, in the past we and others have demonstrated diffusion-less, sub-50 nm resolution microcontact printing with PUA stamps[67, 250, 254, 255].

The quantitative XPS results in **Figure 5.7** demonstrate that both the homogeneous PPh_2-Si surface and the stamped PPh_2-Si surface closely resembled each other chemically, with similar P 2p signals. There was less than a 25% difference in C 1s, N 1s, and P 2p XPS signal ratios between these two surfaces, which suggests that the microcontact printing technique effectively transferred the DPP molecule without degrading the underlying substrate. It also demonstrates that UV-radiation was able to activate the surface carbene groups through the PUA stamp. This was key as it was also shown in **Figure 5.7** that the microcontact printing technique without UV-light exposure resulted in a near-zero P 2p signal, despite exhibiting C 1s, N 1s, and F 1s ratios indicative of previous functionalization with the diazirine precursor. The slight reduction in organic signal on this control sample was likely due to partial hydrolysis of the silane-diazirine linker. It should

also be noted that the P 2p signal from the stamped PPh_2-Si surface was measured from a 400 x 400 μm portion of the surface which included both DPP-functionalized and unmodified regions (i.e. stamped and unstamped) of the surface, and yet still resulted in approximately the same P surface concentration as the homogenous PPh_2-Si surface. Therefore, if corrected for the pattern density of the DPP-modified features (25% of the total analytical area), the overall P 2p signal could be about four times higher in the DPP regions generated via printing. Similar results have been observed in other studies where reactive contact printing has demonstrated higher reaction yield than that of non-contact solution phase chemistry[239]. Lastly, collecting spatially resolved XPS imaging for either P 2p or P 2s electrons would be helpful to further demonstrate the transfer of P atoms exclusively onto the stamped interfaces, however, due to direct overlap of both these signals with strong Si plasmons, it is challenging.

5.5 Conclusion

Semiconductor device manufacturers are facing challenges associated with continuous downsizing of critical dimensions of device components and will continue to do so according to Moore's law[254]. Thus, researchers are now searching for novel and efficient processes for the functionalization and patterning of silicon with active molecule or atomic components such as inorganic-based monomolecular dopant layers. In this study, we have demonstrated an effective method for the micropatterning of P-containing monolayer dopant precursors onto Si(100). This protocol relied upon a bilayer molecule system consisting of a dense amino-silane sublayer and a photoreactive NHS-diazirine overlayer, which is then activated via UV-exposure to chemically trap a phosphine-based molecule. This molecule system was subsequently patterned utilizing photoreactive contact printing of DPP under UV-light exposure and without mechanical force. The resulting surface patterns matched the stamp's surface, displaying the high feature uniformity of

the printing technique. Ultimately, scalable approaches to patterning and doping small molecule systems, such as the micro contact printing technique implemented in this study, can potentially facilitate a higher-resolution and less-energy intensive alternative to traditional top-down micromachining techniques for the continued refinement of templating, ultra-shallow doping, and resist based deposition processes.

Chapter 6 Conclusion and Future Outlook

6.1 Conclusion

Each project presented here pertained to the deposition and patterning of small molecule and atomic (or near atomic) layers on silicon. First, I investigated different chemistries that would allow us to deposit such layers onto a silicon substrate. Once attached, I then studied how these layers were able to inhibit surface film deposition, such that they could be integrated into a complementary resist system for area selective deposition. In chapter 2, a baseline was established for Al_2O_3 thin film growth on OH-Si(100) and H-Si(100) surfaces using our ALD reactor. Next, the functionalization of H-Si(100) with NHS-diazirine and subsequent PFA attachment was validated using XPS. Both NHS-Si(100) and PFA-Si(100) were then evaluated against H-Si(100) as possible NGS for Al_2O_3 ALD. XPS results demonstrated that H-Si(100) exhibited greater ALD blocking than both SMI-functionalized surfaces. In addition to inferior blocking, the PFA molecule was also deposited in the solution phase rendering its use and reapplication in vacuum-based deposition processes such as AS-ALD highly problematic. Thus, it was important to find ALD resists which (1) demonstrate superior or comparable blocking to H-Si(100), (2) can be deposited onto a substrate in the vapor phase, and (3) are small-enough in length to prevent EPE on the sub-10nm level. In chapter 3, XPS, SE, and contact angle goniometry measurements were used to demonstrate the covalent bonding of halogenated monolayers to a H-Si(100) surface prepared via a dry reaction process. NCS, NBS, and NIS were all found to be effective halogenating agents of H-Si(100). However, chlorination resulted in the highest halogen surface coverage by a significant margin followed by bromination and then iodination. This approach exhibited an exclusive bonding of halogen atoms to silicon while maintaining a low rate of oxidation of the underlying silicon interface, especially in the case of

chlorination and bromination. Stability tests in air were then undertaken to determine how long each surface could resist degradation and oxidation relative H-Si(100), a standard NGS material. Over the course of 24 hours, Cl(H)-Si(100) demonstrated the strongest resistance to both halogen deterioration and SiO_2 growth followed by Br(H)-Si(100) and then I(H)-Si(100). These halogenated surfaces then underwent traditional ALD in order to examine the newly formed surface's blocking ability against a metal oxide precursor. Consequently, SE and AFM data demonstrated the improved shielding ability of the halogenated monolayers relative to H-Si(100) and OH-Si(100). Once again Cl(H)-Si(100) demonstrated the most effective blocking ability against the ALD chemistry followed by bromination and then iodination. However, the reduced reactivity that each halogenated surface showed with the ALD chemistry demonstrates that they are each suitable candidates for effective ALD resists and when paired with an ALD growth material such as OH-Si(100) can participate in chemo-selective processing schemes such as AS-ALD.

Next, I looked at different methods for patterning these small molecule and atomic resists. In chapter 4, a method was presented for patterning of atomic and molecule resists using nanosecond pulsed laser radiation. Specifically, Nd:YAG pulsed laser radiation was employed to increase the rate of oxidation on hydrogen-terminated Si(100) under low vacuum and room temperature conditions. An interval of average laser beam energy density was established in which the rate of surface oxidation on H-Si(100) is enhanced, whereas a corresponding OH-Si(100) surface saw minimal oxide growth. Furthermore, XPS demonstrated that the degree of surface oxide content on H-Si(100) increased with energy density and correlated with the formation of small spots (matching the profile of the laser beam) observed with SEM. This imaging was paired with laser fluence mapping to demonstrate the local nature of the oxidizing effect. AFM analysis

was used to verify that these small spot patterns were primarily due to chemical transformation and not physical alteration below the LIDT. From these results it was concluded that pulsed laser exposures of a monoatomic hydrogen-resist layer on Si(100) can promote chemical oxidation of the resist without causing morphology damage to the underlying surface. Such an oxidative patterning technique has the potential to enable universal, *in-situ* patterning of various substrate/resist combinations for ASD manufacturing platforms. In chapter 5, I demonstrated an effective method for the micropatterning of P-containing monolayer dopant precursors onto Si(100). This protocol relied upon a bilayer molecule system consisting of a dense amino-silane sublayer and a photoreactive NHS-diazirine overlayer, which is then activated via UV-exposure to chemically trap a phosphine-based molecule. This molecule system was subsequently patterned utilizing photoreactive contact printing of DPP under UV-light exposure and without mechanical force. The resulting surface patterns matched the stamp's surface, displaying the high feature uniformity of the printing technique. Ultimately, scalable approaches to patterning and doping small molecule systems, such as the micro contact printing technique implemented in this study, can potentially facilitate a higher-resolution and less-energy intensive alternative to traditional top-down micromachining techniques for the continued refinement of templating, ultra-shallow doping, and resist based deposition processes.

6.2 Future Outlook

The main thrusts of the work were to (1) develop nanosecond pulsed laser-promoted patterning of H-Si(100), (2) functionalize Si(100) with effective ALD resists, and (3) evaluate the blocking ability of these resists. The long-term goal would be the integration of these three components into a unified AS-ALD scheme. Below are more near-term projects that would logically follow from the work presented in this document.

6.2.1 Laser Assisted Oxidation of Small Molecule Layers

I theorize that there may be an opportunity to use the same laser exposure method to "pattern" other molecule and atomic layers. The first candidates should be the surface layers halogenated with the N-hal-succinimide molecules. For example, the ability to directly oxidize a Cl-Si(100) monoatomic resist layer would theoretically generate a nonhomogeneous surface of Si-Cl_xO_y/Si-Cl regions. The ALD chemistry would selectively react with Si-Cl_xO_y while the surrounding Si-Cl surface would benefit from the excellent shielding ability of Si-Cl. Thus, this new potential strategy may result in a higher degree of AS-ALD selectivity.

6.2.2 Evaluation of Halogen and Carbene Resists Towards Differing Metal Oxide ALD Chemistries

I am interested in evaluating the PFA-Si(1000) and Hal-Si(100) surfaces against other common ALD metal oxides, namely, hafnium oxide (HfO_2) and titanium oxide (TiO_2). The precursors involved in each of these processes possess different reactivities and kinetics. It will be important to determine which resists pair most effectively with which ALD metal.

On another note, exposure of the halogenated surfaces to air during transfer to the ALD was a major concern that I faced in these studies. Post-reaction, the vacuum jar in which the halogen reaction was carried out was sealed, disconnected from the pump, and transferred to the ALD for rinsing and immediate entry into the chamber which was then put under vacuum. In total, the halogenated surfaces experienced no more than 1 min of air exposure during this transfer. However, the ability to carry out the halogenation reaction in the ALD chamber as a "pre-step" would be very advantageous to avoid any surface oxidation/deterioration pre-ALD. It will also be necessary for any redosing/regeneration step in a fully realized AS-ALD process in which we hope to further pursue. Access to a Rotor ALD which can transfer a sample from one vacuum chamber

(for halogenation) to another (for ALD growth) would be ideal for building a AS-ALD process using dry halogenation. Certain line of sight evaporation techniques could also be tested in the future to enable this dry halogenation within an ALD chamber.

6.2.3 Mechanistic Study of Laser Assisted Oxidation (LAO) of Silicon

There is a need to further elucidate the surface mechanism behind laser patterning of H-Si(100). Namely, I would like to answer the following questions: (1) is this process primarily influenced by the laser exposure or the surface chemistry, (2) is the laser interaction with the Si(100) interface a linear or non-linear process, and (3) is this process driven by laser power or pulse length? We can learn more by conducting various experiments. The first question can be addressed by controlling the amount of ambient water vapor around the substrate (i.e conducting laser exposure at ambient pressure rather than 10 mtorr) or introducing a limited flowrate of O_2, into the H-Si(100) sample holder during the laser exposure. This will determine whether the amount of SiO_2 growth, and the resulting selectivity between the irradiated and non-irradiated sites, scales more with O_2 concentration or laser energy. The second experiment would focus on varying the number of laser pulses (1-10-100) and investigating how that effects oxide growth. This should indicate whether the laser pulse is emitting more electrons or ions from the surface. If there is not a significant increase in SiO_2 or O XPS signal from 1 to 100 pulses, then it is possible that reactivity is being driven by an optical phenomenon such as two-photon absorption where laser photons are absorbed by either the Si or H atoms, consequently bringing them to an excited electronic state. This would be an example of a nonlinear absorption process, since increasing the number exposures does not correlate with an increase probability of a process like two-photon absorption. Alternatively, if the amount of surface oxidation increases with the number of exposure pulses, then that would suggest that we are gradually breaking surface bonds through a

predominantly thermal effect. This is an example of a linear process since the probability of bond activation/dissociation would increase with pulse number. Both explanations will most likely include the ionization of O_2 which has a low ionization energy and theoretically acts as an ideal oxidant. In the past, I have varied the number of pulses (1 vs 10 pulses) during exposure of a H-Si(100) surface. No discernable increase in oxide formation was observed, however, 10 pulses at 5 Hz is probably too short a time to test any prolonged effect. Lastly, determining if laser wavelength is the primary contributing factor should be investigated by comparing the degree of oxide formation generated by a 355 nm-5 ns laser to that generated by a 532 nm-5 ns laser. With longer wavelength exposure, the same amount of surface temperature change can be attained at similar fluences to that of 355 nm, but with a much longer absorption depth and therefore lower carrier densities. This would represent strong evidence of either thermal or photoelectronic modification. Alternatively, shorter wavelength lasers will allow for a greater degree of edge resolution optimization while maintaining less absorption depth in silicon, while shorter pulse length will enhance photon absorption and/or electron emission of Si(100).

Appendix

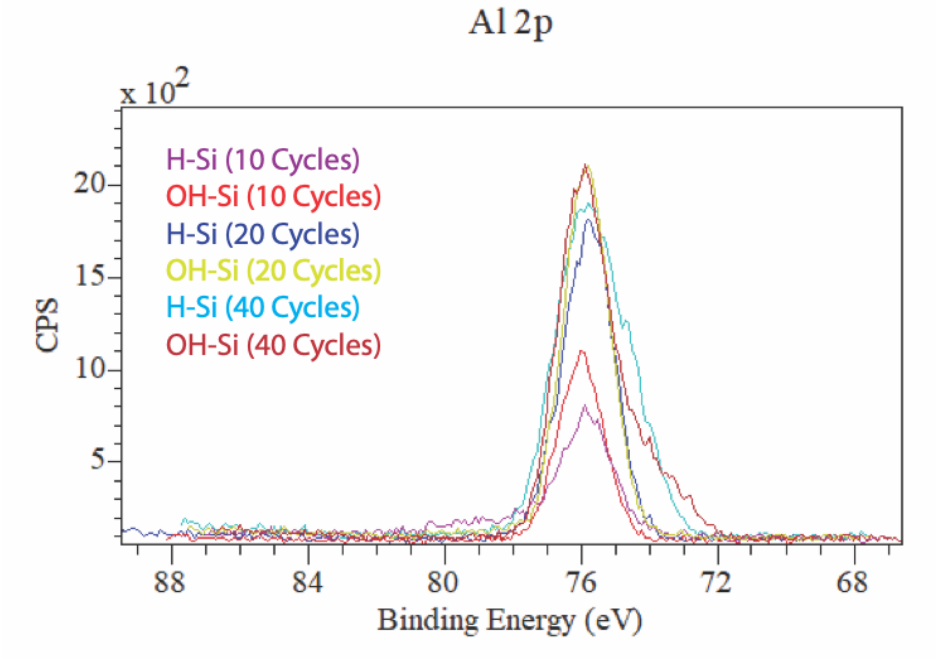

Surface-Cycles	Al / Si
OH-10	0.43
H-10	0.36
OH-20	1.66
H-20	1.33
OH-40	4.68
H-40	5.16

Figure A2.1 Al 2p XPS spectra and table of corresponding signals normalized to Si 2p for OH-Si(100) and H-Si(100) surfaces post Al_2O_3 ALD for 10, 20, and 40 cycles.

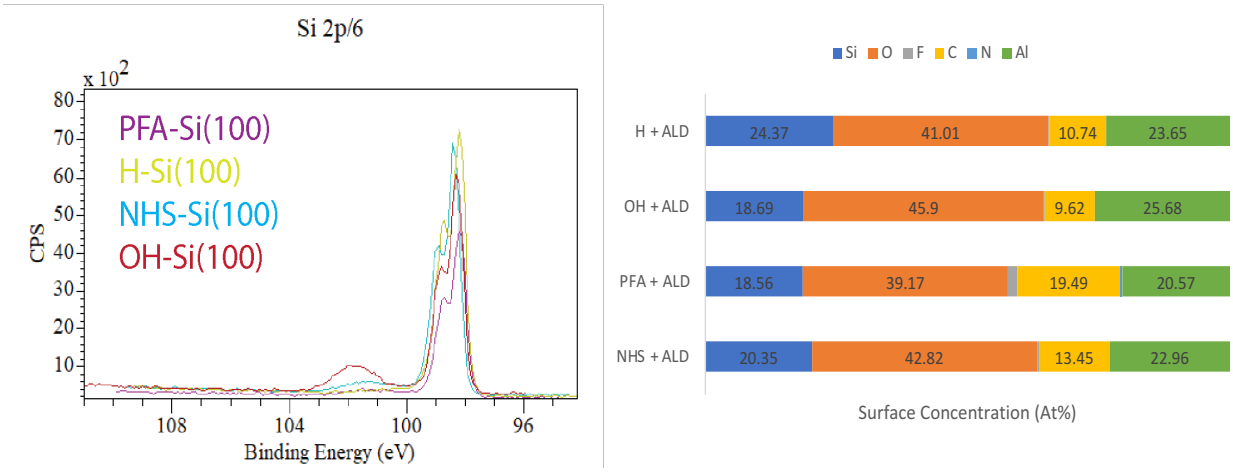

Figure A2.2 (*Left*) Si 2p XPS and (*Right*) histograms showing surface concentration breakdown of elements found on OH-Si(100), H-Si(100), NHS-Si(100), PFA-Si(100) surfaces following 20 cycles of Al_2O_3 ALD.

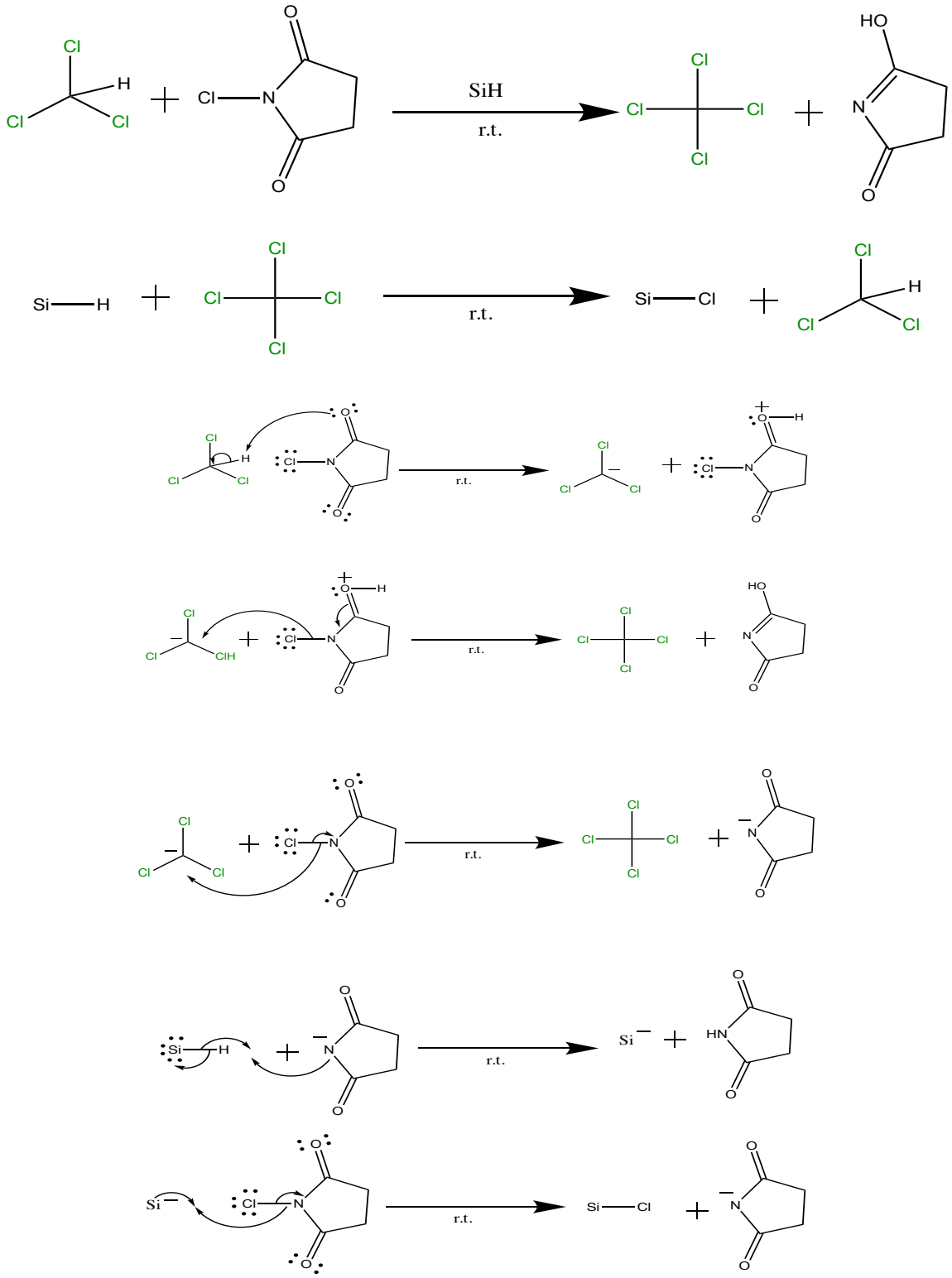

Figure A3.1 Solution phase iodination of H-Si using $CHCl_3$ solvent.

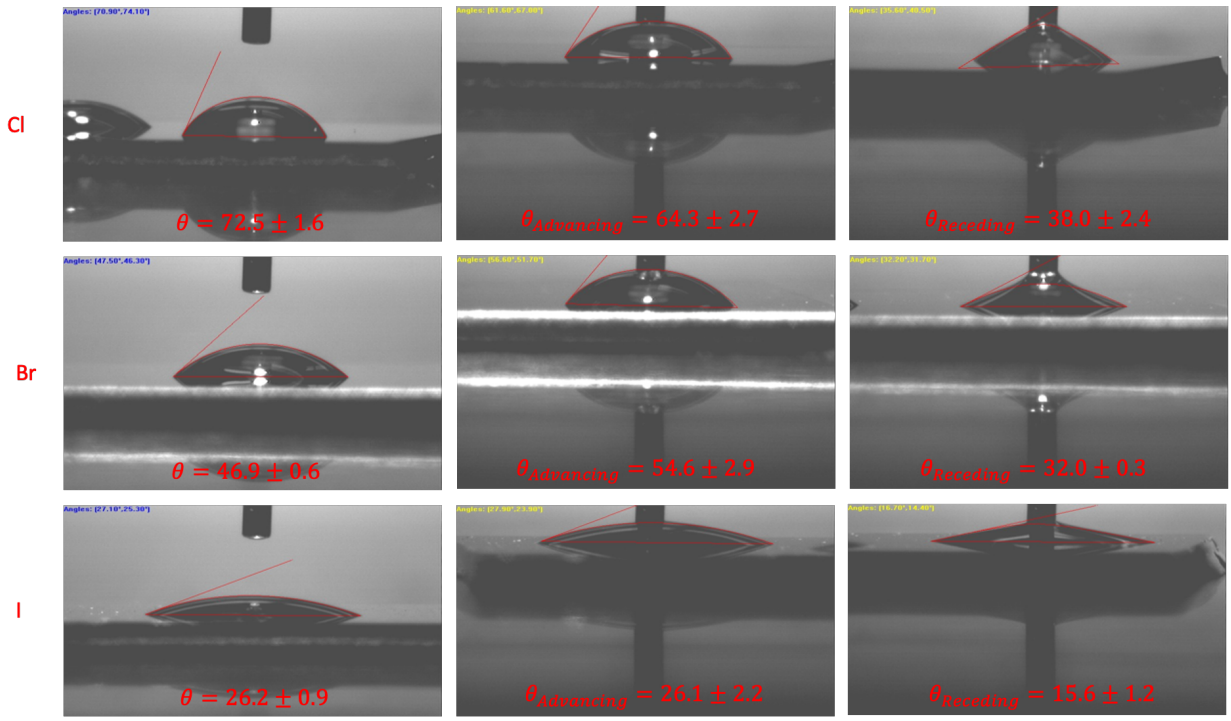

Figure A3.2 Static, advancing, and receding contact angle images for each halogenated surface.

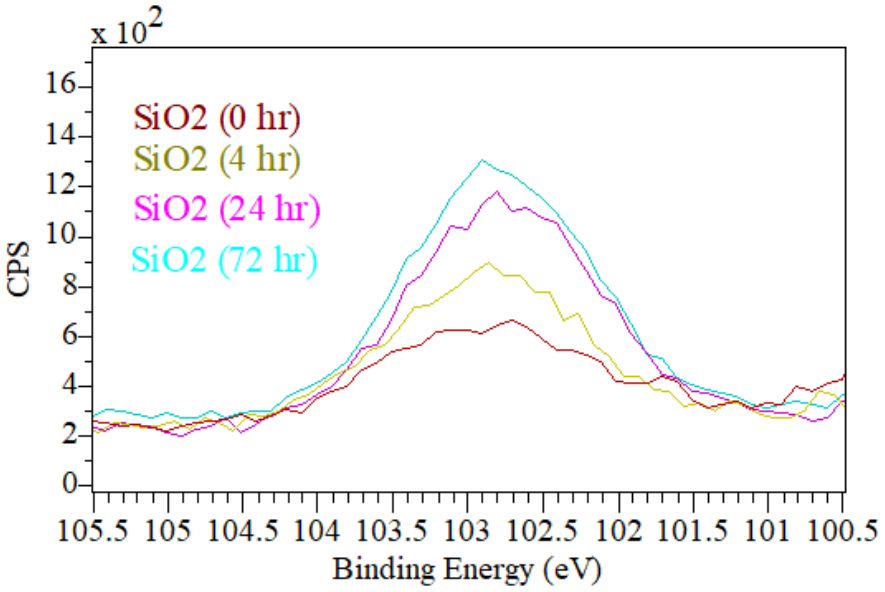

Figure A3.3 Growth of Si_xO_y2p XPS signal due to passive oxidation as H-Si(100) is left under air exposure.

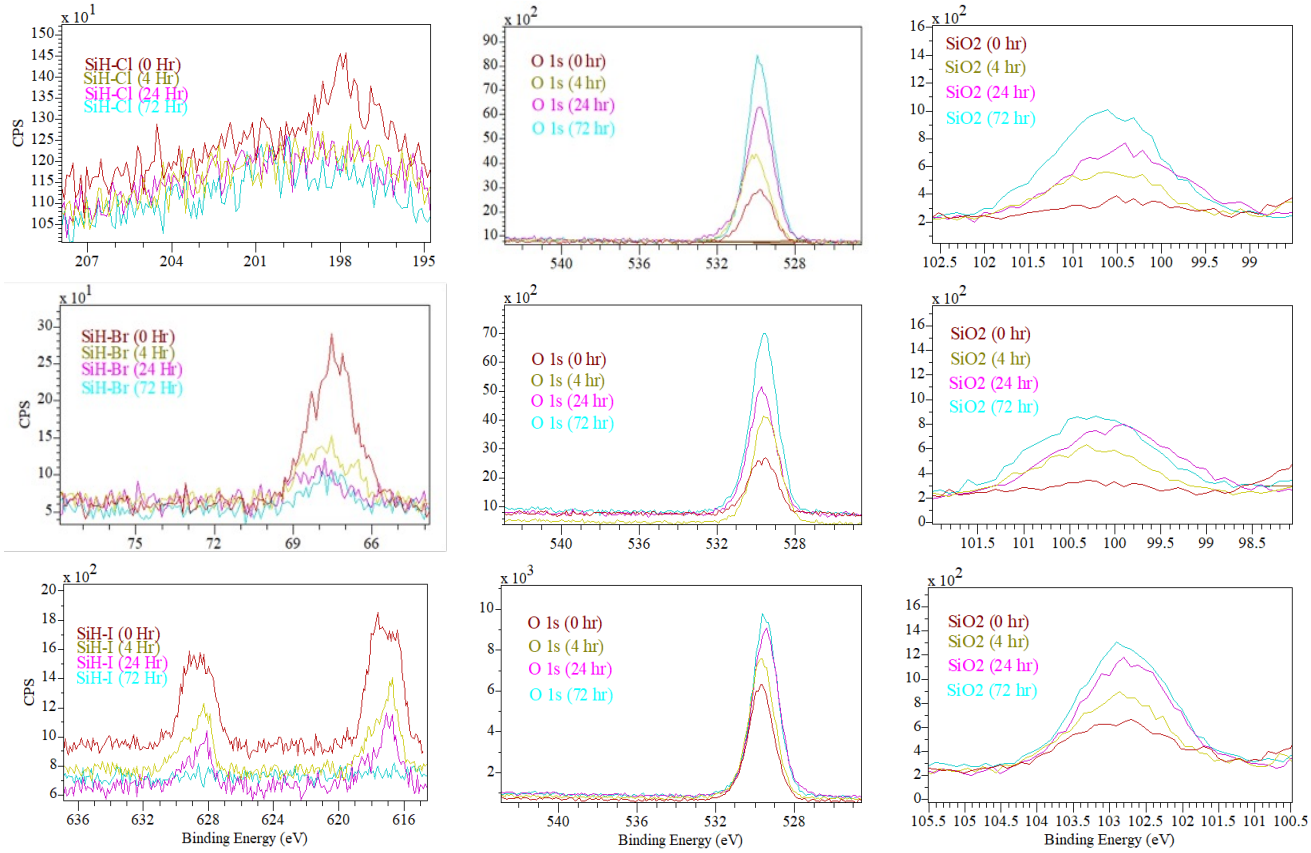

Figure A3.4. XPS spectra showing changes in Hal(H)-Si(100)composition over a 72 hour period. Region scans for each respective halogen (Cl 2p, Br 3d, I 3d) are depicted in the left column. The O 1s spectra and SiO2 signal from the Si 2p spectra for each sample set are depicted in the middle and right columns, respectively. Scans of halogenated substrates after 0 hr, 4 hr, 24 hr, and 72 hr of air exposure are represented by maroon, olive, pink, and turquois lines, respectively.

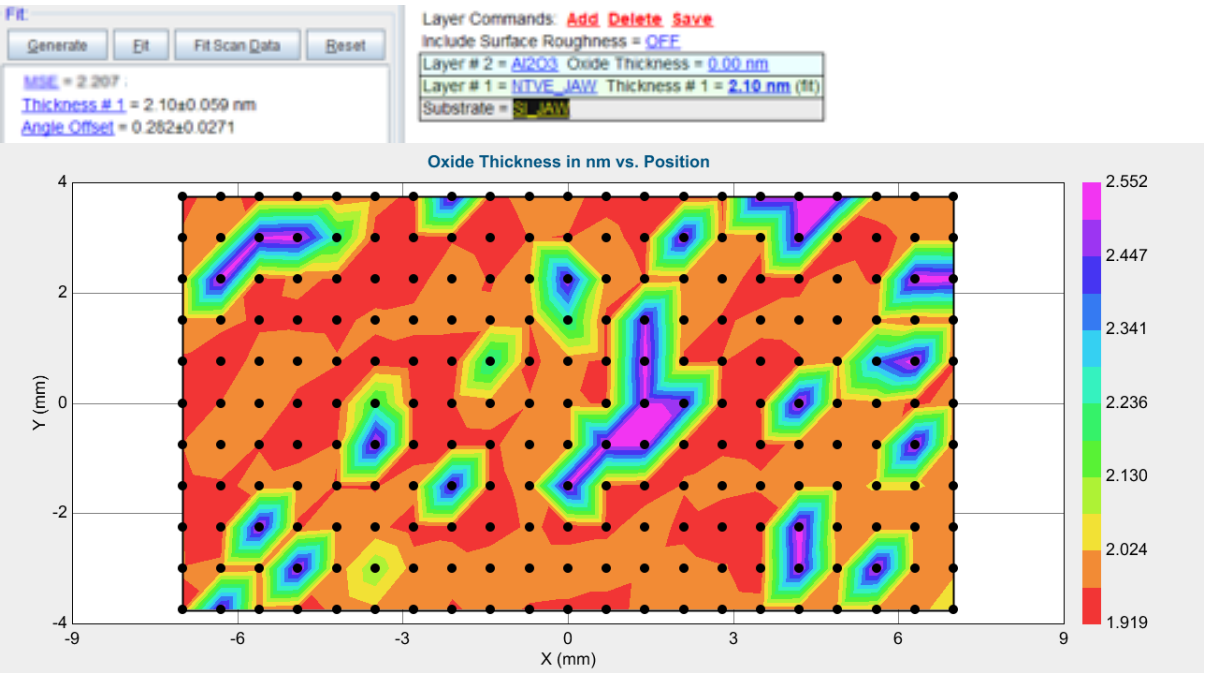

Figure A3.5 Spectroscopic ellipsometry measurement of a reference OH-Si(100) sample following rinsing. The average thickness across a 8 x 14 mm surface was determined to be 2.10 ± 0.059 nm.

Figure A4.1 Code converting spatial intensity pixel profile into a fluence map.

```
% script will generate at fluence map based on the energy profile that is
imported into the script
pixel_width = 4.4; %um
energy_profile = load('0.75 Avg.ascii.csv');
fluence_profile = (energy_profile)./(pixel_width*10^-4)^2;
Avg_fluence = mean(fluence_profile,"all")
figure(1)
subplot(1,2,1)
imagesc(energy_profile)
title('Energy profile in J')
colorbar
subplot(1,2,2)
imagesc(fluence_profile)
title('Fluence profile in J/cm2')
colorbar
```

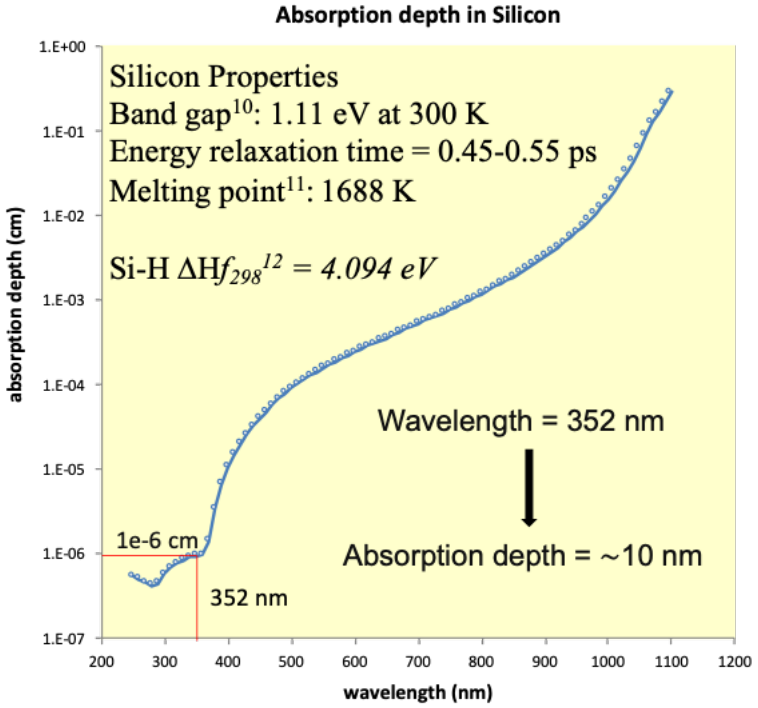

Figure A4.2 Penetration depth of light in silicon versus wavelength[9] with inset of silicon material properties.

9). Data given in: Green, M.A. and Keevers, M. "Optical properties of intrinsic silicon at 300 K ", Progress in Photovoltaics, p.189-92, vol.3, no.3; (1995)

10). Data from Kittel, C., Introduction to Solid State Physics, 6th Ed., New York:John Wiley, 1986, p. 185

11).https://www1.columbia.edu/sec/itc/ee/test2/pdf%20files/silicon%20basics.pdf

12). https://labs.chem.ucsb.edu/zakarian/armen/11---bonddissociationenergy.pdf

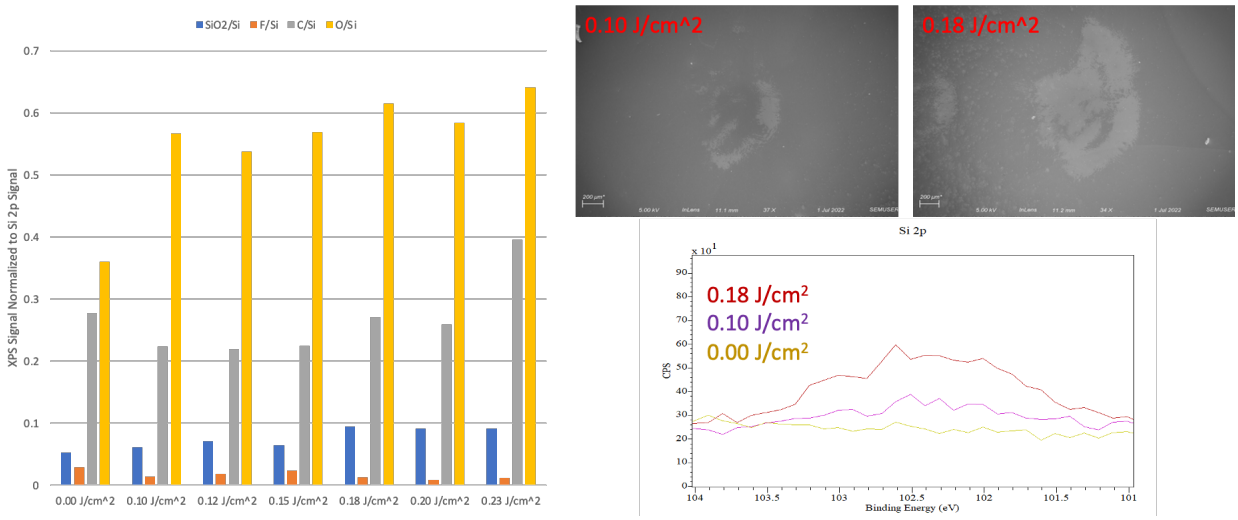

Figure A4.3 (*Left*) Histogram of quantitative XPS results for laser exposed H-Si(100) surface. (*Right*) (Top) SEM images of laser exposure sites, and (Bottom) SixOy2p XPS spectra for different exposure sites.

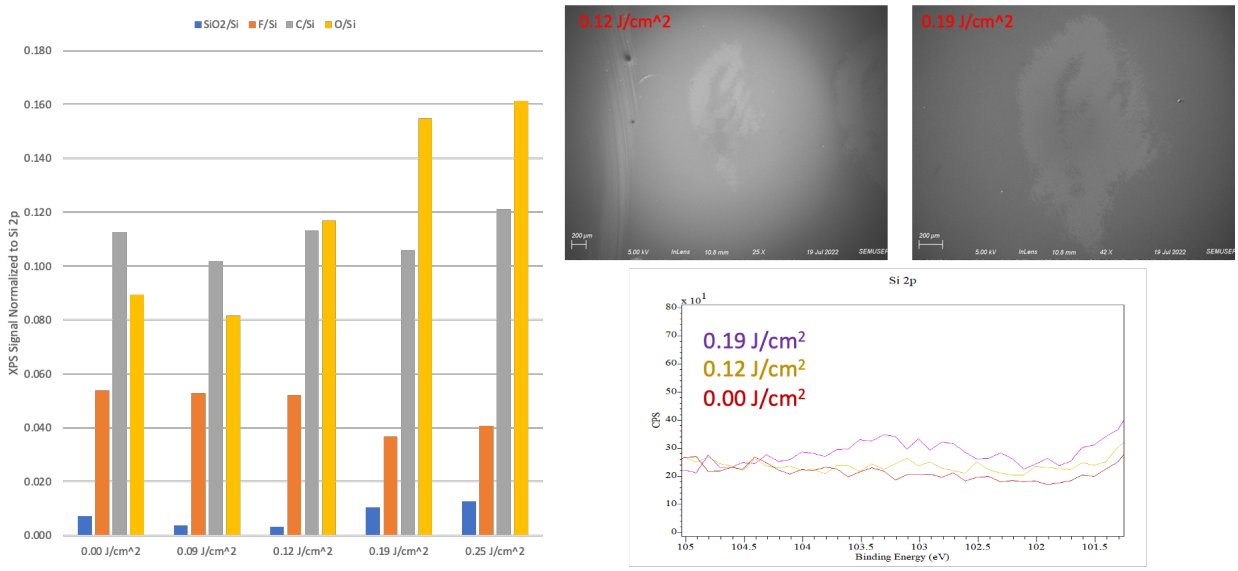

Figure A4.4 (*Left*) Histogram of quantitative XPS results for laser exposed H-Si(100) surface. (*Right*) (Top) SEM images of laser exposure sites, and (Bottom) SixOy2p XPS spectra for different exposure sites.

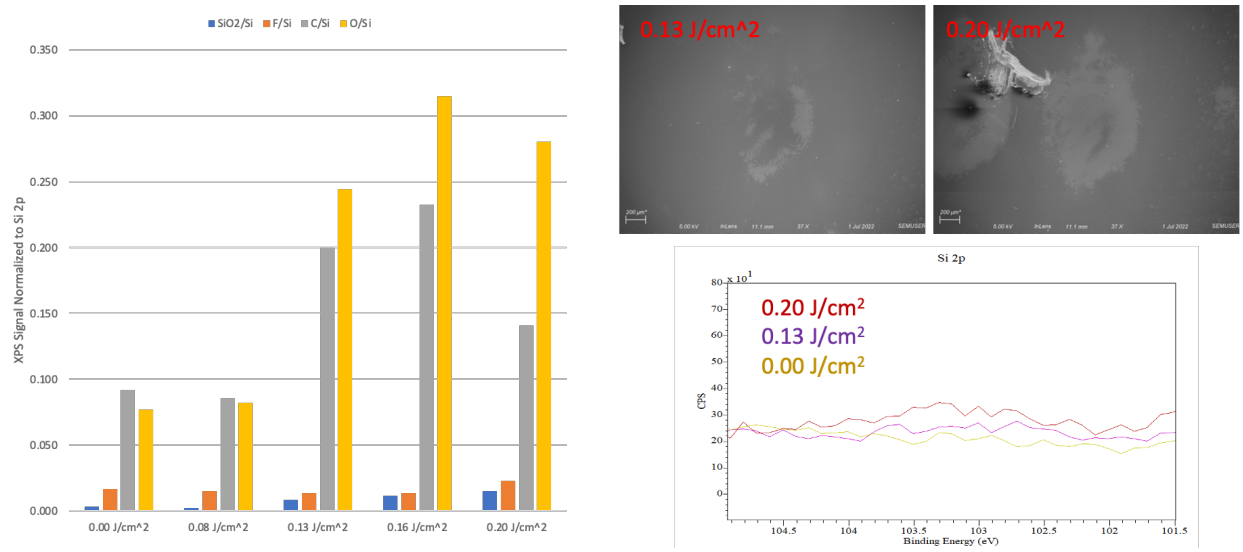

Figure A4.5 (*Left*) Histogram of quantitative XPS results for laser exposed H-Si(100) surface. (*Right*) (Top) SEM images of laser exposure sites, and (Bottom) SixOy2p XPS spectra for different exposure sites.

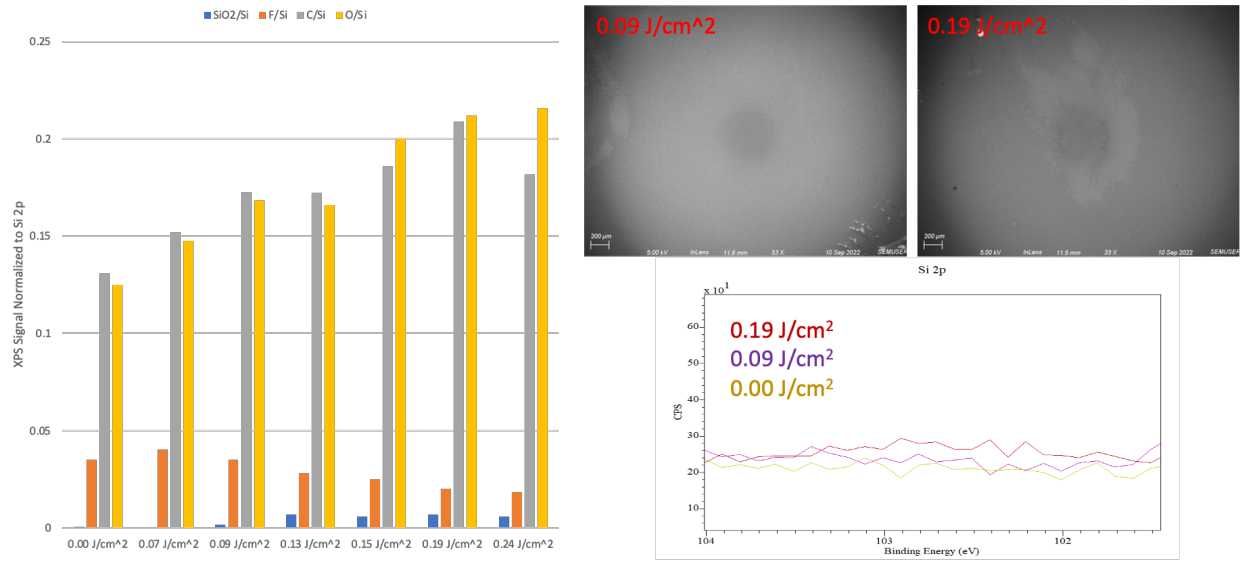

Figure A4.6 (*Left*) Histogram of quantitative XPS results for laser exposed H-Si(100) surface. (*Right*) (Top) SEM images of laser exposure sites, and (Bottom) SixOy2p XPS spectra for different exposure sites.

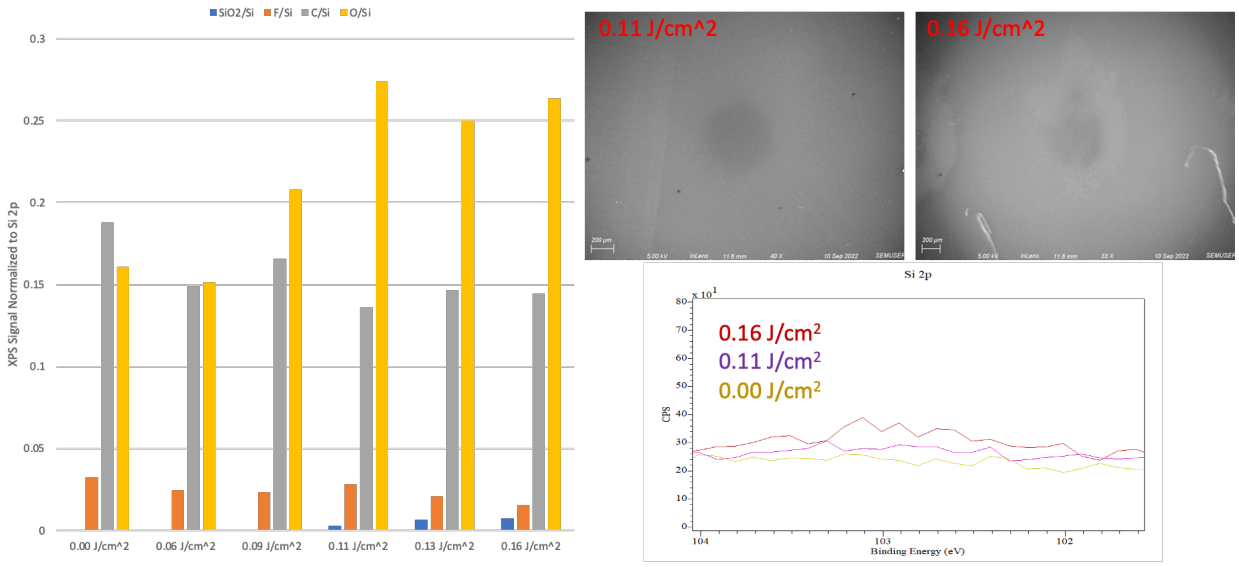

Figure A4.7 (*Left*) Histogram of quantitative XPS results for laser exposed H-Si(100) surface. (*Right*) (Top) SEM images of laser exposure sites, and (Bottom) SixOy2p XPS spectra for different exposure sites.

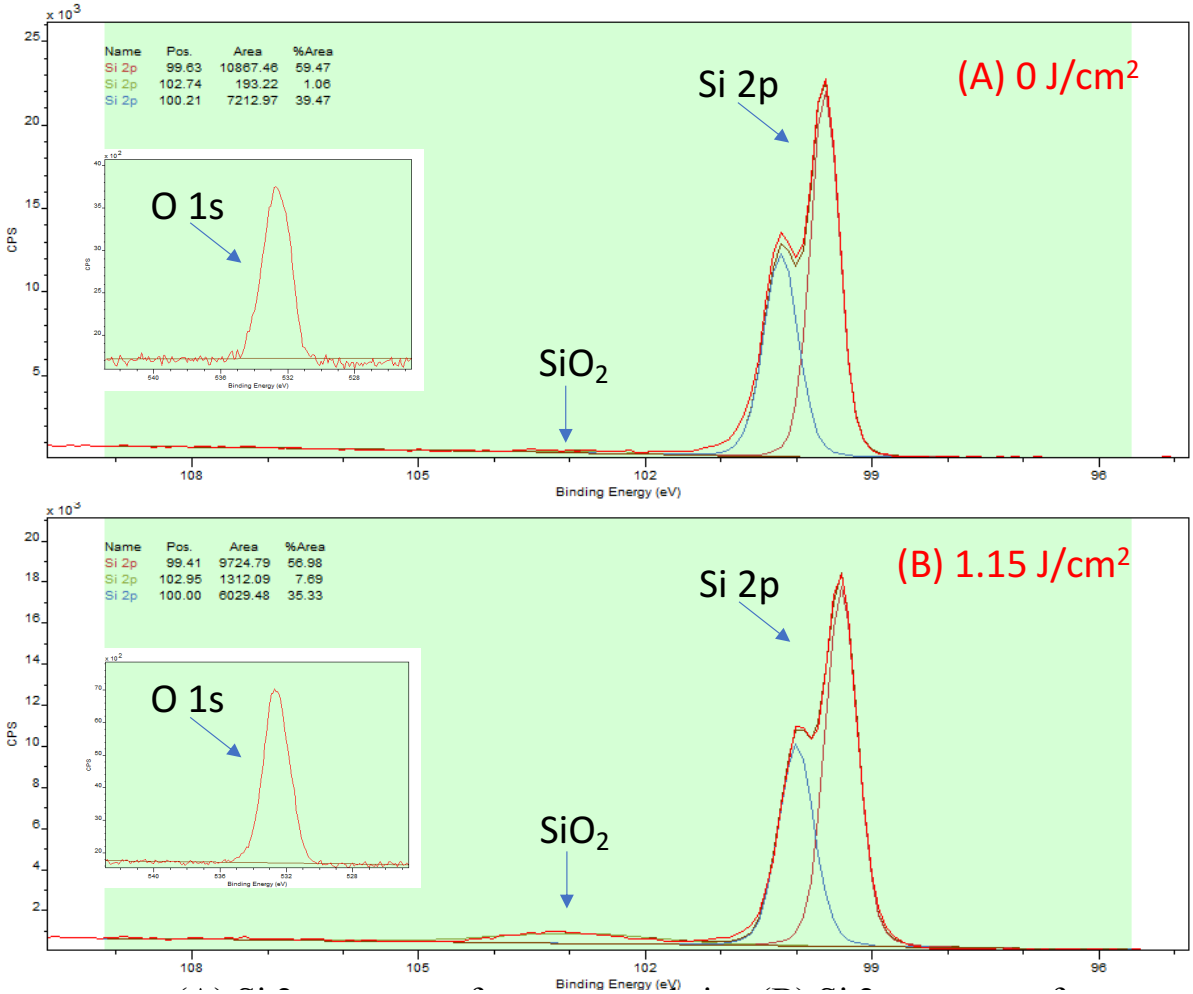

Figure A4.8 (A) XPS Si2p spectrum from unirradiated surface site with O 1s spectrum inset, (B) Si 2p spectrum from site irradiated with 0.34 J/cm^2 (1.15 J/cm^2 peak fluence) with O 1s spectrum inset.

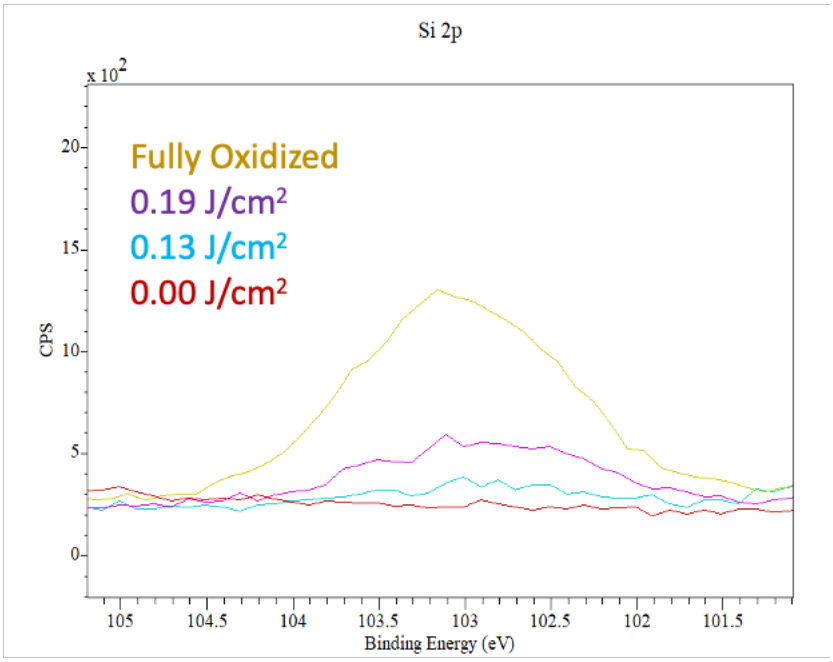

Figure A4.9 SixOy2p XPS spectra for fully oxidized Si(100) surface compared to H-Si(100) and laser exposed H-Si(100).

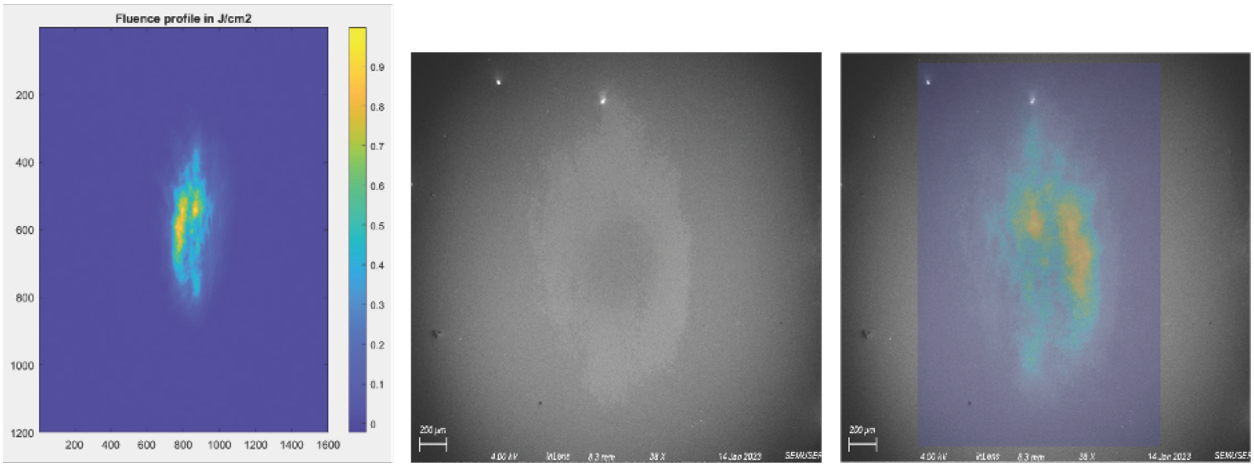

Figure A4.10 (*Left*) Fluence beam map for a 0.33 J/cm^2 peak fluence exposure site, (*Middle*) SEM of a 0.33 J/cm^2 peak fluence exposure site, and (*Right*) magnified fluence beam (matching dimension of beam in SEM) overlayed SEM of same exposure site, showing visual alteration of the sample surface is limited to within the beam imprint and no dissipation (whether chemical or physical) is observed outside the confines of the beam profile.

Figure A4.11 Code for generating thermal profile of Si surface post laser exposure.

```
% script developed by Dr. John Lambropoulos

delta = 10e-9; % Absorption depth [m] = 10 nm
t_pulse = 6e-9; % Pulse time [s] = 6 ns
k = 80; % Thermal conductivity [W/m K]
rho = 2330; % Density [kg/m3]
cp = 700; % Heat capacity [J/kg K]
a = k / (rho * cp); % Thermal diffusivity [m2/s]
% Fixing z = 0.01 nm, see delta_T vs. both time and fluence
z = 0.01e-9; % Distance into sub [m] = 0.01 nm
t = linspace(0, t_pulse, 100); % Time [s]
F = linspace(0, 0.2e4, 101); % Energy flux or fluence [J/m2]
temp = @(z, t, F) (F / t_pulse / k) .* ((-delta * exp(-z / delta)) + sqrt(4 *
a * t / pi) .* exp(-(z^2) / (4 * a * t)) - z * erfc(z / (2 * sqrt(a * t))));
delta_T = zeros(100, 101);
for i = 1:100
for j = 1:101
if t(i) <= t_pulse
delta_T(i, j) = temp(z, t(i), F(j));
else
delta_T(i, j) = temp(z, t(i), F(j)) - temp(z, t(i)-t_pulse, F(j));
end
end
end
[X, Y] = meshgrid(F, t);
% Plot surface
figure;
surf(X / 1e4, Y * 1e9, delta_T, 'EdgeColor', 'none');
colormap hot;
colorbar;
xlabel('Fluence (J/cm^2)');
ylabel('Time (ns)');
zlabel('ΔT (K)');
title('ΔT vs. Time & Fluence');
% Plot contour
figure;
contourf(X / 1e4, Y * 1e9, delta_T, 'LineColor', 'none');
colormap hot;
colorbar;
xlabel('Fluence (J/cm^2)');
ylabel('Time (ns)');
title('ΔT vs. Time & Fluence');
```

K = 80 W/m-¹K-¹

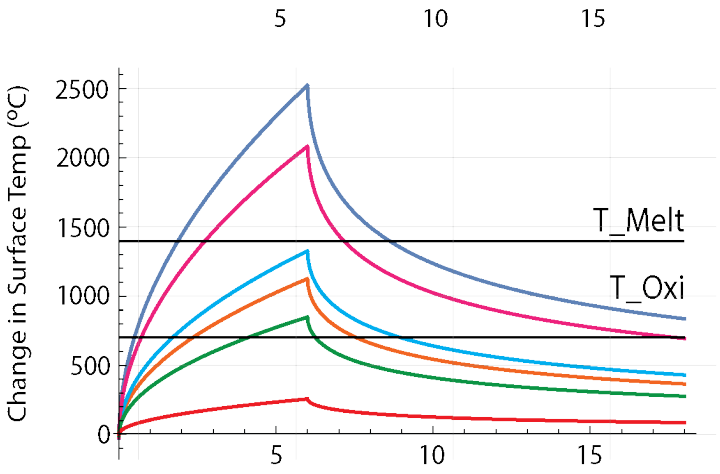
5
10
15
2500
2000
1500
1000
500
0
Change in Surface Temp (°C)
T_Melt
T_Oxi
5
10
15

Figure A4.12 Code for generating 2D and 3D laser intensity profiles.

```
% Constants
delta = 10e-9; % Absorption depth [m] = 10 nm
t_pulse = 6e-9; % Pulse time [s] = 6 ns
rho = 2330; % Density [kg/m3]
cp = 700; % Heat capacity [J/kg K]
% Function to compute temperature
temp = @(z, t, F, k, a) (F ./ t_pulse ./ k) .* ((- delta .* exp(- z ./
delta)) + ...
sqrt(4 .* a .* t ./ pi) .* exp(- (z .^ 2) ./ (4 .* a .* t)) - ...
z .* erfc(z ./ (2 .* sqrt(a .* abs(t)))));
% Distance into substrate [m]
z = 0.01e-9;
% Time [s]
t = linspace(0, 1 * t_pulse, 101);
% Energy flux or fluence [J/m2]
F_values = linspace(0, 0.2e4, 100);
% Prepare a grid for results
[T, F_grid] = meshgrid(t, F_values);
delta_T_grid = zeros(size(T));
% Iterative solution parameters
tolerance = 1e-6;
max_iterations = 1000;
for i = 1:length(F_values)
F = F_values(i);
k_old = 130; % Initial guess for k
delta_T = zeros(size(t));
for iteration = 1:max_iterations
% Calculate thermal diffusivity with current k
a = k_old / rho / cp;
% Compute temperature rise
delta_T = temp(z, t, F, k_old, a) .* heaviside(t) - ...
temp(z, t - t_pulse, F, k_old, a) .* heaviside(t - t_pulse);
% Update k using new delta_T
k_new = 1.8136e5 * ((delta_T + 298.15) .^ (-1.2505));
% Check for convergence
if max(abs(k_new - k_old)) < tolerance
break;
end
% Update k for next iteration
k_old = k_new;
end
% Store results in grid
delta_T_grid(i, :) = delta_T;
end
% Plot
figure;
contourf(T, F_grid ./1e4, delta_T_grid, 10, 'LineColor', 'none');
colorbar;
xlabel('Time (s)');
ylabel('Fluence [J/cm^2]');
title('Temperature Change vs. Time and Fluence');
colormap hot;
```

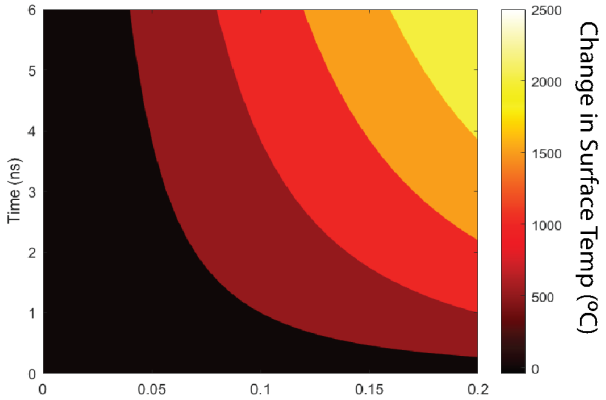
Time (ns)
Change in Surface Temp (°C)
0
0.05
0.1
0.15
0.2
0
1
2
3
4
5
6
500
1000
1500
2000
2500

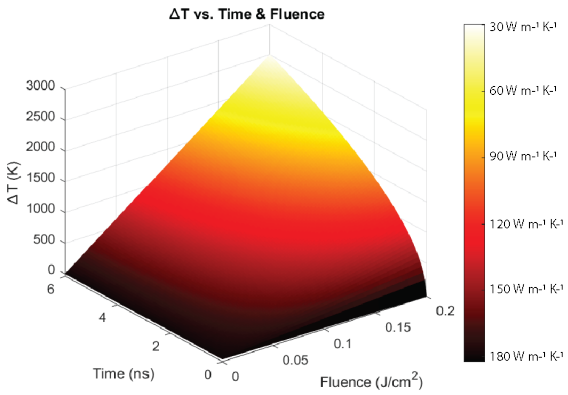
ΔT vs. Time & Fluence
ΔT (K)
Time (ns)
Fluence (J/cm²)
30 W m⁻¹ K⁻¹
60 W m⁻¹ K⁻¹
90 W m⁻¹ K⁻¹
120 W m⁻¹ K⁻¹
150 W m⁻¹ K⁻¹
180 W m⁻¹ K⁻¹

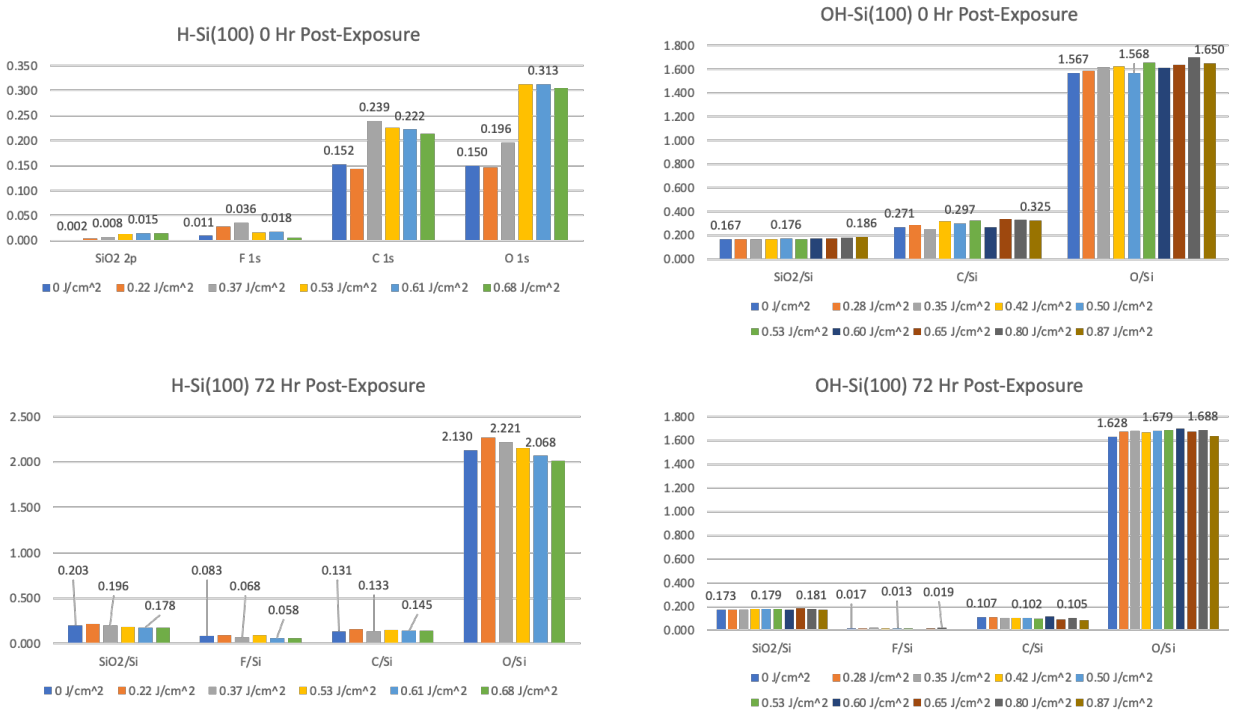

Figure A4.13 Complete XPS quantification characterization of laser exposed H-Si(100) and OH-Si(100) surface over 72 hours of air exposure.

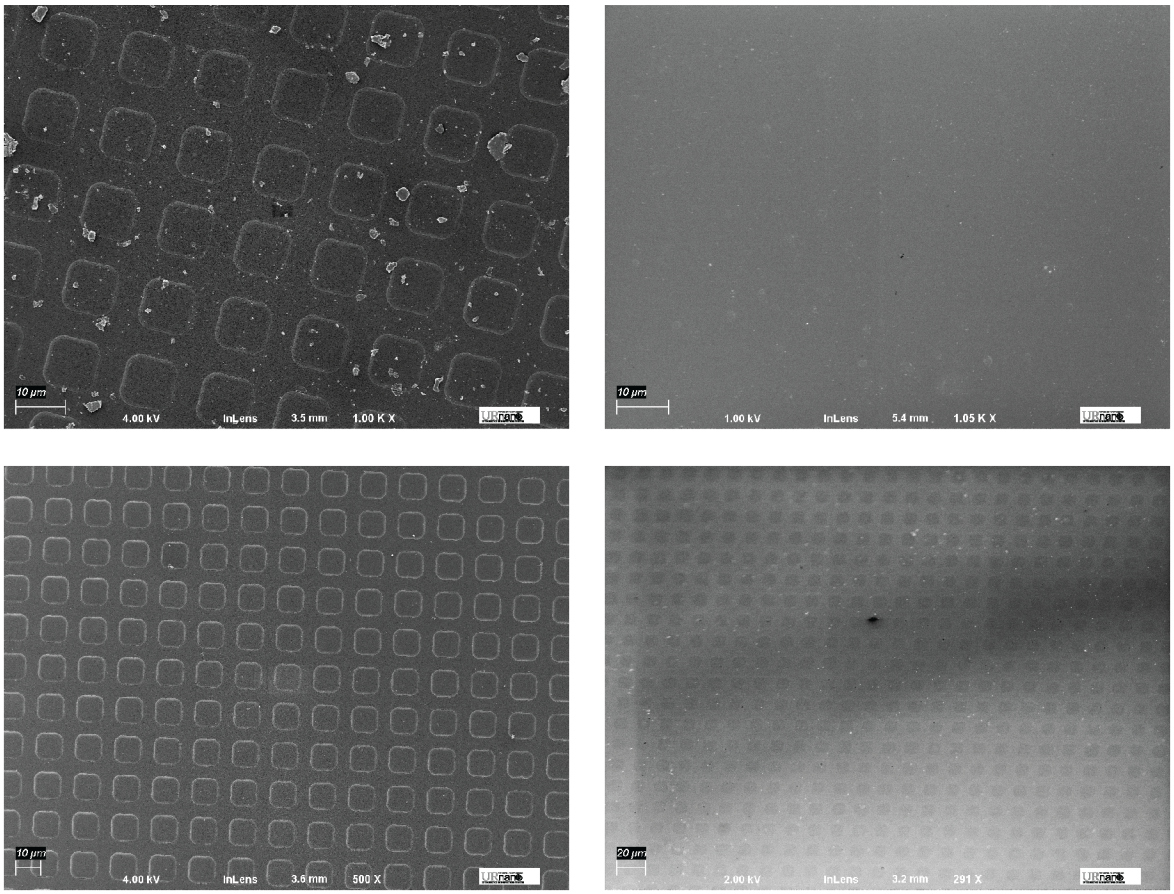

Figure A5.1 SEM Imaging of; (*Top-Left*) PUA stamp surface with debris, (*Top-Right*) Diaz-Si surface post-printing with inkless stamp and UV-exposure, (*Bottom-Left*) larger area of clean PUA stamp surface, (*Bottom-Right*) PPh_2-Si surface post-printing under UV-lamp exposure.

References

(1) Bondyopadhyay, P. K. Moore's law governs the silicon revolution. *P Ieee* **1998**, *86* (1), 78-81. DOI: Doi 10.1109/5.658761.

(2) Chien, A. A.; Karamcheti, V. Moore's Law: The First Ending and a New Beginning. *Computer* **2013**, *46* (12), 48-53. DOI: Doi 10.1109/Mc.2013.431.

(3) IBM. IBM Unveils World's First 2 Nanometer Chip Technology, Opening a New Frontier for Semiconductors. **2021**. (acccessed June 3rd, 2024).

(4) Bohr, M. 14 nm Process Technology: Opening New Horizons. **2014**.

(5) Liao, F. Y.; Wang, H. J.; Guo, X. J.; Guo, Z. X.; Tong, L.; Riaud, A.; Sheng, Y. C.; Chen, L.; Sun, Q. Q.; Zhou, P.; et al. Charge transport and quantum confinement in MoS dual-gated transistors. *J Semicond* **2020**, *41* (7). DOI: Artn 072904 10.1088/1674-4926/41/7/072904.

(6) Najam, F.; Yu, Y. S. Impact of Quantum Confinement on Band-to-Band Tunneling of Line-Tunneling Type L-Shaped Tunnel Field-Effect Transistor. *Ieee T Electron Dev* **2019**, *66* (4), 2010-2016. DOI: 10.1109/Ted.2019.2898403.

(7) GHanatian, H.; Fathipour, M.; Talebi, H. Nanoscale Ultra Thin Body -Silicon-On-Insulator Field Effect Transistor with Step BOX: Self-heating and Short Channel Effects). *Ulis 2009: 10th International Conference on Ultimate Integration of Silicon* **2009**, 325-328. DOI: Doi 10.1109/Ulis.2009.4897601.

(8) Semiconductor-On-Insulator Materials for Nanoelectronics Applications. *Eng Mater* **2011**, 1-447. DOI: 10.1007/978-3-642-15868-1.

(9) Semiconductor Industry Association 2015 International Technology Roadmap for Semiconductors (ITRS). **2015**. (acccessed 05/19/2024).

(10) Vashishtha, V.; Clark, L. T. Comparing bulk-Si FinFET and gate-all-around FETs for the 5 nm technology node. *Microelectron J* **2021**, *107*. DOI: ARTN 104942 10.1016/j.mejo.2020.104942.

(11) Thomas, S. Gate-all-around transistors stack up. *Nat Electron* **2020**, *3* (12), 728-728. DOI: 10.1038/s41928-020-00517-1.

(12) Middleton, C. 5 things you should know about High NA EUV lithography. **2024**. (acccessed 06/05/24).

(13) Liu, C. C.; Cheng, A. C.; Chen, S. H. A Study for Sustainable Development in Optoelectronics Industry Using Multiple Criteria Decision Making Methods. *Technol Econ Dev Eco* **2017**, *23* (2), 221-242. DOI: 10.3846/20294913.2015.1072747.

(14) Coe, N. M. Making microchips: policy, globalization and economic restructuring in the semiconductor industry. *Environ Plann A* **1999**, *31* (8), 1519-1520.

(15) Willson, C. G.; Dammel, R. A.; Reiser, A. Photoresist materials: A historical perspective. *P Soc Photo-Opt Ins* **1997**, *3048*, 28-41. DOI: Doi 10.1117/12.275783.

(16) Totzeck, M.; Ulrich, W.; Göhnermeier, A.; Kaiser, W. Semiconductor fabrication -: Pushing deep ultraviolet lithography to its limits. *Nat Photonics* **2007**, *1* (11), 629-631. DOI: DOI 10.1038/nphoton.2007.218.

(17) Samal, P.; Samal, J. R. K.; Rho, H. S.; van Beurden, D.; van Blitterswijk, C.; Truckenmüller, R.; Giselbrecht, S. Direct deep UV lithography to micropattern PMMA for stem cell culture. *Mater Today Bio* **2023**, *22*. DOI: ARTN 100779
10.1016/j.mtbio.2023.100779.

(18) Piskunen, P.; Shen, B. X.; Keller, A.; Toppari, J. J.; Kostiainen, M. A.; Linko, V. Biotemplated Lithography of Inorganic Nanostructures (BLIN) for Versatile Patterning of Functional Materials. *Acs Applied Nano Materials* **2021**, *4* (1), 529-538. DOI: 10.1021/acsanm.0c02849.

(19) Zhang, L. B.; Dong, L. S.; Su, X. J.; Wei, Y. Y.; Ye, T. C. New alignment mark designs in single patterning and self-aligned double patterning. *Microelectron Eng* **2017**, *179*, 18-24. DOI: 10.1016/j.mee.2017.04.017.

(20) Bijnen, F. G. C.; von Buel, W.; Gui, C. Q.; Lof, J. Front to back alignment metrology. *Proc Spie* **2003**, *5037*, 641-646. DOI: Doi 10.1117/12.487585.

(21) Tseng, L.; Karadan, P.; Kazazis, D.; Constantinou, P. C.; Stock, T. J. Z.; Curson, N. J.; Schofield, S. R.; Muntwiler, M.; Aeppli, G.; Ekinci, Y. Resistless EUV lithography: Photon-induced oxide patterning on silicon. *Sci Adv* **2023**, *9* (16). DOI: ARTN eadf5997
10.1126/sciadv.adf5997.

(22) Chaker, A.; Alty, H. R.; Tian, P.; Kotsovinos, A.; Timco, G. A.; Muryn, C. A.; Lewis, S. M.; Winpenny, R. E. P. Nanoscale Patterning of Zinc Oxide from Zinc Acetate Using Electron Beam

Lithography for the Preparation of Hard Lithographic Masks. *Acs Appl Nano Mater* **2021**, *4* (1), 406-413. DOI: 10.1021/acsanm.0c02756.

(23) Grigorescu, A. E.; Hagen, C. W. Resists for sub-20-nm electron beam lithography with a focus on HSQ: state of the art. *Nanotechnology* **2009**, *20* (29). DOI: Artn 292001 10.1088/0957-4484/20/29/292001.

(24) Li, K. Z.; Li, J. T.; Reardon, C.; Schuster, C. S.; Wang, Y.; Triggs, G. J.; Damnik, N.; Müenchenberger, J.; Wang, X. H.; Martins, E. R.; et al. High speed e-beam writing for large area photonic nanostructures - a choice of parameters. *Sci Rep-Uk* **2016**, *6*. DOI: ARTN 32945 10.1038/srep32945.

(25) Racka-Szmidt, K.; Stonio, B.; Zelazko, J.; Filipiak, M.; Sochacki, M. A Review: Inductively Coupled Plasma Reactive Ion Etching of Silicon Carbide. *Materials* **2022**, *15* (1). DOI: ARTN 123 10.3390/ma15010123.

(26) Wang, M. M.; Kushner, M. J. Modeling of implantation and mixing damage during etching of SiO
over Si in fluorocarbon plasmas. *J Vac Sci Technol A* **2011**, *29* (5). DOI: Artn 051306 10.1116/1.3626533.

(27) Montaño-Miranda, G.; Muscat, A. Etching of silicon dioxide with gas phase HF and water:: Initiation, bulk etching, and termination. *Solid State Phenomen* **2008**, *134*, 3-+. DOI: DOI 10.4028/www.scientific.net/SSP.134.3.

(28) Parsons, G. N.; Clark, R. D. Area-Selective Deposition: Fundamentals, Applications, and Future Outlook. *Chem Mater* **2020**, *32* (12), 4920-4953. DOI: 10.1021/acs.chemmater.0c00722.

(29) O'Connell, C. D.; Higgins, M. J.; Moulton, S. E.; Wallace, G. G. Nano-bioelectronics
dip-pen nanolithography. *Journal of Materials Chemistry C* **2015**, *3* (25), 6431-6444. DOI: 10.1039/c5tc00186b.

(30) Bratton, D.; Yang, D.; Dai, J. Y.; Ober, C. K. Recent progress in high resolution lithography. *Polym Advan Technol* **2006**, *17* (2), 94-103. DOI: 10.1002/pat.662.

(31) Perry, T. S. Gordon Moore's next act. *Ieee Spectrum* **2008**, *45* (5), 40-43. DOI: Doi 10.1109/Mspec.2008.4505311.

(32) Chemical Vapour Deposition: Precursors, Processes and Applications. *Chemical Vapour Deposition: Precursors, Processes and Applications* **2008**, 1-582. DOI: 10.1039/9781847558794.

(33) Yi, K. Y.; Liu, D. H.; Chen, X. S.; Yang, J.; Wei, D. P.; Liu, Y. Q.; Wei, D. C. Plasma-Enhanced Chemical Vapor Deposition of Two-Dimensional Materials for Applications. *Accounts Chem Res* **2021**, *54* (4), 1011-1022. DOI: 10.1021/acs.accounts.0c00757.

(34) Vallée, C.; Bonvalot, M.; Belahcen, S.; Yeghoyan, T.; Jaffal, M.; Vallat, R.; Chaker, A.; Lefèvre, G.; David, S.; Bsiesy, A.; et al. Plasma deposition-Impact of ions in plasma enhanced chemical vapor deposition, plasma enhanced atomic layer deposition, and applications to area selective deposition. *J Vac Sci Technol A* **2020**, *38* (3). DOI: Artn 033007 10.1116/1.5140841.

(35) Mistry, K. A., C.; Auth, C.; Beattie, B.; Bergstrom, D.; Bost, M.; Brazier, M.; Buehler, M.; Cappellani, A.; Chau, R.; Choi, C.-H.; Ding, G.; Fischer, K.; Ghani, T.; Grover, R.; Han, W.; Hanken, D.; Hattendorf, M.; He, J.; Hicks, J.; Huessner, R.; Ingerly, D.; Jain, P.; James, R.; Jong, L.; Joshi, S.; Kenyon, C.; Kuhn, K.; Lee, K. A 45nm Logic Technology with High-k+Metal Gate Transistors, Strained Silicon, 9 Cu Interconnect Layers, 193nm Dry Patterning, and 100% Pb-free Packaging. *2009 IEEE International Electron Devices Meeting* **2009**, 247-250.

(36) Raaijmakers, I. J. ASMI Investor Day 2021. **2021**.

(37) Fund, T. Atomic layer deposition, next-gen transistors, and ASM. **2023**. (acccessed June 11th, 2024).

(38) Ogunfowora, L. A.; Singh, I.; Arellano, N.; Pattison, T. G.; Magbitang, T.; Nguyen, K.; Ransom, B.; Lionti, K.; Nguyen, S.; Topura, T.; et al. Reactive Vapor-Phase Inhibitors for Area-Selective Depositions at Tunable Critical Dimensions. *Acs Appl Mater Inter* **2024**, *16* (4), 5268-5277. DOI: 10.1021/acsami.3c14821.

(39) Mackus, A. J. M.; Merkx, M. J. M.; Kessels, W. M. M. From the Bottom-Up: Toward Area-Selective Atomic Layer Deposition with High Selectivity. *Chem Mater* **2019**, *31* (1), 2-12. DOI: 10.1021/acs.chemmater.8b03454.

(40) Cho, T. H.; Farjam, N.; Allemang, C. R.; Pannier, C. P.; Kazyak, E.; Huber, C.; Rose, M.; Trejo, O.; Peterson, R. L.; Barton, K.; et al. Area-Selective Atomic Layer Deposition Patterned by Electrohydrodynamic Jet Printing for Additive Manufacturing of Functional Materials and Devices. *Acs Nano* **2020**, *14* (12), 17262-17272. DOI: 10.1021/acsnano.0c07297.

(41) Chou, C. Y.; Lee, W. H.; Chuu, C. P.; Chen, T. A.; Hou, C. H.; Yin, Y. T.; Wang, T. Y.; Shyue, J. J.; Li, L. J.; Chen, M. J. Atomic Layer Nucleation Engineering: Inhibitor-Free Area-Selective Atomic Layer Deposition of Oxide and Nitride. *Chem Mater* **2021**, *33* (14), 5584-5590. DOI: 10.1021/acs.chemmater.1c00823.

(42) Bobb-Semple, D.; Zeng, L.; Cordova, I.; Bergsman, D. S.; Nordlund, D.; Bent, S. F. Substrate-Dependent Study of Chain Orientation and Order in Alkylphosphonic Acid Self-Assembled Monolayers for ALD Blocking. *Langmuir* **2020**, *36* (43), 12849-12857. DOI: 10.1021/acs.langmuir.0c01974.

(43) Oh, I. K.; Sandoval, T. E.; Liu, T. L.; Richey, N. E.; Bent, S. F. Role of Precursor Choice on Area-Selective Atomic Layer Deposition. *Chem Mater* **2021**, *33* (11), 3926-3935. DOI: 10.1021/acs.chemmater.0c04718.

(44) Liu, T. L.; Bent, S. F. Area-Selective Atomic Layer Deposition on Chemically Similar Materials: Achieving Selectivity on Oxide/Oxide Patterns. *Chem Mater* **2021**, *33* (2), 513-523. DOI: 10.1021/acs.chemmater.0c03227.

(45) Deminskyi, P.; Haider, A.; Eren, H.; Khan, T. M.; Biyikli, N. Area-selective atomic layer deposition of noble metals: Polymerized fluorocarbon layers as effective growth inhibitors. *J Vac Sci Technol A* **2021**, *39* (2). DOI: Artn 022402
10.1116/6.0000701.

(46) Kim, H. M.; Lee, J. H.; Lee, S. H.; Harada, R.; Shigetomi, T.; Lee, S.; Tsugawa, T.; Shong, B.; Park, J. S. Area-Selective Atomic Layer Deposition of Ruthenium Using a Novel Ru Precursor and H
O as a Reactant. *Chem Mater* **2021**, *33* (12), 4353-4361. DOI: 10.1021/acs.chemmater.0c04496.

(47) de Paula, C.; Bobb-Semple, D.; Bent, S. F. Increased selectivity in area-selective ALD by combining nucleation enhancement and SAM-based inhibition. *J Mater Res* **2021**, *36* (3), 582-591. DOI: 10.1557/s43578-020-00013-4.

(48) Bobb-Semple, D.; Nardi, K. L.; Draeger, N.; Hausmann, D. M.; Bent, S. F. Area-Selective Atomic Layer Deposition Assisted by Self-Assembled Monolayers: A Comparison of Cu, Co, W, and Ru. *Chem Mater* **2019**, *31* (5), 1635-1645. DOI: 10.1021/acs.chemmater.8b04926.

(49) Seo, S.; Yeo, B. C.; Han, S. S.; Yoon, C. M.; Yang, J. Y.; Yoon, J.; Yoo, C.; Kim, H. J.; Lee, Y. B.; Lee, S. J.; et al. Reaction Mechanism of Area-Selective Atomic Layer Deposition for Al
O
Nanopatterns. *Acs Appl Mater Inter* **2017**, *9* (47), 41607-41617. DOI: 10.1021/acsami.7b13365.

(50) Hashemi, F. S. M.; Bent, S. F. Sequential Regeneration of Self-Assembled Monolayers for Highly Selective Atomic Layer Deposition. *Adv Mater Interfaces* **2016**, *3* (21). DOI: ARTN 1600464 10.1002/admi.201600464.

(51) Zhang, W. Y.; Engstrom, J. R. Effect of substrate composition on atomic layer deposition using self-assembled monolayers as blocking layers. *J Vac Sci Technol A* **2016**, *34* (1). DOI: Artn 01a107 10.1116/1.4931722.

(52) Hinckley, A. P.; Muscat, A. J. Detecting and Removing Defects in Organosilane Self-Assembled Monolayers. *Langmuir* **2020**, *36* (10), 2563-2573. DOI: 10.1021/acs.langmuir.9b02753.

(53) Weiss, E. A.; Chiechi, R. C.; Kaufman, G. K.; Kriebel, J. K.; Li, Z. F.; Duati, M.; Rampi, M. A.; Whitesides, G. M. Influence of defects on the electrical characteristics of mercury-drop junctions:: Self-assembled monolayers of
-alkanethiolates on rough and smooth silver. *J Am Chem Soc* **2007**, *129* (14), 4336-4349. DOI: 10.1021/ja0677261.

(54) Yarbrough, J.; Shearer, A. B.; Bent, S. F. Next generation nanopatterning using small molecule inhibitors for area-selective atomic layer deposition. *J Vac Sci Technol A* **2021**, *39* (2). DOI: Artn 021002
10.1116/6.0000840.

(55) Hashemi, F. S. M.; Birchansky, B. R.; Bent, S. F. Selective Deposition of Dielectrics: Limits and Advantages of Alkanethiol Blocking Agents on Metal-Dielectric Patterns. *Acs Appl Mater Inter* **2016**, *8* (48), 33264-33272. DOI: 10.1021/acsami.6b09960.

(56) Lecordier, L.; Herregods, S.; Armini, S. Vapor-deposited octadecanethiol masking layer on copper to enable area selective Hf
N
atomic layer deposition on dielectrics studied by
spectroscopic ellipsometry. *J Vac Sci Technol A* **2018**, *36* (3). DOI: Artn 031605
10.1116/1.5025688.

(57) Soethoudt, J.; Tomczak, Y.; Meynaerts, B.; Chan, B. T.; Delabie, A. Insight into Selective Surface Reactions of Dimethylamino-trimethylsilane for Area-Selective Deposition of Metal, Nitride, and Oxide. *J Phys Chem C* **2020**, *124* (13), 7163-7173. DOI: 10.1021/acs.jpcc.9b11270.

(58) Merkx, M. J. M.; Vlaanderen, S.; Faraz, T.; Verheijen, M. A.; Kessels, W. M. M.; Mackus, A. J. M. Area-Selective Atomic Layer Deposition of TiN Using Aromatic Inhibitor Molecules for Metal/Dielectric Selectivity. *Chem Mater* **2020**, *32* (18), 7788-7795. DOI: 10.1021/acs.chemmater.0c02370.

(59) Metzler, D.; Li, C.; Lai, C. S.; Hudson, E. A.; Oehrlein, G. S. Investigation of thin oxide layer removal from Si substrates using an SiO
atomic layer etching approach: the importance of the reactivity of the substrate. *J Phys D Appl Phys* **2017**, *50* (25). DOI: ARTN 254006
10.1088/1361-6463/aa71f1.

(60) Hennessy, J.; Moore, C. S.; Balasubramanian, K.; Jewell, A. D.; France, K.; Nikzad, S. Enhanced atomic layer etching of native aluminum oxide for ultraviolet optical applications. *J Vac Sci Technol A* **2017**, *35* (4). DOI: Artn 041512
10.1116/1.4986945.

(61) Claridge, S. A.; Liao, W. S.; Thomas, J. C.; Zhao, Y. X.; Cao, H. H.; Cheunkar, S.; Serino, A. C.; Andrews, A. M.; Weiss, P. S. From the bottom up: dimensional control and characterization in molecular monolayers. *Chem Soc Rev* **2013**, *42* (7), 2725-2745. DOI: 10.1039/c2cs35365b.

(62) Cha, S.; Kim, C. Poly(dimethylsiloxane) Stamp Coated with a Low-Surface-Energy, Diffusion-Blocking, Covalently Bonded Perfluoropolyether Layer and Its Application to the Fabrication of Organic Electronic Devices by Layer Transfer. *Acs Appl Mater Inter* **2018**, *10* (28), 24003-24012. DOI: 10.1021/acsami.8b03811.

(63) Wang, C. J.; Linghu, C. H.; Nie, S.; Li, C. L.; Lei, Q. J.; Tao, X.; Zeng, Y. J.; Du, Y. P.; Zhang, S.; Yu, K. X.; et al. Programmable and scalable transfer printing with high reliability and efficiency for flexible inorganic electronics. *Sci Adv* **2020**, *6* (25). DOI: ARTN eabb2393
10.1126/sciadv.abb2393.

(64) Park, J.; Lee, Y.; Lee, H.; Ko, H. Transfer Printing of Electronic Functions on Arbitrary Complex Surfaces. *Acs Nano* **2020**, *14* (1), 12-20. DOI: 10.1021/acsnano.9b09846.

(65) Delamarche, E.; Schmid, H.; Bietsch, A.; Larsen, N. B.; Rothuizen, H.; Michel, B.; Biebuyck, H. Transport mechanisms of alkanethiols during microcontact printing on gold. *J Phys Chem B* **1998**, *102* (18), 3324-3334. DOI: DOI 10.1021/jp980556x.

(66) Li, H. W.; Muir, B. V. O.; Fichet, G.; Huck, W. T. S. Nanocontact printing: A route to sub-50-nm-scale chemical and biological patterning. *Langmuir* **2003**, *19* (6), 1963-1965. DOI: 10.1021/la0269098.

(67) Kim, S.; Liu, N.; Shestopalov, A. A. Contact Printing of Multilayered Thin Films with Shape Memory Polymers. *Acs Nano* **2022**, *16* (4), 6134-6144. DOI: 10.1021/acsnano.1c11607.

(68) Shestopalov, A. A.; Clark, R. L.; Toone, E. J. Inkless Microcontact Printing on SAMs of Boc- and TBS-Protected Thiols. *Nano Lett* **2010**, *10* (1), 43-46. DOI: 10.1021/nl902588d.

(69) Liao, W. S.; Cheunkar, S.; Cao, H. H.; Bednar, H. R.; Weiss, P. S.; Andrews, A. M. Subtractive Patterning via Chemical Lift-Off Lithography. *Science* **2012**, *337* (6101), 1517-1521. DOI: 10.1126/science.1221774.

(70) Chen, C. Y.; Wang, C. M.; Liao, W. S. A Special Connection between Nanofabrication and Analytical Devices: Chemical Lift-Off Lithography. *B Chem Soc Jpn* **2019**, *92* (3), 600-607. DOI: 10.1246/bcsj.20180373.

(71) Eichelsdoerfer, D. J.; Liao, X.; Cabezas, M. D.; Morris, W.; Radha, B.; Brown, K. A.; Giam, L. R.; Braunschweig, A. B.; Mirkin, C. A. Large-area molecular patterning with polymer pen lithography. *Nat Protoc* **2013**, *8* (12), 2548-2560. DOI: 10.1038/nprot.2013.159.

(72) Schlichter, L.; Bosse, F.; Tyler, B. J.; Arlinghaus, H. F.; Ravoo, B. J. Patterning of Hydrophilic and Hydrophobic Gold and Magnetite Nanoparticles by Dip Pen Nanolithography. *Small* **2023**, *19* (18). DOI: 10.1002/smll.202208069.

(73) Urtizberea, A.; Hirtz, M.; Fuchs, H. Ink transport modelling in Dip-Pen Nanolithography and Polymer Pen Lithography. *Nanofabrication* **2015**, *2* (1), 43-53. DOI: 10.1515/nanofab-2015-0005.

(74) Liu, G. Q.; Hirtz, M.; Fuchs, H.; Zheng, Z. J. Development of Dip-Pen Nanolithography (DPN) and Its Derivatives. *Small* **2019**, *15* (21). DOI: ARTN 1900564
10.1002/smll.201900564.

(75) Salaita, K.; Wang, Y. H.; Fragala, J.; Vega, R. A.; Liu, C.; Mirkin, C. A. Massively parallel dip-pen nanolithography with 55000-pen two-dimensional arrays. *Angew Chem Int Edit* **2006**, *45* (43), 7220-7223. DOI: 10.1002/anie.200603142.

(76) Huo, F. W.; Zheng, Z. J.; Zheng, G. F.; Giam, L. R.; Zhang, H.; Mirkin, C. A. Polymer pen lithography. *Science* **2008**, *321* (5896), 1658-1660. DOI: 10.1126/science.1162193.

(77) Gross, N.; Wang, W. L.; Brasel, S.; Searles, E. K.; Bourgeois, B.; Dionne, J. A.; Landes, C. F.; Link, S. High-Throughput Screening of Optical Properties of Glass-Supported Plasmonic Nanoparticles Fabricated by Polymer Pen Lithography. *J Phys Chem C* **2023**, *127* (39), 19607-19619. DOI: 10.1021/acs.jpcc.3c04521.

(78) Ward, D. R., Schmucker, S.W., Anderson, E.M., Bussmann, E., Tracy, L., Lu, T.M., Maurer, L.N., Baczewski, A., Campbell, D.M., Marshall, M.T., Misra, S. Atomic precision advanced manufacturing for digital electronics. *arXiv preprint arXiv:2002* **2020**, (11003).

(79) Ballard, J. B.; Owen, J. H. G.; Owen, W.; Alexander, J. R.; Fuchs, E.; Randall, J. N.; Von Ehr, J. R.; McDonnell, S.; Dick, D. D.; Wallace, R. M.; et al. Pattern transfer of hydrogen depassivation lithography patterns into silicon with atomically traceable placement and size control. *J Vac Sci Technol B* **2014**, *32* (4). DOI: Artn 041804
10.1116/1.4890484.

(80) Bussmann, E.; Butera, R. E.; Owen, J. H. G.; Randall, J. N.; Rinaldi, S. M.; Baczewski, A. D.; Misra, S. Atomic-precision advanced manufacturing for Si quantum computing. *Mrs Bull* **2021**, *46* (7), 607-615. DOI: 10.1557/s43577-021-00139-8.

(81) Moheimani, S. O. R.; Alemansour, H. A new approach to removing H atoms in hydrogen depassivation lithography. *Novel Patterning Technologies for Semiconductors, Mems/Nems and Moems 2020* **2020**, *11324*. DOI: Artn 113240y
10.1117/12.2552138.

(82) McDonnell, S.; Longo, R. C.; Seitz, O.; Ballard, J. B.; Mordi, G.; Dick, D.; Owen, J. H. G.; Randall, J. N.; Kim, J. Y.; Chabal, Y. J.; et al. Controlling the Atomic Layer Deposition of Titanium Dioxide on Silicon: Dependence on Surface Termination. *J Phys Chem C* **2013**, *117* (39), 20250-20259. DOI: 10.1021/jp4060022.

(83) Longo, R. C.; McDonnell, S.; Dick, D.; Wallace, R. M.; Chabal, Y. J.; Owen, J. H. G.; Ballard, J. B.; Randall, J. N.; Cho, K. Selectivity of metal oxide atomic layer deposition on hydrogen terminated and oxidized Si(001)-(2x1) surface. *J Vac Sci Technol B* **2014**, *32* (3). DOI: Artn 03d112 10.1116/1.4864619.

(84) Gaevski, M. E.; Watson, G. P.; Novembre, A. E. High density submicron features using a laser pattern generator and double patterning. *J Vac Sci Technol B* **2009**, *27* (6), 2742-2744. DOI: 10.1116/1.3263192.

(85) Lechthaler, B.; Fox, T.; Slawik, S.; Mücklich, F. Direct laser interference patterning combined with mask imaging. *Opt Laser Technol* **2020**, *123*. DOI: ARTN 105918
10.1016/j.optlastec.2019.105918.

(86) Yoo, J. H.; Ray, N. J.; Nguyen, H. T.; Johnson, M. A.; Feigenbaum, E. Laser-Assisted Tailored Patterning of Au Nanoparticles over an Inch-Sized Area: Implications for Large Aperture Meta-optics. *Acs Appl Nano Mater* **2022**, *5* (7), 10073-10080. DOI: 10.1021/acsanm.2c02590.

(87) Toulouse, A.; Thiele, S.; Hirzel, K.; Schmid, M.; Weber, K.; Zyrianova, M.; Giessen, H.; Herkommer, A. M.; Heymann, M. High resolution femtosecond direct laser writing with wrapped lens. *Opt Mater Express* **2022**, *12* (9), 3801-3809. DOI: 10.1364/Ome.468534.

(88) Kuts, R. I.; Mandrusova, E. O.; Sedukhin, A. G.; Bronnikova, E. V.; Korolkov, V. P. Increasing the spatial resolution of direct laser writing by using a non-Gaussian intensity distribution in the writing laser spot. *Proc Spie* **2022**, *12318*. DOI: Artn 123180o
10.1117/12.2643710.

(89) Ho, J. C.; Yerushalmi, R.; Jacobson, Z. A.; Fan, Z.; Alley, R. L.; Javey, A. Controlled nanoscale doping of semiconductors via molecular monolayers. *Nat Mater* **2008**, *7* (1), 62-67. DOI: 10.1038/nmat2058.

(90) Veerbeek, J.; Ye, L.; Vijselaar, W.; Kudernac, T.; van der Wiel, W. G.; Huskens, J. Highly doped silicon nanowires by monolayer doping. *Nanoscale* **2017**, *9* (8), 2836-2844. DOI: 10.1039/c6nr07623h.

(91) Ye, L.; Pujari, S. P.; Zuilhof, H.; Kudernac, T.; de Jong, M. P.; van der Wiel, W. G.; Huskens, J. Controlling the Dopant Dose in Silicon by Mixed-Monolayer Doping. *Acs Appl Mater Inter* **2015**, *7* (5), 3231-3236. DOI: 10.1021/am5079368.

(92) Zhang, C. F.; Chang, S. N.; Dan, Y. P. Advances in ultrashallow doping of silicon. *Adv Phys-X* **2021**, *6* (1). DOI: Artn 1871407
10.1080/23746149.2020.1871407.

(93) Raffaelle, P. R.; Wang, G. T.; Shestopalov, A. A. Vapor-Phase Halogenation of Hydrogen-Terminated Silicon(100) Using
-Halogen-succinimides. *Acs Appl Mater Inter* **2023**, *15* (47), 55139-55149. DOI: 10.1021/acsami.3c13269.

(94) Sánchez-Bodón, J.; del Olmo, J. A.; Alonso, J. M.; Moreno-Benítez, I.; Vilas-Vilela, J. L.; Pérez-Alvarez, L. Bioactive Coatings on Titanium: A Review on Hydroxylation, Self-Assembled Monolayers (SAMs) and Surface Modification Strategies. *Polymers-Basel* **2022**, *14* (1). DOI: ARTN 165
10.3390/polym14010165.

(95) Li, L. N.; Belcher, A. M.; Loke, D. K. Simulating selective binding of a biological template to a nanoscale architecture: a core concept of a clamp-based binding-pocket-favored N-terminal-domain assembly. *Nanoscale* **2020**, *12* (47), 24214-24227. DOI: 10.1039/d0nr07320b.

(96) Raaijmakers, I. J. Current and Future Applications of ALD in Micro-electronics. *Ecs Transactions* **2011**, *41* (2), 3-17. DOI: 10.1149/1.3633649.

(97) Levy, D. H.; Nelson, S. F. Thin-film electronics by atomic layer deposition. *J Vac Sci Technol A* **2012**, *30* (1). DOI: Artn 018501
10.1116/1.3670748.

(98) Khan, R.; Ali-Loytty, H.; Saari, J.; Valden, M.; Tukiainen, A.; Lahtonen, K.; Tkachenko, N. V. Optimization of Photogenerated Charge Carrier Lifetimes in ALD Grown TiO(2)for Photonic Applications. *Nanomaterials-Basel* **2020**, *10* (8). DOI: ARTN 1567
10.3390/nano10081567.

(99) Knehr, E.; Ziegler, M.; Linzen, S.; Ilin, K.; Schanz, P.; Plentz, J.; Diegel, M.; Schmidt, H.; Il'ichev, E.; Siegel, M. Wafer-level uniformity of atomic-layer-deposited niobium nitride thin films for quantum devices. *J Vac Sci Technol A* **2021**, *39* (5). DOI: Artn 052401 10.1116/6.0001126.

(100) Zarubin, S.; Suvorova, E.; Spiridonov, M.; Negrov, D.; Chernikova, A.; Markeev, A.; Zenkevich, A. Fully ALD-grown TiN/Hf0.5Zr0.5O2/TiN stacks: Ferroelectric and structural properties (vol 109, 192903, 2016). *Appl Phys Lett* **2016**, *109* (25). DOI: Artn 259901 10.1063/1.4972787.

(101) George, S. M. Atomic Layer Deposition: An Overview. *Chemical Reviews* **2010**, *110* (1), 111-131. DOI: 10.1021/cr900056b.

(102) Lee, H.-B.-R.; Bent, S. Nanopatterning by Area-Selective Atomic Layer Deposition. 2012; pp 193-225.

(103) Hong, J.; Porter, D. W.; Sreenivasan, R.; McIntyre, P. C.; Bent, S. F. ALD resist formed by vapor-deposited self-assembled monolayers. *Langmuir* **2007**, *23* (3), 1160-1165. DOI: 10.1021/la0606401.

(104) Halls, M. D.; Raghavachari, K. Atomic layer deposition of Al
O
on H-passivated Si.: I.: Initial surface reaction pathways with H/Si(100)-2X1. *J Chem Phys* **2003**, *118* (22), 10221-10226. DOI: 10.1063/1.1571513.

(105) Tai, T. B.; Cao, L. A.; Mattelaer, F.; Rampelberg, G.; Hashemi, F. S. M.; Dendooven, J.; van Ommen, J. R.; Detavernier, C.; Reyniers, M. F. Atomic Layer Deposition of Al2O3 Using Aluminum Triisopropoxide (ATIP): A Combined Experimental and Theoretical Study. *J Phys Chem C* **2019**, *123* (1), 485-494. DOI: 10.1021/acs.jpcc.8b09198.

(106) Pinder, J. W.; Major, G. H.; Baer, D. R.; Terry, J.; Whitten, J. E.; Cechal, J.; Crossman, J. D.; Lizarbe, A. J.; Jafari, S.; Easton, C. D.; et al. Avoiding common errors in X-ray photoelectron spectroscopy data collection and analysis, and properly reporting instrument parameters. *Appl Surf Sci Adv* **2024**, *19*. DOI: ARTN 100534 10.1016/j.apsadv.2023.100534.

(107) Jiang, X. R.; Bent, S. F. Area-Selective ALD with Soft Lithographic Methods: Using Self-Assembled Monolayers to Direct Film Deposition. *J Phys Chem C* **2009**, *113* (41), 17613-17625. DOI: 10.1021/jp905317n.

(108) Lale, A.; Joly, M.; Mekkaoui, S.; Joly, X.; Scheid, E.; Launay, J.; Temple-Boyer, P. Effect of thermal annealing on the dielectric, passivation and pH detection properties of aluminium oxide

thin films deposited by plasma-enhanced atomic layer deposition. *Thin Solid Films* **2021**, *732*. DOI: ARTN 138761
10.1016/j.tsf.2021.138761.

(109) Zhu, Z.; Merdes, S.; Ylivaara, O. M. E.; Mizohata, K.; Heikkilä, M. J.; Savin, H. Al
O
Thin Films Prepared by a Combined Thermal-Plasma Atomic Layer Deposition Process at Low Temperature for Encapsulation Applications. *Phys Status Solidi A* **2020**, *217* (8). DOI: ARTN 1900237
10.1002/pssa.201900237.

(110) Zhu, Z.; Sippola, P.; Lipsanen, H.; Saving, H.; Merdes, S. Influence of plasma parameters on the properties of ultrathin Al
O
films prepared by plasma enhanced atomic layer deposition below 100 °C for moisture barrier applications. *Jpn J Appl Phys* **2018**, *57* (12). DOI: Artn 125502
10.7567/Jjap.57.125502.

(111) Haeberle, J.; Henkel, K.; Gargouri, H.; Naumann, F.; Gruska, B.; Arens, M.; Tallarida, M.; Schmeisser, D. Ellipsometry and XPS comparative studies of thermal and plasma enhanced atomic layer deposited Al
O
-films. *Beilstein J Nanotech* **2013**, *4*, 732-742. DOI: 10.3762/bjnano.4.83.

(112) Castillo-Saenz, J.; Nedev, N.; Valdez-Salas, B.; Curiel-Alvarez, M.; Mendivil-Palma, M. I.; Hernandez-Como, N.; Martinez-Puente, M.; Mateos, D.; Perez-Landeros, O.; Martinez-Guerra, E. Properties of Al
O
Thin Films Grown by PE-ALD at Low Temperature Using H
O and O
Plasma Oxidants. *Coatings* **2021**, *11* (10). DOI: ARTN 1266
10.3390/coatings11101266.

(113) Li, M. J.; Breeden, M.; Wang, V.; Linn, N. M. K.; Winter, C. H.; Kummel, A.; Bakir, M. S. Characterization of Low-Temperature Selective Cobalt Atomic Layer Deposition (ALD) for Chip Bonding. *Ieee Int Interc Tech* **2021**. DOI: 10.1109/Iitc51362.2021.9537353.

(114) Schilirò, E.; Fiorenza, P.; Greco, G.; Roccaforte, F.; Lo Nigro, R. Plasma enhanced atomic layer deposition of Al
O
gate dielectric thin films on AlGaN/GaN substrates: The role of surface predeposition treatments. *J Vac Sci Technol A* **2017**, *35* (1). DOI: Artn 01b140

10.1116/1.4972257.

(115) Ott, J.; Pasanen, T. P.; Gädda, A.; Garín, M.; Rosta, K.; Vähänissi, V.; Savin, H. Impact of doping and silicon substrate resistivity on the blistering of atomic-layer-deposited aluminium oxide. *Appl Surf Sci* **2020**, *522*. DOI: ARTN 146400
10.1016/j.apsusc.2020.146400.

(116) Salami, H.; Poissant, A.; Adomaitis, R. A. Anomalously high alumina atomic layer deposition growth per cycle during trimethylaluminum under-dosing conditions. *J Vac Sci Technol A* **2017**, *35* (1). DOI: Artn 01b101
10.1116/1.4963368.

(117) Puurunen, R. L. Correlation between the growth-per-cycle and the surface hydroxyl group concentration in the atomic layer deposition of aluminum oxide from trimethylaluminum and water. *Appl Surf Sci* **2005**, *245* (1-4), 6-10. DOI: 10.1016/j.apsusc.2004.10.003.

(118) Ott, A. W.; McCarley, K. C.; Klaus, J. W.; Way, J. D.; George, S. M. Atomic layer controlled deposition of Al2O3 films using binary reaction sequence chemistry. *Applied Surface Science* **1996**, *107*, 128-136. DOI: Doi 10.1016/S0169-4332(96)00503-X.

(119) Kuse, R.; Kundu, M.; Yasuda, T.; Miyata, N.; Toriumi, A. Effect of precursor concentration in atomic layer deposition of Al
O. *J Appl Phys* **2003**, *94* (10), 6411-6416. DOI: 10.1063/1.1618918.

(120) Sonsteby, H. H.; Yanguas-Gil, A.; Elam, J. W. Consistency and reproducibility in atomic layer deposition. *J Vac Sci Technol A* **2020**, *38* (2). DOI: 10.1116/1.5140603.

(121) D. Choudhury, A. U. M., C. M. Patak, A. K. Petford Long, and J. W. Elam. AVS 65th International Symposium & Exhibition. **2018**. (acccessed June 23, 2024).

(122) Methaapanon, R.; Bent, S. F. Comparative Study of Titanium Dioxide Atomic Layer Deposition on Silicon Dioxide and Hydrogen-Terminated Silicon. *J Phys Chem C* **2010**, *114* (23), 10498-10504. DOI: 10.1021/jp1013303.

(123) Silva-Quinones, D.; Mason, J. R.; Norden, R.; Teplyakov, A. V. Inhibition of atomic layer deposition of TiO
by functionalizing silicon surface with 4-fluorophenylboronic acid. *J Vac Sci Technol A* **2024**, *42* (3). DOI: Artn 032402
10.1116/6.0003316.

(124) Mameli, A.; Teplyakov, A. V. Selection Criteria for Small-Molecule Inhibitors in Area-Selective Atomic Layer Deposition: Fundamental Surface Chemistry Considerations. *Accounts Chem Res* **2023**, *56* (15), 2084-2095. DOI: 10.1021/acs.accounts.3c00221.

(125) Parke, T.; Silva-Quinones, D.; Wang, G. T.; Teplyakov, A. V. The Effect of Surface Terminations on the Initial Stages of TiO
Deposition on Functionalized Silicon. *Chemphyschem* **2023**, *24* (7). DOI: 10.1002/cphc.202200724.

(126) Wang, L. M.; Schubert, U. S.; Hoeppener, S. Surface chemical reactions on self-assembled silane based monolayers. *Chem Soc Rev* **2021**, *50* (11), 6507-6540. DOI: 10.1039/d0cs01220c.

(127) Condorelli, G. G.; Tudisco, C.; Motta, A.; Di Mauro, A.; Lupo, F.; Gulino, A.; Fragalà, I. L. Multistep Anchoring Route of Luminescent (5-Amino-1,10-phenanthroline)tris(dibenzoylmethane)europium(III) on Si(100). *Eur J Inorg Chem* **2010**, (26), 4121-4129. DOI: 10.1002/ejic.201000272.

(128) Merkx, M. J. M.; Jongen, R. G. J.; Mameli, A.; Lemaire, P. C.; Sharma, K.; Hausmann, D. M.; Kessels, W. M. M.; Mackus, A. J. M. Insight into the removal and reapplication of small inhibitor molecules during area-selective atomic layer deposition of SiO2. *J Vac Sci Technol A* **2021**, *39* (1). DOI: Artn 012402
10.1116/6.0000652.

(129) Rozyyev, V.; Murphy, J. G.; Barry, E.; Mane, A. U.; Sibener, S. J.; Elam, J. W. Vapor-phase grafting of a model aminosilane compound to Al2O3, ZnO, and TiO2 surfaces prepared by atomic layer deposition. *Appl Surf Sci* **2021**, *562*. DOI: ARTN 149996
10.1016/j.apsusc.2021.149996.

(130) Vos, M. F. J.; Chopra, S. N.; Ekerdt, J. G.; Agarwal, S.; Kessels, W. M. M.; Mackus, A. J. M. Atomic layer deposition and selective etching of ruthenium for area-selective deposition: Temperature dependence and supercycle design. *J Vac Sci Technol A* **2021**, *39* (3). DOI: Artn 032412
10.1116/6.0000912.

(131) Perrine, K. A.; Teplyakov, A. V. Reactivity of selectively terminated single crystal silicon surfaces. *Chem Soc Rev* **2010**, *39* (8), 3256-3274. DOI: 10.1039/b822965c.

(132) Clark, R.; Tapily, K.; Yu, K. H.; Hakamata, T.; Consiglio, S.; O'Meara, D.; Wajda, C.; Smith, J.; Leusink, G. Perspective: New process technologies required for future devices and scaling. *Apl Mater* **2018**, *6* (5). DOI: Artn 058203
10.1063/1.5026805.

(133) He, J.; Patitsas, S. N.; Preston, K. F.; Wolkow, R. A.; Wayner, D. D. M. Covalent bonding of thiophenes to Si(111) by a halogenation/thienylation route. *Chem Phys Lett* **1998**, *286* (5-6), 508-514. DOI: Doi 10.1016/S0009-2614(98)00128-6.

(134) Yu, W. H.; Kang, E. T.; Neoh, K. G.; Zhu, S. P. Controlled grafting of well-defined polymers on hydrogen-terminated silicon substrates by surface-initiated atom transfer radical polymerization. *J Phys Chem B* **2003**, *107* (37), 10198-10205. DOI: 10.1021/jp034330s.

(135) Coffinier, Y.; Piret, G.; Das, M. R.; Boukherroub, R. Effect of surface roughness and chemical composition on the wetting properties of silicon-based substrates. *Cr Chim* **2013**, *16* (1), 65-72. DOI: 10.1016/j.crci.2012.08.011.

(136) Frederick, E.; Dwyer, K. J.; Wang, G. T.; Misra, S.; Butera, R. E. The stability of Cl-, Br-, and I-passivated Si(100)-(2 x 1) in ambient environments for atomically-precise pattern preservation. *J Phys-Condens Mat* **2021**, *33* (44). DOI: ARTN 444001
10.1088/1361-648X/ac1aa4.

(137) Rogozhina, E.; Belomoin, G.; Smith, A.; Abuhassan, L.; Barry, N.; Akcakir, O.; Braun, P. V.; Nayfeh, M. H. Si-N linkage in ultrabright, ultrasmall Si nanoparticles. *Appl Phys Lett* **2001**, *78* (23), 3711-3713. DOI: Doi 10.1063/1.1377619.

(138) Ferng, S. S.; Wu, S. T.; Lin, D. S.; Chiang, T. C. Mediation of chain reactions by propagating radicals during halogenation of H-masked Si(100): Implications for atomic-scale lithography and processing. *J Chem Phys* **2009**, *130* (16). DOI: Artn 164706
10.1063/1.3122987.

(139) Rivillon, S.; Brewer, R. T.; Chabal, Y. J. Water reaction with chlorine-terminated silicon (111) and (100) surfaces. *Appl Phys Lett* **2005**, *87* (17). DOI: Artn 173118
10.1063/1.2119426.

(140) Dumas, P.; Chabal, Y. J.; Jakob, P. Morphology of Hydrogen-Terminated Si(111) and Si(100) Surfaces Upon Etching in Hf and Buffered-Hf Solutions. *Surf Sci* **1992**, *269*, 867-878. DOI: Doi 10.1016/0039-6028(92)91363-G.

(141) Layadi, N.; Donnelly, V. M.; Lee, J. T. C. Cl-2 plasma etching of Si(100): Nature of the chlorinated surface layer studied by angle-resolved x-ray photoelectron spectroscopy. *J Appl Phys* **1997**, *81* (10), 6738-6748. DOI: Doi 10.1063/1.365216.

(142) Butera, R. E.; Suwa, Y.; Hashizume, T.; Weaver, J. H. Adsorbate-mediated step transformations and terrace rearrangement of Si(100)-(2x1). *Phys Rev B* **2009**, *80* (19). DOI: ARTN 193307
10.1103/PhysRevB.80.193307.

(143) Aldao, C. M.; Agrawal, A.; Butera, R. E.; Weaver, J. H. Atomic processes during Cl supersaturation etching of Si(100)-(2x1). *Phys Rev B* **2009**, *79* (12). DOI: ARTN 125303 10.1103/PhysRevB.79.125303.

(144) Biswas, S.; Narasimhan, S. Bromine as a Preferred Etchant for Si Surfaces in the Supersaturation Regime: Insights from Calculations of Atomic Scale Reaction Pathways. *J Phys Chem C* **2016**, *120* (28), 15230-15234. DOI: 10.1021/acs.jpcc.6b04450.

(145) Pavlova, T. V.; Shevlyuga, V. M.; Andryushechkin, B. V.; Eltsov, K. N. Chlorine insertion and manipulation on the Si(100)-2 x 1-Cl surface in the regime of local supersaturation. *Phys Rev B* **2020**, *101* (23). DOI: ARTN 235410 10.1103/PhysRevB.101.235410.

(146) Rivillon, S.; Chabal, Y. J.; Webb, L. J.; Michalak, D. J.; Lewis, N. S.; Halls, M. D.; Raghavachari, K. Chlorination of hydrogen-terminated silicon(111) surfaces. *J Vac Sci Technol A* **2005**, *23* (4), 1100-1106. DOI: 10.1116/1.1861941.

(147) Solares, S. D.; Yu, H. B.; Webb, L. J.; Lewis, N. S.; Heath, J. R.; Goddard, W. A. Chlorination-methylation of the hydrogen-terminated silicon(111) surface can induce a stacking fault in the presence of etch pits. *J Am Chem Soc* **2006**, *128* (12), 3850-3851. DOI: 10.1021/ja055408g.

(148) Kornev, A. N. Tris(trimethylsilyl)silyl group in organic, coordination and organometallic chemistry. *Usp Khim+* **2004**, *73* (11), 1155-1180.

(149) Suarez, D.; Laval, G.; Tu, S. M.; Jiang, D.; Robinson, C. L.; Scott, R.; Golding, B. T. Benzylic Brominations with N-Bromosuccinimide in (Trifluoromethyl)benzene. *Synthesis-Stuttgart* **2009**, (11), 1807-1810. DOI: 10.1055/s-0029-1216793.

(150) Parke, T.; Silva-Quinones, D.; Wang, G. T.; Teplyakov, A. V. The Effect of Surface Terminations on the Initial Stages of TiO2 Deposition on Functionalized Silicon. *Chemphyschem* **2023**. DOI: 10.1002/cphc.202200724.

(151) Bell, J. P.; Cloud, J. E.; Cheng, J. F.; Ngo, C.; Kodambaka, S.; Sellinger, A.; Williams, S. K. R.; Yang, Y. A. N-Bromosuccinimide-based bromination and subsequent functionalization of hydrogen-terminated silicon quantum dots. *Rsc Adv* **2014**, *4* (93), 51105-51110. DOI: 10.1039/c4ra08477b.

(152) Baldwin, R. K.; Pettigrew, K. A.; Ratai, E.; Augustine, M. P.; Kauzlarich, S. M. Solution reduction synthesis of surface stabilized silicon nanoparticles. *Chem Commun* **2002**, (17), 1822-1823. DOI: 10.1039/b205301b.

(153) Zou, J.; Baldwin, R. K.; Pettigrew, K. A.; Kauzlarich, S. M. Solution synthesis of ultrastable luminescent siloxane-coated silicon nanoparticles. *Nano Lett* **2004**, *4* (7), 1181-1186. DOI: 10.1021/nl0497373.

(154) Rogozhina, E. V.; Eckhoff, D. A.; Gratton, E.; Braun, P. V. Carboxyl functionalization of ultrasmall luminescent silicon nanoparticles through thermal hydrosilylation. *J Mater Chem* **2006**, *16* (15), 1421-1430. DOI: 10.1039/b509868h.

(155) Dasog, M.; Veinot, J. G. C. Size independent blue luminescence in nitrogen passivated silicon nanocrystals. *Phys Status Solidi A* **2012**, *209* (10), 1844-1846. DOI: 10.1002/pssa.201200273.

(156) Lee, J. C.; Bae, Y. H.; Chang, S. K. Efficient α-halogenation of carbonyl compounds by
-bromosuccinimide and
-chlorosuccinimde. *B Kor Chem Soc* **2003**, *24* (4), 407-408.

(157) Bergstrom, M.; Suresh, G.; Naidu, V. R.; Unelius, C. R. -Iodosuccinimide (NIS) in Direct Aromatic Iodination. *Eur J Org Chem* **2017**, *2017* (22), 3234-3239. DOI: 10.1002/ejoc.201700173.

(158) Zhao, S.; Liu, W. K. Methods for Brominations at Benzylic Positions. *Curr Org Chem* **2018**, *22* (25), 2444-2459. DOI: 10.2174/1385272822666181031094702.

(159) Williams, P. J. H.; Boustead, G. A.; Heard, D. E.; Seakins, P. W.; Rickard, A. R.; Chechik, V. New Approach to the Detection of Short-Lived Radical Intermediates. *J Am Chem Soc* **2022**, *144* (37), 15969-15976. DOI: 10.1021/jacs.2c03618.

(160) Turecek, F.; Julian, R. R. Peptide Radicals and Cation Radicals in the Gas Phase. *Chem Rev* **2013**, *113* (8), 6691-6733. DOI: 10.1021/cr400043s.

(161) Born, M.; Ingemann, S.; Nibbering, N. M. M. Formation and chemistry of radical anions in the gas phase. *Mass Spectrom Rev* **1997**, *16* (4), 181-200. DOI: Doi 10.1002/(Sici)1098-2787(1997)16:4<181::Aid-Mas2>3.0.Co;2-D.

(162) Bera, S. K.; Mal, P. Mechanochemical-Cascaded C-N Cross-Coupling and Halogenation Using N-Bromo- and N-Chlorosuccinimide as Bifunctional Reagents. *J Org Chem* **2021**, *86* (20), 14144-14159. DOI: 10.1021/acs.joc.1c01742.

(163) O'Leary, L. E.; Rose, M. J.; Ding, T. X.; Johansson, E.; Brunschwig, B. S.; Lewis, N. S. Heck Coupling of Olefins to Mixed Methyl/Thienyl Monolayers on Si(111) Surfaces. *J Am Chem Soc* **2013**, *135* (27), 10081-10090. DOI: 10.1021/ja402495e.

(164) Lauerhaas, J. M.; Sailor, M. J. Chemical Modification of the Photoluminescence Quenching of Porous Silicon. *Science* **1993**, *261* (5128), 1567-1568. DOI: DOI 10.1126/science.261.5128.1567.

(165) Silva-Quinones, D.; He, C.; Dwyer, K. J.; Butera, R. E.; Wang, G. T.; Teplyakov, A. V. Reaction of Hydrazine with Solution- and Vacuum-Prepared Selectively Terminated Si(100) Surfaces: Pathways to the Formation of Direct Si-N Bonds. *Langmuir* **2020**, *36* (43), 12866-12876. DOI: 10.1021/acs.langmuir.0c02088.

(166) C.D. Wagner, A. V. N., A. Kraut-Vass, J.W. Allison, C.J. Powell, J.R.Jr. . *NIST Standard Reference Database 20, Version 3.4* NIST, 2003. (accessed.

(167) Haber, J. A.; Lewis, N. S. Infrared and X-ray photoelectron spectroscopic studies of the reactions of hydrogen-terminated crystalline Si(111) and Si(100) surfaces with Br-2, I-2, and ferrocenium in alcohol solvents. *J Phys Chem B* **2002**, *106* (14), 3639-3656. DOI: 10.1021/jp0102872.

(168) Hinckley, A. P.; Driskill, M. M.; Muscat, A. J. Dense Organosilane Monolayer Resist That Directs Highly Selective Atomic Layer Deposition. *Acs Appl Nano Mater* **2020**, *3* (4), 3185-3194. DOI: 10.1021/acsanm.9b02128.

(169) Ulman, A. Formation and structure of self-assembled monolayers. *Chem Rev* **1996**, *96* (4), 1533-1554. DOI: DOI 10.1021/cr9502357.

(170) Hutchins, D. O.; Acton, O.; Weidner, T.; Cernetic, N.; Baio, J. E.; Ting, G.; Castner, D. G.; Ma, H.; Jen, A. K. Y. Spin cast self-assembled monolayer field effect transistors. *Org Electron* **2012**, *13* (3), 464-468. DOI: 10.1016/j.orgel.2011.11.025.

(171) Mameli, A.; Merkx, M. J. M.; Karasulu, B.; Roozeboom, F.; Kessels, W. M. M.; Mackus, A. J. M. Area-Selective Atomic Layer Deposition of SiO2 Using Acetylacetone as a Chemoselective Inhibitor in an ABC-Type Cycle. *Acs Nano* **2017**, *11* (9), 9303-9311. DOI: 10.1021/acsnano.7b04701.

(172) Fang, M.; Ho, J. C. Area-Selective Atomic Layer Deposition: Conformal Coating, Subnanometer Thickness Control, and Smart Positioning. *Acs Nano* **2015**, *9* (9), 8651-8654. DOI: 10.1021/acsnano.5b05249.

(173) Garín, M.; Khoury, R.; Martin, I.; Johnson, E. V. Direct etching at the nanoscale through nanoparticle-directed capillary condensation. *Nanoscale* **2020**, *12* (16), 9240-9245. DOI: 10.1039/c9nr10217e.

(174) Salimian, S.; Delfino, M. Removal of Native Silicon-Oxide with Low-Energy Argon Ions. *J Appl Phys* **1991**, *70* (7), 3970-3972. DOI: Doi 10.1063/1.349160.

(175) Briggs, D.; Wootton, A. B. Analysis of Polymer Surfaces by Sims .1. An Investigation of Practical Problems. *Surf Interface Anal* **1982**, *4* (3), 109-115. DOI: DOI 10.1002/sia.740040306.

(176) Shircliff, R. A.; Stradins, P.; Moutinho, H.; Fennell, J.; Ghirardi, M. L.; Cowley, S. W.; Branz, H. M.; Martin, I. T. Angle-Resolved XPS Analysis and Characterization of Mono layer and Multi layer Si lane Films for DNA Coupling to Silica. *Langmuir* **2013**, *29* (12), 4057-4067. DOI: 10.1021/la304719y.

(177) Lockett, V.; Sedev, R.; Bassell, C.; Ralston, J. Angle-resolved X-ray photoelectron spectroscopy of the surface of imidazolium ionic liquids. *Phys Chem Chem Phys* **2008**, *10* (9), 1330-1335. DOI: 10.1039/b713584j.

(178) Laibinis, P. E.; Bain, C. D.; Whitesides, G. M. Attenuation of Photoelectrons in Monolayers of Normal-Alkanethiols Adsorbed on Copper, Silver, and Gold. *J Phys Chem-Us* **1991**, *95* (18), 7017-7021. DOI: DOI 10.1021/j100171a054.

(179) Li, X. Z.; Ma, W. C.; Shestopalov, A. A. Vapor-Phase Carbenylation of Hard and Soft Material Interfaces. *Langmuir* **2016**, *32* (44), 11386-11394. DOI: 10.1021/acs.langmuir.6b02471.

(180) Constantinou, P.; Stock, T. J. Z.; Tseng, L.; Kazazis, D.; Muntwiler, M.; Vaz, C. A. F.; Ekinci, Y.; Aeppli, G.; Curson, N. J.; Schofield, S. R. EUV-induced hydrogen desorption as a step towards large-scale silicon quantum device patterning. *Nat Commun* **2024**, *15* (1). DOI: ARTN 694 10.1038/s41467-024-44790-6.

(181) Yang, Y.; Xu, Y. Direct etching of nano/microscale patterns with both few-layer graphene and high-depth graphite structures by the raster STM electric lithography in the ambient conditions. *J Microsc-Oxford* **2023**, *292* (1), 37-46. DOI: 10.1111/jmi.13224.

(182) Dwyer, K. J.; Dreyer, M.; Butera, R. E. STM-Induced Desorption and Lithographic Patterning of Cl-Si(100)-(2 x 1). *J Phys Chem A* **2019**, *123* (50), 10793-10803. DOI: 10.1021/acs.jpca.9b07127.

(183) Green, M. L.; Gusev, E. P.; Degraeve, R.; Garfunkel, E. L. Ultrathin (< 4 nm) SiO(2) and Si-O-N gate dielectric layers for silicon microelectronics:: Understanding the processing, structure, and physical and electrical limits. *J Appl Phys* **2001**, *90* (5), 2057-2121. DOI: Doi 10.1063/1.1385803.

(184) Cottom, J.; Huckmann, L.; Olsson, E.; Meyer, J. From Jekyll to Hyde and Beyond: Hydrogen's Multifaceted Role in Passivation, H-Induced Breakdown, and Charging of Amorphous Silicon Nitride. *J Phys Chem Lett* **2024**, *15* (3), 840-848. DOI: 10.1021/acs.jpclett.3c03376.

(185) Hamoudi, A. M.; Choubani, K.; Ben Rabha, M. Multicrystalline Silicon Passivation by Hydrogen and Oxygen-Rich Porous Silicon Layer for Photovoltaic Cells Applications. *Iran J Mater Sci Eng* **2023**, *20* (2). DOI: ARTN 2908
10.22068/ijmse.2908.

(186) Sun, Z. Y.; Wang, L.; Luo, H.; Hamer, P.; Ye, H.; Hallam, B. Study of the Hydrogen Passivation Effect of Low-Temperature-Deposited Amorphous Silicon Layers on SiGe Solar Cells Grown on a Silicon Substrate. *Acs Appl Energ Mater* **2023**, *6* (23), 12064-12071. DOI: 10.1021/acsaem.3c02283.

(187) Grayson, A. C. R.; Shawgo, R. S.; Johnson, A. M.; Flynn, N. T.; Li, Y. W.; Cima, M. J.; Langer, R. A BioMEMS review: MEMS technology for physiologically integrated devices. *P Ieee* **2004**, *92* (1), 6-21. DOI: 10.1109/Jproc.2003.820534.

(188) Aygun, G.; Atanassova, E.; Alacakir, A.; Ozyuzer, L.; Turan, R. Oxidation of Si surface by a pulsed Nd:YAG laser. *J Phys D Appl Phys* **2004**, *37* (11), 1569-1575. DOI: Pii S0022-3727(04)78415-6
10.1088/0022-3727/37/11/011.

(189) Kailath, B. J.; DasGupta, A.; DasGupta, N.; Singh, B. N.; Kukreja, L. M. Growth of ultra-thin SiO2 by laser-induced oxidation. *Semicond Sci Tech* **2009**, *24* (10). DOI: Artn 105011
10.1088/0268-1242/24/10/105011.

(190) Osipov, A. V.; Patzner, P.; Hess, P. Kinetics of laser-induced oxidation of silicon near room temperature. *Appl Phys a-Mater* **2006**, *82* (2), 275-280. DOI: 10.1007/s00339-005-3415-x.

(191) Jia, Z. C.; Sun, L. H.; Chen, X.; Li, X. H.; Li, Z. W.; Hao, L. Y. Thermal process of a silicon wafer under a CW laser and 100-10000 Hz pulsed laser irradiation. *Appl Optics* **2023**, *62* (36), 9577-9582. DOI: 10.1364/Ao.501947.

(192) Behrenberg, D.; Franzka, S.; Petermann, N.; Wiggers, H.; Hartmann, N. Photothermal laser processing of thin silicon nanoparticle films: on the impact of oxide formation on film morphology. *Appl Phys a-Mater* **2012**, *106* (4), 853-861. DOI: 10.1007/s00339-012-6779-8.

(193) An, H. J.; Wang, J. S.; Fang, F. Z. Study on surface thermal oxidation of silicon carbide irradiated by pulsed laser using reactive molecular dynamics. *J Chem Phys* **2023**, *158* (10). DOI: Artn 104702
10.1063/5.0137778.

(194) Katzenmeyer, A. M.; Dmitrovic, S.; Baczewski, A. D.; Campbell, Q.; Bussmann, E.; Lu, T. M.; Anderson, E. M.; Schmucker, S. W.; Ivie, J. A.; Campbell, D. M.; et al. Photothermal alternative to

device fabrication using atomic precision advanced manufacturing techniques. *J Micro-Nanopattern* **2021**, *20* (1). DOI: Artn 014901
10.1117/1.Jmm.20.1.014901.

(195) Hallam, T.; Butcher, M. J.; Goh, K. E. J.; Ruess, F. J.; Simmons, M. Y. Use of a scanning electron microscope to pattern large areas of a hydrogen resist for electrical contacts. *J Appl Phys* **2007**, *102* (3). DOI: Artn 034308
10.1063/1.2736873.

(196) Srinivasan, C.; Mullen, T. J.; Hohman, J. N.; Anderson, M. E.; Dameron, A. A.; Andrews, A. M.; Dickey, E. C.; Horn, M. W.; Weiss, P. S. Scanning electron microscopy of nanoscale chemical patterns. *Acs Nano* **2007**, *1* (3), 191-201. DOI: 10.1021/nn7000799.

(197) Nayar, V.; Boyd, I. W.; Goodall, F. N.; Arthur, G. Low-Temperature Oxidation of Crystalline Silicon Using Excimer Laser Irradiation. *Appl Surf Sci* **1989**, *36* (1-4), 134-140. DOI: Doi 10.1016/0169-4332(89)90906-9.

(198) Jin, Y. G.; Chang, K. J. Mechanism for the enhanced diffusion of charged oxygen ions in SiO. *Phys Rev Lett* **2001**, *86* (9), 1793-1796. DOI: DOI 10.1103/PhysRevLett.86.1793.

(199) Liu, Y. A.; Ding, Y.; Xie, J. C.; Xu, L. L.; Jeong, I. W.; Yang, L. J. One-Step Femtosecond Laser Irradiation of Single-Crystal Silicon: Evolution of Micro-Nano Structures and Damage Investigation. *Mater Design* **2023**, *225*. DOI: ARTN 111443
10.1016/j.matdes.2022.111443.

(200) Kuladeep, R.; Jyothi, L.; Sahoo, C.; Rao, D. N.; Saikiran, V. Optical, structural and morphological studies of nanostructures fabricated on silicon surface by femtosecond laser irradiation. *J Mater Sci* **2022**, *57* (3), 1863-1880. DOI: 10.1007/s10853-021-06712-5.

(201) Gibbons, J. F. Applications of Scanning Cw Lasers and Electron-Beams in Silicon Technology. *Jpn J Appl Phys* **1980**, *19*, 121-128. DOI: Doi 10.7567/Jjaps.19s1.121.

(202) Boyd, I. W. Laser-Enhanced Oxidation of Si. *Appl Phys Lett* **1983**, *42* (8), 728-730. DOI: Doi 10.1063/1.94041.

(203) Tsetseris, L.; Zhou, X. J.; Fleetwood, D. M.; Schrimpf, R. D.; Pantelides, S. T. Physical mechanisms of negative-bias temperature instability. *Appl Phys Lett* **2005**, *86* (14). DOI: Artn 142103
10.1063/1.1897075.

(204) Fleetwood, D. M. Interface traps, correlated mobility fluctuations, and low-frequency noise in metal-oxide-semiconductor transistors. *Appl Phys Lett* **2023**, *122* (17). DOI: Artn 173504 10.1063/5.0146549.

(205) Gupta, P.; Colvin, V. L.; George, S. M. Hydrogen Desorption-Kinetics from Monohydride and Dihydride Species on Silicon Surfaces. *Phys Rev B* **1988**, *37* (14), 8234-8243. DOI: DOI 10.1103/PhysRevB.37.8234.

(206) Greenlief, C. M.; Armstrong, M. Hydrogen Desorption from Si - How Does This Relate to Film Growth. *J Vac Sci Technol B* **1995**, *13* (4), 1810-1815. DOI: Doi 10.1116/1.587817.

(207) Jellison, G. E.; Modine, F. A. Optical Functions of Silicon between 1.7 and 4.7 Ev at Elevated-Temperatures. *Phys Rev B* **1983**, *27* (12), 7466-7472. DOI: DOI 10.1103/PhysRevB.27.7466.

(208) Prakash, C. Thermal-Conductivity Variation of Silicon with Temperature. *Microelectron Reliab* **1978**, *18* (4), 333-333. DOI: Doi 10.1016/0026-2714(78)90573-5.

(209) Uchida, Y.; Yue, J.; Kamase, F.; Suzuki, T.; Hattori, T.; Matsumura, M. Low-Temperature Thermal-Oxidation of Silicon. *Jpn J Appl Phys 1* **1986**, *25* (11), 1633-1639. DOI: Doi 10.1143/Jjap.25.1633.

(210) Lewis, E. A.; Irene, E. A. The Effect of Surface Orientation on Silicon Oxidation-Kinetics. *J Electrochem Soc* **1987**, *134* (9), 2332-2339. DOI: Doi 10.1149/1.2100881.

(211) Bashouti, M. Y.; Pietsch, M.; Sardashti, K.; Brönstrup, G.; Schmitt, S. W.; Srivastava, S. K.; Ristein, J.; Arbiol, J.; Haick, H.; Christiansen, S. Hybrid Silicon Nanowires: From Basic Research to Applied Nanotechnology. *Nanowires - Recent Advances* **2012**, 177-210. DOI: 10.5772/54383.

(212) Lee, S. W.; Kang, T. H.; Lee, S. K.; Lee, K. Y.; Yi, H. Hydrodynamic Layer-by-Layer Assembly of Transferable Enzymatic Conductive Nanonetworks for Enzyme-Sticker-Based Contact Printing of Electrochemical Biosensors. *Acs Appl Mater Inter* **2018**, *10* (42), 36267-36274. DOI: 10.1021/acsami.8b13070.

(213) Parashkov, R.; Becker, E.; Riedl, T.; Johannes, H. H.; Kowalsky, W. Microcontact printing as a versatile tool for patterning organic field-effect transistors. *Adv Mater* **2005**, *17* (12), 1523-1527. DOI: 10.1002/adma.200401967.

(214) Jiang, X. R.; Chen, R.; Bent, S. F. Spatial control over atomic layer deposition using microcontact-printed resists. *Surf Coat Tech* **2007**, *201* (22-23), 8799-8807. DOI: 10.1016/j.surfcoat.2007.04.126.

(215) Mameli, A.; Karasulu, B.; Verheijen, M. A.; Barcones, B.; Macco, B.; Mackus, A. J. M.; Kessels, W. M. M. E.; Roozeboom, F. Area-Selective Atomic Layer Deposition of ZnO by Area Activation Using Electron Beam-Induced Deposition. *Chem Mater* **2019**, *31* (4), 1250-1257. DOI: 10.1021/acs.chemmater.8b03165.

(216) Seisyan, R. P. Nanolithography in microelectronics: A review. *Tech Phys+* **2011**, *56* (8), 1061-1073. DOI: 10.1134/S1063784211080214.

(217) Quist, A. P.; Pavlovic, E.; Oscarsson, S. Recent advances in microcontact printing. *Anal Bioanal Chem* **2005**, *381* (3), 591-600. DOI: 10.1007/s00216-004-2847-z.

(218) Shestopalov, A. A.; Morris, C. J.; Vogen, B. N.; Hoertz, A.; Clark, R. L.; Toone, E. J. Soft-Lithographic Approach to Functionalization and Nanopatterning Oxide-Free Silicon. *Langmuir* **2011**, *27* (10), 6478-6485. DOI: 10.1021/la200373g.

(219) Jiang, L.; Wu, M. J.; Yu, Q. P.; Shan, Y. X.; Zhang, Y. Y. Investigations on the Adhesive Contact Behaviors between a Viscoelastic Stamp and a Transferred Element in Microtransfer Printing. *Coatings* **2021**, *11* (10). DOI: ARTN 1201
10.3390/coatings11101201.

(220) Kim, J.; Park, J.; Lee, S.; Sohn, D. Surface-grafting of polyglutamate on Si wafer using micro contact printing. *Mol Cryst Liq Cryst* **2007**, *464*, 793-798. DOI: 10.1080/15421400601031017.

(221) Zumeit, A.; Dahiya, A. S.; Christou, A.; Shakthivel, D.; Dahiya, R. Direct roll transfer printed silicon nanoribbon arrays based high-performance flexible electronics. *Npj Flex Electron* **2021**, *5* (1). DOI: ARTN 18
10.1038/s41528-021-00116-w.

(222) Chen, T.; Jordan, R.; Zauscher, S. Extending micro-contact printing for patterning complex polymer brush microstructures. *Polymer* **2011**, *52* (12), 2461-2467. DOI: 10.1016/j.polymer.2011.04.008.

(223) Lu, H. B.; Homola, J.; Campbell, C. T.; Nenninger, G. G.; Yee, S. S.; Ratner, B. D. Protein contact printing for a surface plasmon resonance biosensor with on-chip referencing. *Sensor Actuat B-Chem* **2001**, *74* (1-3), 91-99. DOI: Doi 10.1016/S0925-4005(00)00716-4.

(224) Chen, Y. F. Recent Progress in Nanofabrication of High Resolution X-Ray Zone Plate Lenses by Electron Beam Lithography. *Acta Opt Sin* **2022**, *42* (11). DOI: Artn 1134005
10.3788/Aos202242.1134005.

(225) Pimpin, A.; Srituravanich, W. Review on Micro- and Nanolithography Techniques and their Applications. *Eng J-Thail* **2012**, *16* (1), 37-55. DOI: 10.4186/ej.2012.16.1.37.

(226) Cao, Y. L.; Liu, Z. T.; Chen, L. M.; Tang, Y. B.; Luo, L. B.; Lee, S. T.; Lee, C. S. In-Situ Phosphrous Doping in ZnTe Nanowires with Enhanced p-type Conductivity. *J Nanosci Nanotechno* **2012**, *12* (3), 2353-2359. DOI: 10.1166/jnn.2012.5752.

(227) Gonzalez-Zalba, M. F.; de Franceschi, S.; Charbon, E.; Meunier, T.; Vinets, M.; Dzurak, A. S. Scaling silicon-based quantum computing using CMOS technology. *Nat Electron* **2021**, *4* (12), 872-884. DOI: 10.1038/s41928-021-00681-y.

(228) Leong, M.; Doris, B.; Kedzierski, J.; Rim, K.; Yang, M. Siticon device scaling to the sub-10-nm regime. *Science* **2004**, *306* (5704), 2057-2060. DOI: 10.1126/science.1100731.

(229) Jones, E. C.; Ishida, E. Shallow junction doping technologies for ULSI. *Mat Sci Eng R* **1998**, *24* (1-2), 1-80. DOI: Doi 10.1016/S0927-796x(98)00013-8.

(230) Heo, S.; Hwang, H.; Cho, H. T.; Krull, W. A. Ultrashallow (< 10 nm) p(+)/n junction formed by B18H22 cluster ion implantation and excimer laser annealing. *Appl Phys Lett* **2006**, *89* (24). DOI: Artn 243516
10.1063/1.2405863.

(231) Sasaki, Y.; Godet, L.; Chiarella, T.; Brunco, D. P.; Rockwell, T.; Lee, J. W.; Colombeau, B.; Togo, M.; Chew, S. A.; Zschaetszch, G.; et al. Improved Sidewall Doping of Extensions by AsH3 Ion Assisted Deposition and Doping (IADD) with Small Implant Angle for Scaled NMOS Si Bulk FinFETs. *2013 Ieee International Electron Devices Meeting (Iedm)* **2013**.

(232) Perego, M.; Caruso, F.; Seguini, G.; Arduca, E.; Mantovan, R.; Sparnacci, K.; Laus, M. Doping of silicon by phosphorus end-terminated polymers: drive-in and activation of dopants. *J Mater Chem C* **2020**, *8* (30), 10229-10237. DOI: 10.1039/d0tc01856b.

(233) Ray, A.; Nori, R.; Bhatt, P.; Lodha, S.; Pinto, R.; Rao, V. R.; Jomard, F.; Neumann-Spallart, M. Optimization of a plasma immersion ion implantation process for shallow junctions in silicon. *J Vac Sci Technol A* **2014**, *32* (6). DOI: Artn 061302
10.1116/1.4896756.

(234) Wyrick, J.; Wang, X. Q.; Kashid, R. V.; Namboodiri, P.; Schmucker, S. W.; Hagmann, J. A.; Liu, K. Y.; Stewart, M. D.; Richter, C. A.; Bryant, G. W.; et al. Atom-by-Atom Fabrication of Single and Few Dopant Quantum Devices. *Adv Funct Mater* **2019**, *29* (52). DOI: ARTN 1903475
10.1002/adfm.201903475.

(235) Bowers, C. M.; Shestopalov, A. A.; Clark, R. L.; Toone, E. J. Multicomponent Patterning of Indium Tin Oxide. *Acs Appl Mater Inter* **2012**, *4* (8), 3932-3937. DOI: 10.1021/am300768f.

(236) Yamamoto, N.; Bernardi, F.; Bottoni, A.; Olivucci, M.; Robb, M. A.; Wilsey, S. Mechanism of Carbene Formation from the Excited-States of Diazirine and Diazomethane - an Mc-Scf Study. *J Am Chem Soc* **1994**, *116* (5), 2064-2074. DOI: DOI 10.1021/ja00084a052.

(237) Moss, R. A. Diazirines: Carbene precursors par excellence. *Accounts Chem Res* **2006**, *39* (4), 267-272. DOI: 10.1021/ar050155h.

(238) Ji, L.; Shi, J. Q.; Wei, J.; Yu, T.; Huang, W. Air-Stable Organic Radicals: New-Generation Materials for Flexible Electronics? *Adv Mater* **2020**, *32* (32). DOI: ARTN 1908015 10.1002/adma.201908015.

(239) Bertrand, G. Carbenes for the activation of small molecules and the stabilization of unusual phosphorus and boron species. *Abstr Pap Am Chem S* **2011**, *242*.

(240) Hudnall, T. W.; Rodrigues, R. R.; Dorsey, C. L. Reactivity studies of carbonyl-decorated carbenes with phosphorus- and antimony-containing compounds. *Abstr Pap Am Chem S* **2013**, *245*.

(241) Aissaoui, N.; Bergaoui, L.; Landoulsi, J.; Lambert, J. F.; Boujday, S. Silane Layers on Silicon Surfaces: Mechanism of Interaction, Stability, and Influence on Protein Adsorption. *Langmuir* **2012**, *28* (1), 656-665. DOI: 10.1021/la2036778.

(242) Shestopalov, A. Interfacial carbene reactions on hard and soft material interfaces. *Abstr Pap Am Chem S* **2017**, *253*.

(243) Belli, R. G.; Wu, Y.; Ji, H.; Joshi, A.; Yunker, L. P. E.; McIndoe, J. S.; Rosenberg, L. Competitive Ligand Exchange and Dissociation in Ru Indenyl Complexes. *Inorg Chem* **2019**, *58* (1), 747-755. DOI: 10.1021/acs.inorgchem.8b02915.

(244) Al-Hossainy, A. F.; Ibrahim, A. The effects of annealing temperature on the structural properties and optical constants of a novel DPEA-MR-Zn organic crystalline semiconductor nanostructure thin films. *Opt Mater* **2017**, *73*, 138-153. DOI: 10.1016/j.optmat.2017.08.007.

(245) Beamson, G. B., D. . High Resolution XPS of Organic Polymers **1992**. From Wiley Interscience The Scienta ESCA300 Database

(246) Packard, G.; Spaulding, C.; Taylor, A.; Hirschman, K.; Williams, S.; Kurinec, S. Selective phosphorus doping of polycrystalline silicon on glass using self-assembled monolayer doping (MLD) and flash anneal. *Mater Lett* **2021**, *305*. DOI: ARTN 130780 10.1016/j.matlet.2021.130780.

(247) Gao, X. J.; Guan, B.; Mesli, A.; Chen, K. X.; Dan, Y. P. Deep level transient spectroscopic investigation of phosphorus-doped silicon by self-assembled molecular monolayers. *Nat Commun* **2018**, *9*. DOI: ARTN 118 10.1038/s41467-017-02564-3.

(248) O'Connell, J.; Collins, G.; McGlacken, G. P.; Duffy, R.; Holmes, J. D. Monolayer Doping of Si with Improved Oxidation Resistance. *Acs Appl Mater Inter* **2016**, *8* (6), 4101-4108. DOI: 10.1021/acsami.5b11731.

(249) Gomez, D.; Ghosal, K.; Moore, T.; Meitl, M. A.; Bonafede, S.; Prevatte, C.; Radauscher, E.; Trindade, A. J.; Bower, C. A. Scalability and Yield in Elastomer Stamp Micro-Transfer-Printing. *Elec Comp C* **2017**, 1779-1785. DOI: 10.1109/Ectc.2017.318.

(250) Li, J. H.; Xu, L. S.; Kim, S.; Shestopalov, A. A. Urethane-acrylate polymers in high-resolution contact printing. *J Mater Chem C* **2016**, *4* (19), 4155-4165. DOI: 10.1039/c6tc01125j.

(251) Bonneau, R.; Liu, M. T. H. Kinetic and spectroscopic properties of carbene-diazirine ylides. *J Phys Chem A* **2000**, *104* (17), 4115-4120. DOI: DOI 10.1021/jp993711w.

(252) Liu, M. T. H. Laser Flash-Photolysis Studies - 1,2-Hydrogen Migration to a Carbene. *Accounts Chem Res* **1994**, *27* (10), 287-294. DOI: DOI 10.1021/ar00046a001.

(253) Liu, M. T. H.; Choe, Y. K.; Kimura, M.; Kobayashi, K.; Nagase, S.; Wakahara, T.; Niino, Y.; Ishitsuka, M. O.; Maeda, Y.; Akasaka, T. Effect of substituents on the thermal decomposition of diazirines: Experimental and computational studies. *J Org Chem* **2003**, *68* (19), 7471-7478. DOI: 10.1021/jo034949q.

(254) Duffy, R.; Shayesteh, M.; Thomas, K.; Pelucchi, E.; Yu, R.; Gangnaik, A.; Georgiev, Y. M.; Carolan, P.; Petkov, N.; Long, B.; et al. Access resistance reduction in Ge nanowires and substrates based on non-destructive gas-source dopant in-diffusion. *J Mater Chem C* **2014**, *2* (43), 9248-9257. DOI: 10.1039/c4tc02018a.

(255) Li, X. M.; Péter, M.; Huskens, J.; Reinhoudt, D. N. Catalytic microcontact printing without ink. *Nano Lett* **2003**, *3* (10), 1449-1453. DOI: 10.1021/nl034423l.